

Fatigue Assessment of Steel Frames un- der Aerodynamic Loads

In Application to Steel Hollow
Section Portal Frames Sup-
porting Traffic Signs

B.R. Stamenkovits

Fatigue Assessment of Steel Frames under Aerodynamic Loads

In Application to Steel Hollow Section Portal
Frames Supporting Traffic Signs

by

B.R. Stamenkovits

to obtain the degree of Master of Science
at the Delft University of Technology,
to be defended publicly on Monday May 30th, 2022 at 09:30 AM.

Student number: 4292146
Project duration: May 26th, 2021 – May 30th, 2022
Thesis committee: Prof. dr. M. Veljkovic, TU Delft, chair
Dr. ir. P. van der Male, TU Delft, supervisor
Ir. R. Yan, TU Delft, supervisor
Ir. T.J. Focks, Antea Group, supervisor

An electronic version of this thesis is available at <http://repository.tudelft.nl/>.

Abstract

Although modern technologies such as smartphones with GPS functionality make navigation substantially easier, automobilists still rely on traffic signs to inform them which exit to take or which lane to follow. These traffic signs on highways are of substantial size rendering them, and their support structures, extremely susceptible to aerodynamic load induced fatigue damage.

In this thesis traffic sign support structures in the form of steel portal frames consisting of square hollow sections are considered. *Antea Group* designs such structures using conservative generalized methods prescribed by the *Eurocode* and *ROK* norms. In order to investigate whether or not the structures may be optimized with respect to fatigue, a more elaborate load and dynamic response model is formulated.

Aerodynamic loads are primarily considered as these are the most significant dynamic loads, which are governing for fatigue damage. The two types of aerodynamic loads that are considered are traffic induced pulse loads generated by large vehicles passing close to the sign, and stochastic turbulent wind flow. The former is in the form of a pulse load, while the latter is in the form of a super-position of sinusoidal waves based on the Solari wind turbulence spectrum. These loads are applied to a dynamic finite element method developed in Python specifically for this thesis, consisting of one dimensional Euler-Bernoulli beam elements. The dynamic response is evaluated using a modal analysis. The resulting dynamic cross-sectional signals are transformed into weld-stress signals using a finite element model in *IDEA StatiCa*. Finally the Rainflow Cycle Counting algorithm is used in combination with the Palmgren-Miner rule and SN-curves provided by the Eurocode in order to estimate the fatigue damage of the structure during its lifetime.

This methodology is applied to an existing reference structure, and an optimized design. The optimized design is optimized according to the Eurocode with respect to the ultimate and serviceability limit state, but fails in the fatigue limit state. From the results it is established that the calculation model presented in this thesis yields much lower magnitudes of stress range cycles compared to those found in the design norms, leading to significantly reduced fatigue damage. However this model does not take instantaneous wind gust loads into account, reducing its range of applicability. It is suggested to utilize the simulation model for loads that occur more than 10^5 times in a 50 year life time, but utilize the existing design norm models for loads that occur less often. The traffic induced pulse loads are found to be of significant size under the current assumptions, but due to a lack of research in this field the validity of the magnitude of the pulse loads remains uncertain.

Ultimately it is shown that there is potential for optimization with respect to fatigue, but the simulation model should be used on more structures and should be further evaluated in order to create a more simplified and generalized analytical model that may be applied quickly to any design or even structure.

Preface

This past year I have devoted myself to final stages of my Masters program. Especially with the pandemic sweeping across the globe this has not always been smooth sailing, but nevertheless it was an interesting challenge I am glad to have successfully tackled.

Throughout my studies I have gained a passion for parametric design and automation within engineering. Not only does this reduce the amount of mundane calculations in the design process, it also allows for more complex calculations to be performed more quickly. During my Bachelors at the TU Delft I received a solid introduction into the Python programming language, which I developed a great affinity towards. Ever since I have continued to pursue this interest, which has helped me greatly for this thesis. Even though my specialization track within the Structural Engineering Master's is primarily focused on steel structures, I have always had a great interest in the dynamic behavior of structures. *Antea Group* had the perfect project for me: combining dynamic models with a complex parametric calculation model for steel structures.

The road towards this thesis has been a formidable challenge and I most certainly could not have done it on my own. Firstly I would like to thank my committee. Milan Veljkovic has provided me with invaluable guidance and advice, as the largest challenge for this thesis was finding the right focus within the broad topic at hand. Pim van der Male has helped me greatly by extended his knowledge on stochastic load modelling and numeric methods for solving dynamic systems, as both aspects were only introduced in the main Master's program. Rui Yan has been very helpful in providing me with suggestion with respect to the joint modelling even though the focus of the thesis ended up somewhat shifting away from this aspect. Thijmen Jaspers Focks has helped me immensely with guiding me through every aspect of the thesis and providing me with valuable feedback. I got to meet with him on a weekly basis, and he always had great suggestions every time I came with a problem or question. Even though I did not end up interacting with the company as much as I would have liked due to the pandemic, everybody at *Antea Group* has been incredibly kind and helpful.

I would also like to thank the staff of *Codam Coding College* for allowing me to work along side them in their office, providing me with a great work environment while living in Amsterdam during the pandemic. And finally I would like to thank all my friends and family that have supported me during this last stage of my Masters.

B.R. Stamenkovits
Delft, May 2022

Contents

1	Introduction	1
1.1	Problem Statement	2
1.2	Research Questions	2
1.2.1	Sub-Research Questions	2
1.3	Overview	3
1.3.1	Reference Structure	3
1.3.2	Calculation Model Overview	4
1.3.3	Report Overview	4
1.4	Scope	5
2	Traffic Induced Aerodynamic Loads	7
2.1	Creamer et al. (1979)	8
2.1.1	Limitations of Model	9
2.2	Cook (1996) & Hosch (2011).	9
2.2.1	Cook (1996).	9
2.2.2	Hosch (2011)	10
2.2.3	Limitations of Approach	10
2.3	Lichtneger and Ruck (2015)	11
2.4	Design Pulse Load	13
2.4.1	Peak Pressure	14
2.4.2	Lateral Transient Load	14
2.4.3	Torsional Load	16
2.4.4	Limitations of Approach	17
2.4.5	Application of Approach	18
3	Atmospheric Wind Loads	21
3.1	Eurocode Wind Loads	21
3.1.1	Mean Wind Speed	21
3.1.2	Wind Gusts	22
3.2	Simulation of Stochastic Wind Load	23
3.2.1	Load Definition	23
3.2.2	Wind Speed Simulation	23
3.2.3	Cut-Off Frequency	25
3.2.4	Frequency Sampling	26
3.3	Application of Approach	27
3.4	Limitations of Approach	28
4	Dynamic Finite Element Analysis	31
4.1	Finite Element Discretization.	31
4.1.1	Element Definition	32
4.1.2	Sub-Systems	32
4.1.3	Shape Functions	33
4.1.4	Sub-System Mass and Stiffness Matrices.	33
4.1.5	Element Matrices	34
4.1.6	Local and Global Coordinate Systems	35
4.2	Damping	36
4.2.1	Material Damping.	37
4.2.2	Thermoelastic Damping	37
4.2.3	Mechanical Damping Ratio	38

4.3	Equation of Motion	38
4.3.1	Assembly of System Matrices and Vectors	38
4.3.2	Boundary Conditions	38
4.4	Direct Integration Solution	39
4.4.1	Numerical Solution First Order Ordinary Differential Equation	39
4.4.2	Numerical Solution Simple Mass-Spring System	40
4.4.3	Numerical Solution Full System	40
4.5	Modal Solution	40
4.6	Internal Loads	42
4.7	Model Validation	43
4.7.1	System Verification	43
4.7.2	Solver Verification	45
4.7.3	Internal Load Verification	46
4.8	Element Size	46
4.9	Limitations of Model	48
5	Joint Load Distribution	51
5.1	Joint Description	51
5.2	Finite Element Analysis Software	52
5.2.1	Component Method	52
5.2.2	Component Based Finite Element Method	53
5.3	CBFEM Model Overview	53
5.3.1	Element Types	53
5.3.2	Loads	54
5.3.3	Boundary Conditions	54
5.3.4	Limitations of FEM Model	55
5.4	Stresses in Welds	55
5.4.1	Overview of Welds	55
5.4.2	Fatigue Weld Stress	56
5.4.3	Stress Components	57
5.5	Governing Weld	58
6	Fatigue Verification	61
6.1	Fatigue Damage Estimation	61
6.1.1	Damage	61
6.1.2	Cycles to Failure	61
6.2	Cycle Counting	63
6.2.1	Cycle Counting in Norms	63
6.2.2	Narrow-band Stochastic Process	64
6.2.3	Wide-band Stochastic Process	65
6.3	Reference Structure	65
6.3.1	Norms Fatigue Damage Evaluation	66
7	Calculation Model	69
7.1	Overview of Model	69
7.2	Relative Wind Load	69
7.3	Probabilistic Loads	70
7.3.1	Traffic Induced Pulse Loads	71
7.3.2	Turbulent Atmospheric Wind Loads	71
7.3.3	Combination of loads	72
7.3.4	Limitations of Approach	73
7.4	Stability	74
8	Design Optimization	79
8.1	Member Optimization	79
8.1.1	Design Considerations	79
8.1.2	Design Choices	79

8.2	Joint Optimization	79
8.2.1	Component Method	80
8.2.2	Design Considerations	81
8.2.3	Design Choices	82
9	Results	85
9.1	Accuracy of Analytical Joint Model	85
9.2	Wind and Traffic Load Comparison	86
9.3	Norms and Simulation Comparison	88
9.3.1	Load Definition	88
9.3.2	Cycle Counting	91
9.4	Fatigue	93
9.4.1	Applicability of Simulated Results	94
9.4.2	Traffic Induced Fatigue Damage	96
10	Conclusion	97
10.1	Calculation Model	97
10.2	Research Questions	98
10.3	Results and Design Recommendations	99
10.4	Further Work	99
	Bibliography	101
A	Setup of Dynamic Model	105
B	Shape Functions	129
C	Analytical Eigenfrequencies	131
D	Case Study	137

1

Introduction

Millions of people utilize automotive transportation means in order to reach their destinations on a daily basis. Although modern technologies such as smartphones with GPS functionality make navigation substantially easier, automobilists still rely on traffic signs to inform them which exit to take or which lane they should follow. On highways or high-speed roads these traffic signs are metallic plated structures of sizable dimensions as the text must be large enough to be read at a suitably large distance from the sign for fast traveling vehicles. Due to the substantial dimensions of the signs, they are extremely susceptible to aerodynamic effects. The resulting loads are transferred to the support structure. For busy highways with a multitude of traffic lanes the span of the support structure is large and a truss-like structure is required. However for less busy highways and some regular roads there is no need for a complex truss structure, and a simple square hollow section will suffice. The traffic sign support structures for these types of roads may come in various designs: mast structures, cantilevered beam-column structures, portal frames, etc. In the case of steel hollow section portal frames the main function of the support structure is to support the traffic signs, by transferring their self-weight and aerodynamic loads to ground.



Figure 1.1: Photograph of typical hollow section steel frame located in Amsterdam near the RAI convention center. Photograph taken from Google Street View [17]

1.1. Problem Statement

The engineering firm *Antea Group B.V.* helps design traffic sign support structures for Dutch roads and highways. In order to speed up the design process a design tool has been developed: the *PMO Tool*. This tool has been developed in Python and fully automates the design process including verification of the structure and generating all of the relevant reports; it connects various Excel calculations with finite element models and geotechnical analyses. In the verification the ultimate, serviceability, and fatigue limit state are considered, and many design aspects of the structure can be optimized with respect to these limit states.

This tool may be used to design new structures or evaluate existing structures. Many of the designs *Antea Group* is asked to review are over-dimensioned, and it is suspected they are designed based on a set of extremely conservative rules-of-thumb. As these support structures do not require to carry a lot of static weight, they can be dimensioned relatively slender, especially with respect to the dynamic loads in the form of turbulent wind loads or gust loads due to passing traffic. The dynamic response of a structure is always a complex and time consuming analysis. As a result it is often more economical to increase the amount of steel in a structure, than pay an engineer to determine the exact dynamic response.

Traffic sign support structure are predominantly loaded by dynamic loads, which may be orders of magnitude larger than the static self-weight of the structure. Gaining a better understanding of the dynamic response of these structures could be very valuable. The dynamic response of the structure determines how the loads and stresses in the structure change over time, which mainly affects the accumulation of fatigue damage over the life time of the structure. It is therefore of interest to investigate more in depth what type of dynamic response is expected due to the aerodynamic loads on the structure, and what effect this will have on the fatigue life-time of the structure.

The relevant building codes and norms allow the dynamic response to be approximated by a simple formula, relating the dynamic behavior to a single parameter: the maximum instantaneous wind gust load. In reality the dynamic response depends on the dimensions, geometry, and stiffness of the structure, which are omitted in the aforementioned simplified method. Furthermore these norms and codes do not explicitly take wind gusts generated by traffic into account, instead conservative methods and assumptions are required to be taken in order to ensure any possible traffic induced loads fall under the "umbrella" of loads defined.

1.2. Research Questions

In order to investigate the dynamic behavior of these type of support structures the following set of research questions is determined. In order to narrow the scope of the research, only steel square hollow section portal frame support structures are considered. The main research question this thesis aims to answer is as follows:

What is the most appropriate way of modelling the dynamic behavior of traffic sign portal frame support structures, and what influence does this have on the fatigue assessment of the structure in question?

It is of importance to determine an appropriate and accurate model which determines the dynamic response of the structure relative to the existing model in the design codes. Furthermore it is of interest to determine what the effects on the fatigue-life of the structures of this more accurate model are, as the fatigue limit state is primarily affected by the dynamic loads in question.

1.2.1. Sub-Research Questions

In order to aid in answering the main research question and goal of this thesis, the following sub-research questions are developed:

How well can the load distribution within a structural detail be approximated by analytical models?

How do simulated dynamic wind loads compare to static instantaneous wind gust loads, such as the ones employed by the design norms?

Do traffic induce aerodynamic loads play a significant role in the dynamic response of a traffic sign steel portal frame support structure, and to what extent does this influence the fatigue life of the structure?

It is important to perform an accurate global dynamic analysis, but ultimately the fatigue damage is expected to occur in a small detail of the structure. In the case of steel portal frames, the welds utilized in the corner joints are highly susceptible to fatigue damage. Hence, it is important to translate the dynamic global response into a dynamic local response at the location of the welds. For this the load distribution within the joint detail should be approximated by an appropriate model.

Using a more elaborate calculation model compared to the design norms to determine the dynamic response of the structure will yield different results. It is important to investigate how and why these results are different, and in what range of applicability the different results lie.

A previous thesis by Fikkers suggests that wind loads induced by large trucks passing near the sign may lead to fatigue damage [10]. It is therefore important to consider how those loads differ from the turbulent atmospheric wind loads, and how the dynamic response of these type of loads affects the fatigue life of the structure compared to the atmospheric wind loads.

1.3. Overview

The overall structure of the thesis consists of the development of a parametric calculation model in Python which can be applied to a variety of structures, and may be integrated with the existing PMO tool if desired, seeing as the PMO tool is at its core driven by python scripts. This model is used to help investigate the relevant aspects of the presented research questions by applying it to a reference structure design and an optimized structure design.

1.3.1. Reference Structure

A reference structure, consisting of an existing design, is used to analyze and compare the calculation model to the methods found in the Dutch and European building codes and norms. The reference structure considered in this thesis is illustrated in figure 1.2 and consists of a simple steel frame made up of Square Hollow Sections (SHS), which are used to suspend two large traffic signs (the left being smaller than the right). Several key dimensions are shown in table 1.1. Figure 1.3 illustrates a 3d impression of the joint, for a more in depth description of the joint see chapter 5. The structure in question has been designed based on simple conservative rules of thumb, and is over-dimensioned in most regards. Nevertheless it is a characteristic representation of a typical existing traffic sign portal frame support structure, and is therefore useful for the evaluation of the calculation models.

Table 1.1: Key dimensions of the reference structure found in figure 1.2

Description	Symbol	Value	Units
Span support structure	L	16100	mm
Height support structure	H	6000	mm
Width sign 1 (left)	b_1	3000	mm
Width sign 2 (right)	b_2	3500	mm
Height sign 1 (left)	h_1	2100	mm
Height sign 2 (right)	h_2	3000	mm
Profile beam	[-]	SHS300/8	[-]
Profile column	[-]	SHS350/10	[-]



Figure 1.2: Overview of traffic sign support structure

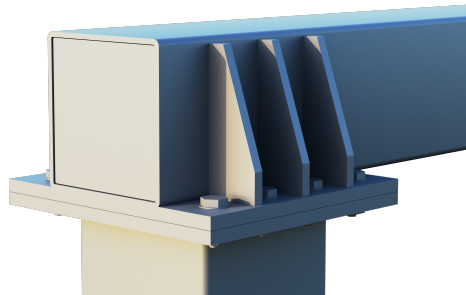


Figure 1.3: 3D impression of joint

1.3.2. Calculation Model Overview

In this thesis the research questions are answered by developing a calculation model performed entirely in Python. This calculation model consists of four distinct steps: load definition, dynamic response evaluation, joint load distribution analysis, and fatigue damage estimation. These four steps are shown in figure 1.4, identifiable by their distinct colors. The first step: load definition is split into two sub steps for the two different types of loads present.

The first step is the load definition, in which two sub-models are developed: a load model for the traffic induce pulse loads, and a load model for the turbulent atmospheric wind loads. The wind loads are applied to a discretized structure in the dynamic model, which performs a dynamic simulation resulting in a set of internal cross-sectional load signals. In the subsequent step in the calculation model the load distribution within the joint is analyzed and the internal cross-sectional load signals are converted into weld stress signals. Finally this stress signal is analyzed using a Rainflow Cycle Counting algorithm to determine which stress range cycles and number of stress cycles occur. This data is then applied to the Palmgren-Miner Rule in order to estimate the fatigue damage of the relevant weld.

1.3.3. Report Overview

The way this thesis report is structured is as follows: in the first couple of chapters the individual model components shown in figure 1.4 are outlined. Then two representative structures are analyzed using the calculation model, from which the relevant conclusions are drawn.

In chapters 2 and 3 the load model for the traffic induce pulse loads and atmospheric turbulent wind loads respectively are outlined. The traffic loads are based on load models found in literature, while the atmospheric loads are based on common techniques for simulating wind loads based on a power

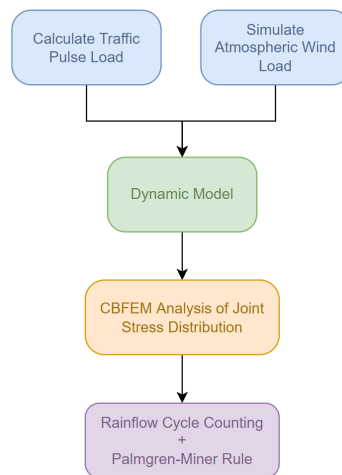


Figure 1.4: General overview of calculation model

spectral density distribution. In chapter 4 a finite element method approach is used to discretize the structure into 1D beam elements. This dynamic system is then used to numerically solve the dynamic response of the structure due to traffic and wind loads. The choice of element size is discussed as it determines the accuracy of the solution, but also significantly impacts the simulation run-time. In chapter 5 the joint at the corner of the frame is analyzed in order to determine the joint load distribution by creating curve fitted functions for each type of cross-sectional load applied to the joint. In chapter 6 the Rainflow Cycle Counting algorithm and the Palmgren-Miner rule in combination with SN-curves for fatigue damage estimation are discussed.

In chapter 7 the model components are aggregated into the complete calculation model. Several considerations with respect to the calculation model as a whole are also discussed. In chapter 8 the design of the reference structure is discussed and an optimized structure with respect to the ultimate and serviceability limit state is developed. In chapter 9 the calculation model from chapter 7 is used in order to analyze the dynamic response and fatigue damage estimation for the reference structure and optimized structure, which are then extensively compared. Finally chapter 10 discusses the conclusions and recommended future work.

1.4. Scope

The scope and range of applicability of the model is primarily governed by the loads. The structure in question is exposed to a variety of loads such as wind, snow, temperature, accidental, uneven soil settlement. However as the dynamic behavior of the structure influences its fatigue life-time the most, it is primarily the aerodynamic loads which are of interest.

For the atmospheric wind loads this is specifically limited to general turbulence, which is extensively discussed in chapter 9. Furthermore the loads are mainly applied to the signs in the form of concentrated loads, the distributed loads on the members are for the most part disregarded. The loads are evaluated with respect to structural integrity, deformations, and fatigue. The effects of stability through second-order effects and aerodynamic effects such as flutter are assumed to be negligible.

The fatigue damage of a structure in general is assessed by considering details most susceptible to large stress fluctuations under dynamic loads. In this thesis it is assumed that these details are located inside of the corner joints as discussed in chapters 5 and 6. However different details of the structure should also be considered: beam end-plate splices, sign attachment to beam, foundation details.

This research as a whole is unfortunately limited in scope due to the complexity of the simulation model at hand, and the time consuming nature of the required calculations. The simulation model should be translated into an analytical model, this is however beyond the scope of this thesis. What this thesis does is lay the foundation for future work by developing a sophisticated model, and illustrating its potential; the applicability of the model is contextualized through its application to two structural designs outlined in this thesis.

2

Traffic Induced Aerodynamic Loads

When a large vehicle travels at high speeds a significant amount of air is displaced resulting in large wind gusts in its vicinity as it passes. Unfortunately these types of wind loads are highly complex as they depend on several parameters [10]:

- Vehicle size
- Vehicle shape
- Vehicle speed
- Distance between vehicle and traffic sign
- Number of vehicles grouped together
- Size of structural element (traffic sign)

As a vehicle travels, especially at high speeds, it displaces air in front of it. Larger vehicles will have a large frontal surface area, leading to a larger volume of displaced air [29]. The three-dimensional shape of the vehicle does not necessarily influence the amount of air displaced, as this is primarily dictated by the frontal surface area; however it does determine how aerodynamic the vehicle is; this influences the turbulence of the airflow around the vehicle. The speed of the vehicle will determine how fast the air around the vehicle is displaced. Based on Bernoulli's flow principle, aerodynamic loads are quadratically proportional to the speed of the medium (in this case atmospheric air at ground level). Air flowing around a vehicle is non-uniform as can be seen in figure 2.1, hence the distance between the passing vehicle and traffic sign is of a large influence. The wind gusts will ultimately be acting on the traffic signs themselves, the larger the surface area of the sign, the larger the wind load.



Figure 2.1: Aerodynamic profile for a truck [5]

Due to the complex nature of these traffic induced aerodynamic loads building codes (including the Eurocode) tend to not provide any explicit models that simulate this type of loading. Instead they provide simplified conservative static models, which have various (dynamic) factors applied to them in

order to take dynamic actions into account. In scientific literature various studies have been conducted on fatigue damage of highway signs. However the scope and focus vary greatly due to the variability in types of sign structure design, highway types, and vehicle types. In a thesis by S. Ginal [16] a review of various studies has been outlined, and has been further expanded upon by C.D. Fikkers [10]. The next sections will outline the most applicable models for the scope of this thesis and how they may be implemented.

2.1. Creamer et al. (1979)

The first significant research publication on traffic induced aerodynamic loads originates from a research report by Creamer et al (1979) [6]. In this report three truss structured cantilevered sign support are analyzed through the use of strain gauges applied to the webs and chords of the truss structure. The structure was manually excited in order to obtain strain measurements, which were used in conjunction with wind tunnel studies about the flow of air particles around "vehicle shaped obstructions" in order to create an analytical aerodynamic load.

The resulting pulse load starts at 0 seconds, contains a single peak at 0.125 seconds and ends at 0.375 seconds. The peak pressure applied to the sign is $p_{max} = 1.23$ psf (pounds per square foot) or $p_{max} = 5.89 \cdot 10^{-5}$ N/mm². The time signature of this pulse load (see figure 2.2) is based on an "average" representative truck of roughly 30 feet (9.14 meters) traveling at a speed of 55 mph (88.51 kph). This analytical model assumes that the pulse starts at the same time as the truck passes underneath the sign, has a peak after the first 10 feet (3.05 meters) of the truck have passed the sign and ends as the end of the truck passes underneath the sign. This pulse describes the pressure applied to the sign, which decreases linearly over the height. At the bottom of the sign the pressure acting on the sign is equal to the value computed by the pulse load, and decreases linearly to zero pressure at the top of the sign, see figure 2.3. From this distribution the pulse load of a truck passing may be computed according to equation 2.1 .

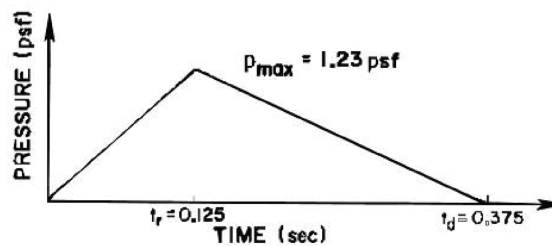


Figure 2.2: Pulse (pressure) load according to Creamer [6]

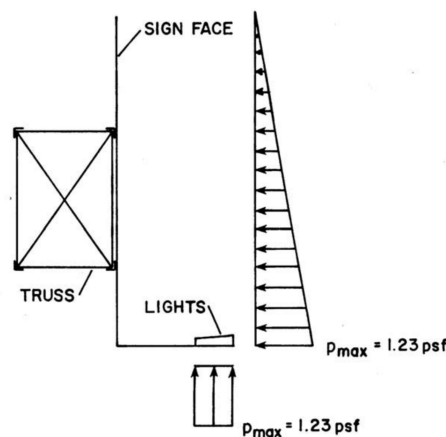


Figure 2.3: Side view of theoretical pressure distribution acting on sign structure and catwalk according to Creamer [6]

$$F(t) = \frac{1}{2}Ap(t) \quad (2.1)$$

Where:

$F(t)$ = Pulse load as a function of time in N

A = Sign surface area in mm^2

$p(t)$ = Pressure described by Creamer [6] as a function of time in N/mm^2

2.1.1. Limitations of Model

This model has been the basis of a significant number of other research examining sign structures and traffic induced wind loads, however the load model is largely based on assumptions. The load applied to the structure is based on a simplistic pulse load containing only one peak, which has been calibrated to fit the strain gauge measurements. As a result the load model is relatively accurate for the specific vehicle type and sign structure outlined in the research report, but may not scale well for other vehicle types and/or sign structures. Two separate measurements were done (strain gauges excited manually and wind tunnel experiments), which are then related to each other through numerical calibration.

When it comes to the wind tunnel experiments it is unclear what the exact shape of the vehicle was, only the general dimensions. This research originates from the United States of America where trucks have the engine block in front of the driver, while European trucks have the engine underneath the driver; the latter resulting in a flatter profile with different (less) aerodynamic properties. Furthermore the time signature of the pulse load assumes that the loading is restricted to the time that the truck is underneath the sign. In reality air particles are displaced not only at the location of the truck, but also in front and behind the truck, resulting in a theoretically longer pulse load. It is also assumed that only a single peak occurs, in reality turbulent air flow around the truck will be more complex with multiple peaks. Finally a linear pressure distribution is assumed across the height of the sign, which is most likely not linear but rather has a quicker fall of over an increasing height. The distance between the truck and the sign is also not taken into account, and it is assumed that the pressure distribution goes to zero at the top of the sign.

When it comes to the strain gauge measurements, these were done for a truss structure containing maintenance walkways with lights, while the structure under consideration in this thesis is composed of slender hollow sections without such walkways. It is also important to note that the loads on the signs in this research were established not based on measurements on the signs, but from the structure's response as a whole. These two different structures will have a different dynamic response to dynamic loads. This model as a whole can be used as a reference point in terms of load magnitude but does not suffice to describe various load scenarios for the structure under consideration in this thesis.

2.2. Cook (1996) & Hosch (2011)

In a research conducted by Cook et al (1996) in collaboration with Florida Department of Transportation wind loads acting on sign structures were experimentally determined [31]. This research was expanded upon and translated into an analytical load model by Hosch (2011) [9].

2.2.1. Cook (1996)

Opposed to Creamer et al. the wind loads measured by Cook were determined directly from empirical measurements, resulting in a more accurate representation of the pulse load. In this research pressure transducers were placed on a highway bridge in order to directly measure aerodynamic pressures. The bridge is relatively stiff compared to wind loads, mitigating any stiffness effects of the structure on the experienced wind load.

For this research a specific type of truck is considered: a large (American) semitrailer with an air deflector over the cab. The measurements were taken from an active highway where a spotter would look out for trucks fitting the aforementioned specifications, after which the measurements were started. As a result the exact dimensions are unknown (only a picture was taken to classify the profile/shape of the truck). On this particular highway the average speed of the trucks was 70 mph (112.65 kph). A typical plot of pressure over time for this research is shown in figure 2.4.

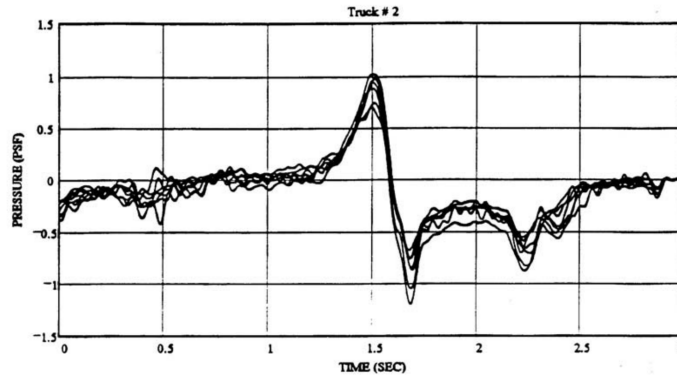


Figure 2.4: Typical plot of pressure over time measurements by Cook et al [31]

2.2.2. Hosch (2011)

In a research by Hosch (2011), the experimental data from the research by Cook et al. is used in order to develop an analytical load model which incorporates different vehicle speeds [9]. The main time signature is derived based on measurements of typical truck induced wind loads of trucks traveling 70mph. These are then quadratically extrapolated to other vehicle speeds. These load models were then validated using different structures (cantilever type, bridge type, and variable message sign structures) represented as single degree of freedom systems. Using a modal analysis of the structures it was found that the modal shapes could be considered to be vibrating independently from each other, hence the structures could be modeled by a single degree of freedom system.

The magnitude of the peak pressure can be computed using equations 2.2 and 2.3, which take the speed of the truck and the height of the sign attachment location into account. The pressure distribution across the height is linear, and based on the design rules provided by the American Association of State Highway and Transportation Officials (AASHTO) [9].

$$P(z) = P_v - 0.0763h \quad (2.2)$$

$$P_v = P_0 \left(\frac{v}{70} \right)^2 \quad (2.3)$$

Where:

$P(z)$ = Peak pressure distributed over height z in pounds per square feet (psf)

P_v = Peak pressure scaled by velocity v

P_0 = Base peak pressure

h = Elevation increase from 6 meters above the road

α = Magnitude factor

v = Truck speed in mph

Hosch recommends an equation for computing the base peak pressure P_0 for "bridge-type VMS support structures" [9] consisting of truss sections. This formula is not directly applicable for slender hollow section frames under consideration in this thesis. Instead the base peak pressure is conservatively estimated as 1.5 psf (pound per square foot) based on visual inspection of the design graphs provided by Hosch [9]. Using the aforementioned method the total transient load on the sign may be determined, see figure 2.5 as an example.

2.2.3. Limitations of Approach

The research conducted by Cook and Hosch is significant improvement over the older research by Creamer. Firstly it is based on direct measurements of pressures experienced at a location above the road where trucks pass instead of obtaining the load/pressure backwards through numerical calibration. Secondly Hosch has translated the measured pressures into an analytical load model which can be scaled for different vehicle speeds.

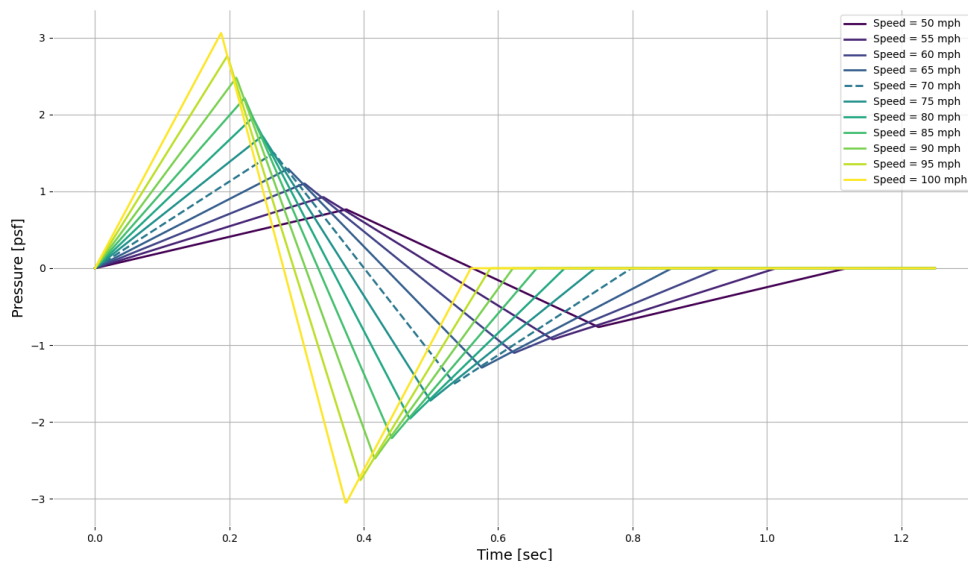


Figure 2.5: Pressure pulse load according to Hosch [9] for different vehicle speeds

However this model is not perfect, firstly the original pressure measurements were conducted by variable reluctance pressure transducers at a single location above the road [31]. There may be significant variations in pressure in the area above the road, the research does not seem to take this into account by taking measurements at different locations relative to the center of the road. Further more for the pressure distribution across a sign Hosch recommends a continuous distribution across the width and a linearly decreasing distribution across the height according to the American design codes. In reality there will be a pressure fall off along the width and a non-linear pressure fall off along the height of the sign.

The load model by Hosch also does not distinguish between vehicle types, this is due to the original measurements by Cook which were based on observational data. The exact dimensions of the vehicles could not be determined as the measurements were done on-site and the only information recorded for each truck was its measured speed and a photograph to indicate its general profile.

2.3. Lichtneger and Ruck (2015)

The most extensive study to date done on traffic induced loads on sign structures is a research conducted by Lichtneger and Ruck [29]. In this study full-scale experiments were conducted to quantify the aerodynamic loads produced by six different vehicle types (car, van, truck, truck with trailer, trailer-truck, bus) on three different square structural plate elements (0.5x0.5m, 1.0x1.0m, 1.5x1.5m) at different orientations relative to the traveling direction of said vehicles. At different locations on the plates the differential pressure was measured, by integrating these values over the plate surface-area the total transient load acting on the plate could be calculated. Aerodynamic loads are generally governed by the square of velocities, which is why the measured transient load was normalized through a factor $c_F(t)$ (see equation 2.4), which depends on an arbitrary vehicle aerodynamic load F_v . It should be noted that this arbitrary aerodynamic load has no physical meaning, but simply takes the velocity and frontal surface area of the vehicle and the air density into account by representing the load by an equation which is similar to the aerodynamic drag load of the vehicle.

$$c_F = \frac{F_p}{F_v} = \frac{F_p(t)}{\frac{1}{2}\rho A_v U^2} \quad (2.4)$$

Where:

- c_F = Non-dimensional transient force coefficient
 F_p = Transient force acting on plate in N
 F_v = Aerodynamic vehicle load in N
 t = Time in s
 ρ = Air density in kg/m³
 A_v = Frontal surface area of vehicle m²
 U = Vehicle speed in km/h

The coefficient c_F is a dimensionless function which depends on various variables. In order to compare the behavior of each vehicle type, this coefficient was normalized for the vehicle length, vehicle speed, and relative distance between the plate and the vehicle; resulting in the coefficient c_F^* (see equation 2.5)

$$c_F^*(\tau) = \frac{c_F(\tau)}{k(z)} \quad \text{where} \quad \tau = \frac{t \cdot L}{U} \quad (2.5)$$

Where:

- c_F^* = Non-dimensional normalized transient force coefficient
 c_F = Non-dimensional transient force coefficient
 k = Non-dimensional reduction factor depending on the distance between the plate and vehicle
 z = Distance between top of vehicle and bottom of sign in m
 t = Time in seconds
 L = Vehicle length in m
 U = Vehicle speed in km/h

The non-dimensional reduction factor taking into account the distance between the plate and the top of the vehicle $k(z)$ is different for each vehicle as each vehicle has a different aerodynamic profile, resulting in different loads. This reduction decrease over distance can be described by a cubic function as shown in figure 2.6.

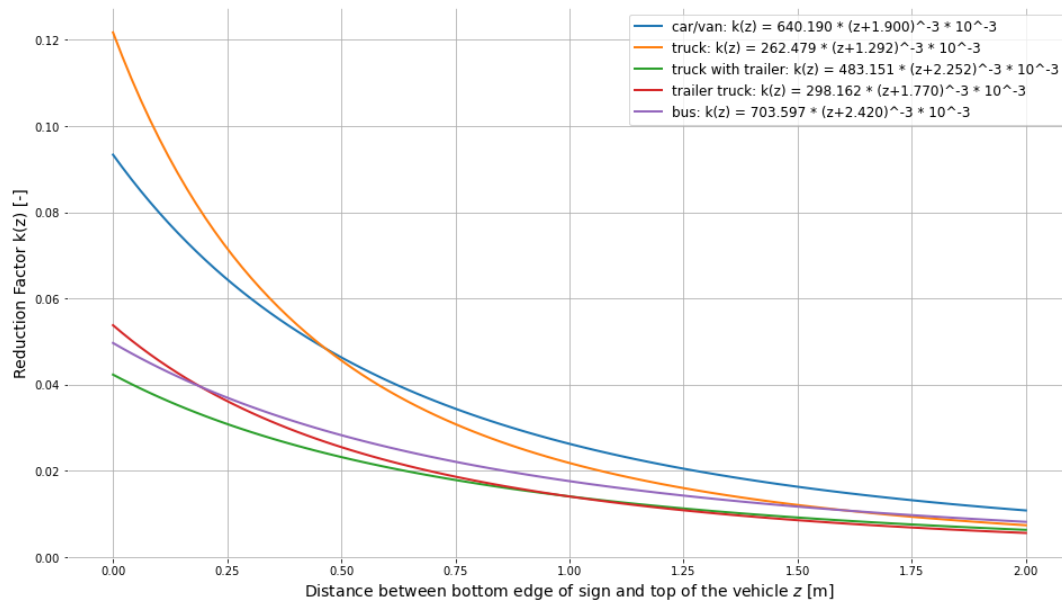


Figure 2.6: Non-dimensional reduction factor taking into account the distance between the plate and the top of the vehicle $k(z)$ [29]

Various graphical representations of coefficient $c_F^*(\tau)$ varying over time have been published by Lichtneger and Ruck [29], an example of which is given by figure 2.7 showing the results for a trailer-truck passing underneath a 1.5x1.5m square sign. In this thesis the ensemble average of various runs

for the various vehicles have been approximated by a set of linear functions. By using these estimated values of $c_F^*(\tau)$ and the definitions given by equations 2.4 and 2.5, the theoretical transient load for different vehicle types may be determined, and is shown in figure 2.8. The distance between the top of the vehicle and the bottom edge of the sign have been taken into account for a typical head clearance of 5 meters. For the smaller vehicles such as cars and vans a maximum velocity of 120 km/h was assumed, and for the larger vehicles (e.g. trucks) a maximum velocity of 80 km/h was assumed.

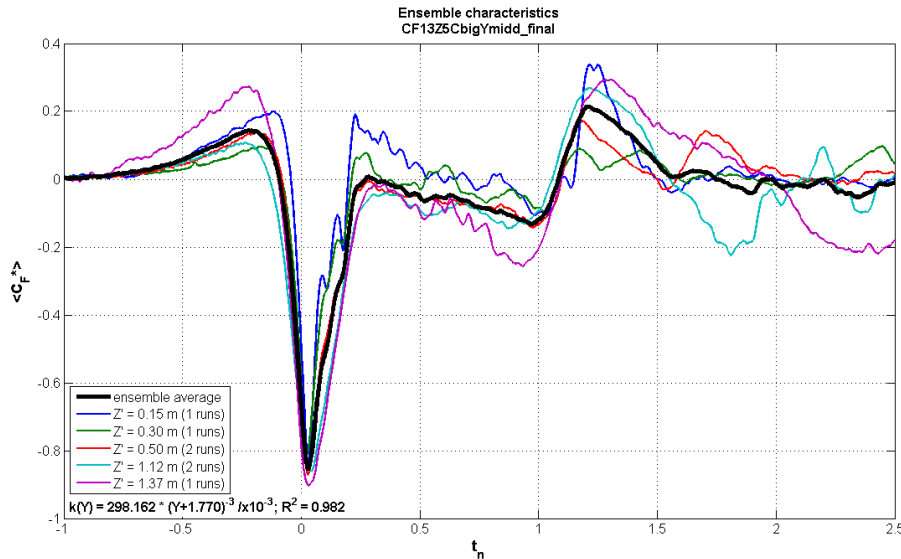


Figure 2.7: Normalized transient load factor varying over time for a trailer-truck traveling 80 km/h underneath a 1.5x1.5m plate [29]

From figure 2.8 it can be inferred that the trailer-truck is the governing vehicle type as the resulting pulse is the largest in amplitude and length, which will induce the largest dynamic response in the structure. The reason for this is that the trailer truck has the largest frontal surface area resulting in a large displacement of air. Furthermore it is the tallest vehicle meaning the top of the vehicle is closest to the sign which has the most influence on the aerodynamic loads on the sign. Finally it is one of the longest vehicles, resulting in one of the longest pulses.

The final pulse load is computed through equation 2.6, where $c_F^*(\tau)$ describes the time signature of the vehicle, k takes the distance between the vehicle and the sign into account, and F_v determines the load magnitude based on the vehicle dimensions and speed.

$$F_p(t) = c_F^*(\tau) \cdot k(z) \cdot F_v \quad \text{where} \quad \tau = \frac{t \cdot L}{U} \quad (2.6)$$

Where:

- c_F^* = Non-dimensional normalized transient force coefficient
- k = Non-dimensional reduction factor depending on the distance between the plate and vehicle
- F_v = Aerodynamic vehicle load in N as described by equation 2.4
- z = Distance between top of vehicle and bottom of sign in m
- t = Time in seconds
- L = Vehicle length in m
- U = Vehicle speed in km/h

2.4. Design Pulse Load

From the three aforementioned studies the latter conducted by Lichtneger and Ruck [29] is the most detailed by analyzing different vehicles in a controlled environment, taking the vehicle dimensions and the distance between the vehicle and the sign into account. The main draw back compared to the other studies is that it doesn't take larger plate sizes (larger than 1.5m x 1.5m) into account and has

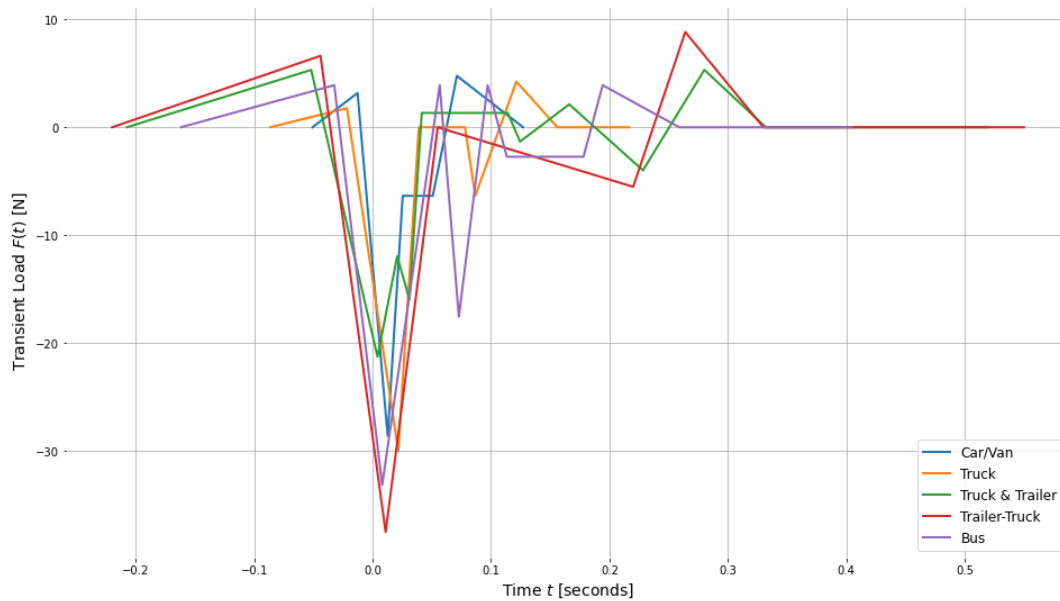


Figure 2.8: Estimated transient load acting on a 1.5x1.5m sign for various vehicles. Vans and cars have an assumed velocity of 120 km/h, the other larger vehicles an assumed velocity of 80 km/h. A head clearance of 5 meters was assumed between the bottom of the sign and the ground, allowing the distance between the bottom of the sign and the top of the vehicle to be taken into account. [5]

not be verified with empirical measurements. Therefore the magnitude of the load may not accurately describe the true load on the sign.

2.4.1. Peak Pressure

In order to formulate a design load for traffic induced loads the different methods are compared to each other. The design method of defining a traffic induced pulse load by Creamer et al. and the method provided by the research of Cook and Hosch are both based on an aerodynamic pressure which is integrated across the sign using an assumed pressure distribution. The method proposed by Lichtneger and Ruck on the other hand provides equations that provide the total transient load on the sign. Their research does not provide any conclusions with respect to the pressure distribution, therefore in order to compare the three aforementioned pulse loads, an equivalent pressure for the Lichtneger pulse load is calculated using a simple linear pressure distribution similar to the one used by Creamer et al.

Figure 2.9 shows a comparison of peak pulse loads for a truck (length = 17.6m, width = 2.6m, height=4.0m) passing directly under a 1.5x1.5m sign, where the truck is traveling at 80km/hr, and the top of the truck is one meter away from the sign. As can be seen from the figure the Lichtneger pulse significantly underestimates the load magnitude compared to the other studies. In the thesis by Coen [10] a variation of the Lichtneger and Ruck method was applied and compared with empirical measurements on the structure. In the thesis it was concluded that the calculated loads were off by a factor 4.2 compared to the measured loads. In figure 2.9 this factor 4.2 is taken into account in the lighter colored bar, which puts it above the other studies. It should be noted that this factor 4.2 was based on a truss structure (opposed to the hollow section frame considered in this thesis), and the pressure distribution across the sign height was logarithmic compared to the linear distribution used in the comparison calculation in figure 2.9. Compared to the Creamer pulse load the Fikkers adjusted Lichtneger pressure may still underestimate the load effects of passing vehicles, instead a adjustment factor of magnitude 8.0 is suggested in order to provide a safe albeit conservative load.

2.4.2. Lateral Transient Load

For the lateral transient load acting on the structure the pulse load described by Lichtneger and Ruck is the most detailed approach that takes into account the most contributing factors, and is also the

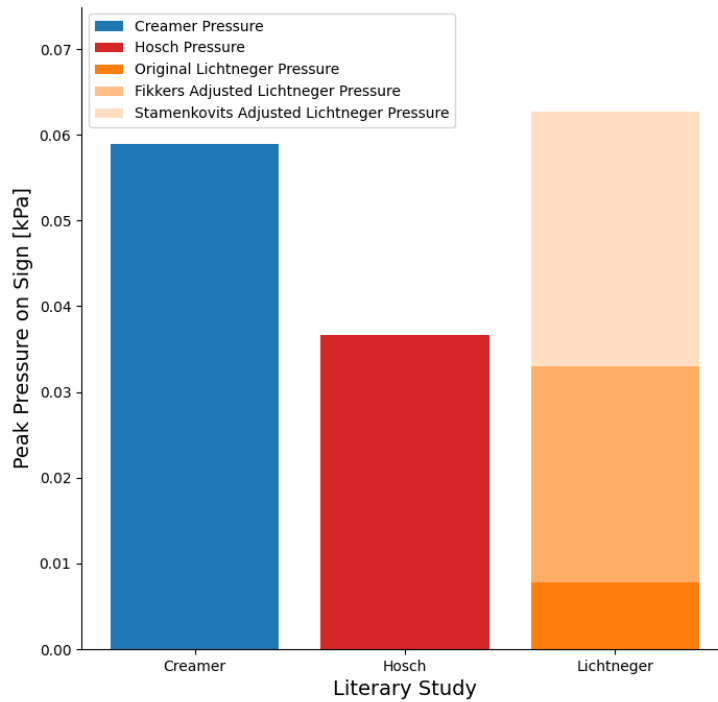


Figure 2.9: Comparison of pulse peak pressure for different studies for a truck (length = 17.6m, width = 2.6m, height=4.0m) traveling at 80 km/hr passing underneath a 1.5m x 1.5m sign, where the truck and sign are separated by 1 meter.

most conservative if a correction factor of 8.0 is used. However as discussed, the calculation model in the research by Lichtneger [29] provides a transient load for a 1.5mx1.5m sign, and provides no way to scale this up. In order to use this model for larger signs a conversion calculation is used. For a given vehicle traveling at a given speed the Lichtneger transient load for a reference sign of 1.5mx1.5m sign structure is calculated, and distributed across the sign with a constant reference pressure. This reference pressure is then applied to the full scale sign under consideration. The horizontal pressure distribution is assumed to be constant, i.e. the pressure on the full scale sign at a given height remains constant over the sign width. Up to a height of 1.5 meters it is assumed that the pressure is constant, if the sign height exceeds this reference height the pressure is assumed to decrease linearly. Figure 2.10 provides a visual representation of the steps taken in order to scale the transient load for signs larger than the 1.5mx1.5m reference sign. This approach can be summarized into a single size factor α relating the desired transient pulse load F_p to the reference Lichtneger transient pulse load $F_{p.ref}$.

$$F_p(t) = \alpha * F_{p.ref}(t) \quad (2.7)$$

$$\alpha = 1 + 0.5 \cdot \frac{h - 1.5}{1.5} \quad (2.8)$$

Where:

- F_p = Transient pulse load for a full-scale sign in N
- t = Time in s
- α = Non-dimensional size factor
- $F_{p.ref}$ = Reference Lichtneger transient pulse load in N
- h = Sign height in m

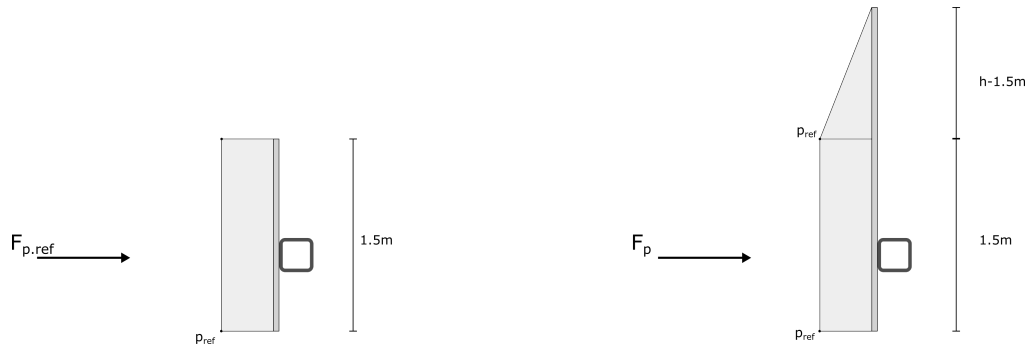


Figure 2.10: Conversion calculation used to apply Lichtneger and Ruck model to signs larger than 1.5m x 1.5m. The Lichtneger transient pulse load $F_{p,ref}$ is calculated and used to determine the uniformly distributed pressure p_{ref} , which is then applied to the full-scale sign using a bi-linear pressure-distribution.

2.4.3. Torsional Load

The transient load acting on the sign is transferred to the steel structure (frame). There is vertical eccentricity between the application of the load and the attachment location of the sign to the steel hollow section beam. As a result a torque moment is applied to the steel frame. This torque moment could be calculated based on the resultant force of the pressure distribution shown in figure 2.10. However as the truck passes underneath the sign the distribution of the pressures varies greatly, at times it is relatively homogeneously distributed, but at others the pressure is more concentrated in certain areas of the sign than others. Figure 2.11 shows the pressure distribution across the sign at the point in time when the maximum total load due to a "trailer-truck" on a 1.5x1.5m sign was measured in Lichtneger and Ruck's research [29]. Here it can be observed that the pressure is concentrated at the bottom of the sign, resulting in a much larger torsional moment. As the pressure distribution as a function of time is unknown, this extreme case will be used to determine the load eccentricity at all points in time, resulting in a conservative estimation of the torsional moment applied to the steel frame. Equation 2.9 is used to determine the torsional load, which depends on the transient load and its eccentricity.

$$T = F_p \cdot e \quad (2.9)$$

Where:

T = Torsional load

F_p = Transient load determined according to figure 2.10 and equations 2.6 and 2.8

e = Transient load eccentricity

The pressure coefficient values in figure 2.11 at the center of the sign have been estimated and plotted over the sign height, and subsequently fitted with a logarithmic function, as can be seen in figure 2.12. The eccentricity of the load is then defined as the difference between the center of mass of the logarithmic pressure distribution (which can be calculated according to equation 2.10) and the attachment location of the sign.

$$z_e = \frac{\int_0^h z \cdot c_p(z) dz}{\int_0^h c_p(z) dz} \quad (2.10)$$

$$c_p(z) = 2.44 - \frac{21.41}{\log(z - 35.16)} \quad (2.11)$$

Where:

z_e = Pressure coefficient distribution center of mass in mm

c_p = Pressure coefficient distribution across height of sign z

z = Height along sign in mm

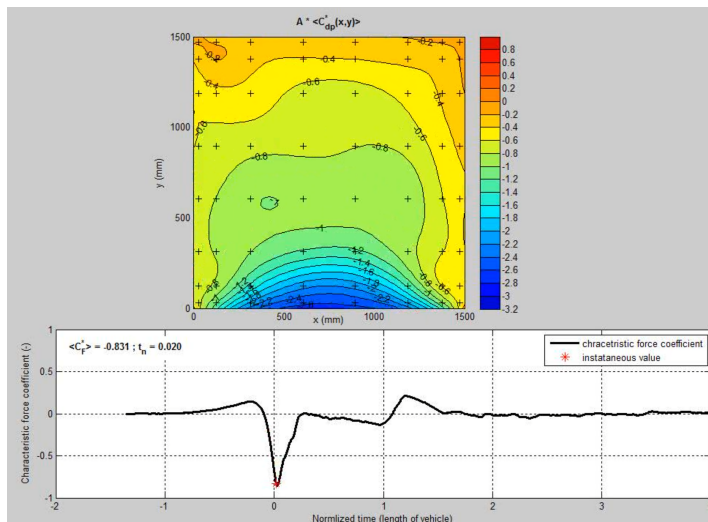


Figure 2.11: Pressure distribution across the sign at the point in time when the maximum total load due to a "trailer-truck" on a 1.5x1.5m sign was measured in Lichtneger and Ruck's research [29]

h = Total sign height in mm

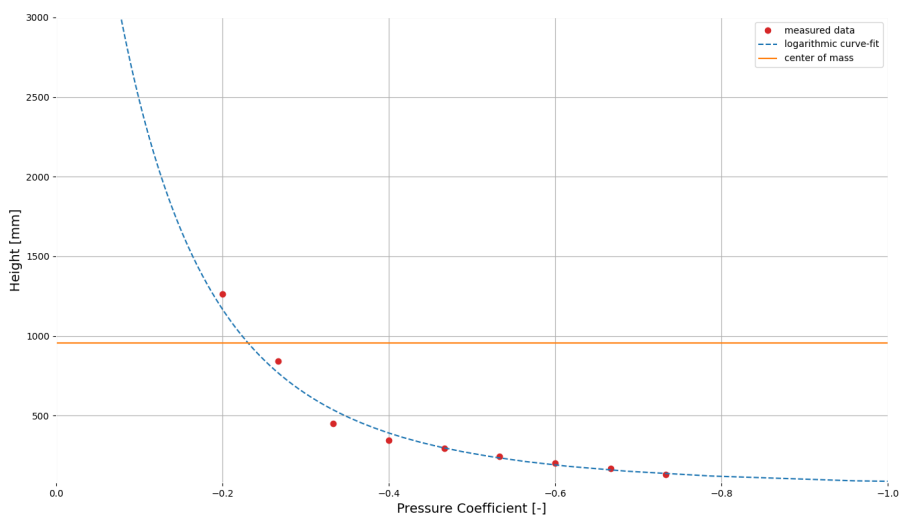


Figure 2.12: Pressure coefficient distributed over sign height from fig 2.11 fitted by a logarithmic function. The center of mass for the logarithmic function for a sign height of 3000mm is calculated (center of mass with respect to bottom of sign = 956mm)

2.4.4. Limitations of Approach

These types of aerodynamic loads are complex in nature as a lot of different variables influence transient loads on traffic signs due to passing vehicles. This phenomenon has not received a significant amount of research, and as such it should be noted that the proposed approach has several significant limitations.

Firstly, in the research conducted by Lichtneger and Ruck it is mentioned that due to the complex nature of the phenomenon individual runs could not be replicated exactly, resulting in large (but undocumented) uncertainties.

Furthermore a great deal of assumptions are made with respect to the pressure distribution across the sign for both the transient load and the torsional load determination. From published animations by Dr. h.c. Bodo Ruck [29] it can be observed that the pressure distribution changes greatly over time as the truck passes underneath. Figure 2.13 shows various possible pressure distributions which may resemble the true pressure distribution at various points in time. Pressure distribution p_1 is used for the transient load determination as this provides an easy to understand and implement scale factor α for signs larger than the documented reference sign (1.5m x 1.5m). Pressure distribution p_3 is used for the torsional load as this conservatively leads to the largest possible torsion in the structure. It should be noted that the original research by Lichtneger and Ruck analyzes small signs, which allows air to flow around the sides of the sign freely. For larger wider signs the air that normally would be allowed to flow around the sign would be forced to flow underneath it creating perhaps larger loads [10]. Similar empirical research should be conducted on larger sign structures in order to gain a better understanding of how the transient loads scale with sign width and sign height.

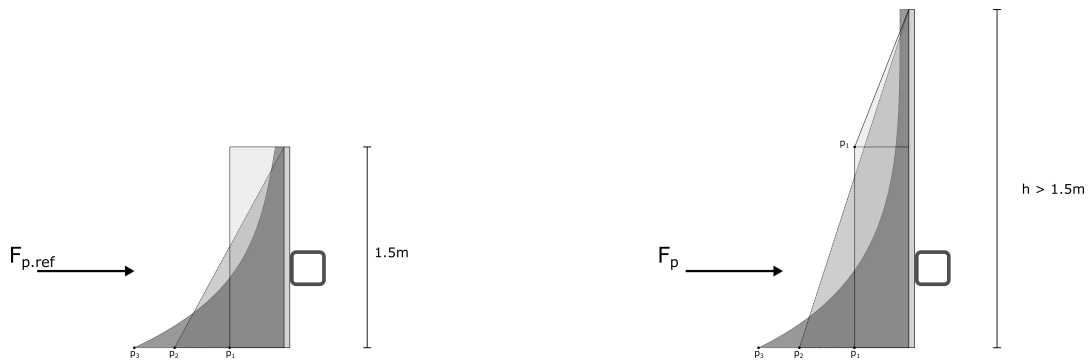


Figure 2.13: Possible pressure distributions

It is also assumed that the shape of the pulse load used to describe any large trailer-truck passing underneath a rectangular sign is the same as the one given in figure 2.8, which is a linear approximation of an ensemble average like the one given in figure 2.7. The individual runs for that particular vehicle and plate can be seen to vary significantly around the ensemble average leading to large (but undocumented) uncertainties.

Finally when utilizing this approach in practice in a previous thesis, it was observed that the resulting displacements were off by a factor 4.2. This was attributed to the inaccuracies of the pressure integration such as the ones previously mentioned. Whether this factor is applicable to the model used in this thesis is hard to judge. The dynamic model used to determine the dynamic structural response is substantially different than the one used in the thesis by C.D. Fikkers, it incorporates more degrees of freedom and uses more complex mass, stiffness, and damping matrices. On top of this the highway gantry sign considered by C.D. Fikkers is truss structure, while this thesis focuses on structures consisting of rectangular hollow sections. Ultimately a significantly larger adjustment factor is used in this load model (8.0 opposed to 4.2), the accuracy of this adjustment factor should be evaluated through empirical measurements. Even then this adjustment factor may not be a constant, but could vary based on various factors including the structures dimensions and type of traffic.

2.4.5. Application of Approach

The reference structure in question consists of two signs, this subsection will illustrate the application of the traffic pulse load model for the right-hand-side sign in figure 1.2. In this calculation the governing vehicle type "trailer-truck" from the Lichtneger and Ruck research is considered, which is assumed to pass underneath the sign at 80 kilometer per hour. For this vehicle traveling at the indicated speed, the reference pulse load may be computed according to 2.6. This reference pulse load is amplified by the size factor (taking the larger sign dimensions into account) and the load correction factor (to ensure the correct order of magnitude is given). The amplified pulse load is plotted in the top plot of figure 2.15.

The eccentricity of the sign transient load used to calculate the torsional moment follow from the sign attachment eccentricity e_a in figure 2.14 and the center of mass e_{cm} calculated in 2.12. The torsional pulse load is plotted in the bottom plot of figure 2.15.

Table 2.1: Traffic induced pulse load input parameters for the right right-hand-side sign of the reference structure, see figure 1.2

Property	Symbol	Value	Units
Sign width	b_2	3.5	m
Sign height	h_2	3.0	m
Vehicle type	[-]	trailer-truck	[-]
Vehicle width	b_v	2.6	m
Vehicle height	h_v	4.0	m
Vehicle length	L_v	17.6	m
Vehicle speed	v_v	80	kph
Distance between bottom of sign and top of truck	z	1.0	m
Distance factor	$k(z)$	0.014	[-]
Size factor	α	3.5	[-]
Load correction factor	β	8.0	[-]
Sign attachment eccentricity (with respect to bottom of sign)	e_a	500	mm
Transient load center of mass (with respect to bottom of sign)	e_{cm}	956	mm
Transient load eccentricity (with respect to attachment location)	e	456	mm

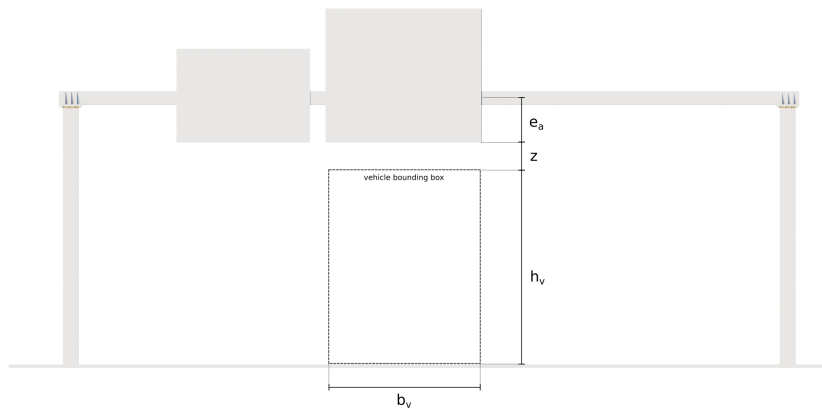


Figure 2.14: Illustration of key parameters when determining a traffic induced pulse load acting on a traffic sign.

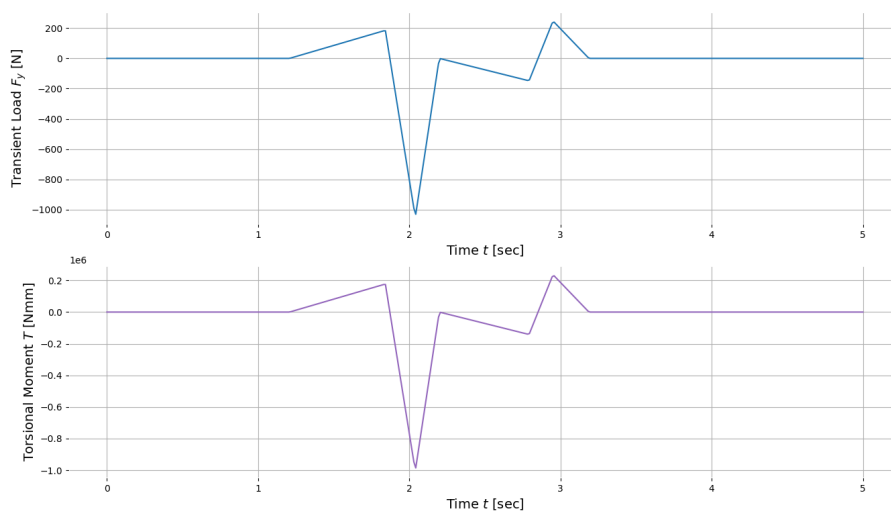


Figure 2.15: Example of single transient load pulse and torsional moment pulse according to the parameters in table 2.15

3

Atmospheric Wind Loads

The structure of a traffic sign support structure has a relatively low elevation with respect to the ground. At higher altitudes the wind will have predominantly laminar flow, however close to the ground surface turbulence plays a large role due to friction with the ground [28]. Due to the unpredictable nature of turbulent air flow a probabilistic load approach is required when evaluating the atmospheric wind loads.

3.1. Eurocode Wind Loads

In the Eurocode the effects of wind on a structure are taken into account by looking at the mean wind speed value and adding the maximum wind gust value on top.

3.1.1. Mean Wind Speed

When designing a structure for the ultimate limit state (ULS) and serviceability limit state (SLS) the maximum wind load to be expected in the structure's lifetime should be used. The Eurocode provides guidelines for wind loads on structures that are generalized in order to encompass as large a scope as possible. According to these guidelines the mean wind speed a structure is exposed to is determined according to formulas 3.2 and 3.1. The fundamental basic wind speed $v_{b,0}$ is defined as:

"the characteristic 10 minutes mean wind velocity, irrespective of wind direction and time of year, at 10 m above ground level in open country terrain with low vegetation such as grass and isolated obstacles with separations of at least 20 obstacle heights." [11]

The Eurocode and Dutch National Annex provide tables according to which the fundamental basic mean wind speed $v_{b,0}$ may be determined. The basic mean wind speed v_b follows from the fundamental basic mean wind speed modified by the seasonal factor $c_{seasonal}$ and directional factor c_{dir} which take the seasonal and directional variability of the wind speeds into account. The overall mean wind speed v_m follows from the basic mean wind speed modified by the terrain roughness factor $c_r(z)$, which takes general obstacles on the ground into account, and the terrain orography factor c_o which takes increased wind speed gradients due to geographical features such as cliffs and hills into account. Due to the relative mild climate and flat terrain the seasonal, directional, and orography factors may all be taken as equal to 1.0 [11].

$$v_b(z) = c_{dir} \cdot c_{seasonal} \cdot v_{b,0} \quad (3.1)$$

$$v_m(z) = c_r(z) \cdot c_o(z) \cdot v_b \quad (3.2)$$

Where:

v_m = Mean wind speed in m/s
 c_r = Roughness factor

c_0	= Orography factor
v_b	= Basis wind velocity in m/s
c_{dir}	= Directional factor
c_{season}	= Seasonal factor
$v_{b,0}$	= Fundamental basis wind speed in m/s
z	= Height above ground

3.1.2. Wind Gusts

The mean wind speed v_m represents the mean wind speed which occurs during a 10 minute interval and is expected to occur once in 50 years. However due to turbulence the true wind speed varies over time around this mean wind speed, the effect of which can be described by a probabilistic distribution. Davenport analyzed the magnitude of the peak turbulent gusts for different return periods [7]. Figure 3.1 illustrates how the wind speed values are distributed around the mean, and how a distribution of peak gust values can be described. The mean values of peak wind gusts lies somewhere between 3 and 5 standard deviations of the wind speed distributions from the mean wind speed depending on the return period.

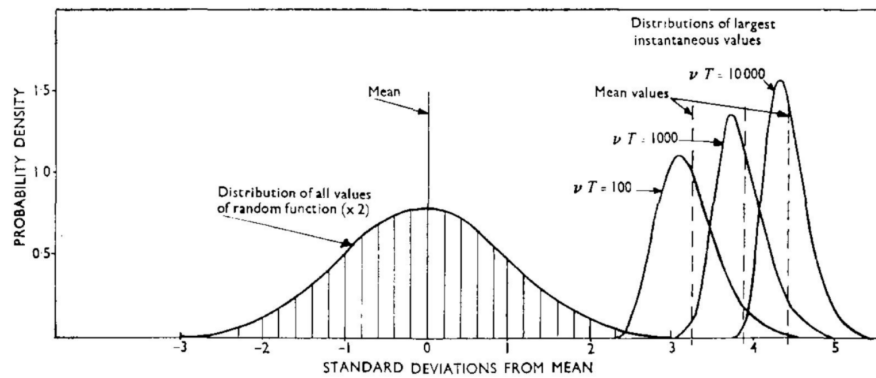


Figure 3.1: Relationship of distribution of largest instantaneous values of random function to the distribution of all values for different values of the response factor μT

The peak factor k_p represents how many standard deviations a peak wind speed gust value lies above the mean wind speed v_m . The peak pressure a structure endures should therefore be based on the largest wind gust speed according to equation 3.3, which can be linearized into the simplified form according to equation 3.4. In the Eurocode the largest wind gust in a 50 year period is desired, which corresponds a peak factor of $k_p = 3.5$, which results in equation 3.5 for the peak wind pressure used in the Eurocode.

$$q_p = \frac{1}{2} \rho \cdot (k_p \sigma_v + v_m)^2 = \frac{1}{2} \rho \cdot (1 + k_p I_v)^2 \cdot v_m^2 \quad (3.3)$$

$$q_p \approx (1 + 2k_p I_v) \cdot \frac{1}{2} \rho v_m^2 \quad (3.4)$$

$$q_p \approx (1 + 7I_v) \cdot \frac{1}{2} \rho v_m^2 \quad (3.5)$$

$$I_v = \frac{\sigma_v}{v_m} \quad (3.6)$$

Where:

q_p	= Peak wind pressure in N/mm ²
ρ	= Air density (= 1.25 kg/m ³)
k_p	= Peak intensity factor
σ_v	= Standard deviation of wind speeds

v_m = Mean value of wind speeds in m/s, see equation 3.2
 I_v = Wind turbulence intensity

These loads are applicable in the ultimate and serviceability limit state as they represent an instantaneous wind load that is expected to occur one instance in a 50 year period. The fatigue limit state however looks at what load ranges are expected to occur throughout the entirety of the structures lifetime. The Eurocode takes this into account by providing a distribution of load cycles, and how often these load cycles occur, based on the peak wind pressure. This method is discussed more in depth in the chapter on *Fatigue Resistance*. The fatigue limit state calculation according to the Eurocode describes takes a distribution of wind speeds and uses a statistical model to evaluate the instantaneous maximum gust wind load. From there it uses a second statistical model to translate the instantaneous wind load into a distribution of wind loads once again. This method is reasonable considering that the maximum instantaneous wind load calculation needs to be performed for the ultimate and serviceability limit state anyways, and therefore saves time in the overall design process. However it is not the most accurate method of performing the fatigue analysis as accuracy is lost when going from the wind speed distributions to the instantaneous wind load, and accuracy is lost when going from the instantaneous wind load back to a distribution of loads. Using a different method for the fatigue load, while time consuming could lead to more accurate results.

3.2. Simulation of Stochastic Wind Load

3.2.1. Load Definition

According to Eurocode EN 1990 section 4.1.4(2) the representation of fatigue actions may also be defined from *"the evaluation of measurements or equivalent studies of the expected action spectra"* [11]. As the aforementioned method outlined in Eurocode EN 1991-1-4 could be less conservative and more accurate, a more comprehensive load definition may be used. One such a load model is the simulation of wind speeds based on a mean wind speed based on empirical measurements and the effects of turbulence taken into account using wind speed spectra, see equation 3.12 and 3.9. The load on a square structure due to a flowing medium such as air particles, i.e. wind, is generally well understood and is given by equation 3.7, which is the same type of formulation the Eurocode uses for static wind loads.

$$F_w(t) = \frac{1}{2} \cdot c_s c_d c_f \cdot \rho A (v(t))^2 \quad (3.7)$$

$$v(t) = v_m + \Delta v(t) \quad (3.8)$$

$$v_m = c_r(z) \cdot c_0(z) \cdot c_{dir} \cdot c_{season} \cdot v_{b0,KNMI} \quad (3.9)$$

Where:

F_w = Wind load in N
 ρ = Air density in kg/m³
 A = Surface Area m²
 v = Wind speed in m/s
 c_r = Dimensionless roughness factor
 c_0 = Dimensionless Orography factor
 c_{dir} = Dimensionless directional factor
 c_{season} = Dimensionless seasonal factor
 $v_{b0,KNMI}$ = Basic mean wind speed based on KNMI data
 $\Delta v(t)$ = Wind fluctuations over time due to turbulence

3.2.2. Wind Speed Simulation

The weather is a dynamic phenomenon resulting in wind speeds which change over time on various length scales. Van der Hoven observed that variations in wind speeds take place across various periods

of time and has documented this in what is known as the Van der Hoven wind spectrum [8], see figure 3.2. From this spectrum three distinct peaks can be observed corresponding to wind speeds varying every couple of days (4 day synoptic peak), wind speeds varying between day and night (diurnal peak), and wind speeds varying across minutes and even seconds (turbulent peak). Different peaks will also exist for seasonal changes for example, where wind speeds cycle in the order of magnitude of months, but is not shown in figure 3.2.

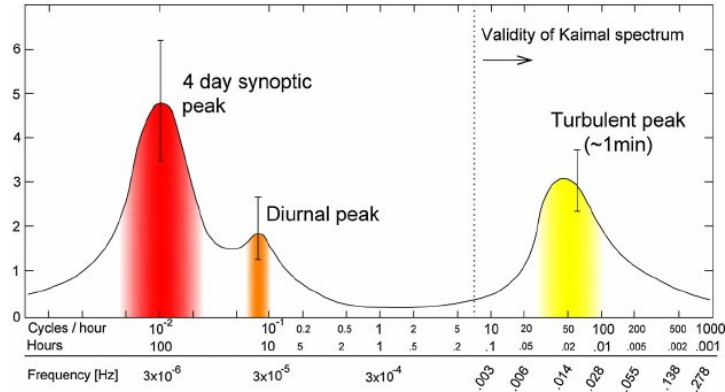


Figure 3.2: Van der Hoven spectrum [24]

Annex B of the Eurocode 1991-1-4 provides the Solari wind speed spectrum is similar to the Kaimal spectrum mentioned in figure 3.2 and also corresponds to the turbulent peak in said figure. The version of the Solari spectrum used by the Eurocode is given by the dimensionless power spectral density function in equation 3.11 where the dimensionless frequency depends on the average gust size determined by the turbulence length scale L and the basic mean wind speed v_m . Figure 3.3 illustrates the spectrum evaluated for various basic mean wind speeds.

$$S_L = \frac{6.8f_L}{(1 + 10.2f_L)^{5/3}} \quad (3.10)$$

$$f_L = \frac{nL}{v_m} \quad (3.11)$$

Where:

- S_L = Non-dimensional power spectral density
- f_L = Non-dimensional frequency
- n = Frequency in Hz
- v_m = Basic mean wind speed in m/s
- L = Turbulent Length scale in m

According to the Fourier analysis any physical signal, such as the wind speed of turbulent atmospheric air flow, can be represented by a set of trigonometric functions with varying frequencies and amplitudes. For a stochastic signal whose behavior cannot be modelled exactly, a random component is required.

$$\Delta v(t) = \sum_{n=1}^N V_{0,n} \sin(\omega_n t + \phi_n) \quad (3.12)$$

The turbulent component of the wind speed can be modeled according to equation 3.12, where the amplitude $V_{0,n}$ depends on the sampled frequency ω_n according to the Solari spectrum provided by figure 3.3. A random phase-shift ranging between 0 and 2π is introduced in order to take the stochastic nature into account. The general definition of the wind variance spectrum S_L as a function of a frequency ω_n is defined by equation 3.13, which can be rearranged in order to obtain the amplitude of the sampled wind speed wave $V_{0,n}$, see equation 3.14.

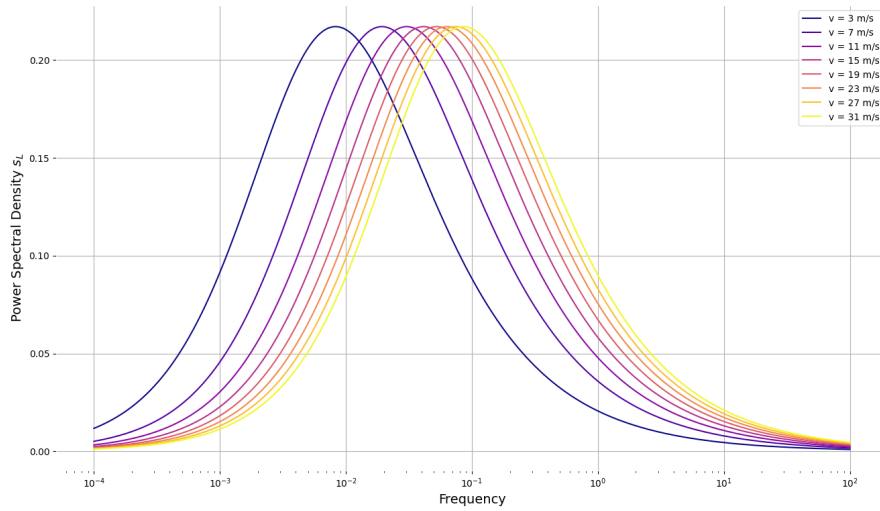


Figure 3.3: Eurocode Solari spectrum evaluated for various basic mean wind speeds

$$S_L(\omega_n) = \lim_{\Delta\omega \rightarrow 0} \frac{\frac{1}{2}V_{0,n}^2}{\Delta\omega} \quad (3.13)$$

$$V_{0,n} = \sqrt{2\Delta\omega S_L(\omega_n)} \quad (3.14)$$

$$\omega_n = n\Delta\omega \quad (3.15)$$

$$\Delta\omega = \frac{\omega_u}{N} \quad (3.16)$$

Where:

- $V_{0,n}$ = Amplitude of sinusoidal wave
- ω_n = Frequency associated with n^{th} wave in simulation
- ϕ_n = Randomly generated phase shift associated with n^{th} wave in simulation
- ω_u = Upper cut-off limit frequency
- N = Number of waves used in simulation

3.2.3. Cut-Off Frequency

The wind-load is simulated based on the power spectral density function given by the Eurocode, which is defined from zero to infinity. The simulation is based on a finite number of samples, which means only a finite part of the power spectral density function $S_L(n)$ can be considered. Normally the upper cut-off frequency is chosen based on an acceptable error ϵ such that equation 3.17 is satisfied.

$$\int_0^{n_u} S_L(n)dn = (1 - \epsilon) \int_0^{\infty} S_L(n)dn \quad (3.17)$$

However the integral from zero to infinity of the power spectral density function $S_L(n)$ described by the Eurocode in equation 3.11 does not converge. Instead the upper (and lower) cut-off frequency is determined by only taking frequencies into account that correspond to 10% of the maximum variance in the power spectral density function. According to the national annex to Eurocode 1 part 1-4 table NB1.1 the basic wind-speed for the structure under consideration that has a return period of 50 years is 29.5 m/s, which will be used to scale the power spectral density function. This ensures the largest

possible upper cut-off frequency is taken into account. Figure 3.4 depicts the power spectral density function and the chosen upper and lower cut-off frequencies.

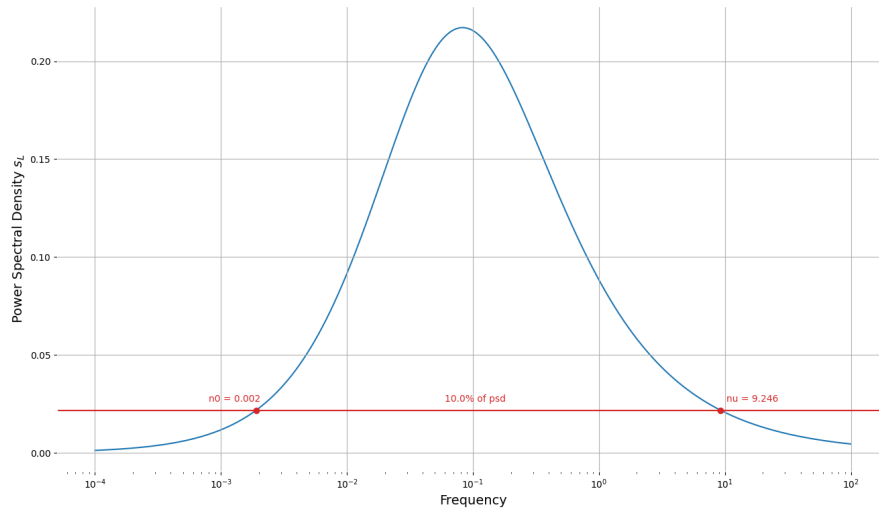


Figure 3.4: Upper and lower cut-off frequency based on the peak value of the power spectral density function $S_L(n)$.

3.2.4. Frequency Sampling

The wind speed is described by a signal built up of sinusoidal waves whose frequency and corresponding amplitude follow from the power spectral density function defined by the Eurocode [11] according to equations 3.12 through 3.16. If a constant frequency step size $\Delta\omega$ is used, the signal will become periodic over a period $T_0 = \frac{2\pi}{\Delta\omega}$ [25]. To mitigate this, one could use a larger number of waves N in the simulation in order to reduce $\Delta\omega$ such that the periodic period T_0 exceeds the simulation length. However, depending on the length of the simulation this could prove computationally expensive. An alternative solution is to randomly vary the size of the frequency step size $\Delta\tilde{\omega}_n$, while ensuring that the sum of these step sizes over the number of waves N is equal to the upper cut-off limit [30], see equation 3.18. The values of a_n can be determined by creating a list a of random numbers which vary between 0.5 and 1.5 of length N , whose sum is equal to N (each entry in this list is then denoted by a_n).

$$\sum_{n=1}^N a_n \Delta\omega = \sum_{n=1}^N \Delta\tilde{\omega}_n = \omega_u \quad (3.18)$$

Where:

- a_n = A random number between 0.5 and 1.5
- $\Delta\omega$ = Standard frequency step size as described in equation 3.16
- $\Delta\tilde{\omega}_n$ = Frequency step size whose magnitude varies randomly around $\Delta\omega$ based on the value of a_n
- ω_u = Upper cut-off limit frequency

However, the variance spectrum defined by the Eurocode is not distributed linearly across all frequencies; the horizontal axis in figure 3.3 has a log base 10 scale. In order to sample the most relevant frequencies from this spectrum (i.e. the frequencies associated with the largest variance), a variable frequency step size should be used. A variable y is introduced which is directly correlated to the frequency ω according to equation 3.19.

$$\omega_n = 10^{y_n} \quad (3.19)$$

If this variable y is distributed in n steps across the spectrum with a constant step-size Δy , then the governing frequencies are sampled equally. This is achieved through the use of the step-size defined in equation 3.21, based on the start and end frequency ω_0 and ω_u respectively. The variable frequency step-size $\Delta\omega_n$ used in the signal simulation of the stochastic wind speed can then be obtained through equation 4.43.

$$y_n = n\Delta y \quad (3.20)$$

$$\Delta y = \frac{\log_{10} \omega_u - \log_{10} \omega_0}{N} \quad (3.21)$$

$$\Delta\omega_n = 10^{y_n} (10^{\Delta y} - 1) \quad (3.22)$$

Where:

- y_n = A variable used to help create the variable frequency step-size
- Δy = Constant step-size of variable y
- $\Delta\omega_n$ = Variable frequency step-size

In order to maintain an accurate signal simulation and avoid aliasing (i.e. ensure different signal component can be distinguished from one another) according to Nyquist–Shannon sampling theorem, the time step Δt should adhere to the criterion outlined in equation 3.23 [25].

$$\Delta t \leq \frac{2\pi}{2\omega_u} \quad (3.23)$$

The signal is sampled using discrete frequency steps, but should accurately reflect the variance of the continuous variance spectrum distributed across frequencies. To assess this accuracy the standard deviation of the computed simulated signal is numerically determined. The computed standard deviation is then compared to the theoretical standard deviation, which follows from integrating the power spectral density function $S_L(n)$ across the defined frequencies according to equation 3.25.

$$\sigma = \int_{n_0}^{n_u} S_L(n) dn \quad (3.24)$$

A higher sampling rate (more waves per simulation) will yield a more accurate signal. To determine the minimum sampling rate the stochastic signal can be generated for different sampling rates and graphed, as can be seen in figure 3.5. As the signal is a stochastic process each sampling rate has been computed 10 times with a different random seed. For the same number of waves the accuracy of the signal can still change based on the stochastic phase-shift of the wave. The more waves in a simulation, the more variation there will be in the signal accuracy. If one aims for a signal accuracy of at least 5% for the chosen spectrum, then according to figure 3.5 at least 23 waves should be taken into account; this sampling of frequencies for the different waves in the simulation is visualized by figure 3.6.

$$\sigma = \int_{n_0}^{n_u} S_L(n) dn \quad (3.25)$$

3.3. Application of Approach

The reference structure in question consists of two signs. This subsection will illustrate the application of the wind load simulation for the right-hand-side sign in figure 1.2. A very large basic mean wind speed of 30 m/s is considered, which is representative of a storm with a return period of 50 years. The various load and wind factors are determined according to the Eurocode. The effects of turbulence are considered through a summation of 10 sinusoidal waves

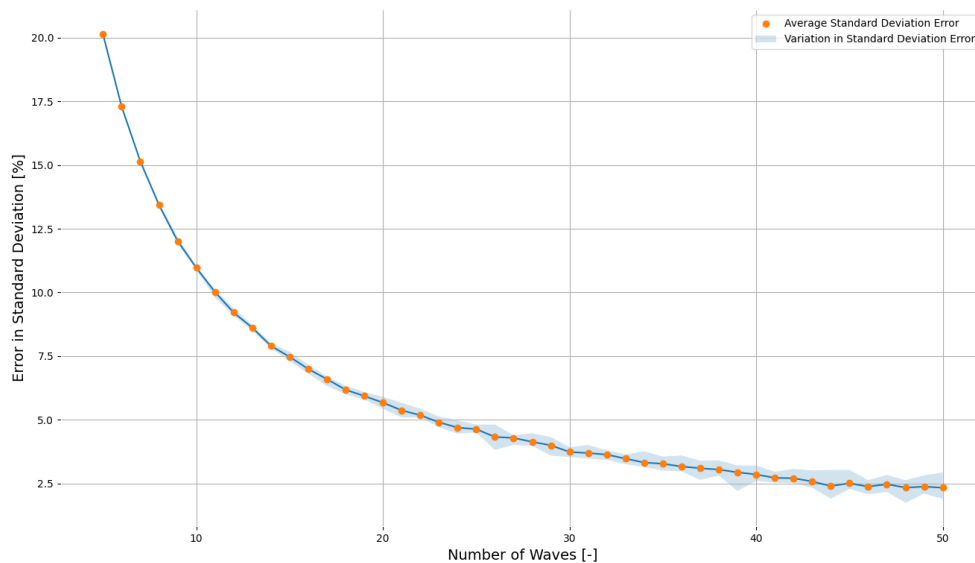


Figure 3.5: Signal accuracy for different sampling rates (number of waves per simulation)

3.4. Limitations of Approach

The accuracy of the wind load on the structure is governed by the wind velocity, which is assumed to be a stochastic process which is modelled by a set of sinusoidal waves. The daily mean wind velocity in this simulation is obtained from 10 years of empirical data taken from weather stations taking measurements every 10 minutes according to the KNMI the accuracy of wind measurements is ± 0.5 m/s for measurements up to 5 m/s and $\pm 10\%$ for measurements greater than 5 m/s. The weather station measuring equipment is located 10 meters above the ground, which is representative for highway gantry sign structures. The stations are located in relatively open areas, but any additional obstructions on the ground near the structure can be taken into account with various factors provided by the Eurocode. In order to take long-term wind speeds deviating from the 10 year mean daily wind speed into account a probabilistic approach is required.

The turbulence effects are taken into account through a spectral density function defined by the Eurocode, which is used to simulate short-term wind speed fluctuations around the mean wind speed. This spectral density function is based on the *Equivalent Wind Spectrum Technique (EWST)* developed by G. Solari, and has been shown to be an accurate technique to simulate wind speeds, and is widely used [19].

Any computer simulation is limited by computational power, and a trade-off needs to be made between accuracy and computation time. The main factors affecting the computation time is the number of waves N , the upper cut-off limit frequency ω_u , and the number of time steps Δt in the simulation. The requirement for the value of N is usually set by the length of the simulation. However by using a varying frequency step this can be mitigated, instead a sensitivity analysis with respect to the fatigue damage has to be performed. The upper cut-off limit frequency needs to be chosen by minimizing the error ϵ , but may also need to be fine-tuned through a sensitivity analysis. Finally the time step Δt has a clearly defined limit in order to avoid aliasing, but through this criterion it is directly linked to the upper cut-off frequency and is subject to change if that value is fine-tuned.

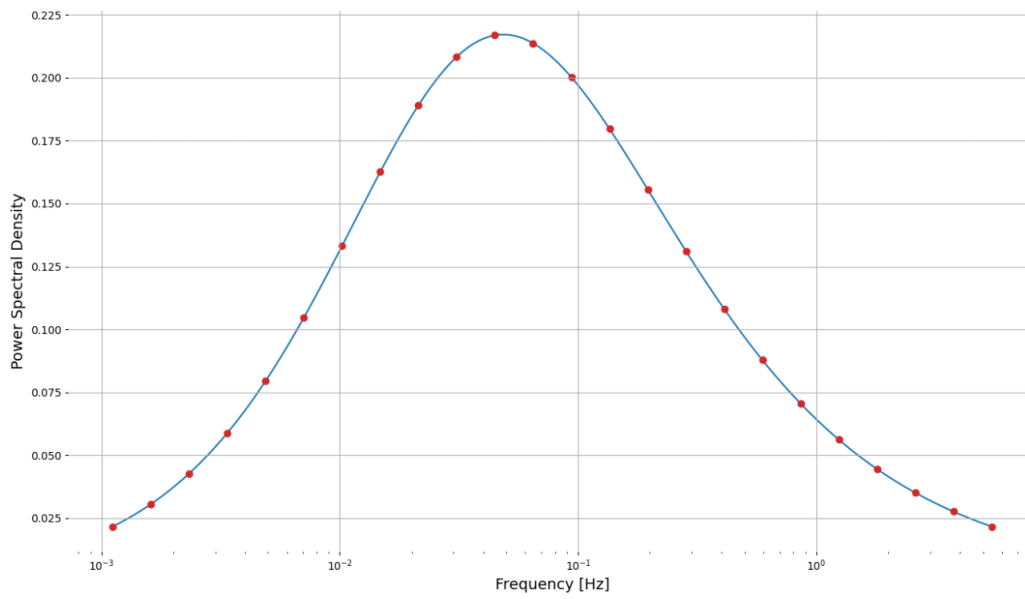


Figure 3.6: Frequencies that are sampled from the variance spectrum described by S_L in the case of a simulation where 23 waves are used.

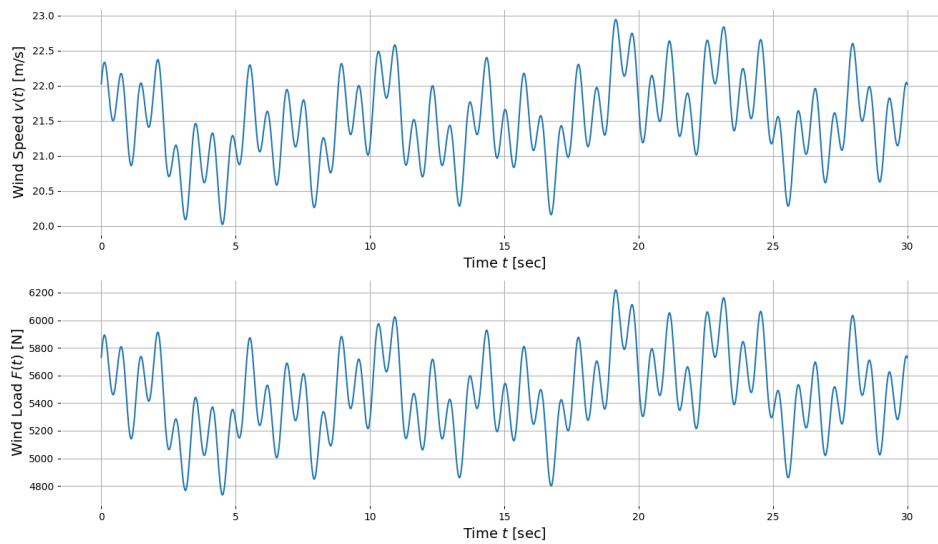


Figure 3.7: Wind load signal simulating the effects of turbulence through sinusoidal waves.

Table 3.1: Input parameters of wind load simulation

Property	Symbol	Value	Units
Sign width	b_2	3.5	m
Sign height	h_2	3.0	m
Structure height	z	6.0	m
Terrain category	[-]	II	[-]
Basic mean wind speed	v_b	30.0	m/s
Number of waves in simulation	N	10	[-]
Structural factor	C_s, C_d	1.0	m
Force coefficient	c_f	1.8	kph
Terrain roughness factor	C_r	0.71	m
Terrain orography factor	C_o	1.0	[-]
Directional factor	C_{dir}	1.0	
Seasonal factor	C_{season}	1.0	[-]

Table 3.2: Parameters of sinusoidal waves used to model the turbulent wind load in figure 3.7

Sample	Frequency	Frequency Step	Amplitude	Random Phase Shift
n	ω	$\Delta\omega$	V_0	φ
1	0.002	0.002	0.010	6.032
2	0.005	0.003	0.018	1.445
3	0.013	0.008	0.042	0.754
4	0.033	0.020	0.086	2.513
5	0.085	0.052	0.150	6.032
6	0.217	0.132	0.220	2.953
7	0.555	0.338	0.287	2.388
8	1.418	0.862	0.352	5.781
9	3.620	2.203	0.420	0.503
10	9.246	5.626	0.494	0.754

4

Dynamic Finite Element Analysis

This chapter will outline the numerical model that is used to determine the dynamic response of the structure. The aim is to create a parametric model in which the dimensions of the structure are variable, including the span, height, cross-section, sign location, sign size and load types. This is achieved by creating a finite element method (FEM) model that is able to numerically solve second order differential equations. The chosen programming language is Python, the reason for this choice is to keep the model highly customizable to this specific application: wind loads on highway traffic signs. Furthermore the existing calculation setup relies heavily on Python for both the calculations and their automation. Creating this model in Python allows for easy integration with the existing calculations should that be desired.

4.1. Finite Element Discretization

The structure is discretized into a series of nodes connected by one-dimensional beam elements. Figure 4.1 illustrates the global coordinate system and a typical structure (traffic signs and their support structure) overlain by the discretization of the system through nodes and elements.

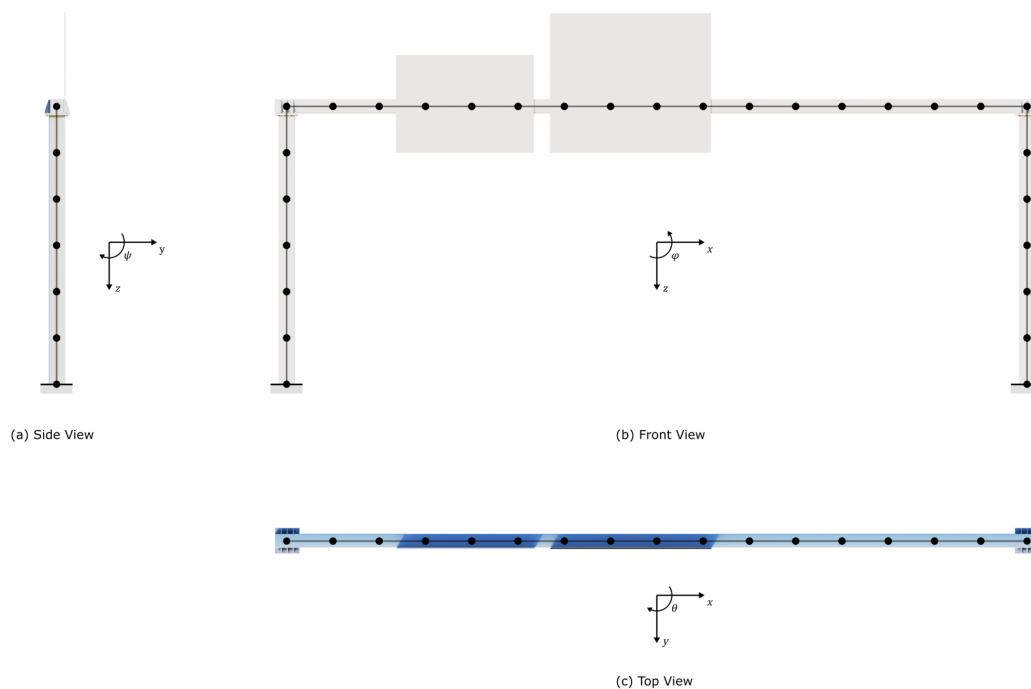


Figure 4.1: Discretization of structure into 1D beam elements in global coordinate system

4.1.3. Shape Functions

In order to describe the behavior of the system the behavior of each element needs to be described, for which the displacement fields $u_e(x)$, $v_e(x)$, and $w_e(x)$ of the element between two connected nodes needs to be described. This can be done by interpolating between the nodal displacement values through the use of shape functions. As the degrees of freedom of each sub-system are decouples from the other degrees of freedom they can be considered on their own. For example the sub-system for bending around the element y -axis is governed by the displacement w in the element z -direction and the rotation φ around the element y -axis. As a result the nodal w and φ values need to be considered, as shown in equation 4.1.

$$w_e(x) = w_1 N_{w_1}(x) + \varphi_1 N_{\varphi_1}(x) + w_2 N_{w_2}(x) + \varphi_2 N_{\varphi_2}(x) \tag{4.1}$$

The shape function for a given degree of freedom is computed by generating a displacement field for the sub-system displacement where one of the nodal values is equal to 1.0 and all others are equal to 0.0. This concept is illustrated in figure for the shape functions used in equation 4.1. A complete overview of all of the shape functions and their values is given in appendix B.

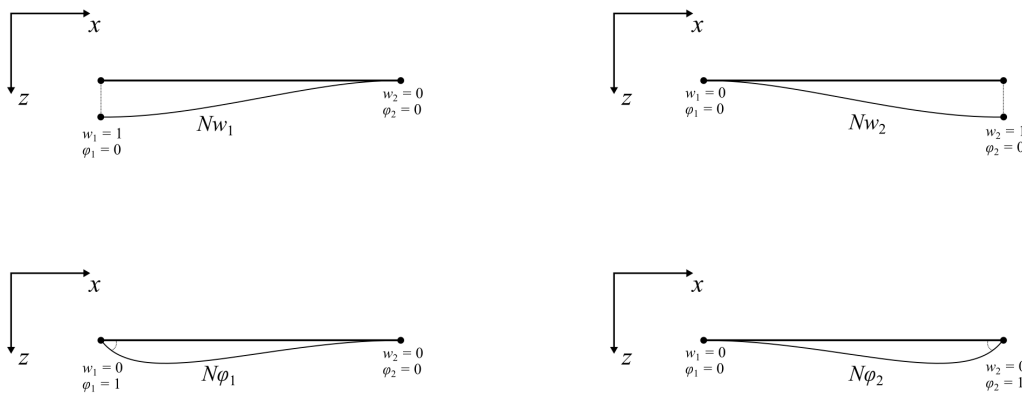


Figure 4.3: Shape functions for bending around y -axis described by equation 4.1

4.1.4. Sub-System Mass and Stiffness Matrices

The mass and stiffness matrices for the individual sub-systems for a single element are derived based on the Lagrangian energy method. The Lagrangian is the difference between the kinetic and potential energy, from which the equation of motion may be derived [4], see equations 4.2 and 4.3. This method requires the kinetic and potential energy of the element to be described in order to obtain the mass and stiffness matrices [38], which can be done according to the displacement fields described by the interpolating shape functions. This allows the mass and stiffness matrices to be described for each sub-system, appendix A provides a full overview of this process for each sub-system. The resulting matrices are given by table 4.3, and are in accordance with those found in literature [21][23].

$$L \equiv E_k - E_p \tag{4.2}$$

$$\frac{\partial L}{\partial q} - \frac{d}{dt} \frac{\partial L}{\partial \dot{q}} = Q \tag{4.3}$$

Where:

- L = Lagrangian
- E_k = Kinetic energy
- E_p = Potential energy
- q = Degree of freedom
- Q = External load

Description	Mass Matrix	Stiffness Matrix	DoF
Bending around y axis	$M_y = \frac{\rho Al}{420} \begin{bmatrix} 156 & -22l & 54 & 13l \\ & 4l^2 & -13l & -3l^2 \\ \text{sym.} & & 156 & 22l \\ & & & 4l^2 \end{bmatrix}$	$K_y = \frac{EI}{l^3} \begin{bmatrix} 12 & -6l & -12 & -6l \\ & 4l^2 & 6l & 2l^2 \\ \text{sym.} & & 12 & 6l \\ & & & 4l^2 \end{bmatrix}$	$\begin{Bmatrix} w_1 \\ \phi_1 \\ w_2 \\ \phi_2 \end{Bmatrix}$
Bending around z axis	$M_z = \frac{\rho Al}{420} \begin{bmatrix} 156 & 22l & 54 & -13l \\ & 4l^2 & 13l & -3l^2 \\ \text{sym.} & & 156 & -22l \\ & & & 4l^2 \end{bmatrix}$	$K_z = \frac{EI}{l^3} \begin{bmatrix} 12 & 6l & -12 & 6l \\ & 4l^2 & -6l & 2l^2 \\ \text{sym.} & & 12 & -6l \\ & & & 4l^2 \end{bmatrix}$	$\begin{Bmatrix} v_1 \\ \theta_1 \\ v_2 \\ \theta_2 \end{Bmatrix}$
Axial loading	$M_a = \frac{\rho Al}{6} \begin{bmatrix} 2 & 1 \\ 1 & 2 \end{bmatrix}$	$K_a = \frac{EA}{l} \begin{bmatrix} 1 & -1 \\ -1 & 1 \end{bmatrix}$	$\begin{Bmatrix} u_1 \\ u_2 \end{Bmatrix}$
Torsion around x axis	$M_T = \frac{\rho Al}{6} r_g^2 \begin{bmatrix} 2 & 1 \\ 1 & 2 \end{bmatrix}$	$K_T = \frac{GI_t}{l} \begin{bmatrix} 1 & -1 \\ -1 & 1 \end{bmatrix}$	$\begin{Bmatrix} \phi_1 \\ \phi_2 \end{Bmatrix}$

Table 4.3: Sub-system mass and stiffness element matrices

4.1.5. Element Matrices

The element matrices are assembled by combining the matrices derived for the individual sub-systems, given by equations 4.4 and 4.5, by assigning the matrix elements to corresponding degrees of freedom. These matrices are also in accordance with those found in literature [21][23].

$$K_{el} = \begin{bmatrix} \frac{EA}{l} & 0 & 0 & 0 & 0 & 0 & -\frac{EA}{l} & 0 & 0 & 0 & 0 & 0 \\ & \frac{12EI}{l^3} & 0 & 0 & 0 & \frac{6EI}{l^2} & 0 & -\frac{12EI}{l^3} & 0 & 0 & 0 & \frac{6EI}{l^2} \\ & & \frac{12EI}{l^3} & 0 & -\frac{6EI}{l^2} & 0 & 0 & 0 & -\frac{12EI}{l^3} & 0 & -\frac{6EI}{l^2} & 0 \\ & & & \frac{GI_t}{l} & 0 & 0 & 0 & 0 & 0 & -\frac{GI_t}{l} & 0 & 0 \\ & & & & \frac{4EI}{l} & 0 & 0 & \frac{6EI}{l^2} & 0 & \frac{2EI}{l} & 0 & 0 \\ & & & & & \frac{4EI}{l} & 0 & -\frac{6EI}{l^2} & 0 & 0 & \frac{2EI}{l} & 0 \\ & & & & & & \frac{EA}{l} & 0 & 0 & 0 & 0 & 0 \\ & & & & & & & \frac{12EI}{l^3} & 0 & 0 & 0 & -\frac{6EI}{l^2} \\ & & & & & & & & \frac{12EI}{l^3} & 0 & \frac{6EI}{l^2} & 0 \\ & & & & & & & & & \frac{GI_t}{l} & 0 & 0 \\ & & & & & & & & & & \frac{4EI}{l} & 0 \\ \text{sym.} & & & & & & & & & & & 4l^2 \end{bmatrix} \quad (4.4)$$

$$M_{el} = \rho Al \begin{bmatrix} \frac{1}{3} & 0 & 0 & 0 & 0 & 0 & \frac{1}{6} & 0 & 0 & 0 & 0 & 0 \\ & \frac{156}{420} & 0 & 0 & 0 & \frac{22l}{420} & 0 & \frac{54}{420} & 0 & 0 & 0 & -\frac{13l}{420} \\ & & \frac{156}{420} & 0 & -\frac{22l}{420} & 0 & 0 & -\frac{54}{420} & 0 & \frac{13l}{420} & 0 & 0 \\ & & & \frac{r_g^2}{3} & 0 & 0 & 0 & 0 & \frac{r_g^2}{6} & 0 & 0 & 0 \\ & & & & \frac{4l^2}{420} & 0 & 0 & -\frac{13l}{420} & 0 & -\frac{3l^2}{420} & 0 & 0 \\ & & & & & \frac{4l^2}{420} & 0 & \frac{13l}{420} & 0 & 0 & 0 & -\frac{3l^2}{420} \\ & & & & & & \frac{1}{3} & 0 & 0 & 0 & 0 & 0 \\ & & & & & & & \frac{156}{420} & 0 & 0 & 0 & -\frac{22l}{420} \\ & & & & & & & & \frac{156}{420} & 0 & \frac{22l}{420} & 0 \\ & & & & & & & & & \frac{r_g^2}{3} & 0 & 0 \\ & & & & & & & & & & \frac{4l^2}{420} & 0 \\ \text{sym.} & & & & & & & & & & & \frac{4l^2}{420} \end{bmatrix} \quad (4.5)$$

$$\bar{u} = \begin{bmatrix} u_1 \\ v_1 \\ w_1 \\ \psi_1 \\ \varphi_1 \\ \theta_1 \\ u_2 \\ v_2 \\ w_2 \\ \psi_2 \\ \varphi_2 \\ \theta_2 \end{bmatrix}, \bar{f} = \begin{bmatrix} F_{x1} \\ F_{y1} \\ F_{z1} \\ T_1 \\ M_{y1} \\ M_{z1} \\ F_{x2} \\ F_{y2} \\ F_{z2} \\ T_2 \\ M_{y2} \\ M_{z2} \end{bmatrix}$$

4.1.6. Local and Global Coordinate Systems

The mass and stiffness matrices for individual elements is defined in their local coordinate system. However solving the system requires the use of a global coordinate system that every element adheres to. In order to take the rotation of a local coordinate system with respect to the global coordinate system into account, a rotational transformation matrix \mathbf{R}_R (right side) is applied, see equations 4.7 through 4.10. These matrices are derived in appendix A and can be modified for any rotation in any plane.

$$\mathbf{R}_\alpha = \begin{bmatrix} \cos(\alpha) & \sin(\alpha) & 0 & 0 & 0 & 0 \\ -\sin(\alpha) & \cos(\alpha) & 0 & 0 & 0 & 0 \\ 0 & 0 & 1 & 0 & 0 & 0 \\ 0 & 0 & 0 & \cos(\alpha) & \sin(\alpha) & 0 \\ 0 & 0 & 0 & -\sin(\alpha) & \cos(\alpha) & 0 \\ 0 & 0 & 0 & 0 & 0 & 1 \end{bmatrix} \quad (4.7)$$

$$\mathbf{R}_\beta = \begin{bmatrix} \cos(\alpha) & 0 & -\sin(\beta) & 0 & 0 & 0 \\ 0 & 1 & 0 & 0 & 0 & 0 \\ \sin(\beta) & 0 & \cos(\beta) & 0 & 0 & 0 \\ 0 & 0 & 0 & \cos(\beta) & 0 & -\sin(\beta) \\ 0 & 0 & 0 & 0 & 1 & 0 \\ 0 & 0 & 0 & \sin(\beta) & 0 & \cos(\beta) \end{bmatrix} \quad (4.8)$$

$$\mathbf{R}_\gamma = \begin{bmatrix} 1 & 0 & 0 & 0 & 0 & 0 \\ 0 & \cos(\gamma) & \sin(\gamma) & 0 & 0 & 0 \\ 0 & -\sin(\gamma) & \cos(\gamma) & 0 & 0 & 0 \\ 0 & 0 & 0 & 1 & 0 & 0 \\ 0 & 0 & 0 & 0 & \cos(\gamma) & \sin(\gamma) \\ 0 & 0 & 0 & 0 & -\sin(\gamma) & \cos(\gamma) \end{bmatrix} \quad (4.9)$$

$$\mathbf{R} = \mathbf{R}_\alpha \cdot \mathbf{R}_\beta \cdot \mathbf{R}_\gamma \quad (4.10)$$

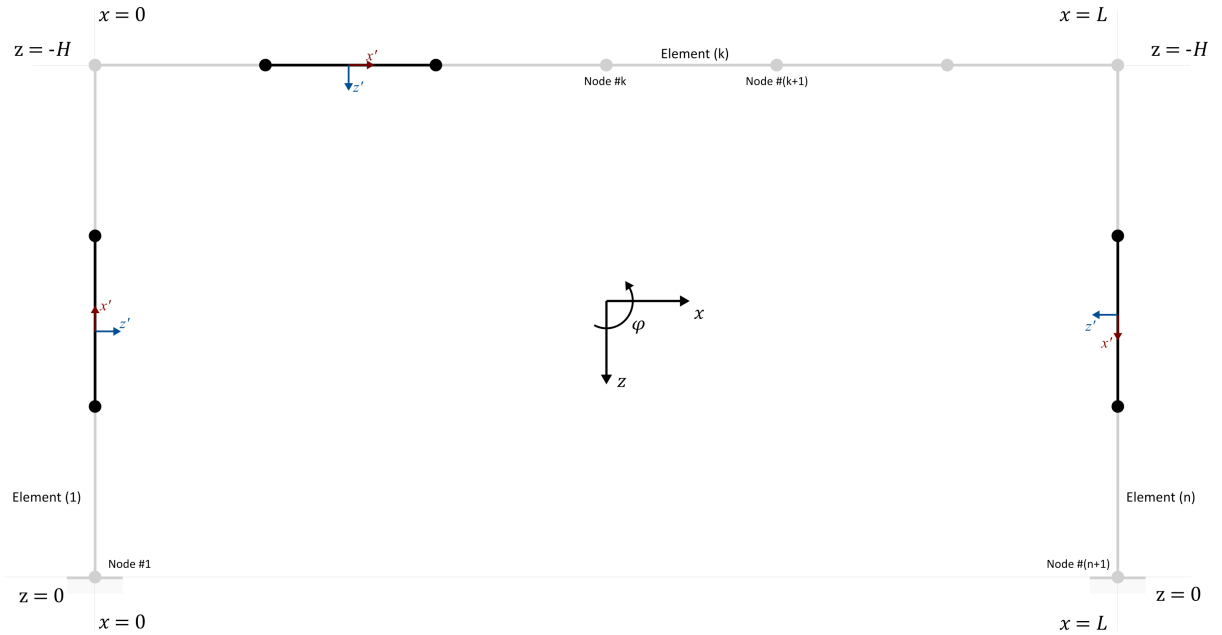


Figure 4.4: Local coordinate system of various elements within the structure with respect to the global coordinate system

4.2. Damping

Damping of a system with a large number of degrees of freedom is complex and as such there are currently no physical damping models that accurately reflect the structure's behavior. Instead proportional damping is utilized, which relates the damping matrix to the mass and stiffness matrix. The most commonly employed damping model for an n degree of freedom system is the Rayleigh Damping Model, which is not related to any physical process but adequately reflects the total damping of the structure[source]. In this model the damping matrix is given by a linear combination of the mass and stiffness matrix as shown in equation 4.11.

$$\mathbf{C} = \alpha \mathbf{M} + \beta \mathbf{K} \quad (4.11)$$

Where:

- C** = Damping matrix
- M** = Mass matrix
- K** = Stiffness matrix
- α = Mass proportional damping coefficient
- β = Stiffness proportional damping coefficient

According to the Rayleigh Damping Model the proportional damping coefficients α and β can be determined choosing two reference vibration modes i and j . The corresponding vibrations (ω_i and ω_j) and corresponding damping ratios (ζ_i and ζ_j) are then used in equation 4.12 in order to compute the damping ratios. The vibrations (natural frequencies) can be determined by performing an eigenvalue analysis of the system using the mass and stiffness matrices. The damping ratios have to be determined through empirical measurements. There is very limited data available for determining the damping ratio, which is why a single damping ratio $\zeta = \zeta_i = \zeta_j$ is often used to describe the structure as a whole; this simplifies equation 4.12 to equation 4.13.

$$\begin{Bmatrix} \alpha \\ \beta \end{Bmatrix} = \frac{2\omega_i\omega_j}{\omega_j^2 - \omega_i^2} \begin{bmatrix} \omega_j & -\omega_i \\ -\frac{1}{\omega_j} & \frac{1}{\omega_i} \end{bmatrix} \begin{Bmatrix} \zeta_i \\ \zeta_j \end{Bmatrix} \quad (4.12)$$

$$\begin{Bmatrix} \alpha \\ \beta \end{Bmatrix} = \frac{2\zeta}{\omega_i + \omega_j} \begin{Bmatrix} \omega_i\omega_j \\ 1 \end{Bmatrix} \quad (4.13)$$

Where:

- α = Mass proportional damping coefficient
- β = Stiffness proportional damping coefficient
- ω_i = i^{th} natural frequency
- ω_j = j^{th} natural frequency
- ζ_i = i^{th} damping ratio
- ζ_j = j^{th} damping ratio

When considering a steel structure the damping characteristics follow mainly from mechanical damping, which in turn consists mainly of three components: *material damping*, *thermoelastic damping*, and *air damping*. The total mechanical damping may be calculated by taking the sum of these individual components as seen in equation 4.14.

$$\zeta = \zeta_m + \zeta_T + \zeta_a \quad (4.14)$$

Where:

- ζ = Total mechanical damping
- ζ_m = Material damping
- ζ_T = Thermal damping
- ζ_a = Air damping

4.2.1. Material Damping

Material damping is affected by a wide array of factors such as: material type, stress amplitude, internal loads, number of cycles, sizes of geometry, surface quality [35]. In literature various values for the material damping ratio ζ_m can be found. According to Adams and Askenasi the damping ratio for continuous metal structures lies between 0.02 and 0.04, while the damping ratio for metal structures with joints lies between 0.03 and 0.07. The structure in question is modeled under the assumption that the joints are fully rigid, resulting in structural behavior akin to a continuous metal structure. However in reality there is still energy dissipated in the joints when deformed dynamically, as a result a value of 0.04 is chosen for the analysis. This value lies in the overlapping region of the two aforementioned ranges, and should sufficiently model the semi-continuous nature of the metal structure in question.

4.2.2. Thermoelastic Damping

As the structure vibrates the steel profiles undergo flexural deformation, resulting in compression and tension in the cross-section. This creates a temperature gradient which is a source of internal energy loss resulting in damping of the vibrations. Zener [34] related the damping of a structural beam element to the thermal properties of the material of the beam.

$$\zeta_T = \frac{1}{2} \Delta_E \frac{\omega \tau}{1 + (\omega \tau)^2} \quad (4.15)$$

Where Δ_E and τ are defined as:

$$\Delta_E = \frac{E \alpha^2 T_0}{\rho C_p} \quad (4.16)$$

$$\tau = \frac{b^2}{\pi^2 k} \quad (4.17)$$

Where:

- ω = Frequency at which structure vibrates
- E = Isothermal Young's modulus
- α = Thermal expansion coefficient

T_0	= Ambient temperature
ρ	= Material density
p	= Specific heat capacity
k	= Thermal diffusivity
b	= Beam width

Equations 4.15 through 4.17 assume that the viscous damping ratio is half the damping loss factor of the hysteretic damping, which holds true for proportional damping models such as the Rayleigh Damping Model. The expression for the relaxation time τ (time required for an object to return to ambient temperature) corresponds to the case where relaxation occurs through the first mode, which is valid for approximately 98.6% of thin solid rectangular beams according to Zener [34]. The structure under consideration does not contain solid rectangular beams, but instead uses rectangular hollow sections. Hollow sections of width b contain significantly less mass than solid beams of width b , which means that if these equations are used for hollow sections, the calculated relaxation time τ is much higher than the true relaxation time. As a result equation 4.15 underestimates the damping ratio, which is a safe but conservative assumption as damping reduces the amplitude of the measured stress ranges with respect to fatigue.

4.2.3. Mechanical Damping Ratio

Ultimately it is assumed that the effects of thermoelastic damping and air damping are negligible with respect to the material damping. As such the mechanical damping ratio is taken as equal to the material damping ratio.

4.3. Equation of Motion

The displacements of the dynamic system are governed by the equations of motion by said system. The system is discretized into N number of elements, leading to $N + 1$ number of nodes. Each node has six degrees of freedom (DoF), leading to a total of $6(N + 1)$ degrees of freedom in the system and $6(N + 1)$ equations of motion. Due to the coupling between certain degrees of freedom, the equations of motion are represented through matrices and vectors, see equation 4.18.

$$\mathbf{M}\ddot{\mathbf{u}} + \mathbf{C}\dot{\mathbf{u}} + \mathbf{K}\mathbf{u} = \mathbf{f} \quad (4.18)$$

Where:

\mathbf{M}	= Mass matrix
\mathbf{C}	= Damping matrix
\mathbf{K}	= Stiffness matrix
\mathbf{u}	= Displacement vector
$\dot{\mathbf{u}}$	= Velocity vector
$\ddot{\mathbf{u}}$	= Acceleration vector
\mathbf{f}	= Force vector

4.3.1. Assembly of System Matrices and Vectors

The equation of motion describes the system as a whole in the global coordinate system. Each mass and stiffness matrix can be multiplied by the relevant rotation matrix to ensure each element stiffness and mass matrix corresponds to a global degree of freedom. Then each element matrix can be placed in the system matrix depending on which global degrees of freedom it relates to, see figure 4.5.

4.3.2. Boundary Conditions

The boundary conditions of the system are located at the bottom supports of the columns, and dictate how the degrees of freedom at said location are restricted. The boundary conditions at the location where the structure interacts with the ground are assumed to be fully rigid. In reality the ground supports the structure elastically, but this would require the elastic spring model of the ground to be integrated with the dynamic model outlined in this chapter, which is beyond the scope of this thesis. The way the

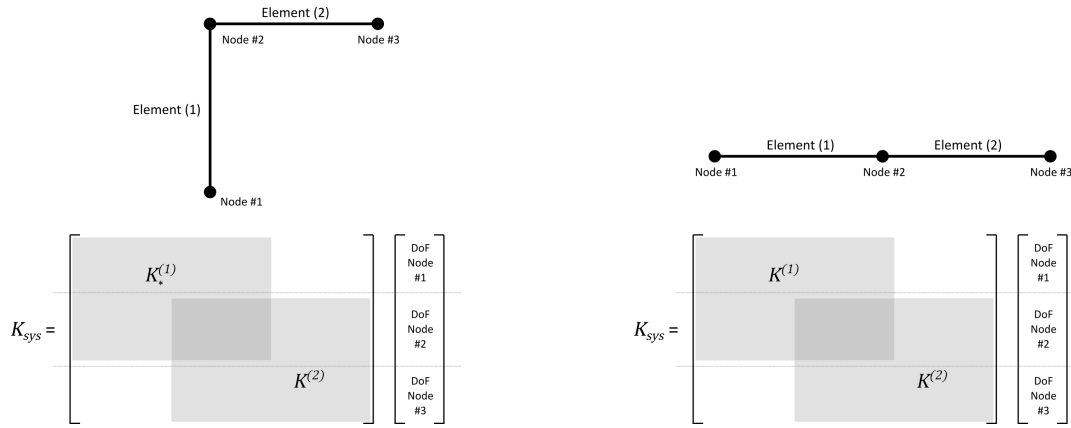


Figure 4.5: Assembly of system matrices by superposition of element matrices

boundary conditions are applied to the model (in case of a fixed boundary condition) is to remove all vector rows, and matrix rows and columns associated with the constrained degree of freedom.

4.4. Direct Integration Solution

The system that describes the structure and the loads acting upon it is solved using the open source coding language Python, and several open source Python packages. Most notably the *NumPy* library [20] is used for matrix and vector operations using arrays, the *SciPy* library [37] is used for numerical integration when solving the system of equations governing the vibrations of the structure, and the *Matplotlib* library [22] is used for visualization of the results.

4.4.1. Numerical Solution First Order Ordinary Differential Equation

Given a first order ordinary differential equation where the first time derivative of a function $y(x, t)$ (for example a displacement field) is dependent on the original function y (i.e. in the form of equation 4.19), then the solution for $y(x, t)$ can be obtained through numerical integration. One tool that is able to achieve this is the *solve_ivp* function from the *SciPy* library [37].

$$\frac{\partial}{\partial t}y(x, t) = h(y, t) \tag{4.19}$$

$$y(x, t) = \int h(y, t)dt \tag{4.20}$$

Where:

- y = Function to be solved, in this case a displacement field
- x = Some variable of function y , in this case a spatial coordinate
- t = Some variable of function y , in this case time
- h = Function describing the first time derivative of y

The *solve_ivp* function takes as input primarily three items: a function h describing the first (time) derivative of y , a set of initial conditions y_0 , and a time span t over which will be integrated, as shown in equation 4.21. The user may also define a integration method, in this case the default Explicit Runge-Kutta method of order 5(4) is used. The algorithm chooses an optimal integration step size and performs the numerical calculation. By default the function outputs the time array t and solution array y , whose lengths depend on the time span and integration steps. Often a small integration step size is required for accurate integration and accurate representation of the loads, which results in extremely large output arrays which are slow to parse. An alternative output is an interpolation function which is created using an algorithm which provides the correct interpolant for each point in the t and y arrays.

$$y = \text{solve_ivp}(h, y_0, t) \tag{4.21}$$

Where:

- y = Output array the same length as input array t
- h = Function describing the first derivative with respect to variable t
- y_0 = Initial conditions of y corresponding to the first array element of array t
- t = Input array representing variable over which h is integrated

The Explicit Runge-Kutta method is a widely used numerical integration method whose step size is taken using the 5th order accurate formula, and an error controlled by the 4th order method [37]. The advantage of the Runge-Kutta method is that it is relatively easy to implement, generally stable, and is "self starting" (no special algorithm needs to be implemented for the initial conditions steps). The main disadvantage is that it is a slower algorithm compared to multi-step methods.

4.4.2. Numerical Solution Simple Mass-Spring System

The governing equation of motion for a simple damped mass-spring system is given by equation 4.22. This is a second order differential equation, however it can be rewritten as a set of coupled first order differential equations as shown in equation 4.23 and 4.24.

$$\begin{aligned} m\ddot{u} + c\dot{u} + ku &= F \\ \ddot{u} + 2\zeta\omega\dot{u} + \omega^2u &= \frac{F}{m} \end{aligned} \quad (4.22)$$

$$y = \begin{cases} y_1 = u \\ y_2 = \dot{u} \end{cases} \quad (4.23)$$

$$h = \begin{cases} h_1 = y_2 \\ h_2 = \frac{F}{m} - \omega^2y_1 \end{cases} \quad (4.24)$$

Where:

- m = Concentrated mass
- k = Linear spring stiffness
- u = Displacement field
- F = Load
- ω = Natural frequency

4.4.3. Numerical Solution Full System

The `solve_ivp` function can also be used for a system with n degrees of freedom by using the matrix and vector form of the governing equation of motion (see equation 4.18). In this case the variables y_1 and y_2 used in the `solve_ivp` function are no longer individual values, but are arrays of values, as can be seen in equations 4.25 and 4.26.

$$y = \begin{cases} \bar{y}_1 = \bar{u} \\ \bar{y}_2 = \dot{\bar{u}} \end{cases} \quad (4.25)$$

$$h = \begin{cases} h_1 = \bar{y}_2 \\ h_2 = \mathbf{M}^{-1}\bar{f} - \mathbf{M}^{-1}\mathbf{C}\bar{y}_2 - \mathbf{M}^{-1}\mathbf{K}\bar{y}_1 \end{cases} \quad (4.26)$$

4.5. Modal Solution

The aforementioned integration method describes the full response of the system step-by-step using small time increments. While accurate, it is also time consuming. An alternative solution method is to solve the system in modal space as opposed to "real" space. This method determines the eigenmodes of the system, and calculates the response to each mode. The advantage here is that the structure will respond more strongly to lower modes whose frequency lie close to the loading frequencies, and as a result the higher frequencies provide a negligible response and may be omitted while maintaining a high degree of accuracy.

The general solution vector of the system \bar{u} can be written as a summation of sinusoidal waves which are composed of eigenvectors \hat{u} and a temporal component x containing the sinusoidal time signature. Each item in the summation represents the response of the k^{th} mode as shown in equation 4.5.

$$\bar{u} = \sum_{k=1}^n \hat{u}_k \cdot x_k(t) = \sum_{k=1}^n \hat{u}_k \cdot A_k e^{i\omega t} = \mathbf{E}\bar{x}$$

Where:

- \bar{u} = Response displacement vector of system
- \bar{u}_k = k^{th} eigenvector
- \bar{x}_k = k^{th} temporal component of eigenmode response
- e = Natural exponent
- i = imaginary unit equal to $\sqrt{-1}$
- ω_k = k^{th} eigenfrequency
- \mathbf{E} = Eigenmatrix of system
- \bar{x} = Vector containing all temporal components of eigenmode response
- n = Total number of modes considered

The matrix equation of motion can be rewritten by substituting equation 4.5 into equation 4.18. Both side of the equation can then be premultiplied by the transverse of the eigenmatrix in order to obtain the modal mass, and stiffness matrices, see equations 4.28 through 4.30.

$$\mathbf{E}^T \mathbf{M} \mathbf{E} \ddot{\bar{x}} + \mathbf{E}^T \mathbf{C} \mathbf{E} \dot{\bar{x}} + \mathbf{E}^T \mathbf{K} \mathbf{E} \bar{x} = \mathbf{E}^T \bar{f} \quad (4.28)$$

$$\mathbf{M}^* \ddot{\bar{x}} + (\alpha \mathbf{M}^* + \beta \mathbf{K}^*) \dot{\bar{x}} + \mathbf{K}^* \bar{x} = \mathbf{E}^T \bar{f} \quad (4.29)$$

$$\mathbf{M}^* \ddot{\bar{x}} + (\alpha \mathbf{M}^* + \beta \Omega^2 \mathbf{M}^*) \dot{\bar{x}} + \Omega^2 \mathbf{M}^* \bar{x} = \mathbf{E}^T \bar{f} \quad (4.30)$$

Where:

- \mathbf{M}^* = Modal mass matrix
- \mathbf{K}^* = Modal stiffness matrix = $\Omega^2 \mathbf{M}^*$
- Ω = Eigenfrequency matrix; diagonal matrix containing the eigenfrequencies of the system
- \bar{x} = Modal temporal component vector

The system under consideration contains symmetric matrices part of the well understood standard eigenvalue problem in linear algebra, which holds true for the damped system as well as the damping matrix is a linear combination of the mass and stiffness matrix (proportional damping). As a result the eigenvectors of this system are orthogonal. One of the properties of two orthogonal vectors is that the dot product between one of these vectors and the transverse of the other will equal zero. This will result in modal system matrices that are diagonal, which means that while solving the system each time-step no longer requires a $N \times N$ matrix calculation (where N is the number of degrees of freedom in the system), but simply solving n decoupled equations (where n is the number of modes taken into consideration), see equations 4.31 and 4.32.

$$m_{kk}^* \ddot{x}_k + (\alpha m_{kk}^* + \beta \omega_k^2 m_{kk}^*) \dot{x}_k + \omega_k^2 m_{kk}^* x_k = \hat{u}_k \bar{f} = \bar{f}_k^* \quad (4.31)$$

$$\ddot{x}_k + (\alpha + \beta \omega_k^2) \dot{x}_k + \omega_k^2 x_k = \frac{\bar{f}_k^*}{m_{kk}^*} \quad (4.32)$$

Where:

- m_{kk}^* = k^{th} diagonal modal mass matrix element
- \bar{x}_k = k^{th} temporal component of eigenmode response
- ω_k = k^{th} eigenfrequency
- \bar{f}_k = k^{th} modal load vector

4.6. Internal Loads

Once the response of the system in the form of a displacement vector is known the internal loads may be calculated based on the internal load formulation for slender structures. Equations 4.33 through 4.38 provide the relevant formulas for determining the load distribution across a given element based on the displacement field of said element.

$$N(x) = EA \frac{du_e}{dx} \quad (4.33)$$

$$V_y(x) = EI \frac{d^3 v_e}{dx^3} \quad (4.34)$$

$$V_z(x) = -EI \frac{d^3 w_e}{dx^3} \quad (4.35)$$

$$T(x) = GI_t \frac{d\psi}{dx} \quad (4.36)$$

$$M_y(x) = -EI \frac{d^2 \varphi}{dx^2} \quad (4.37)$$

$$M_z(x) = -EI \frac{d^2 \theta}{dx^2} \quad (4.38)$$

The internal load values for each node can be determined by evaluating the relevant expression in equations 4.33 through 4.38 using the shape functions to describe the displacement field. The expression can be evaluated at either $x = 0$ for the internal load value at the element start node or at $x = l$, where l is the element length, for the internal load value at the element end node. This concept is illustrated for the shear force in the z -direction for the start node of an arbitrary element in equations 4.39 and 4.40. In the latter expression the number of x 's in the shape function's subscript represents how many times the shape function is differentiated with respect to x , as shown in equation 4.41.

$$V_{z,1}(x) = -EI \frac{d^3 w_e}{dx^3}(x=0) = -EI \cdot \frac{d^3}{dx^3}(w_1 N_{w_1}(0) + \varphi_1 N_{\varphi_1}(0) + w_2 N_{w_2}(0) + \varphi_2 N_{\varphi_2}(0)) \quad (4.39)$$

$$V_{z,1}(x) = -EI(w_1 N_{w_1,xxx}(0) + \varphi_1 N_{\varphi_1,xxx}(0) + w_2 N_{w_2,xxx}(0) + \varphi_2 N_{\varphi_2,xxx}(0)) \quad (4.40)$$

$$N_{w_1,xxx} = \frac{d^3}{dx^3}(N_{w_1}(x)) \quad (4.41)$$

This calculation can be repeated for each load type and and sub-system. By aggregating the relevant terms associated with the relevant degrees of freedom the internal load matrices for the various sub-systems may be determined. Table 4.4 gives an overview of the internal load matrices for the various sub-systems. The element internal load matrix may be formed according to the same procedure described for the element mass and stiffness matrices. Determining the internal loads is done according to equation 4.42.

$$\bar{F}_{int} = \mathbf{Q}\bar{u} \quad (4.42)$$

Table 4.4: Overview of sub-system internal load matrices, the number of x 's in the shape function subscript denotes how many times it is differentiated with respect to x

Sub-System		Internal Load Matrix Q	Loads	DoF
Bending around y axis	$-EI$	$\begin{bmatrix} N_{w_1.xxx}(0) & N_{\varphi_1.xxx}(0) & N_{w_2.xxx}(0) & N_{\varphi_2.xxx}(0) \\ N_{w_1.xx}(0) & N_{\varphi_1.xx}(0) & N_{w_2.xx}(0) & N_{\varphi_2.xx}(0) \\ N_{w_1.xxx}(l) & N_{\varphi_1.xxx}(l) & N_{w_2.xxx}(l) & N_{\varphi_2.xxx}(l) \\ N_{w_1.xxx}(l) & N_{\varphi_1.xxx}(l) & N_{w_2.xxx}(l) & N_{\varphi_2.xxx}(l) \end{bmatrix}$	$\begin{Bmatrix} V_{z1} \\ M_{y1} \\ V_{z2} \\ M_{y2} \end{Bmatrix}$	$\begin{Bmatrix} w_1 \\ \varphi_1 \\ w_2 \\ \varphi_2 \end{Bmatrix}$
Bending around z axis	EI	$\begin{bmatrix} -N_{v_1.xxx}(0) & -N_{\theta_1.xxx}(0) & -N_{v_2.xxx}(0) & -N_{\theta_2.xxx}(0) \\ N_{v_1.xx}(0) & N_{\theta_1.xx}(0) & N_{v_2.xx}(0) & N_{\theta_2.xx}(0) \\ -N_{v_1.xxx}(l) & -N_{\theta_1.xxx}(l) & -N_{v_2.xxx}(l) & -N_{\theta_2.xxx}(l) \\ N_{v_1.xxx}(l) & N_{\theta_1.xxx}(l) & N_{v_2.xxx}(l) & N_{\theta_2.xxx}(l) \end{bmatrix}$	$\begin{Bmatrix} V_{y1} \\ M_{z1} \\ V_{y2} \\ M_{z2} \end{Bmatrix}$	$\begin{Bmatrix} v_1 \\ \theta_1 \\ v_2 \\ \theta_2 \end{Bmatrix}$
Axial		$EA \begin{bmatrix} N_{u_1.x}(0) & N_{u_2.x}(0) \\ N_{u_1.x}(l) & N_{u_2.x}(l) \end{bmatrix}$	$\begin{Bmatrix} N_1 \\ N_2 \end{Bmatrix}$	$\begin{Bmatrix} u_1 \\ u_2 \end{Bmatrix}$
Torsion		$GI_t \begin{bmatrix} N_{\psi_1.x}(0) & N_{\psi_2.x}(0) \\ N_{\psi_1.x}(l) & N_{\psi_2.x}(l) \end{bmatrix}$	$\begin{Bmatrix} T_1 \\ T_2 \end{Bmatrix}$	$\begin{Bmatrix} \psi_1 \\ \psi_2 \end{Bmatrix}$

Where:

- \vec{F}_{int} = System internal load vector
- \mathbf{Q} = System internal load conversion matrix
- \vec{u} = System displacement vector

4.7. Model Validation

The model outlined in this chapter consists of three main steps: first the structure is represented by a dynamic system described by the mass and stiffness matrices, second the response of the system due to a load is determined through integration of the equation of motion, and finally thirdly the internal loads of the system are determined using the internal load matrix and the deformation vectors. The method used in each of these steps should be verified.

4.7.1. System Verification

The mass and stiffness matrices of the system describe the dynamic system. In order to evaluate the accuracy of these matrices the eigen-frequencies of the system can be computed and compared to analytical expressions. There are no readily available equations for the eigen-frequencies of specific portal frames, but those for a simple structure may easily be determined. In appendix B an analytical expression for the eigen-frequencies for a simple beam clamped on either end, i.e. fixed-fixed boundary conditions, is determined and shown in equation 4.43,

$$\omega_n = \sqrt{\frac{EI}{\rho A}} \cdot \left(\frac{3 + 2n\pi}{2L} \right)^2 \quad (4.43)$$

Where:

- ω_n = The beam's eigen-frequency of the n^{th} mode
- E = Modulus of elasticity (= 210 GPa)
- I = Beam profile moment of inertia in mm^4
- ρ = Density of steel (= $7800 \cdot 10^{-9} \text{ kg/mm}^3$)
- A = Beam profile cross-sectional area in mm^2
- L = Beam length in mm

The numeric eigen-frequencies of the un-damped system follow from the eigen value problem in equation 4.47, which is created by substituting the general solution in equation 4.45 into the matrix equation of motion in equation 4.44.

$$\mathbf{M}\ddot{\bar{u}} + \mathbf{K}\bar{u} = 0 \quad (4.44)$$

$$\bar{u} = \bar{u}_0 e^{i\omega t} \quad (4.45)$$

$$\mathbf{K}\bar{u} = \lambda \mathbf{M}\bar{u} \quad (4.46)$$

$$\lambda = \omega^2 \quad (4.47)$$

Where:

- M** = System mass matrix
- K** = System stiffness matrix
- \bar{u} = System general solution
- \bar{u}_0 = System general solution amplitude matrix
- ω = System eigenfrequency
- λ = System eigenvalue

The eigenvalue problem given by equation 4.47 can be solved using the python *SciPy* library using the *eig* function [37]. This function takes as input the left-hand-side and right-hand-side eigenvalue problem matrices, which in this case are the stiffness matrix K and mass matrix M respectively, and outputs an array of eigenvalues and the eigenmatrix. The numeric eigenfrequencies can be compared to the analytical eigenfrequencies as shown in figure 4.6.

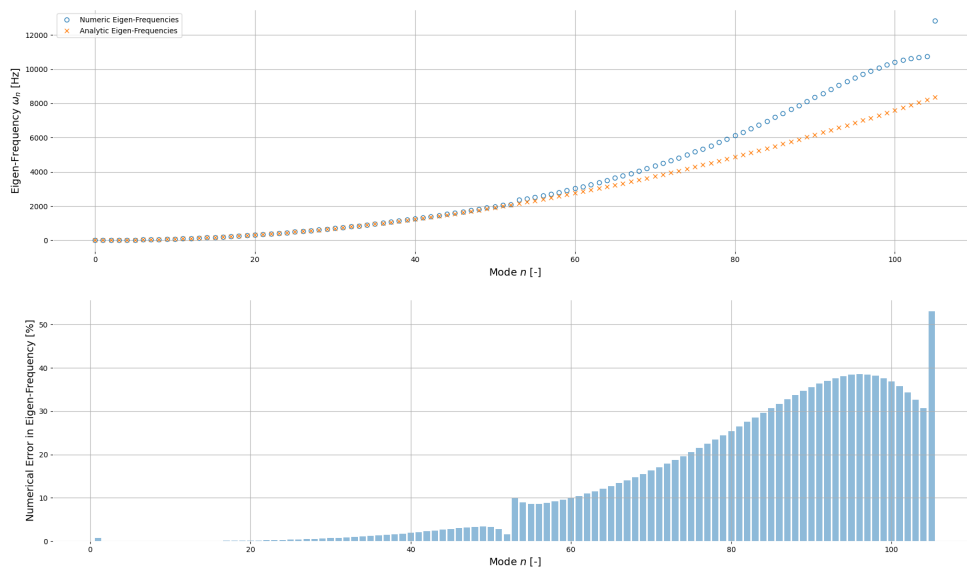


Figure 4.6: Comparison of numerically and analytically computed eigenfrequencies. The top plot shows the values for each eigenmode, the bottom shows the difference in value relative to the analytical value.

From this figure it can be seen that the eigenfrequencies corresponding to the lower eigen-modes are accurately calculated. A smaller element size will result in a larger number of nodes, which leads to larger system matrices which are able to describe more eigenmodes. When comparing the numeric and analytical eigenfrequencies, it turns out that there is a significant increase in inaccuracy at the eigenmode roughly half of the largest eigenmode the numeric approach is able to calculate. This is most likely due to a computational error in the numeric approach used by the *LAPACK* driver routine

which is used in the *SciPy* library when evaluating the *eig* function [37]. Fortunately this does not pose any significant problems as the loading occurs at low frequencies up to 10 Hz; special care should be taken that a sufficiently small element size is used in order to make the relevant eigen-frequencies as accurate as possible.

4.7.2. Solver Verification

When running a simulation the dynamic system is solved by integrating the matrix equation of motion. This can be done through the direct integration approach, also known as the brute force method, where the entire equation of motion is integrate numerically with a small time step. To verify the accuracy of the numerical integration method a simple damped mass-spring system containing a single degree of freedom, such as the one in figure 4.7 is considered. The system is solved according to the method described in section 4.4.2, the code for which can be found in listing 4.1, and the results in figure 4.8. In this calculation the numeric results are compared to the analytical solution which is given by equation 4.48 [3]. In this comparison it can be seen that the *solve_ivp* function is able to integrate over the time domain in only a couple of time steps, and then uses a cubic interpolation function to define the displacement x for all values in the considered time-domain, which corresponds extremely well to the analytical solution. Unfortunately the integration time steps need to be much smaller when considering loads on the system, as the value of the load changes significantly between two instances in time.

$$x(t) = 0.5e^{-t} \cdot \sin 2t + e^{-t} \cdot \cos 2t \quad (4.48)$$

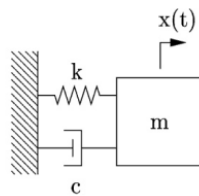


Figure 4.7: A simple damped mass-spring system containing a single degree of freedom $x(t)$

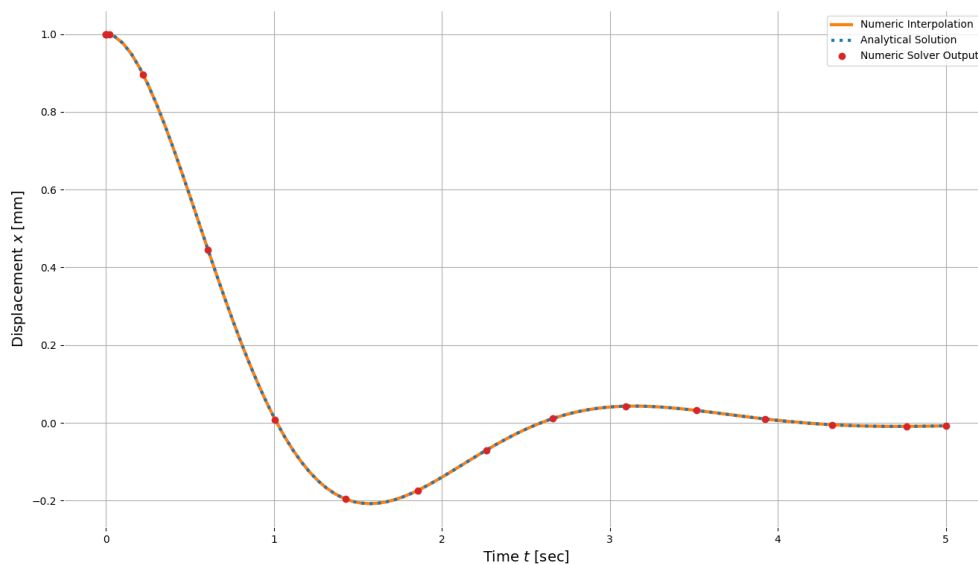


Figure 4.8: A simple damped mass-spring system containing a single degree of freedom $x(t)$

```
1 import numpy as np
```

```

2 import plot_curve as pltc
3 from scipy.integrate import solve_ivp
4
5 # constants
6 m = 1 # kg
7 c = 2 # kg/s
8 k = 5 # N/mm
9
10 # initial conditions y0 = [x0, v0]
11 y0 = [1, 0]
12
13 # time domain
14 t_start = 0
15 t_end = 5
16
17
18 # first order differential
19 def h(t, y):
20     x1, x2 = y
21
22     h1 = x2
23     h2 = -c/m*x2 - k/m*x1
24
25     return [h1, h2]
26
27
28 res = solve_ivp(fun=h, t_span=[t_start, t_end], y0=y0, dense_output=True)
29
30 # analytic solution
31 t = np.linspace(t_start, t_end, 100)
32 x_a = 0.5*np.exp(-t)*np.sin(2*t) + 1*np.exp(-t)*np.cos(2*t)
33
34 # numeric raw solution
35 to = res.t
36 xo, vo = res.y
37
38 # numeric interpolated solution
39 x, v = res.sol(t)
40
41
42 fig = pltc.create_empty_figure()
43 ax = pltc.add_empty_subplot(fig, x_label='Time $t$ [sec]', y_label='Displacement $x$ [mm]'
44                             )
45 ax.plot(t, x, label='Numeric Interpolation', color='tab:orange', lw=3)
46 ax.plot(t, x_a, linestyle=':', label='Analytical Solution', color='tab:blue', lw=3)
47 ax.plot(to, xo, 'o', label='Numeric Solver Output', color='tab:red')
48
49 ax.legend()
50 pltc.show()

```

Listing 4.1: Sample code for solving a simple damped mass-spring system. The plot_curve package is a custom package created to streamline the creation of graphs using the matplotlib.pyplot library

4.7.3. Internal Load Verification

The dynamic FEM model developed in Python can also be used to perform static analyses of slender structures. The internal load calculation is verified by considering a cantilever beam loaded by a static concentrated load F_E and static concentrated moment M_E at the free end. The analytical solution to the internal load distribution is given by figure 4.9, while the numerical calculation is given by figure 4.10.

4.8. Element Size

As the number of elements increases in the discretized structure, so does the accuracy of the dynamic model and response. However it also becomes significantly more computationally expensive to perform the simulations. When solving the dynamic system in modal space the minimum element sizes will be governed by accuracy of the modal shapes. One way to measure this is by considering the natural frequencies of the system. The minimum number of modes that need to be accurately described is governed by the loading frequency. As a rule of thumb, the eigenmode with an eigenfrequency

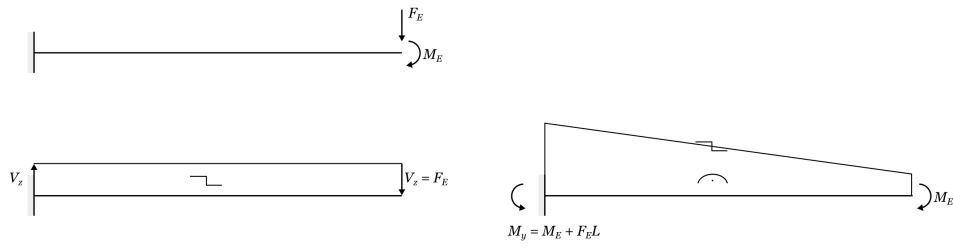


Figure 4.9: Analytical internal loads results

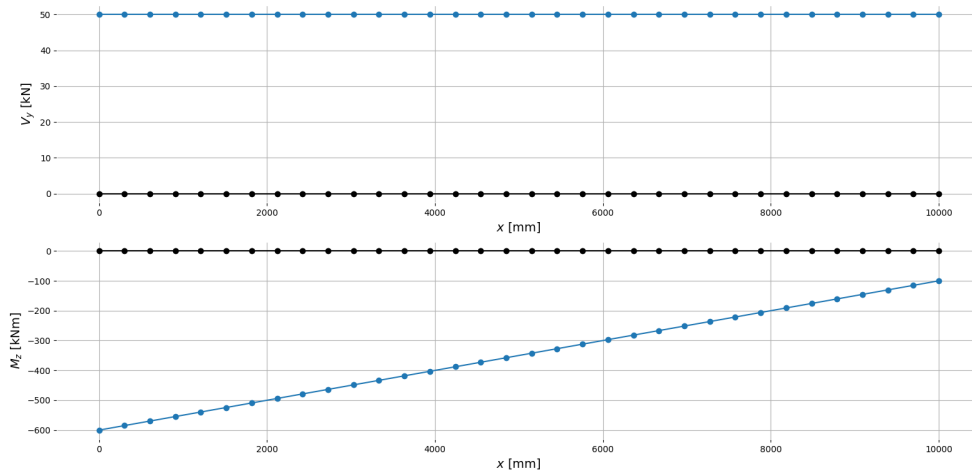


Figure 4.10: Numeric finite element method internal loads results

corresponding to twice the largest loading frequency needs to be described accurately.

The loads on the structure consist of two types of loads: the stochastic wind simulation and the traffic induced pulse loads. The frequencies of the former can be derived from the power spectral density function and the chosen cut-off frequencies. The load is derived from the square of the wind speed, which has a sinusoidal turbulence component. According to the trigonometric identity given by equation 4.49 the square of a sinusoidal wave is equal to a phase shifted sinusoidal wave with a frequency that is twice as large. The minimum eigenfrequency is twice the loading frequency, and therefore four times the upper cut-off frequency from the wind speed variance spectrum.

$$\cos(2\theta) = 1 - 2 \sin^2(\theta) \tag{4.49}$$

The pulse loads on the other hand are not intrinsically composed of sinusoidal waves, instead a Discrete Fourier Transform (DFT) in the form of a Fast Fourier Transform (FFT) needs to be taken. For a single pulse the frequencies are well described as can be seen from figure 4.11. For a set of randomly distributed pulse loads (representing daily traffic) the frequencies are distributed less smoothly, but still retain the general peaks due to the random distribution disrupting any periodic characteristics of the signal; as can be seen in figure 4.12

When considering the cut-off frequency of 9.246 Hz for the wind speed variance spectrum, the wind load frequency is twice as large at 18.492Hz. When looking at the FFT of the pulse loads in figure 4.12 it becomes clear that there are no significant peaks at these large frequencies, and the wind load can therefore be considered as the governing loading frequency.

With a load frequency of 18.492 Hz the eigenmode corresponding to an eigenfrequency of twice the loading frequency is 36.984 Hz. In order to establish which mode has an eigenfrequency that comes closest to this frequency an eigen analysis is performed on a structure with element sizes of 350mm. This is the smallest element size possible for the chosen element types: Euler Bernoulli 1D beam elements. These type of elements do not take shear deformations into account, which start to

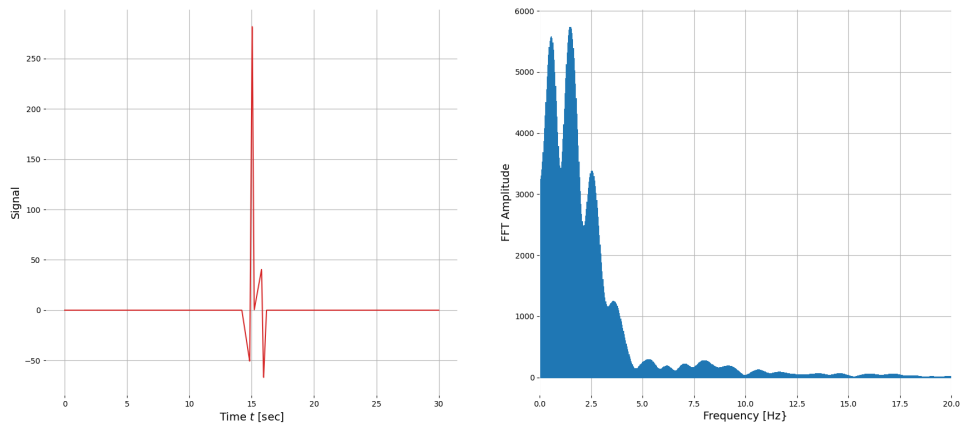


Figure 4.11: Fast Fourier Transform of single pulse load signal due to a single truck)

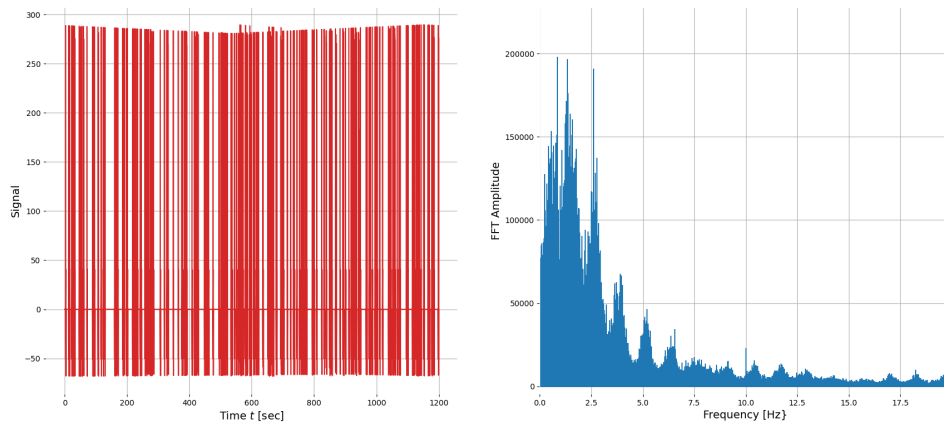


Figure 4.12: Fast Fourier Transform of a signal consisting of a random distribution of pulse loads representing daily traffic during a period of 20 minutes)

play a large role if the element length is shorter than the cross-sectional dimensions. The columns of the reference structure are SHS350/10 profiles, meaning they are 350mm wide and high. From this eigen analysis it follows that the 27th eigen mode has an eigen frequency of 39.52 Hz. As this eigen analysis is the most accurate description of the eigen-modes the dynamic model can provide it will be considered as a reference point to compare meshes with larger elements to. The reference structure is discretized into a mesh of 1D elements of varying element sizes, for each case the 27th eigen frequency is computed and compared to the reference eigen frequency (39.52Hz), which is shown in figure 4.13. As the element size increases the computation time is reduced, but the model also loses accuracy. However from figure 4.13 it becomes evident that using a mesh size of 1400mm will result in only 1% worse accuracy, which is deemed acceptable.

4.9. Limitations of Model

The model finite element method model that is developed for the analysis of the dynamic response of the system incorporates every degree of freedom of the structure, allowing the structure to deform in every possible way. This also allows every type of load at every location in the structure to be extracted. The deformations at the location of each node in the system is governed by the behavior of the elements that connect the nodes. This behavior is described based on mass and stiffness matrices that are derived

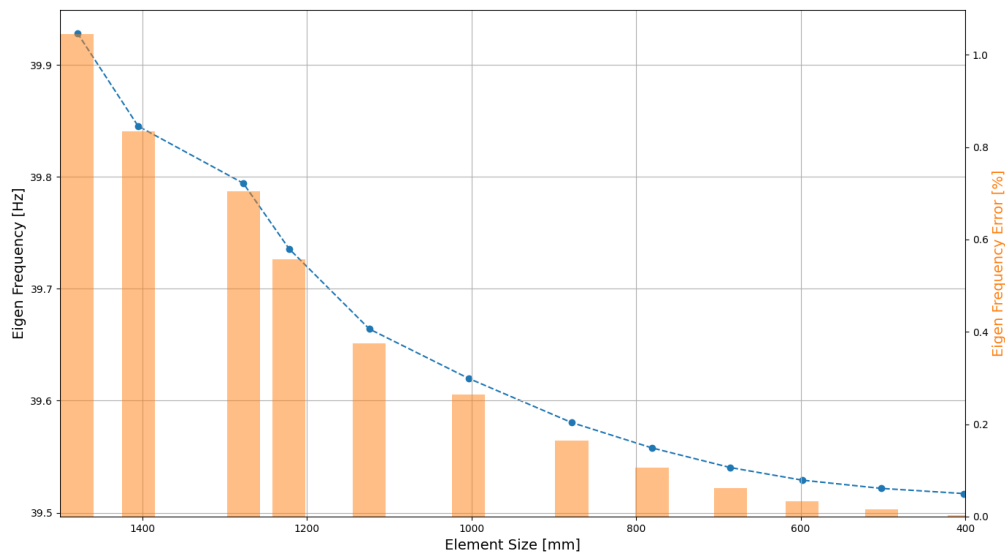


Figure 4.13: The 27th eigenfrequency computed for meshes of varying element sizes (blue) compared to the 27th eigenfrequency for a mesh with elements of 350mm (orange)

based on Euler-Bernoulli beam elements. If the structure was described by a continuous system, i.e. a set of 1D members with infinite degrees of freedom described by continuous displacement fields, the Euler-Bernoulli approach is easily justified as the members of the structure are very slender, and shear deformations play an insignificant role in the structural response of the member as a whole. However when analyzing the structure based on smaller elements, the length of the members that are analyzed becomes shorter, but the profile remains the same dimensions. This results in less slender, and more stocky elements. The less slender the element becomes the more shear deformations start to play a role in the total structural response of the system. As a rule of thumb the element size should not be smaller than the maximum cross-sectional dimension of the elements. For a column with an SHS350/10 profile such as the one found in the reference structure, the element size should be at least 350mm as the profile height and width are 350mm. This limitation to the element size may severely restrict the accuracy of the desired system. Especially if large frequencies need to be described by the system then the larger natural frequencies of the system need to be described, which can only be done accurately if small element sizes are used. Timoshenko beam elements allow smaller element sizes to be taken into account, but also adds an additional degree of freedom to the system: shear deformations of the elements. This in turn increases the computation complexity and computation time of the model.

One of perhaps the largest drawbacks of the dynamic model described in this chapter is the computation time for running a single simulation. Solving the system in modal space based on the eigenmodes of the system significantly improves the computation time relative to the direct integration method. The modal analysis requires more calculations while setting up the system, mostly in the form of computing the eigenmodes of the system and computing the modal-masses used in the modal equations of motion. However during the simulation itself it is significantly faster. However if larger load frequencies need to be taken into account, then more modal responses per integration step need to be calculated, increasing the computation time. An alternative method to determining the dynamic structural response is to use the system, i.e. the system matrices, to perform a general frequency response analysis for various loads instead of computing the exact structural response for various loads. This is beyond the scope of this thesis, but is certainly interesting for future research.

5

Joint Load Distribution

The fatigue resistance of the structure is determined by the critical structural components most susceptible to fatigue damage. In steel structures this is generally governed by details in the joints of the structure, namely the bolts and welds. Based on the dynamic analysis of the structure outlined in the previous chapter, the internal loads acting on the joint are obtained in the form of a set of time dependent signals. The relationship between the stresses in the critical components (with respect to fatigue) due to these internal loads is determined through a Finite Element Method (FEM) analysis of the joint in question.

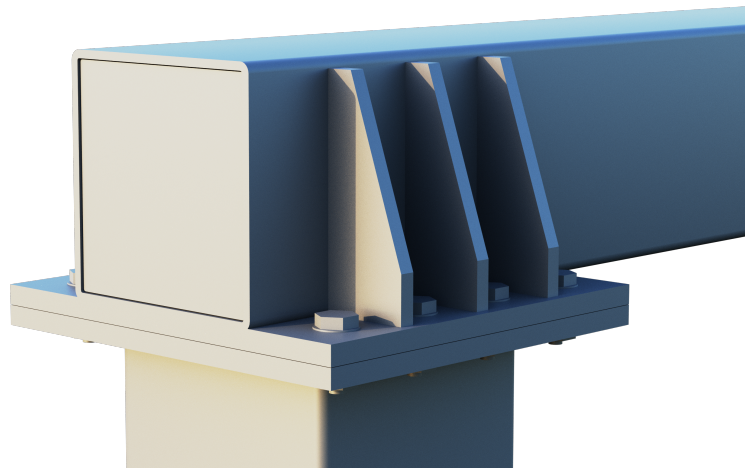


Figure 5.1: 3D impression of joint

5.1. Joint Description

The joint in question, see figure 5.1, connects the horizontal beam of the traffic sign support structure to its vertical columns. The bottom web of the square hollow section (SHS) is welded to an end plate parallel to the beam. The top of the column is welded to a separate perpendicularly orientated end plate. These two end plates are connected to each other through eight pre-tensioned bolts in slotted holes. To ensure the loads and stresses are properly transferred from the beam to the end plate a set of stiffeners is employed. The stiffeners are connected to the beam by vertical welds, and to the end plate by horizontal welds. The stiffeners also include a small hole (not included in figure 5.1) where the end plate and the beam meet in order to allow for a continuous longitudinal weld connecting the end plate and SHS beam directly. An overview of the joint dimensions can be found in figure 5.2 and table 5.1.

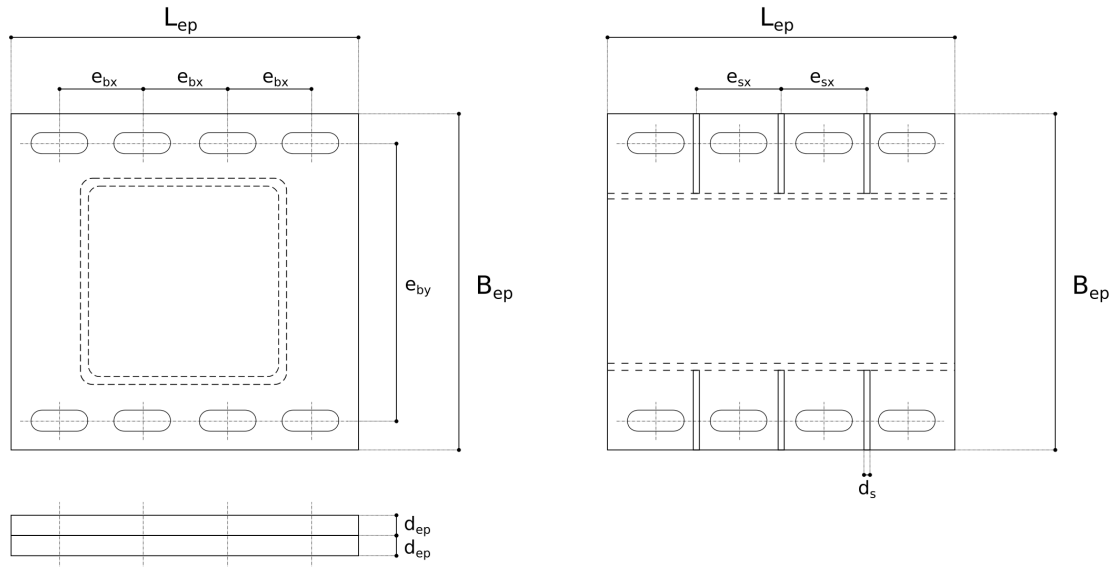


Figure 5.2: Overview of joint dimensions

Table 5.1: Dimensions of joint in reference structure

Description	Symbol	Value	Units
Beam profile	[-]	SHS300/8	[-]
Column profile	[-]	SHS350/10	[-]
End-plate width	B_{ep}	550	mm
End-plate length	L_{ep}	530	mm
End-plate thickness	d_{ep}	25	mm
Stiffener longitudinal spacing	e_{sx}	130	mm
Stiffener thickness	d_s	5	mm
Bolt type	[-]	M24 10.9	[-]
Bolt lateral spacing	e_{by}	130	mm
Bolt longitudinal spacing	e_{bx}	440	mm

5.2. Finite Element Analysis Software

The finite element method (FEM) has been around since the 1980's and is a popular tool to analyze structures with complex geometry and/or loads. When it comes to joint design research has shown that utilizing FEM in combination with an elastic-plastic analysis is required for accurate joint design [36]. There are many FEM software available, one that specializes in joint design specifically is *IDEA StatiCa*. This program utilizes a specialized FEM analysis specifically developed for joints: Component Based Finite Element Method (CBFEM), and has out-of-the-box building codes integration. On top of that the software has a clear and concise user interface allowing for a quick and effect design process.

5.2.1. Component Method

The component method is a calculation model which allows the complex structural properties of the joint to be described by a set of analytical expressions without the need of complex numerical calculation models. The way this is achieved is by decomposing the joint into a set of simple to model components. An analytical expression for the resistance and stiffness of each component can be derived based on simplified models. One such simplified model is a T-stub connection, whose failure mechanism resembles that of the various plate and bolt elements in a typical steel joint. The joint resistance follows from the component which fails first; the joint stiffness may be estimated by combining the various compo-

nents as a set of parallel and/or serial springs defined by the component's location and stiffness. An illustration of the component method being applied to an open section steel beam-to-column connection is shown in figure 5.3

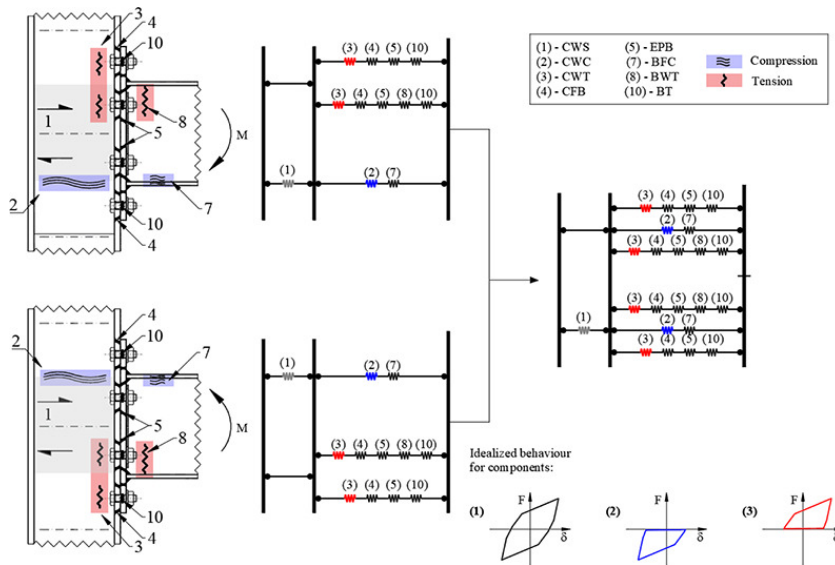


Figure 5.3: Example of the component method being applied to a beam-to-column connection. [33]

The component method simplifies the complex nature of the joint and through its generic nature it may be utilized for a large variety of connections. The main down side of the component method is also one of its advantages: the simplification of a complex structure into an analytical expression. The resistance is calculated based on a simplified failure mechanism, which sometimes over-simplifies the reality and no longer accurately describes the stresses within the joint.

5.2.2. Component Based Finite Element Method

The Component Based Finite Element Method is a method developed by the company *IDEA StatiCa* in collaboration with the *Czech Technical University in Prague* and *Brno University of Technology*. This method retains the useful aspects of the component method, namely the decomposition of a joint into components which can be analyzed individually and later combined back to a whole, but aims to improve the main down side of the component method: stress analysis of the individual components. This is achieved by analyzing the components numerically through a FEM analysis.

5.3. CBFEM Model Overview

The CBFEM used by the *IDEA StatiCa* software is utilized in order to analyze the joint in question, and ultimately describe the relationship between the cross-sectional loads acting on the joint, and the stresses within its critical components. The following section outlines various aspects of the model.

5.3.1. Element Types

The joint in question requires different element types in order to accurately describe the stress distribution and displacement of the connection. The beam and column consists of shell elements rigidly connected, *IDEA StatiCa* offers various default profiles allowing the user to model these parts with ease. The mesh-size is also automatically configured based on a sensitivity analysis, where the element size is allowed to vary between 10mm and 50mm. [1]

The beam, column and various plates (i.e. end plates and stiffeners) are connected by welds. The stresses between two plates connected by welds is transmitted through force-deformation constraints based on the Lagrangian formulation of the opposing plate. Plates of varying densities are able to be connected to one another using this approach. The finite element nodes are not directly connected to one another, allowing certain off-sets to be taken into account which represent the true weld dimensions;

this also allows the stress to be calculated directly in the weld throat.[1]

In order to eliminate unfavorable stress peaks in welds that form from a linear analysis near plate edges and at corners, an additional elasto-plastic element at the location of the weld is implemented. This additional element takes the weld location, position and the throat thickness into account. A non-linear material analysis is performed, based on which the unfavorable stress peaks in the welds are redistributed among the weld. This analysis is more accurate than traditional linear FEM elements as it ensures no averaging or interpolation is required.[1]

The other way plates in the connection are connected is through bolts. In the CBFEM the bolt elements (components) connect two shell elements through non-linear springs. These springs take the bolt axial initial stiffness, design resistance, initialization of yielding, and deformation capacity into account. For these components it is assumed that the initialization of yielding and deformation capacity is limited to the threaded portion of the bolt shank. [1]

The lateral bolt loads, which induce plate bearing, are modeled by default through interpolation links between the bolt shank nodes and the plate hole edge nodes, and can only transfer compressive stresses. The bolt holes in the plate in question are slotted holes, which is an option which can be selected in *IDEA StatiCa*. The slotted holes allow the bolt components to translate freely in the selected free direction. The bolts in question are pre-loaded, in which case the axial behavior of the bolt is modeled through the same non-linear spring. However the lateral loads are not transferred through interpolation links simulating the bearing, but through a slip-resistance check. [1]

5.3.2. Loads

When performing a global analysis of a structure, irregardless of a static or dynamic analysis, most FEM programs calculate the joint load at the center of the joint. However when performing the local analysis of the joint using the CBFEM utilized by *IDEA StatiCa* a portion, approximately one meter, of the connected members are included in the joint model. As a result the applied loads cannot follow from the node at the center of the joint, but must follow from a small distance away from the joint. In the dynamic model the output node is chosen based on an algorithm, which chooses the node closest to the point in space one meter towards the center of the beam relative to the given node, see figure 5.4.

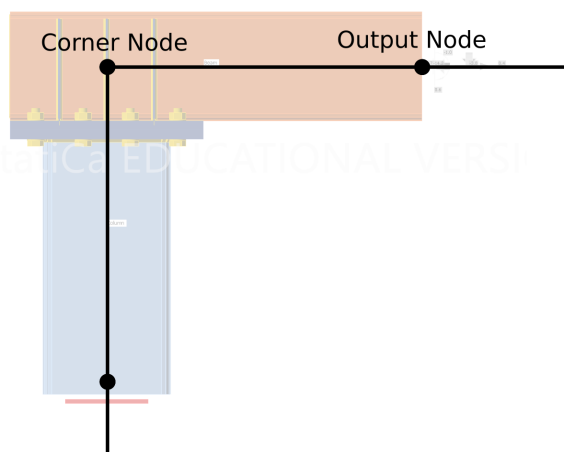


Figure 5.4: Nodes from global dynamic analysis overlaid with CBFEM joint model

5.3.3. Boundary Conditions

In order to make the joint design process as streamlined as possible the boundary conditions in *IDEA StatiCa* are only available for members, i.e. beams and columns. The default state of such boundary conditions is fully constrained (fixed/clamped) allowing for no rotations or displacements. This is a valid choice as the boundaries of the joint model are connected rigidly to the connected members. In the case of the joint under consideration the fully constrained boundary conditions are applied at the bottom of the column segment, and the loads are applied at the end of the beam. Figure 5.5 shows the

front, side, and top view of the joint model in *IDEA StatiCa*, and illustrates the location of the boundary conditions (red) and load application (grey).

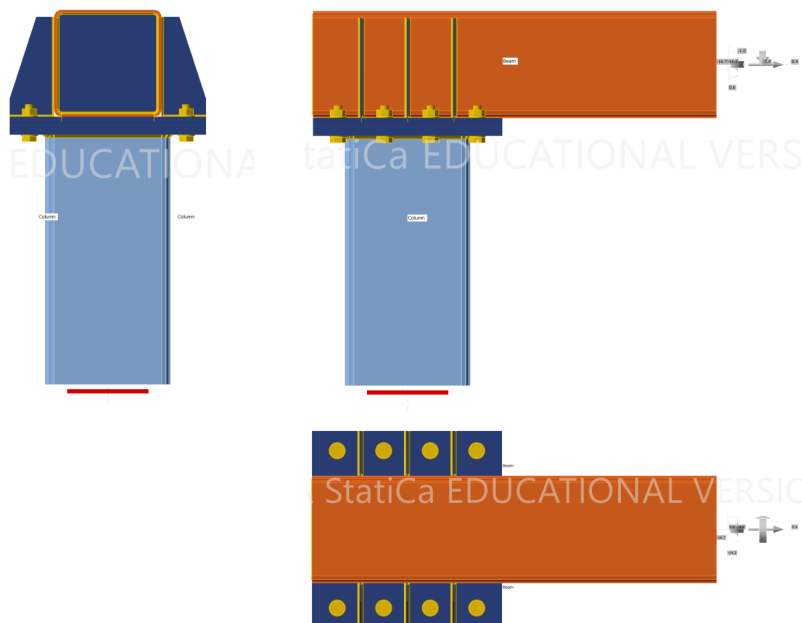


Figure 5.5: Front, side and top view of CBFEM model in *IDEA StatiCa*

5.3.4. Limitations of FEM Model

Although the CBFEM utilized by *IDEA StatiCa* is a great tool for joint design in general, it does have its limitations with respect to the applications in this thesis. Firstly the non-linear spring model analysis of the pre-tensioned bolts happens in the back-end of the application, meaning the user is unable to extract any of the non-linear analysis data. Instead only the effective tensile reaction loads of a regular bolt are presented. For this reason the true stresses varying non-linearly cannot be recorded and analyzed, a more in depth analysis of the fatigue damage in the bolts is therefore not possible. Instead it is assumed that the bolts are pre-tensioned to a sufficiently high degree that fatigue damage will not occur.

Due to a limitation in time it is assumed that no interaction between the dynamic loads occurs. More specifically the dynamic components are analyzed separately and the individual contributions are summed up towards the end of the total fatigue analysis. A more accurate and less conservative approach would be to consider all possible load combinations, where the dynamic components are applied simultaneously. If n is the number of data points required in order to describe the relationship between an external load and a weld stress, then n analyses need to be run per load type in the current approach, leading to a total of $3n$ FEM calculations. If the aforementioned more accurate approach is implemented then the total number of FEM calculations goes from $3n$ to n^3 .

Finally the boundary conditions may provide an accurate representation of how the joint is connected to its connecting members, which ensures an accurate stress distribution with the joint. However if one desires to use the calculated displacements in the global analysis, they will not translate over directly. In this case additional calculation steps and assumptions may need to be made.

5.4. Stresses in Welds

5.4.1. Overview of Welds

As mentioned in the Joint Description subsection, there are four different weld types considered in the joint, a visual overview of these welds is given in figure 5.9.

- *Beam-to-End-Plate Welds*: The beam member sits parallel to the top end-plate and is connected to it by two welds which run longitudinally along the base of the beam. See the red welds in figure

5.9.

- *Column-to-End-Plate Welds*: The column member sits perpendicular to the bottom end-plate and is connected to it by a continuous weld running along the perimeter of the column profile. See the orange welds in figure 5.9.
- *Horizontal Stiffener Welds*: The stiffeners are connected to the end-plate by welds running horizontally along the base of the stiffener. See the blue welds in figure 5.9.
- *Vertical Stiffener Welds*: The stiffeners are connected to the beam member by welds running vertically along the height of the stiffener. See the purple welds in figure 5.9.

5.4.2. Fatigue Weld Stress

The most accurate way to determine the stresses in the welds for any combination of cross-sectional loads would be to run a FEM analysis with said loads. However the dynamic analysis of the frame will result in thousands of unique combinations of cross-sectional loads. Instead the aim of the joint analysis described in this chapter is to develop an analytical expression that can be used to determine the stress in any weld. *IDEA StatiCa* provides the maximum value of the weld perpendicular normal stress σ_{\perp} , perpendicular shear stress τ_{\perp} , and parallel shear stress τ_{\parallel} for each weld in the model. Unfortunately the location of this maximum is not directly given. The user may visually inspect a graph of the weld in order to view the weld stress distribution, but cannot be given as an output value. According to the Eurocode these weld stress components should be combined according to equation 5.1 and 5.2 based on figure 5.6 in order to determine the weld stresses relevant for a fatigue analysis. A separate fatigue check should be done for the weld normal stress and weld shear stress transverse to the weld axis, σ_{wf} and τ_{wf} respectively. [15].

$$\sigma_{wf} = \sqrt{\sigma_{\perp}^2 + \tau_{\perp}^2} \quad (5.1)$$

$$\tau_{wf} = \tau_{\parallel} \quad (5.2)$$

Where:

- σ_{wf} = Normal stress transverse to axis of weld
- σ_{\perp} = Normal stress perpendicular to weld
- τ_{\perp} = Shear stress perpendicular to weld
- τ_{wf} = Shear stress transverse to axis of weld
- τ_{\parallel} = Shear stress parallel to weld

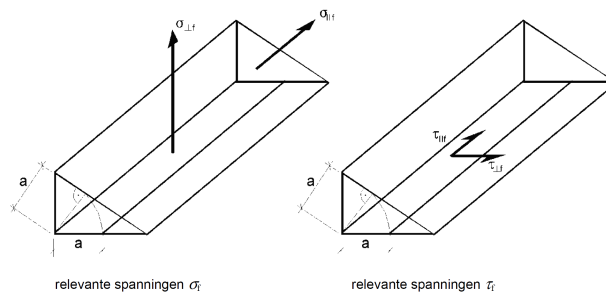


Figure 5.6: Stresses acting on welds for fatigue analysis according to the Eurocode [15]

5.4.3. Stress Components

The stresses in the welds can be deconstructed into components perpendicular and parallel to the weld, as shown in figure 5.6. It is assumed that each of these stress components can be split into a stress sub-components relating to the type of cross-sectional load that is acting on the joint, as depicted in equations 5.3 through 5.5. Each cross-sectional load is considered on its own, and it is assumed no interaction takes place. In order to investigate the exact load distribution within the joint more in depth research would be required, and is beyond the scope of this thesis.

$$\sigma_{\perp} = \sigma_{\perp.N} + \sigma_{\perp.V_y} + \sigma_{\perp.V_z} + \sigma_{\perp.T} + \sigma_{\perp.M_y} + \sigma_{\perp.M_z} \quad (5.3)$$

$$\tau_{\perp} = \tau_{\perp.N} + \tau_{\perp.V_y} + \tau_{\perp.V_z} + \tau_{\perp.T} + \tau_{\perp.M_y} + \tau_{\perp.M_z} \quad (5.4)$$

$$\tau_{\parallel} = \tau_{\parallel.N} + \tau_{\parallel.V_y} + \tau_{\parallel.V_z} + \tau_{\parallel.T} + \tau_{\parallel.M_y} + \tau_{\parallel.M_z} \quad (5.5)$$

The results from the CBFEM analysis suggests that a linear relationship exists between an external load acting on the joint and a given weld stress component. Each weld stress sub-component can therefore be modeled by the external load multiplied by a conversion factor α , an example of this is given by equation 5.6 for the sub-component relating to σ_{\perp} . The values for the various α conversion factors are given in table 5.2.

$$\sigma_{\perp.N} = \alpha_{\sigma_{\perp.N}} \cdot N \quad (5.6)$$

Where:

- σ_{\perp} = Normal stress perpendicular to weld
- τ_{\perp} = Shear stress perpendicular to weld
- τ_{\parallel} = Shear stress parallel to weld

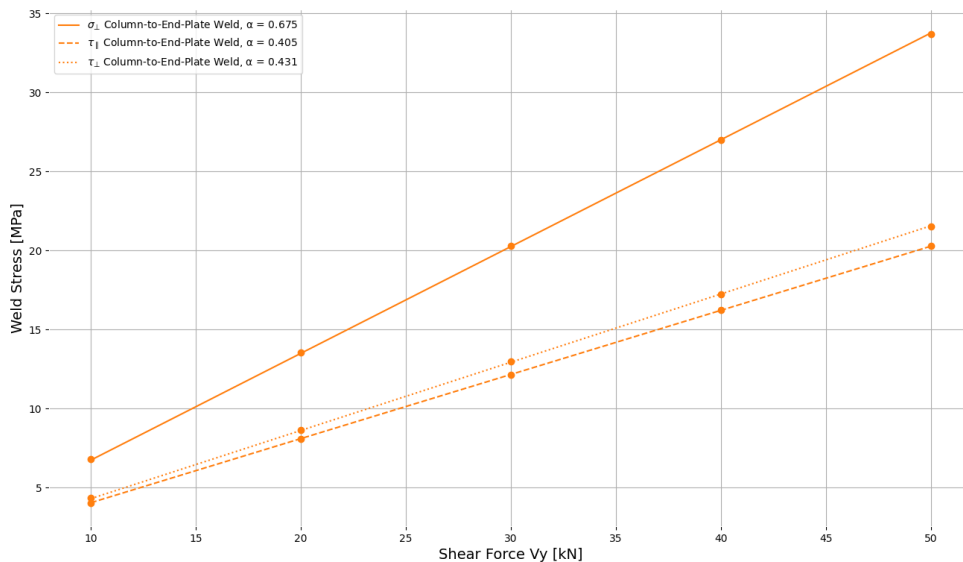


Figure 5.7: Example of joint analysis curve fit performed for the weld stress components against a shear force in the y -direction V_y for the *Column-to-End-Plate* weld

Table 5.2: Conversion factor α based on curve fit data

Parameter	Column-to-End-Plate Welds	Beam-to-End-Plate Welds	Horizontal Stiffener Welds	Vertical Stiffener Welds
$\alpha_{\sigma \perp N}$	-0.803	0.223	-0.196	-0.248
$\alpha_{\sigma \perp Vy}$	-0.671	-0.180	0.219	-0.251
$\alpha_{\sigma \perp Vz}$	-0.934	0.313	-0.474	-0.187
$\alpha_{\sigma \perp T}$	-3.711	-0.615	-0.949	-1.882
$\alpha_{\sigma \perp My}$	-4.398	0.920	1.410	-1.493
$\alpha_{\sigma \perp Mz}$	-0.593	-0.984	0.495	0.682
$\alpha_{\perp N}$	0.475	-0.424	-0.194	-0.247
$\alpha_{\perp Vy}$	0.424	-0.374	0.192	-0.251
$\alpha_{\perp Vz}$	0.672	-0.210	-0.453	-0.182
$\alpha_{\perp T}$	2.168	-1.492	-0.981	1.882
$\alpha_{\perp My}$	2.652	-2.577	-1.533	-1.483
$\alpha_{\perp Mz}$	0.406	-1.107	-0.419	-0.666
$\alpha_{\parallel N}$	-0.220	0.066	0.162	-0.224
$\alpha_{\parallel Vy}$	0.402	1.100	0.197	0.272
$\alpha_{\parallel Vz}$	-0.025	1.194	0.245	-0.352
$\alpha_{\parallel T}$	0.053	-1.705	0.933	-1.694
$\alpha_{\parallel My}$	-0.031	3.467	-0.907	1.282
$\alpha_{\parallel Mz}$	-0.926	-3.609	-0.444	-0.384

5.5. Governing Weld

When it comes to the fatigue damage it is not necessarily the absolute magnitude of the signal that is of importance, but the size of the stress cycles. For the fatigue analysis a cycle-counting algorithm is implemented to get the exact number of cycles each stress range occurs. In order to estimate the size of these stress ranges the standard deviation of the signal can be taken as this is a measure of how much the signal deviates from its mean value. Figure 5.8 represents the fatigue normal stress σ_{\perp} signal in the steady-state regime due to a wind load with a basic mean wind speed of 31 m/s. The dotted lines represent the values of one standard deviation below or above the mean value of the signal. A signal such as the one in figure 5.8 can be computed for each weld type for a wind load of 31 m/s or a traffic load with an intensity of 1000 vehicles per hour. For each of these signals a characteristic stress range can be computed, which is defined as two times the standard deviation of said signal. Table 5.3 gives an overview of the characteristic stress ranges in the various weld types present in the reference structure due to the aforementioned wind and traffic load. From these results it can be seen that the welds for the stiffeners are not as significant as the end-plate welds. In terms of the weld stress range, *Beam-to-End-Plate* weld seems to be governing fatigue action. However when performing a fatigue check and determining the expected fatigue damage of the structure the fatigue resistance of each weld needs to be taken into account as well as the fatigue action. The fatigue resistance of the various welds is discussed in the next chapter.

Table 5.3: Characteristic stress ranges [MPa] of fatigue weld stress signals (i.e. two standard deviations of the stress signal) for the different weld types present in the reference structure.

Parameter	Column-to-End-Plate Welds	Beam-to-End-Plate Welds	Horizontal Stiffener Welds	Vertical Stiffener Welds
σ_{wf} Due to Wind Load	1.596	0.921	0.331	0.500
τ_{wf} Due to Wind Load	0.474	1.816	0.278	0.578
σ_{wf} Due to Traffic Load	0.593	0.257	0.166	0.331
τ_{wf} Due to Traffic Load	0.099	0.535	0.143	0.283

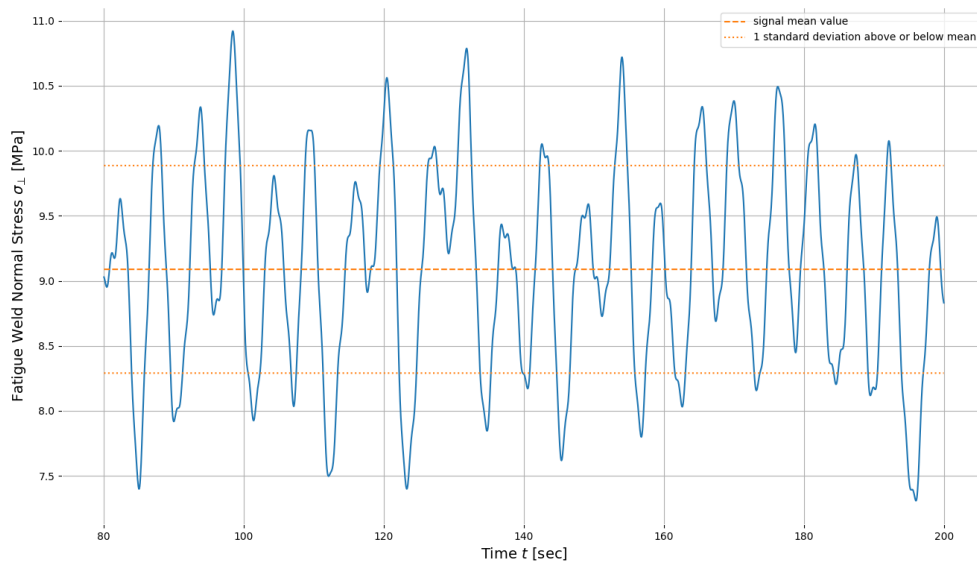


Figure 5.8: Fatigue weld normal stress signal in the steady-state regime for the *Column-to-End-Plate* weld for the reference structure loaded by a wind load with a basic mean wind speed of 31 m/s. The dashed line represents the mean value of the signal, the dotted lines represent the value of one standard deviation above or below the mean value.

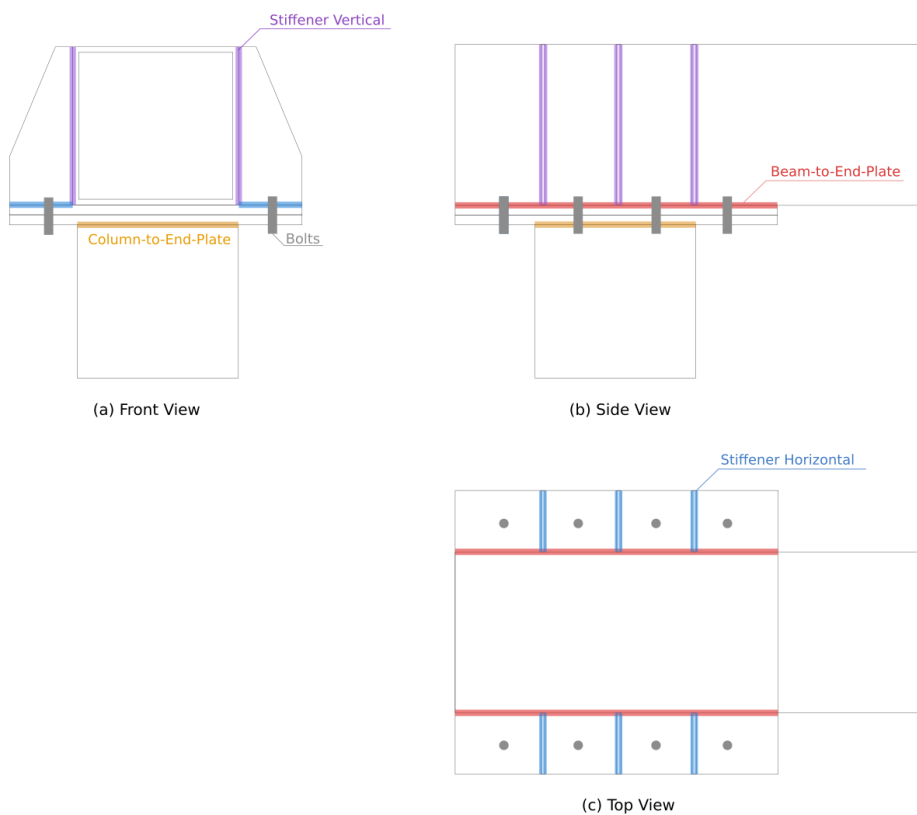


Figure 5.9: Overview of weld types included in the joint and their locations.

6

Fatigue Verification

6.1. Fatigue Damage Estimation

In the fatigue limit state the structure is assessed based on the total fatigue damage that accumulates over the structure's life-time.

6.1.1. Damage

The accumulation of fatigue damage can be modeled using the Palmgren-Miner rule [27], which states that the fatigue damage due to n_i cycles can be given by equation 6.1.

$$D = \sum_i \frac{n_i}{N_i} \quad (6.1)$$

If a structural element is subjected to n_i number of cycles at stress range S_i , then N_i corresponds to the theoretical number of cycles at which the element fails for the given stress range. The number of cycles to failure N_i can be determined from the SN curve, whose parameters for different structural elements are outlined in the Eurocode. The general relationship between the stress range S_i and the corresponding number of cycles to failure N_i is given by equations 6.2 and 6.3.

$$N_i = A \cdot S_i^{-m} \quad (6.2)$$

$$\log N_i = \log A - m \log S_i \quad (6.3)$$

Where:

- D = Accumulated damage; $D = 0$ corresponds to no damage and $D = 1$ to failure
- n_i = Number of cycles the structural element is exposed to for a given stress range S_i
- N_i = Theoretical number of cycles at which the structural element fails
- S_i = Stress range applied to structural element
- A, m = SN curve parameters

6.1.2. Cycles to Failure

For a given stress range the number of cycles to failure can be determined using an SN curve, the Eurocode provides several SN curves which are based on various fatigue limits [15]. For normal stress stress-cycles there exists a Constant Amplitude Fatigue Limit (CAFL) below which no fatigue damage is expected to accumulate given that there is no significant changes in the stress range. In the Eurocode this limit $\Delta\sigma_D$ corresponds to N_D cycles. There also exists a cut-off limit $\Delta\sigma_L$, corresponding to N_L cycles, below which no fatigue damage is expected irrespective of the changes in stress range. Each curve is characterized by the detail category stress range $\Delta\sigma_C$, which represents the stress range corresponding to two million cycles to failure N_C . Similarly for the shear stress stress-cycles, there exists a fatigue cut-off limit $\Delta\tau_L$, but no CAFL. Figure 6.1 illustrates various SN curves for different detail categories, and table 6.2 gives an overview of the various key points on said SN curves.

Table 6.1: Stress ranges and cycles to failures for key points on the SN curves in figure 6.1

Description	Stress Range	Number of Cycles to Failure
Normal stress detail category	$\Delta\sigma_c$	$N_c = 2 \times 10^6$
Shear stress detail category	$\Delta\tau_D$	$N_c = 2 \times 10^6$
Normal stress constant amplitude fatigue limit (CAFL)	$\Delta\sigma_D$	$N_D = 5 \times 10^6$
Normal stress cut-off limit	$\Delta\sigma_L$	$N_L = 5 \times 10^8$
Shear stress cut-off limit	$\Delta\tau_L$	$N_L = 5 \times 10^8$

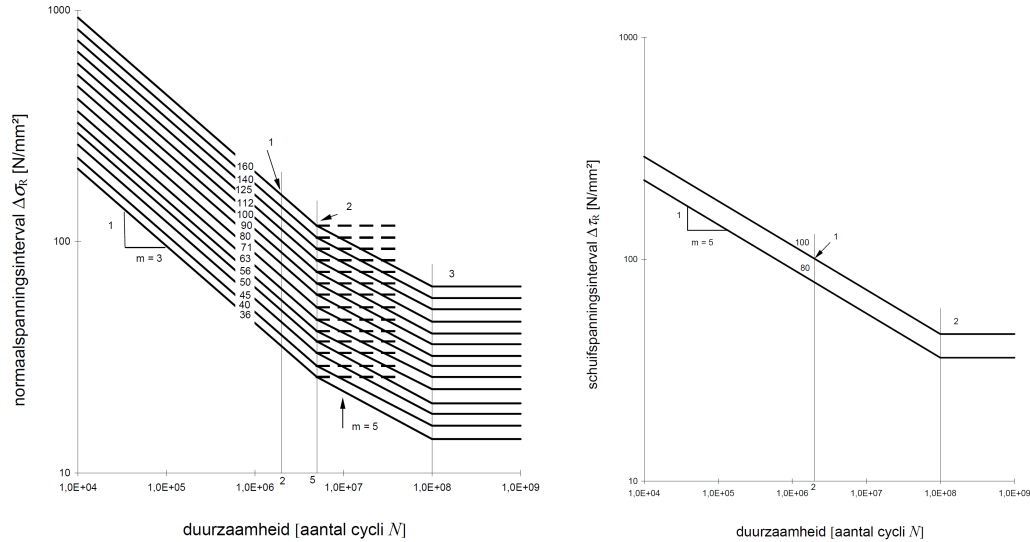


Figure 6.1: SN curves provided by the Eurocode for normal stress ranges (left) and shear stress ranges (right) [15]

The relationship described by equation 6.3 can be used in order to determine the relationship between two points on a given SN curve with the same slope m . The expected number of cycles to failure N_E corresponding to a applied stress range $\Delta\sigma_E$ can be determined through equation 6.4, which calculates the $(N_E, \Delta\sigma_E)$ point on the relevant SN curve based on a reference point $(N_{ref}, \Delta\sigma_{ref})$. The reference values will depend in which domain of the SN curve the applied stress range $\Delta\sigma_E$ is located in, and can be determined according to table 6.2

$$N_E = 10 \cdot \exp(m \cdot \log_{10}(\Delta\sigma_{ref}) + \log_{10}(N_{ref}) - m \cdot \log_{10}(\Delta\sigma_E)) \quad (6.4)$$

Where:

- N_E = Number of cycles to failure for an applied stress range $\Delta\sigma_E$
- $\Delta\sigma_E$ = Applied stress range in MPa
- m = Slope of SN curve for the relevant stress range domain according to table 6.2
- $\Delta\sigma_{ref}$ = Reference stress range for the relevant stress range domain according to table 6.2
- N_{ref} = Reference cycles to failure for the relevant stress range domain according to table 6.2

Table 6.2: Reference values to be used in equation 6.4 depending on the stress range domain $\Delta\sigma_E$ in the SN curve in 6.1 is located in

Description	Stress Range Domain	$\Delta\sigma_{ref}$	N_{ref}	m
Normal stress range is above CAFL	$\Delta\sigma_E > \Delta\sigma_D$	$\Delta\sigma_c$	N_c	3
Normal stress range is below CAFL, but above cut-off limit	$\Delta\sigma_D > \Delta\sigma_E > \Delta\sigma_L$	$\Delta\sigma_D$	N_D	5
Shear stress range is above cut-off limit	$\Delta\tau_E > \Delta\tau_L$	$\Delta\tau_c$	N_c	5

6.2. Cycle Counting

In order to evaluate the fatigue damage according to the Palmgren-Miner rule, it is of importance to know which stress ranges are expected to occur and how often these are expected to occur. The way the cycle counting is performed in the norms is relatively simple, a more accurate approach is to analyze the response signal.

6.2.1. Cycle Counting in Norms

When evaluating the fatigue resistance of a structure a set of stress ranges and the number of times said stress range occurs need to be determined. The Eurocode determines how often a given stress range occurs based on the maximum load S_k expected in a 50 year period. A given stress range ΔS is expected to occur N_g number of times in a 50 year period according to the maximum stress S_k according to equation 6.5. This is a generalized approach relevant for any structure under going fatigue loading, independent of the type of loading that is expected to occur, making it relatively inaccurate and conservative.

$$\frac{\Delta S}{S_k} = 0.7(\log(N_g))^2 - 17.4\log(N_g) + 100 \quad (6.5)$$

Where:

ΔS = Dynamic wind load range

S_k = Characteristic wind load for a 50 year return period

N_g = Number of times the dynamic wind load range ΔS is expected to occur

Rijkswaterstaat, a Dutch government agency responsible for public works and water management, has supplementary guidelines to the Eurocode: Richtlijnen Ontwerp Kunstwerken (ROK). In these guidelines equation 6.5 has been modified based on additional research which suggested that larger stress ranges may be expected to occur, especially those that are expected to occur less than ten thousand times for a 50 year reference period [18]. Figure 6.2 illustrates the difference between the two approaches.

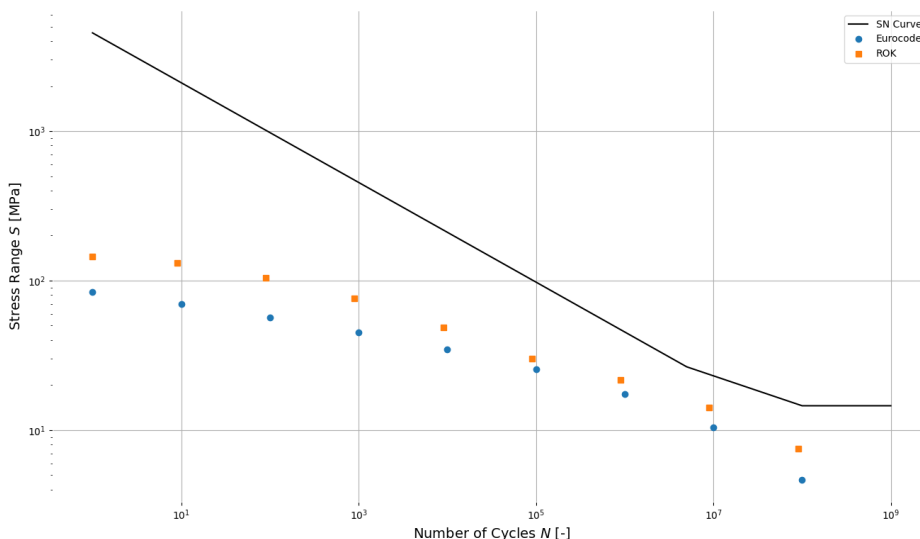


Figure 6.2: Stress range magnitude for different number of stress cycles for a maximum weld stress of 84MPa, plotted alongside a SN-curve for a detail of detail category 36

6.2.2. Narrow-band Stochastic Process

A simple system is considered, which is excited by a time-dependent arbitrary stationary Gaussian process $F(t)$, see equation 6.6. As a result the response $u(t)$ has the same time signature and is also considered a Gaussian stationary process, see equation 6.7.

$$F(t) = \mu_F + \sum_n F_{0,n} \sin(\omega_n t + \phi_n) \quad (6.6)$$

$$u(t) = |H_0| \mu_F + \sum_n |H_n| F_{0,n} \sin(\omega_n t + \phi_n) \quad (6.7)$$

Where:

- F = Time-dependent load
- u = Time-dependent displacement
- t = Time
- μ_F = Mean load
- $F_{0,n}$ = Load amplitude
- ω_n = Load frequency
- ϕ_n = Random phase shift
- H_n = Amplification factor, $H_n = H(\omega_n)$

For a simple system with a single natural frequency the amplification function $|H(\omega)|$ will have a strong peak near the natural frequency of the system. As a result the system will vibrate primarily at said frequency, returning a narrow-band response, even though the loading may have been a wide-band process.

In order to evaluate the fatigue life of a structure, it is of relevance to analyze the peaks of the stress fluctuations following from the narrow-band response. It can be shown that the stress peaks of a narrow-band process can be described by the Rayleigh distribution [26], with a probability density function (pdf) given by equation 6.8. The expected damage can then be determined using said probability density function of the stress and the Palmgren-Miner rule (see equation 6.1), as shown in equations 6.9 through 6.11.

$$f(s) = \frac{s}{\sigma^2} e^{-\frac{s^2}{2\sigma^2}} \quad (6.8)$$

$$E(D_T) = E\left(\sum_i \frac{n_i}{N_i}\right) = \int_0^\infty \frac{n_T f(s)}{N(s)} ds \quad (6.9)$$

$$E(D_T) = \frac{\omega_e T}{2\pi} \int_0^\infty \frac{\frac{s}{\sigma^2} e^{-\frac{s^2}{2\sigma^2}}}{A \cdot (2s)^{-m}} ds \quad (6.10)$$

$$E(D_T) = \frac{\omega_e T}{2\pi A} \cdot (2\sqrt{2}\sigma)^m \cdot \Gamma\left(1 + \frac{1}{2}m\right) \quad (6.11)$$

Where:

- $f(s)$ = Probability density function of the Rayleigh distribution of the stresses
- s = Stresses distributed over time
- σ = Standard deviation of Rayleigh distribution
- n_T = Number of cycles in period T
- ω_e = Eigenfrequency of system
- T = Period over which the damage is evaluated
- Γ = Gamma function ($\Gamma(x) = (x-1)!$)

6.2.3. Wide-band Stochastic Process

Unfortunately the system under consideration, the highway gantry sign, is more complex and can therefore not be accurately modeled using a one degree of freedom system. Due to the numerical nature of the system there will be a substantial number of natural frequencies, all of which will be activated during loading. As output from the numerical dynamic model will be in the form of a fluctuating stress across a predetermined time period. In order to estimate the fatigue damage over this period of time, the number of stress cycles and their corresponding stress range needs to be determined. This can be done using the Rainflow Cycle Counting method, which is able to analyze any load-time history and extract the number of cycles for a given stress range around a given mean stress []. In theory this method could be applied for cycle counting of any fluctuating signal, but in this case it is used for stress fluctuations. The general approach of the Rainflow Cycle Counting method can be described by four steps [], see also figure :

1. Hysteresis Filtering
2. Peak-Valley Filtering
3. Discretization
4. Four Point Counting Method

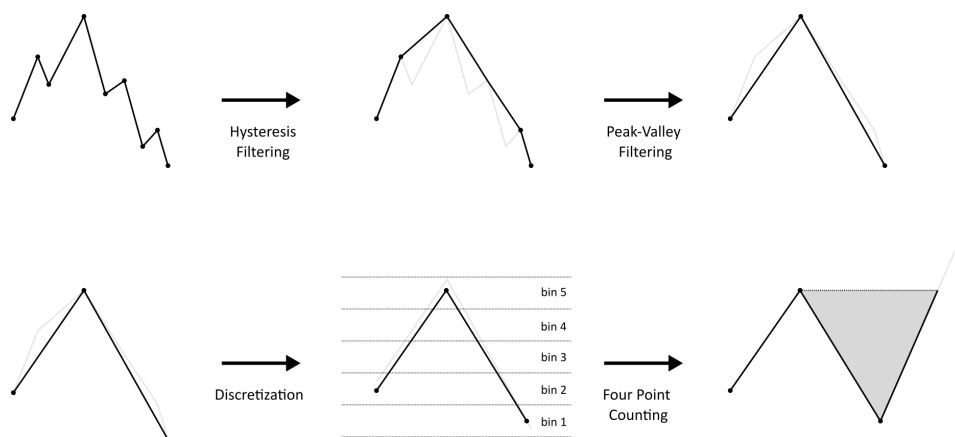


Figure 6.3: Overview of Rainflow Cycle Counting Method

First any cycles whose amplitude fall below a certain threshold are eliminated from the data set because the stress range cycle can be considered negligible. Then the data-set is filtered to remove any points that are not reversals, i.e. only data points where the slope before the data point is the opposite sign as the slope after the data point. The remaining data points are discretized into bins, where a bin is a fixed amplitude range used to map the data to. The Four Point Counting Method is finally used to count the number of cycles, their range, and the mean value of said range. The exact recommended algorithm is outlined in a standard produced by the American Society of Testing and Materials: *ASTM: E 1049-85 standard practice for cycle counting in fatigue analysis* []. Based on the algorithm described in this report a python package called *Rainflow* has been developed, which takes as input a fluctuating signal and outputs the count and mean per cycle range.

6.3. Reference Structure

For the reference structure the fatigue damage needs to be determined for the details most susceptible to fatigue damage. In case of the joints the most critical components tend to be the bolts and the welds due to the large stress concentrations that form when transferring the loads and stresses from one of the connected members to the other, i.e. transferring the loads from the beam to the column members. In the joint design the bolts are pre-loaded to 70% of the ultimate strength of the bolt, which is assumed to be sufficiently high that no significant stress ranges will occur in these details. This analysis will therefore primarily focus on the welds. For the different welds in the joint different fatigue categories

according to the Eurocode can be identified, which have been summarized in table 6.3. From here it can be observed that the welds connecting the hollow section column perpendicularly to the end-plate has a very low detail category of $\Delta\sigma_C = 36MPa$, and will therefore be the most susceptible to fatigue damage.

Table 6.3: Overview of the weld types in the structure, and their fatigue detail category according to the Eurocode[15]

Weld Type	EN 1993-1-9 Table	Detail	Category	$\Delta\sigma_C$	$\Delta\sigma_D$	$\Delta\sigma_L$	$\Delta\tau_C$	$\Delta\tau_L$
Beam-to-End-Plate	Table 8.2: Welded built-up sections	5) Manual fillet or butt weld	100	100	74	40	100	46
Column-to-End-Plate	Table 8.6: Hollow sections	9) Rectangular structural hollow sections, fillet-welded end-to-end with an intermediate plate	36	36	27	15	36	16
Vertical Stiffener	Table 8.4 Weld attachments and stiffeners	7) Vertical stiffeners welded to a beam or plate girder	80	80	59	32	80	37
Horizontal Stiffener	Table 8.4 Weld attachments and stiffeners	7) Vertical stiffeners welded to a beam or plate girder	80	80	59	32	80	37

6.3.1. Norms Fatigue Damage Evaluation

The column-to-end-plate weld is the most critical with respect to the fatigue behavior, and its fatigue behavior has been evaluated according to the aforementioned Eurocode and ROK design norms. Appendix D contains the relevant calculations for determining the static loads. These are then applied to the reference structure modeled in the dynamic FEM model created in python, and the static cross-sectional loads are evaluated at the location in the beam near the left joint. These loads are then applied to the CBFEM model in *IDEA StatiCa*, from which the weld stresses are evaluated. The complete calculation is given in appendix D, but the most critical results with respect to fatigue are given by table 6.4. In this case the results for the column-to-end-plate welds are given.

Table 6.4: Full fatigue damage calculation according to the norms for the reference structure for the normal stresses in the column-to-end-plate welds

	Ng [cycles]	$\Delta S/S_k$ [%]	$\Delta\sigma_E$	$\Delta\sigma_{ref}$	Nref	Slope	N	Ng/N
Eurocode	100000000	6	5	[-]	[-]	[-]	[-]	[-]
	10000000	13	10	[-]	[-]	[-]	[-]	[-]
	1000000	21	17	27	5,000,000.00	5	41,417,624	0.02
	100000	31	25	27	5,000,000.00	5	6,109,458	0.02
	10000	42	35	36	2,000,000.00	3	2,220,581	0.00
	1000	54	45	36	2,000,000.00	3	1,009,613	0.00
	100	68	57	36	2,000,000.00	3	508,417	0.00
	10	83	70	36	2,000,000.00	3	276,574	0.00
	1	100	84	36	2,000,000.00	3	159,863	0.00
Fatigue Damage:								0.05 [-]
ROK	90000000	9	8	[-]	[-]	[-]	[-]	[-]
	9000000	17	14	[-]	[-]	[-]	[-]	[-]
	900000	26	22	27	5,000,000.00	5	13,571,727	0.07
	90000	36	30	36	2,000,000.00	3	3,426,408	0.03
	9000	58	48	36	2,000,000.00	3	819,337	0.01
	900	91	76	36	2,000,000.00	3	212,140	0.00
	90	125	104	36	2,000,000.00	3	81,850	0.00
	9	158	132	36	2,000,000.00	3	40,530	0.00
	1	174	145	36	2,000,000.00	3	30,346	0.00
Fatigue Damage:								0.11 [-]

Due to the larger stress range values in the ROK norms, see figure 6.4, the calculated fatigue damage is significantly larger than the one calculated according to the Eurocode. However as the reference structure as a whole is over-dimensioned, both fatigue calculations yield low damage numbers. The maximum weld stresses found in the column-to-end-plate weld are shown in table 6.5. The expected fatigue damage has been calculated for various values of the maximum stress S_k , based on fatigue

limit state loads, and are plotted in figure 6.4. From here it can be seen that in order to obtain a unity check of at least 0.8, the maximum stress during the structures lifetime S_k should be at least roughly 120MPa for the ROK method, and 150MPa for the Eurocode method. In the graph the lines are not continuous, and several discontinuities can be observed, these are a result of the cycles to failure calculation according to equation 6.4. In this equation a reference point is chosen based on which branch of the SN-curve the stress range $\Delta\sigma_E$ is located. The discontinuities specifically coincide with a change in the slope m of the SN-curve.

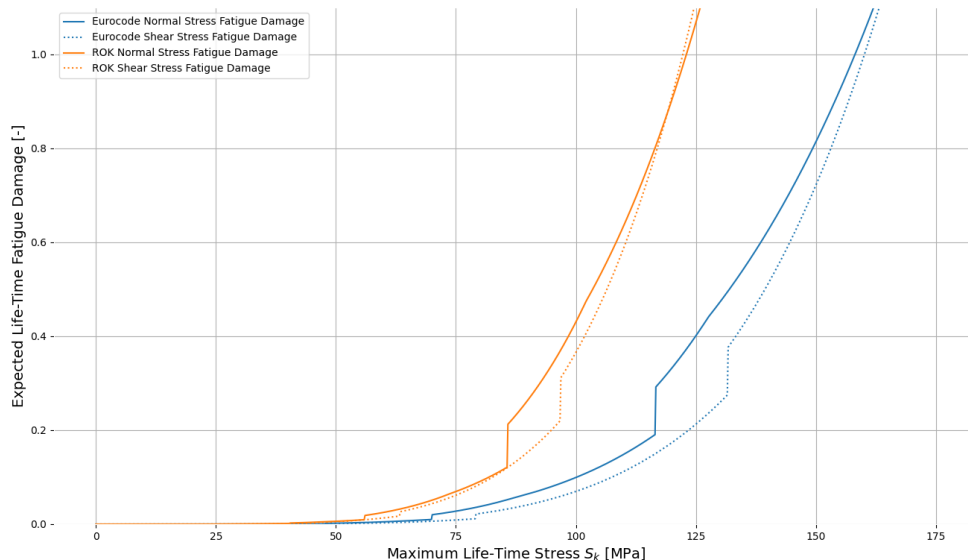


Figure 6.4: Fatigue damage for various maximum loads calculated according to the norms

Table 6.5: Fatigue damage calculation overview according to the norms for the reference structure for the column-to-end-plate welds

Description	Symbol	Value	Units
<i>Action</i>			
Perpendicular normal stress	σ_{\perp}	72	MPa
Perpendicular shear stress	τ_{\perp}	43	MPa
Parallel shear stress	τ_{\parallel}	5	Mpa
<i>Verification</i>			
Eurocode normal stress fatigue damage	[-]	0.05	[-]
Eurocode shear stress fatigue damage	[-]	0.00	[-]
ROK normal stress fatigue damage	[-]	0.11	[-]
ROK shear stress fatigue damage	[-]	0.00	[-]

Calculation Model

7.1. Overview of Model

The calculation model in question can be broken down into several sub-models. First the traffic induce pulse loads and aerodynamic turbulent loads are defined. These are then applied to the dynamic model, which simulates the dynamic response over the course of 600 seconds, i.e. 10 minutes. From this dynamic response the internal loads at the location of the loads are determined. Using the analytical expressions developed for the relationship between a cross-sectional load and a weld-stress the stresses in the relevant welds are determined. A Rainflow Cycle Counting algorithm is then applied to the resulting weld stress signal, from which the fatigue damage is estimated. A visualization of these calculation steps is given in figure 7.1.

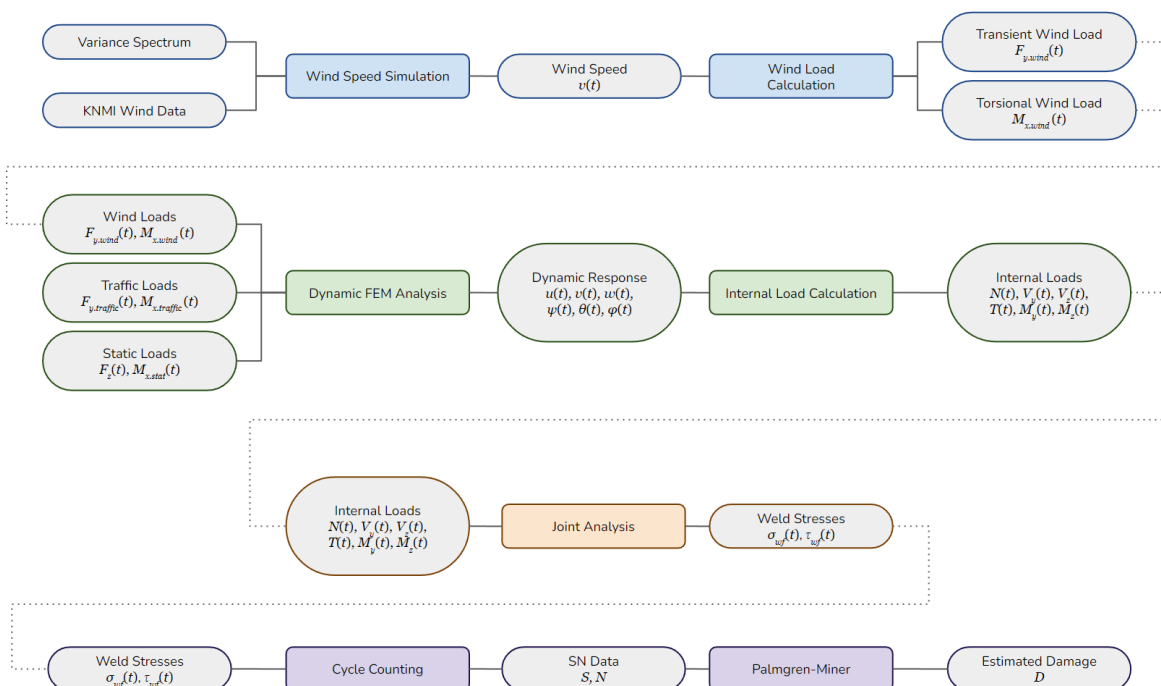


Figure 7.1: Overview of calculation model

7.2. Relative Wind Load

The external load on the system consists of a wind load and a pulse load, both of these loads originate from a medium (atmospheric air) flowing past the structure/system. As a result due to these loads the

system has a dynamic response, during which the system will have a certain velocity. The true load on the system will not follow from the speed of the medium alone, but instead from the effective relative wind speed (i.e. the difference between the speed of the medium and the speed of system). If this is taken into account, the equation of motion of the system becomes non-linear, see equation 7.1.

$$\mathbf{M}\ddot{\mathbf{u}}(t) + \mathbf{C}\dot{\mathbf{u}}(t) + \mathbf{K}\mathbf{u}(t) = \bar{\mathbf{f}}(\dot{\mathbf{u}}(t), t) \quad (7.1)$$

Although this new equation of motion is relatively easy to implement in the direct integration (brute force) solution method, it is more computationally expensive. Furthermore the non-linear nature of the equation of motion in equation 7.1 means the eigenanalysis, which is necessary for the time saving modal solution method, requires a significantly more complex calculation.

Instead of using this more complex equation of motion, the deviation between the calculated wind load and the true relative wind load will be taken into account through a simple load factor. The signals of these two wind loads have been plotted for a 300 second (5 minute) period for a basic mean wind speed of 30m/s, the largest expected wind speed, in figure 7.2. From this figure it can be seen that after the first 50 seconds the damping has smoothed out the signal to return the steady state of the system, in which the absolute deviation between the calculated and true wind load varies roughly between 0 and 20%.

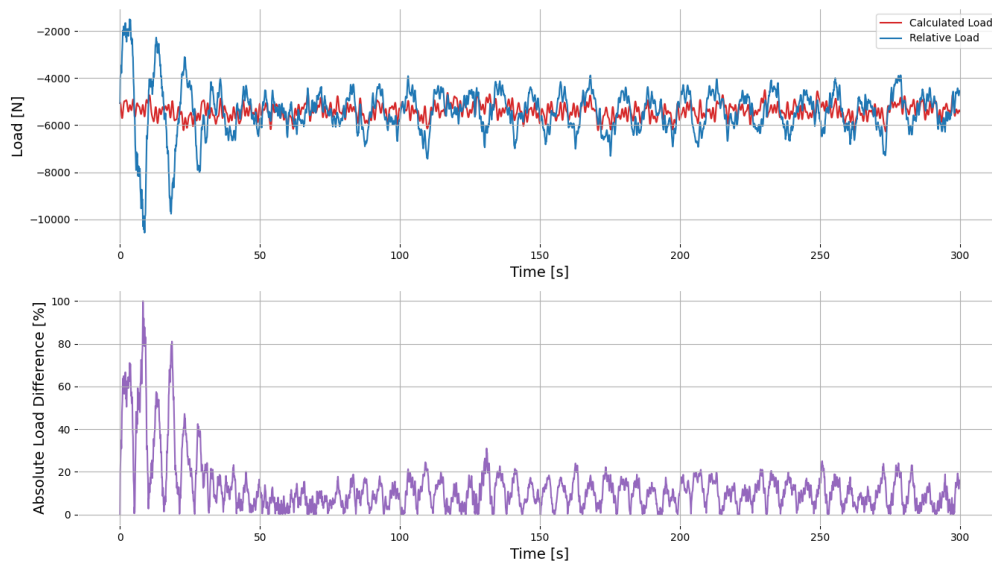


Figure 7.2: Signals of the calculated and true relative wind load (top) and the absolute difference between the two relative to the relative wind load as a percentage (bottom)

By analyzing the absolute deviation signal in the steady-state regime a load factor can be computed. The mean of the signal can be computed in order to take the average offset of the calculated load with respect to the true relative wind load into account. For safety the mean value is increased by one standard deviation of the signal. This calculation has been performed for various basic mean wind speeds and in all cases the wind speed factor was equal to 1.15, accurate to 0.005. For this reason it will be assumed that the relative wind speed factor is constant and equal to 1.15.

7.3. Probabilistic Loads

Both traffic induced pulse loads and atmospheric wind loads are considered in this thesis. Both of these loads are not continuous throughout the life-time of the structure, so their probabilistic distribution over time should be taken into account.

7.3.1. Traffic Induced Pulse Loads

Each truck that passes underneath the traffic sign support structure will induce a pulse load. The number of pulse loads and their distribution will ultimately have an effect on the stress signal and the subsequent fatigue damage. The *Nationaal Dataportaal Wegverkeer* (NDW) is an organization created by various Dutch municipalities and government instances which provides an open source database containing traffic information at various locations in the Netherlands [2]. The data sets that are available to download contain data for a period of up to a year per data set. In this data set the average total traffic intensity per hour of the day is made available, this is the traffic intensity for all vehicle types, and does not distinguish between cars, trucks, and other modes of transportation.

For the fatigue analysis the loads produced by cars is assumed to be negligibly small such that they may be omitted from the loading model, instead only the traffic intensity of the number of trucks will be taken into account. The consultancy firm Goudappel Coffeng has produced an extensive traffic model for Dutch motorways called the *Nationaal Verkeersmodel* (NVM) [32] which concludes that the total freight traffic on Dutch highways is 18% of the total traffic. For rural and urban roads this percentage goes down to 6% and 4% respectively, however for a conservative approach the upper bound value of 18% will be assumed for the load model for all roads. Table 4.5 in Eurocode 1 part 2 [12] provides an estimate for the number of heavy traffic vehicles to be expected on European roads.

As there is no clear data on how the traffic is distributed within a given hour from the NDW database, the trucks (i.e. pulse loads) will be randomly distributed within a given time frame. Figure 7.3 shows a distribution of trucks for a period of 150 seconds based on trucks 10 meters long traveling at a speed of 80km/h and with a minimum separation distance between vehicles of one vehicle length (10 meters), based on a traffic intensity of 800 vehicles per hour. The time axes and truck graphics have been scaled in such a way that the plot depicts both the temporal and spatial distribution of the trucks.

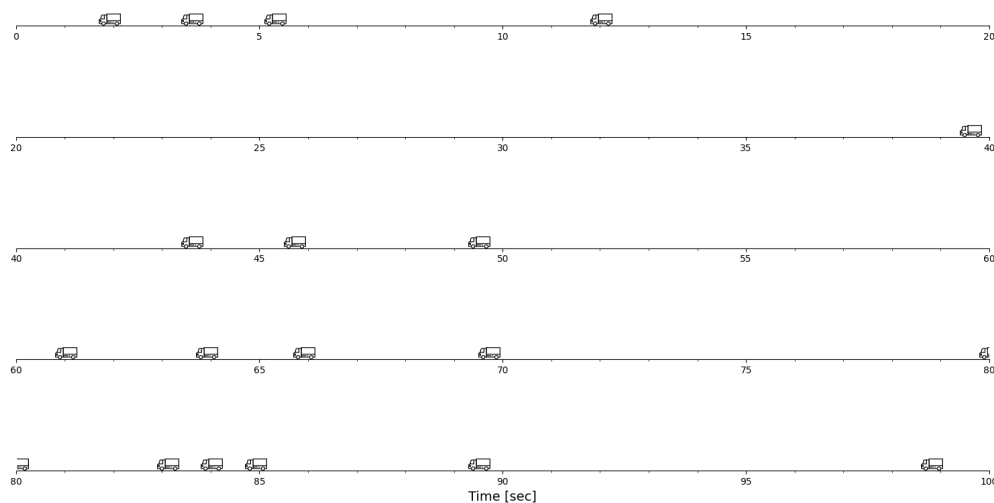


Figure 7.3: Traffic intensity of 800 trucks (10 meters wide traveling at 80km/h) per hour distributed randomly across a period of 150 seconds with a minimum separation distance of 1 vehicle length

7.3.2. Turbulent Atmospheric Wind Loads

The wind speed simulation outlined in the chapter on Atmospheric Wind Loads is valid for periods with an order of magnitude of several minutes or a couple of hours, based on the frequencies given by the turbulence spectrum. This simulation does not take the variation of days or time of day into account, for the former the $c_{seasonal}$ wind speed factor in the Eurocode [11] is used, while for the latter additional data is required. The dutch KNMI weather stations provide publicly available data for various meteorological measurements including wind speeds. The smallest time step in which this may be measured is a 10 minute average wind speed. This measurement is recorded every hour, where the measurement

represents the average wind speed across the 10 minutes preceding the hour; i.e. a 10 minute average wind speed measured once an hour. Depending on the structure in question the data from the closest or most relevant KNMI weather station should be chosen; a weather station located in an environment representative of the traffic sign support structure. Figure 7.4 shows a wind rose plot showing wind speed data measured across 10 years for the *Rotterdam Geulhaven* KNMI weather station in the form of the various wind speeds, their direction, and frequency. Here the discrete measurement step sizes can be seen: the direction has an accuracy of ± 5 degrees and the wind speed an accuracy of ± 0.5 m/s.

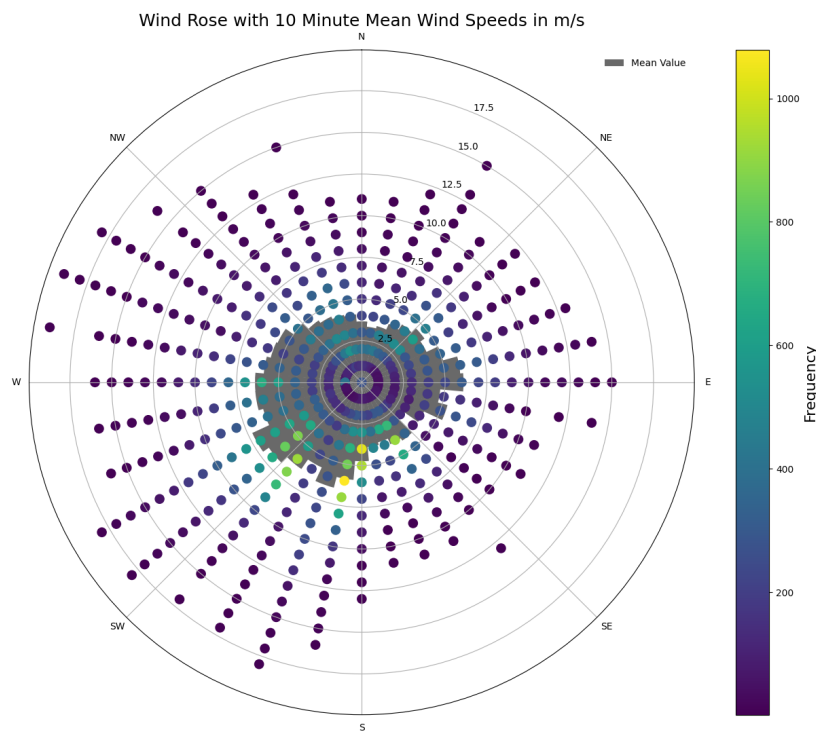


Figure 7.4: Wind rose for the 10 minute average wind speed (measured hourly) for the *Rotterdam Geulhaven* KNMI weather station measured across 10 years (2011-01-01 till 2020-12-31)

For a given structure not every wind direction is relevant, wind speeds occurring parallel to the sign will induce negligibly small loads on the structure and therefore do not need to be taken into account. For a given sign orientation only the wind direction component perpendicular to the sign is of relevance, therefore based on the relative angle between the sign orientation and wind direction a wind speed factor may be computed, resulting in an effective wind speed for each direction. This wind speed factor is simply defined as the ratio of the perpendicular wind speed component to the total wind speed. In an ideal world every wind speed adjusted by the wind speed factor would be taken into account in the fatigue analysis. However to reduce the complexity and size of the calculation a single wind direction is chosen to perform the fatigue analysis. For each wind direction the mean wind speed across 10 years is computed and multiplied by the effective wind speed factor depending on the sign orientation. The direction with the largest governing wind speed is chosen and will result in a data set of wind speeds that particular direction.

7.3.3. Combination of loads

For the fatigue analysis both the traffic loads and atmospheric wind load should be taken into account simultaneously for the most accurate results. From the NDW database the traffic intensity for a given

road or location can be obtained, from the relevant KNMI weather station the wind data for that same location may be determined. From there the governing wind direction may be chosen based on the aforementioned wind speed factor method. The subset of wind speed data that corresponds to a single direction is then analyzed in combination with the traffic data of said location.

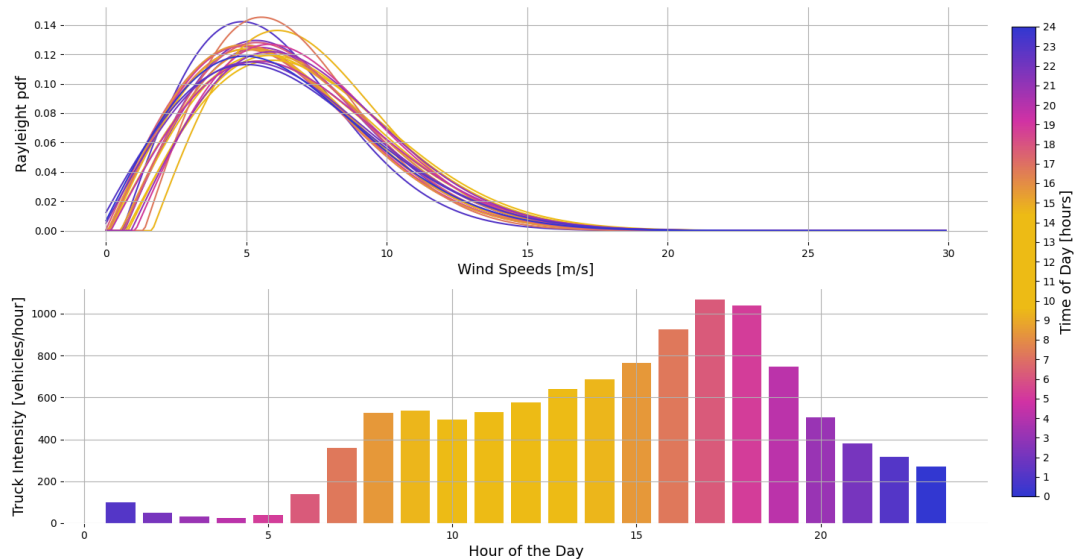


Figure 7.5: Traffic and wind data per hour of the day in the south of Rotterdam

Figure 7.5 shows how for each hour of the day there is a Rayleigh distribution and a traffic intensity. The top plot shows the Rayleigh wind speed distributions, where each color represents an hour of the day. The bottom plot shows the truck traffic intensity for each hour of the day, and has been scaled up such that the total traffic across a lane is equal to the Eurocode estimate for freight traffic. This ensures that the relative distribution of trucks over time remains accurate to the chosen location, but that the total volume of trucks (and therefore the total load) adheres to the general Eurocode guideline.

This method, however, requires a substantial number of time consuming simulations to be performed. This is beyond the scope of this thesis, so a simplified approach is taken. Instead of analyzing each hour of the day separately, a single characteristic hour is chosen. The simulation results of this hour are then extrapolated to the life-time of the structure. For the wind speeds each hour of the day has a probability distribution function (pdf) from which the average value for the hourly mean wind speed across the 10 year period may be obtained. The hour of the day with the largest hourly mean wind speed is conservatively chosen as the governing hour of the day, and the corresponding pdf is used for the simulation. The same cannot be done for the truck intensity as a single hour is taken and extrapolated to the life-time of the structure. This would result in taking too many trucks into account during the 50 year period, instead the average truck intensity is taken.

Each mean wind speed has a probability of occurrence, which may be computed by integrating over the relevant ranges of wind speeds in the Rayleigh distribution corresponding to said hour of the day. This calculation has been done for the following wind-speeds in m/s: 3, 7, 11, 15, 19, 23, 27, 31; and is illustrated in figure 7.6. A value of up to 31 m/s was chosen based on the order of magnitude of the basic fundamental wind speed used to calculate the maximum wind speed due to wind gusts occurring in a period of 50 years according to the Eurocode [11].

7.3.4. Limitations of Approach

In an ideal situation many different combinations of wind speeds and traffic loads would be performed and combined based on the relevant probabilities of occurrence. The simplified approach taken in order to save computation time conservatively over estimates the wind speeds slightly by taking into account the most severe wind speed distribution. However, as can be seen in figure 7.5, the variation in wind

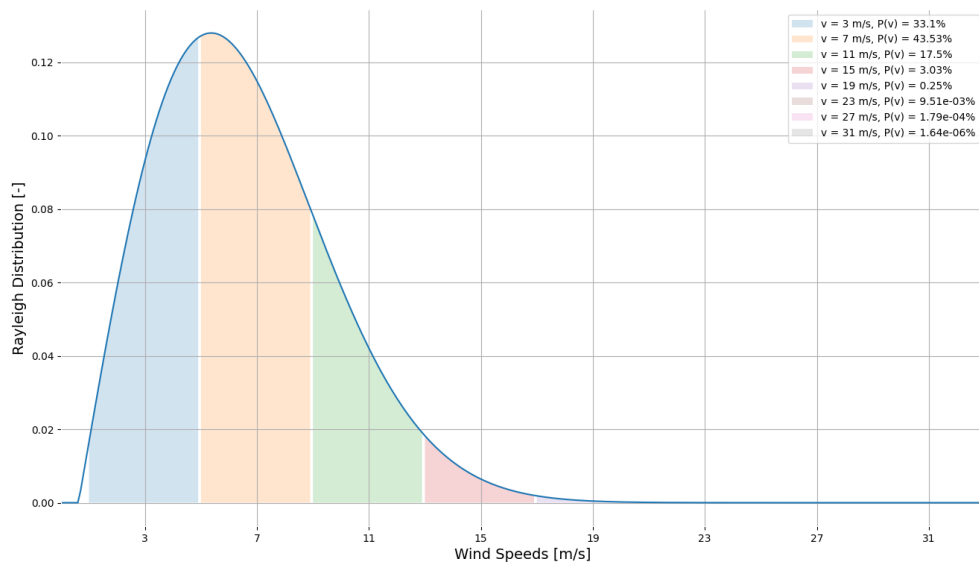


Figure 7.6: Probability of occurrence of a given wind speed based on a Rayleigh distribution

speed distributions is not very significant. Aside from this simplification there are also other limitations to this approach.

Firstly the traffic data that is obtained is for a road representative of the one where the traffic sign will be placed. The measurements are only taken at a couple of key locations on certain roads, often only highways. The chosen location for the traffic intensity data should be carefully chosen. This data is then scaled up to match the Eurocode guideline. This may be a somewhat conservative measure as it overestimates the average traffic a certain road experiences.

Furthermore the distribution of pulse loads is currently simply assumed to be randomly distributed as there is no clear data on how trucks are distributed. A pure random distribution may not be an exact representation of reality, but it does ensure no bias is taken. In addition this distribution is based on the largest vehicle intensity of the day, which occurs during rush hour, when traffic may be traveling at significantly slower speeds and may even come to a full stop.

When it comes to the wind loads there are a lot of parameters to take into account. A significant parameter is the wind direction, wind in every direction will induce some fatigue damage. If one night there are very large wind speeds at a 45 degree angle to the sign, this may be much more significant than the average wind speed perpendicular to the sign on a given day. The current method assumes the wind will always be blowing perpendicular to the sign, which may be a gross overestimation of the perpendicular wind speeds the traffic sign will encounter in its lifetime.

In the current approach the most severe hour is taken into account in order to determine the probability of occurrence of a given mean wind speed. This allows the Diurnal peak in figure 3.2 to be taken into account. However the 4 day synoptic peak in that same figure is not taken into account as the wind distribution across days is not taken into account. By not taking this variation into account, one may underestimate the number of times higher wind speeds occur, though the variation from the current employed method is not expected to be very significant with respect to the total fatigue life of the structure.

7.4. Stability

Compared to other building materials steel is very strong per unit of volume, resulting in slender structural designs. In such structures instability phenomena are much more likely to occur, requiring the stability verifications and analyses to be performed. In general when performing structural analyses one can either use a:

- *First-Order Analysis*: the internal loads and displacements are obtained with respect to initial undeformed structure or,
- *Second-Order Analysis*: the internal loads and displacements are obtained while taking into account the influence of the deformed structure

Whether a first-order analysis suffices, or a more comprehensive second-order analysis is required according to the Eurocode [13] depends on the global instability failure mode of the structure. A first order analysis is sufficient if the criterion in equation 7.2 is satisfied. For steel portal frames the elastic instability factor α_{cr} may be determined according to equation 7.3.

$$\alpha_{cr} \geq \begin{cases} 10 & \text{for elastic analysis} \\ 15 & \text{for elastic analysis} \end{cases} \quad (7.2)$$

$$\alpha_{cr} = \left(\frac{H_{Ed}}{V_{Ed}} \right) \left(\frac{h}{\delta_{H_{Ed}}} \right) \quad (7.3)$$

Where:

- α_{cr} = Elastic instability factor
- H_{Ed} = Horizontal load
- V_{Ed} = Vertical load
- h = Portal frame height
- $\delta_{H_{Ed}}$ = Displacement

The vertical load V_{Ed} follows from the self-weight of the structure, while the horizontal load takes the effects of imperfections into account. In this case initial sway and initial bow imperfections are taken into account according to equation 7.4 as illustrated in figure 7.7. In the design of the traffic sign support structures all of the members consist of SHS profiles, which are almost always cross-sections which correspond to buckling curve *a*. For these type of structures the bow imperfection deflection e_0 may be estimated by equation 7.6

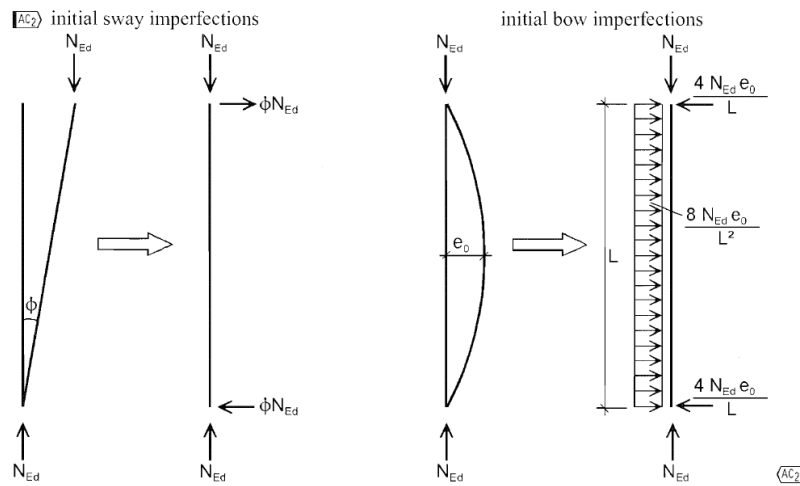


Figure 7.7: Initial sway and initial bow imperfections according to Eurocode 3 part 1-1 [13]

$$H_{Ed} = H_{wind} + \phi N_{Ed} + 4 \frac{N_{Ed} e_0}{L} = H_{wind} + H_{sway} + H_{bow} \quad (7.4)$$

$$\phi = \frac{\alpha_h \alpha_m}{200} \quad (7.5)$$

$$e_0 = \begin{cases} \frac{L}{350} & \text{for elastic analysis} \\ \frac{L}{300} & \text{for plastic analysis} \end{cases} \quad (7.6)$$

Where:

- H_{Ed} = Total horizontal load at the top of the frame
- H_{wind} = Horizontal load due to wind
- ϕ = Initial sway angle
- N_{Ed} = Vertical load due to self-weight
- e_0 = Initial bow deflection
- L = Member length (height of column)
- α_h = height factor (= 2/3 for structures where $h < 9m$)
- α_m = storey factor (= 1.0 for single storey frame)

For the reference structure the vertical loads are calculated using the Python finite element analysis software package developed for the dynamic analysis. Based on the structure's dimensions, and the member profile properties, the initial sway and bow imperfection loads are determined. The displacement due to the total horizontal load $\delta_{H_{Ed}}$ is determined through the simplified engineering formula for the displacement of a cantilever beam given by figure 7.8.

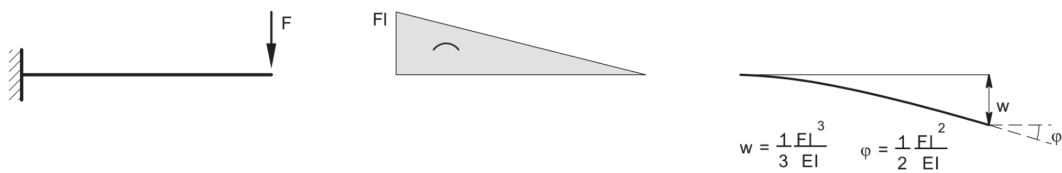


Figure 7.8: End displacement of a cantilever beam loaded by a concentrated force

The results for the reference structure calculation for both the elastic (fatigue limit state) and plastic (ultimate limit state) are summarized in table 7.1. The structure is relatively low in terms of height h , resulting in low initial imperfection loads. In addition, the lateral wind load parallel to the frame is also very small. Small horizontal loads lead to small horizontal displacements, which yields a very stable structure as can be seen by the computed elastic instability factor α_{cr} . The calculation for the horizontal displacement of the frame due to horizontal loads $\delta_{H_{Ed}}$ is simplified by calculating the horizontal displacement due to half of the horizontal load applied to a cantilever beam with the same dimensions and geometry as the frame's columns. Any inaccuracies due to this simplification can be neglected as the instability factor α_{cr} is orders of magnitude larger than the minimum requirement for the use of a first-order analysis.

The aforementioned calculation shows that the structure is very stable in the context of the global sway stability failure mechanism. However the lateral loads perpendicular to the structure, i.e. wind loads on the traffic signs, are significantly larger than the vertical loads. This may result in large deformations which influences the load distribution within the structure. The Eurocode unfortunately does not provide a simplified method to take this global instability failure mechanism into account. Instead this failure mechanism would have to be researched and analyzed in more depth in order to provide an analytical formula. Another option is to use commercial software to establish the critical instability load and compute α_{cr} according to equation 7.7.

$$\alpha_{cr} = \frac{F_{cr}}{F_{Ed}} \quad (7.7)$$

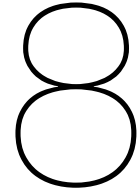
Where:

- α_{cr} = Elastic instability factor
- F_{cr} = Critical load associated with the structure's global instability mechanism
- F_{Ed} = Applied load

If it turns out that a second-order analysis is required, then one could perform a second-order analysis directly. For the fatigue limit state this would require a significant modification of the dynamic finite element analysis currently implemented. An alternative would be to increase the loads in the global analysis, and check the member stability individually according to section 6.3 in Eurocode 3 part 1-1 [13].

Table 7.1: Calculation of elastic instability factor for the reference frame

Description	Symbol	Elastic Analysis (FLS)		Plastic Analysis (ULS)	
		Value	Units	Value	Units
Vertical Load	V_{Ed}, N_{Ed}	7.12	kN	7.82	kN
Beam profile	[-]	SHS300/8	[-]	SHS300/8	[-]
Column profile	[-]	SHS350/10	[-]	SHS350/10	[-]
Column width	b	0.3	m	0.3	m
Column height	h	6.0	m	6.0	m
Column profile moment of inertia	I	258800000	mm ⁴	258800000	mm ⁴
Steel modulus of elasticity	E	210000	MPa	210000	MPa
Initial sway angle	ϕ	0.003	rad	0.003	rad
Initial bow deflection	e_o	0.02	m	0.02	m
Wind load (side of column)	H_{wind}	1.490	kN	2.236	kN
Sway imperfection equivalent load	H_{sway}	0.024	kN	0.026	kN
Bow imperfection equivalent load	H_{bow}	0.095	kN	0.104	kN
Total horizontal load	H_{Ed}	1.609	kN	2.366	kN
Displacement due to total horizontal load	$\delta_{H_{Ed}}$	1.07	mm	1.57	mm
Elastic instability factor	α_{cr}	1272	[-]	1159	[-]



Design Optimization

The design in the reference structure is based on an extremely conservative and general approach. The advantage is that it can be calculated and verified quite quickly without the need for iterative calculations, the disadvantage is that it is not very economical from both a financial and sustainability point of view. For the optimized design the main design criteria will remain the same compared to the reference structure: the traffic sign support structure will be a steel portal frame supporting the same two signs at the same locations. The total height and span of said portal frame will also remain unchanged. What is allowed to vary are the choice of square hollow section profiles used for the frame, and the design of the corner joint. The optimized design will be created according to the ultimate limit state, serviceability limit state, and the fatigue limit state using purely Eurocode and ROK procedures. The optimized design is then evaluated in the fatigue limit state using the more elaborate verification methodology developed in this thesis. The aforementioned ULS, SLS and FLS verification calculations are outlined and performed in annex D in the form of a case study which verifies various traffic support sign portal frames, among which the reference structure and optimized structure.

8.1. Member Optimization

During the optimization process the global analysis is performed first. The global loads remain mostly unchanged, the loads on the signs will remain constant. In the member optimization process two parameters can be changed: the cross-sectional profile of the beam and the column. The choice of cross-section will be limited to a selection of standard square hollow section (SHS) profiles in order to ensure all the previously made assumptions about the structure remain valid.

8.1.1. Design Considerations

Reducing the profiles of the members will reduce the self-weight of the structure, but also reduce the resistance of the members. In addition the stiffness of the members changes, which means the load distribution within the structure will be affected. A decreased member stiffness will also induce larger deformations in the structure, which is relevant for both the dynamic behavior and limiting excessive deformations in the serviceability limit state.

8.1.2. Design Choices

Based on this the SHS300/8 beam used in the reference design can be reduced to a SHS180/10 beam, and the SHS350/10 columns may be reduced to SHS200/12.5 columns. An overview of the results from the optimization in the global analysis is given in table 8.1.

8.2. Joint Optimization

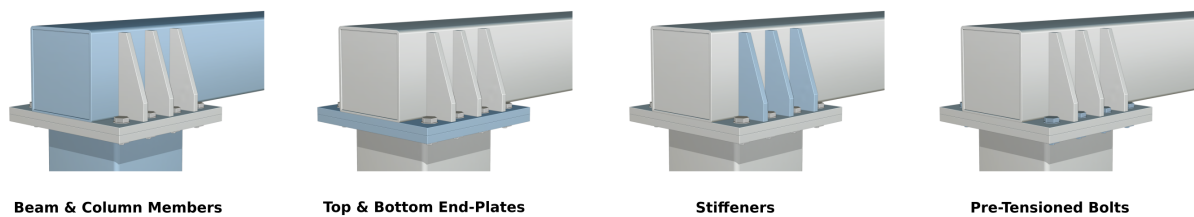
When optimizing the joint each structural element is subject to change, it is therefore of importance to isolate the relevant elements and identify their structural role within the joint. The connection in question consists of a moment-resisting joint, for which the component method may be used in order to aid in

Table 8.1: Results from the optimization in the global analysis

Description	Symbol	Reference Structure	Optimized Design
<i>Member Profiles</i>			
Beam profile	[-]	SHS300/8	SHS80/10
Column profile	[-]	SHS350/10	SHS200/12.5
<i>Governing Unity Checks (ULS)</i>			
Beam bending	$U_{C_{bending,beam}}$	0.40	0.81
Column bending	$U_{C_{bending,column}}$	0.42	0.89
Beam lateral torsional buckling	$U_{C_{stability,beam}}$	0.33	0.84
Column flexural buckling	$U_{C_{stability,column}}$	0.36	0.92
<i>Deflections (SLS)</i>			
Beam maximum deflection [mm]	U_{beam}	18	62
Beam deflection limit [mm]	$U_{beam,max}$	64	64
Column maximum deflection [mm]	U_{column}	10	36
Column deflection limit [mm]	$U_{column,max}$	40	40
<i>Joint Loads (ULS)</i>			
Internal normal load [kN]	N	-4.96	-4.81
Internal shear load [kN]	V_y	-31.88	-30.44
Internal shear load [kN]	V_z	7.82	7.65
Internal torsional moment [kNm]	T	-5.87	-5.32
Internal bending moment [kNm]	M_y	-14.35	-13.65
Internal bending moment [kNm]	M_z	-26.63	-22.14

the evaluation of each element. The following elements may be isolated in the joint of the reference structure:

- Beam & Column Member
- Top & Bottom End-Plate
- Stiffeners
- Pre-Tensioned Bolts
- Various Welds

Figure 8.1: Elements isolated from reference structure (*Various Welds*) not shown

8.2.1. Component Method

In chapter 5 the joint load distribution is discussed and the component method is briefly touched upon. The software used to determine the distribution of loads and stresses within the connection, IDEA StatiCa, utilizes a modified version of the component method: *Component-Based Finite Element Method* (CBFEM), which improves upon the standard component method by integrating more accurate finite element method calculations in the overall design approach. There are no additional hand calculations using the traditional component method required in order to evaluate the resistance of the joint, as IDEA StatiCa automatically incorporates this into its analysis. However the component method concepts may be utilized in order to make informed design decisions.

In moment resisting joints the component method can be used to determine the strength of individual components. For the plate and bolt elements of the joint the strength of the component is evaluated based on the equivalent T-Stub model. This model is based on a simple connection: a horizontal plate rigidly connected to a vertical plate with bolts on either side of the rigid plate. The first two out of three failure modes of the T-Stub are based on the formation of plastic hinges in the horizontal plate. The yield line of the real component, see figure 8.2, corresponds to the yield line in the equivalent T-Stub connection, from which the plastic bending moments in the plastic hinges can be determined.

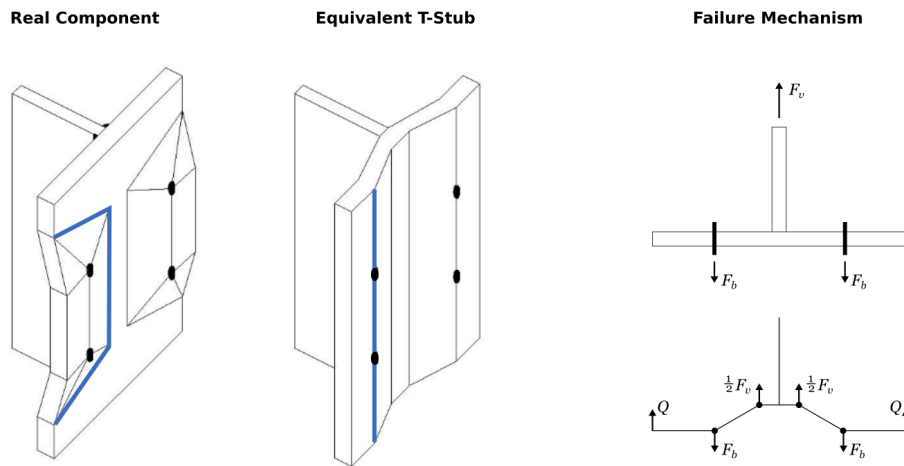


Figure 8.2: Real component and equivalent T-Stub failure mechanism (failure mode 1), the blue line indicates the length of the yield line of the T-Stub

The component method can also be used in order to determine the rotational stiffness of the joint, which can be used to determine its classification. The global analysis of the structure is performed using the dynamic FEM model, which assumes all of the discretized elements are rigidly connected. This assumption is only valid if the joint at the corners can be classified as rigid according to the Eurocode. This classification is based on the initial rotational stiffness $S_{j,ini}$, which should be greater than the minimum rigid rotational stiffness for un-braced frames according to the Eurocode [14] as seen in equation 8.1.

$$S_{j,ini,min} \geq \frac{25EI_b}{L_b} \quad (8.1)$$

Where:

- $S_{j,ini}$ = Joint minimum initial rotational stiffness
- E = Steel modulus of elasticity
- I_b = Beam cross-sectional moment of inertia
- L_b = Beam span

8.2.2. Design Considerations

The beam and column member dimensions are determined in the global analysis based on the ultimate and serviceability limit state, and will not directly be considered in the joint optimization. The loads on the beam are transferred to the column through the two end plates, which are connected together by a set of bolts. The end-plates dimensions are governed by various factors. The end-plates need to be thick enough to limit bending around the x and y axes, in order to ensure sufficient rotational stiffness. They should also be thick enough to prevent punching-shear of the bolts loaded in shear.

The end plate should also be long and wide enough to accommodate all of the required bolts. The bolts cannot be too close to the edges or to each other as this would compromise the structural integrity of the shear load transfer between the bolts and the end-plate. The bolts should also have sufficient spacing between themselves and the beam, column, stiffeners, or any other plated element

in order to allow installation, pre-tensioning, maintenance, and the application of welds elsewhere in the connection.

As the name suggests, the stiffeners are implemented in order to increase the stiffness of the joint. Removing the stiffeners will affect the rotational stiffness of the joint, which should remain sufficiently high according to equation 8.1. In addition the stiffeners have an effect on the resistance of the *end-plate in bending* component with respect to the component method. When it comes to the *end-plate in bending* the failure mechanism is evaluated according to the equivalent T-Stub method, which is governed by yield lines of the end-plate. In the case that the stiffeners are removed the shape of the yield lines will change slightly as the surrounding area of the plate element is less stiff, resulting in smaller yield lines. The bigger effect however is that the equivalent T-stub of the bolts acting in a group needs to be considered. The yield line, and therefore the T-stub resistance will be much larger, but the applied load also increases as all of the bolt loads are included. The yield line of a group of bolts is in general smaller than the summation of individual yield lines of the same set of bolts, as can be seen in figure 8.3, where some of the possible yield lines for the end-plate in the reference structure have been drawn. However when considering the individual bolts the maximum load needs to be considered. With the group of bolts all of the bolt loads, also the smaller loads, are included. Whether the group of bolts becomes governing would need to be checked on a case-by-case basis depending on the type of loading and geometry.

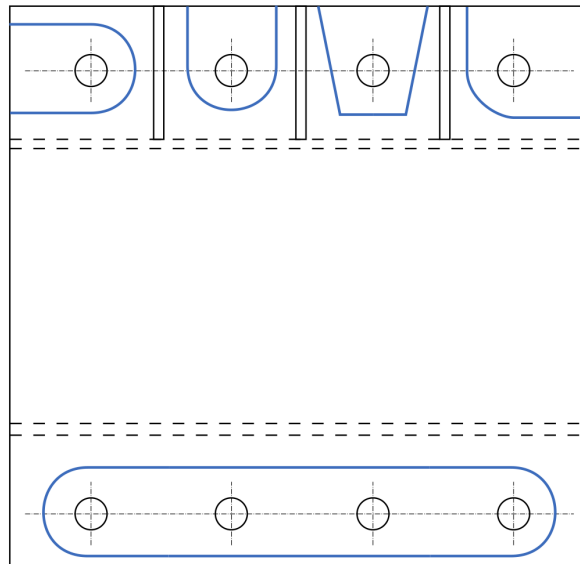


Figure 8.3: Top view of the top end-plate in the reference structure joint. Possible yield lines have been drawn for the end-plate in bending component in the component method. Yield lines in case of stiffeners present are drawn at the top, yield lines for the group of bolts in case no stiffeners are included are drawn on the bottom.

Finally, the most critical elements of the joint, the welds, can be reduced. From a practical point of view all of the weld throats can realistically speaking be no smaller than 4mm. Changing the throat thickness of the welds will increase the weld stresses, which are both relevant for the ultimate limit state and the fatigue limit state. Larger weld stresses may lead to the compromise of structural integrity in the ultimate limit state, and to larger stress ranges in the fatigue limit state when using the fatigue evaluation outlined in the design norms such as the Eurocode and ROK. Larger stresses in the welds lead to larger stress ranges as these are calculated based on the maximum weld value.

8.2.3. Design Choices

As stated before, the beam and column profiles follow from the global analysis. First the number of bolts was reduced from 4 rows of 2 bolts to 3 rows of 2 bolts. Based on the new dimensions of the beam, column, and bolts the end plate width B_{ep} and length L_{ep} are reduced. From a structural integrity point of view the longitudinal beam-to-end-plate welds are sufficient to transfer any loads from the beam to the end-plate, which means the stiffeners could be removed. From a stiffness point of view

however the stiffeners are probably required. Using equation 8.1, the minimum bending rotation can be determined. One can achieve this stiffness by either increasing the end-plate thickness sufficiently, or by adding stiffeners. Unfortunately the Eurocode does not provide a minimum rotational stiffness for torsional rotation, yet the dynamic model still assumes a rigid connection. For this reason the two sets of stiffeners are kept in order to ensure no excessive torsional displacements occur. The plate thickness is then governed by the rotational stiffness, but also checked for punching shear. Finally the welds are dimensioned based on the ULS loads, with a minimum throat thickness of 4mm. The resulting joint design dimensions are given by table 8.2.

Table 8.2: Results from the optimization for the joint

Description	Symbol	Reference Structure	Optimized Design
<i>Member Profiles</i>			
Beam profile	[-]	SHS300/8	SHS80/10
Column profile	[-]	SHS350/10	SHS200/12.5
<i>Joint Geometry Dimensions</i>			
End-plate width	B_{ep}	550	420
End-plate length	L_{ep}	530	360
End-plate thickness	d_{ep}	25	20
Stiffener longitudinal spacing	e_{sx}	130	110
Stiffener thickness	d_s	5	5
Bolt type	[-]	M24 10.9	M24 10.9
Bolt lateral spacing	e_{by}	130	110
Bolt longitudinal spacing	e_{bx}	440	300
<i>Governing Unity Checks (ULS)</i>			
Pre-tensioned bolts	uc_{bolts}	0.07	0.78
Welds	uc_{welds}	0.05	0.98
Plated elements	uc_{plates}	0.04	0.61
<i>Stiffness (FLS)</i>			
Joint stiffness around y-axis [MNm/rad]	$S_{int,y}$	150	18
Joint stiffness around z-axis [MNm/rad]	$S_{int,z}$	145	51
Joint stiffness rigid limit [MNm/rad]	S_R	43	15

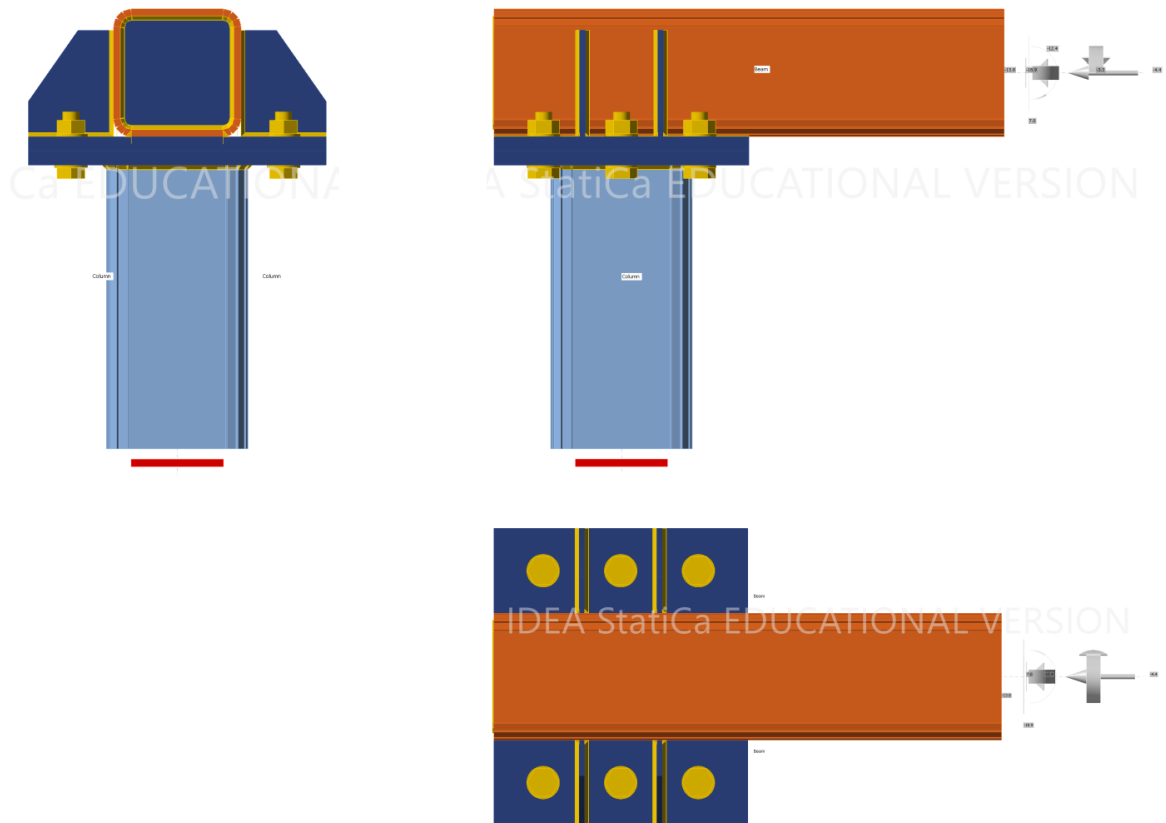


Figure 8.4: Overview of joint dimensions

9

Results

In this chapter the calculation model is applied to both the reference and optimized design in order to investigate the dynamic behavior of the structure and determine how a more accurate dynamic analysis compares to the currently employed calculations according to the Eurocode and ROK norms, and what effects this has on the fatigue life of the structure. As the Column-to-End-Plate weld has the lowest fatigue resistance as seen in chapter 6, and one of the highest fatigue actions as seen in chapter 5, it will be the primary focus for the results analysis. For this specific weld it is the weld normal stress which is governing.

Throughout this chapter the term *simulation* is used, in the context of this chapter it entails defining a set of loads which are applied to the structure, applying them in the dynamic analysis, and extracting the relevant dynamic signals in the form of deformations and internal loads.

9.1. Accuracy of Analytical Joint Model

In chapter 5 a simplified analytical calculation model is developed in order to determine the relationship between cross-sectional loads acting on the beam at the joint location and the stresses within the welds most susceptible to fatigue damage. This is an important step as it connects the global structural analysis to the local structural analysis, and helps answer the following sub-research question:

How well can the load distribution within the joint be approximated by analytical models?

Ideally an in-depth analysis of the geometry of the joint would be performed, based on which the load distribution would be determined, and then validated using a numeric finite element method calculation. However this is beyond the scope of this thesis, and instead the load-stress relationship is directly curve-fitted from the finite element analysis by considering each of the cross-sectional loads isolated and individually. The relevant curve-fit constants are given in table 5.2 in chapter 5.

However it is important to determine how accurate this analytical model is, especially since the loads are analyzed isolated from one-another, which means no load interaction is taken into account. In order to evaluate the accuracy of the analytical equations several load cases are evaluated using both the numeric finite element method and the developed analytical equations. In these load cases the maximum loads due to instantaneous wind gusts in the ultimate and fatigue limit state are considered, in addition five random load cases with loads of similar order of magnitudes are analyzed. These load cases are summarized in table 9.1.

Tables 9.2 and 9.3 summarize the resulting stresses in the Column-to-End-Plate welds. On average the analytical model overestimates the weld stresses by 30% to 40%. This is a significant overestimation, but fortunately it is a conservative approach. A more accurate approach which takes the geometry and load interactions into account would be preferable, especially as it would yield a more generalized model which can be applied to variations of similar joint designs. If the design of the joint is altered in the current approach, then an entire new set of FEM calculations has to be performed and the results

Table 9.1: Loads applied to the joint in the reference structure in order to estimate the accuracy of the analytical load-stress relationship

Load Case	N [kN]	V_y [kN]	V_z [kN]	T [kNm]	M_y [kNm]	M_z [kNm]
Reference Structure ULS	-5	-32	8	-6	-14	-27
Reference Structure FLS	-5	-19	7	-4	-13	-16
Random Combination 1	-6	-23	8	-5	-11	-4
Random Combination 2	-2	-16	4	-3	-10	-6
Random Combination 3	-1	-13	6	-2	-7	-14
Random Combination 4	-4	-9	8	-4	-10	-13
Random Combination 5	-3	-13	10	-7	-8	-14

Table 9.2: Stress components in the Column-to-End-Plate weld in the reference structure under various load cases

Load Case	σ_{\perp}		τ_{\parallel}		τ_{\perp}	
	CBFEM	Analytical	CBFEM	Analytical	CBFEM	Analytical
Reference Structure ULS	96.2	119	8.8	13	-56.7	-72
Reference Structure FLS	71.9	90	4.8	8	-42.6	-54
Random Combination 1	60.7	82	-7.4	-4	-36.4	-49
Random Combination 2	57	67	-2	0	-34	-41
Random Combination 3	40	50	7	8	-24	-31
Random Combination 4	51	68	7	9	-30	-41
Random Combination 5	53	71	6	8	-31	-42

of which have to be curve fitted in order to determine the relationship between the cross-sectional load and the weld stress of that specific new joint, which is very time consuming.

9.2. Wind and Traffic Load Comparison

In the Eurocode and ROK norms only turbulent wind gust loading is explicitly taken into account, the building codes do not take traffic induced pulse loads on structures near roads specifically into account. From this one of the main sub-research questions of the thesis follows:

Do traffic induce aerodynamic loads play a significant role in the dynamic response of a traffic sign steel portal frame support structure, and to what extent does this influence the fatigue life of the structure?

In order to investigate this various simulations are performed in which the different types of loads which may occur are considered on their own. The dynamic analysis is based on a set of linear equations of motion, which entails that the total response to a set of loads is equal to the summation of individual load responses. This allows each type of load which is expected to occur to be considered and analyzed on its own.

An atmospheric turbulent wind load is simulated based on a basic mean wind speed, during the life time of the structure this wind speed may vary anywhere between 0, and up to roughly 31 m/s in case of an extreme storm. For this reason a set of wind speeds ranging between these values is considered. For the traffic induced pulse loads two traffic intensities are considered: 456 trucks per hour corresponding to the average traffic intensity expected on the road, and 1000 trucks per hour corresponding to the maximum traffic intensity expected on the road. For each of the described loads an individual simulation of 600 seconds, or 10 minutes, is run for the reference structure.

Figure 9.1 illustrates the loads acting on the right sign, which is largest in the reference structure, for a 30 second period within the 600 second simulation. From these graphs it can be seen that the transient load F_y , which acts perpendicular to the sign, is significantly larger in magnitude for the wind loads corresponding to high wind speeds compared to the traffic loads. Though it should be noted that they are of similar magnitude as the wind loads of lower wind speeds, which are much more common. When the torsional load M_x is considered, it can be seen that the traffic load is much larger in magnitude. The reason for this is that the concentrated wind load is assumed to be located at the center of the sign, which means the only torsion originates from the difference between the center of the sign and the sign attachment location to the steel portal frame. The load due to the passing trucks is located

Table 9.3: Fatigue weld stresses in the Column-to-End-Plate weld in the reference structure under various load cases

Load Case	σ_{ref}			τ_{ref}		
	CBFEM	Analytical	Difference	CBFEM	Analytical	Difference
Reference Structure ULS	112	139	25%	8.8	13	48%
Reference Structure FLS	84	105	26%	4.8	8	67%
Random Combination 1	71	96	35%	-7.4	-4	46%
Random Combination 2	66	79	18%	-2	0	[-]
Random Combination 3	47	59	26%	7	8	14%
Random Combination 4	59	80	35%	7	9	42%
Random Combination 5	61	82	34%	6	8	33%
		Average:	28%		Average:	42%

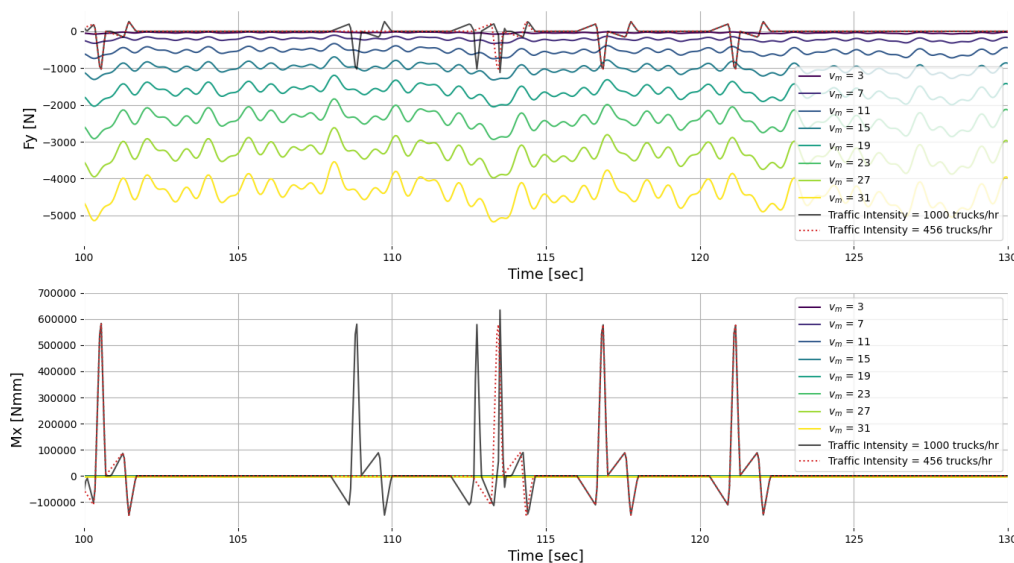


Figure 9.1: Comparison of various load cases applied to the largest sign in the reference structure for a 30 second period within the 600 second simulations

near the bottom of the sign, creating a much larger torsional load on the portal frame, increasing its relevance to the total dynamic response.

Ultimately the applied load alone does not determine the total dynamic response of the system. The relevance of a given load is best evaluated by considering the stresses it induces in the welds of the joints, as these stresses are used to evaluate the fatigue resistance of the structure. Figure 9.2 shows the resulting weld stress signals found in the *Column-to-End-Plate welds*, which follow from the dynamic analysis for the loads outlined in figure 9.1. The stresses in these specific welds are shown as these welds are the most susceptible to fatigue damage, as discussed in chapter 6. When considering the weld stress signal in figure 9.2 it is not necessarily the absolute stress magnitude that is of relevance, but the magnitude of the stress ranges, as these induce fatigue damage in the welds. Especially when considering the weld normal stress, the traffic loads induce significant stress ranges of roughly 4MPa with each pulse load. This stress range is larger than the maximum turbulent wind load corresponding to 31 m/s. Increasing the traffic intensity will not have a large influence on the stress range magnitude, but will influence how often this load occurs within the structure.

It should be noted that the traffic induced pulse load applied in this particular comparative calculation are very conservative. They are amplified by a factor 8.0 in order to match other loads found in literature. They are also assumed to occur at rate of 1000 vehicles per hour traveling at 80 km/hour, which is not realistic for Dutch highways. The most relevant aspect of the load, the torsional load, is based on an extreme case where most of the wind pressure is concentrated at the bottom of the sign, which does not necessarily describe the pressure distribution at all points in time.

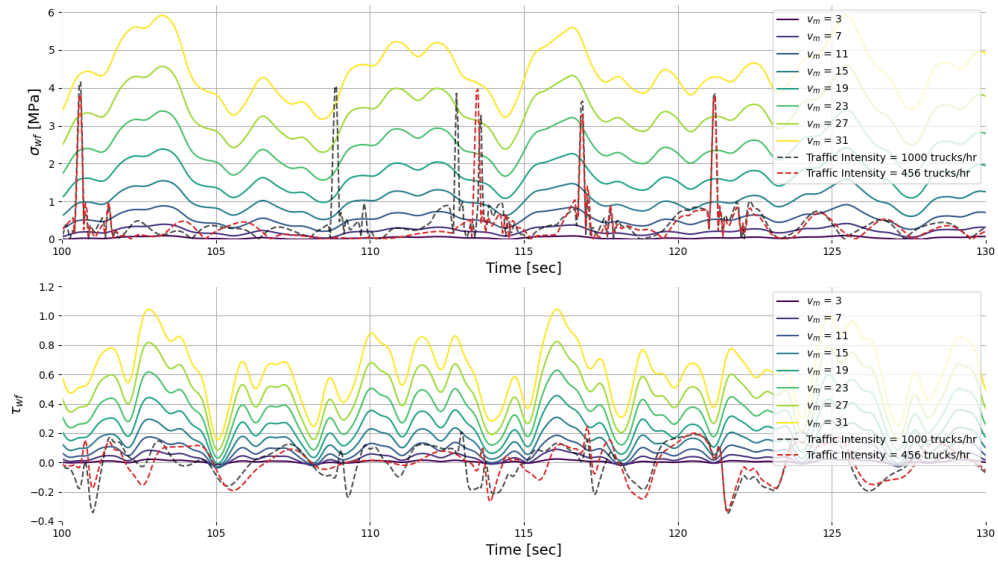


Figure 9.2: Comparison of weld stress signals in the Column-to-End-Plate weld in the joint due to the various load cases found in figure 9.1

9.3. Norms and Simulation Comparison

The way in which the fatigue damage is estimated for a structure differs significantly based on how the wind loads and their dynamic responses are modeled. The norms utilize a generalized approach based on a single formula, while the proposed calculation model in this thesis utilizes a more elaborate simulation method. When comparing the fatigue damage estimates for the structure's lifetime it is important to consider the following sub-research question:

How do simulated dynamic wind loads compare to static instantaneous wind gust loads, such as the ones employed by the design norms?

9.3.1. Load Definition

At the root, the difference in fatigue damage estimation between the design norm and the proposed method lies in the way the loads are defined. At its core the way the wind load is calculated is the same for the two load models according to the generalized form shown in equation 9.1.

$$F_w = \frac{1}{2} \rho A v_w^2 \quad (9.1)$$

The difference mainly lies in which wind speed is considered for this load. In the norms a mean wind speed is taken from which the maximum instantaneous gust speed is calculated based on the Davenport model [7]. This model increases the mean wind speed v_m by a multiple of the standard deviation of the turbulent wind speed distribution σ_w according to equation 9.2. The simulation load model on the other hand takes this same mean wind speed and adds a summation of sinusoidal loads whose amplitude is determined based on the variance spectrum $S_L(\omega_n)$ as shown in equation 9.3.

$$v_{w.ec.max} = v_m + 3.5\sigma_w \quad (9.2)$$

$$v_{w.sim}(t) = v_m + \sum (\sqrt{2\Delta\omega S_L(\omega_n)} \sin(\omega_n t + \varphi)) \quad (9.3)$$

$$\sigma_w = \frac{v_m}{c_o(z) \ln z/z_0} \tag{9.4}$$

The variance spectrum S_L represents the total variance, i.e. σ_w^2 , distributed across frequencies, which means the total wind speed calculated by the Eurocode $v_{w.ec.max}$ and the one calculated using the simulation method $v_{w.sim}$ are based on the same turbulence spectrum. As such, one would expect similar load magnitudes. However if the wind loads from a simulation are compared to the maximum instantaneous load used in the code, a significant discrepancy is present. This discrepancy results from the large difference in wind speed shown in figure 9.3.

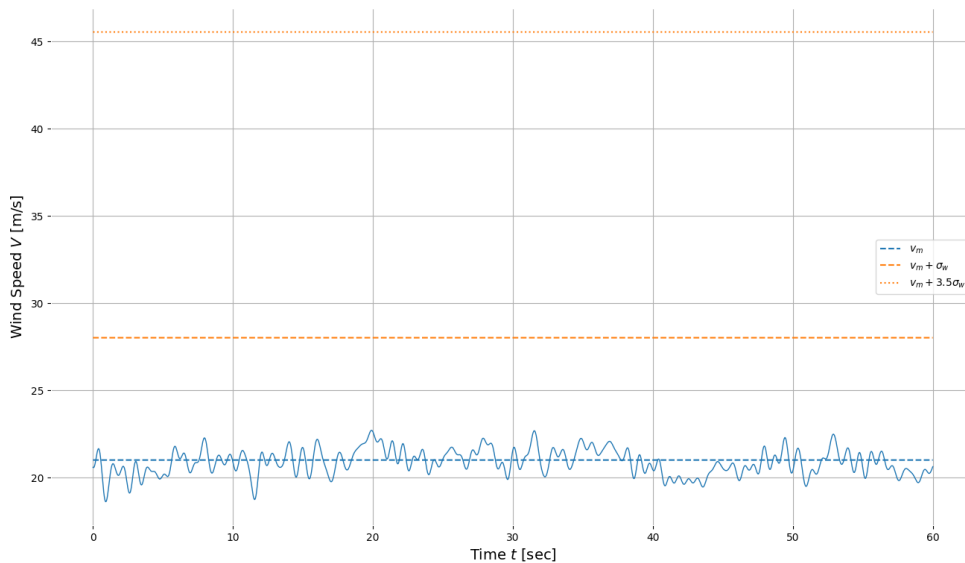


Figure 9.3: Wind speed simulation compared to the Eurocode wind speed values

This contrast in wind speed magnitudes arises from an assumption made in the Eurocode with regards to the standard deviation of the wind turbulence. This assumed standard deviation is given by equation 9.4, derived from the definition of the turbulence intensity factor I_v . For a sign at a height of 6m and a basic mean wind speed v_b of 29.5 m/s, values representative of the reference structure, the standard deviation assumed by the Eurocode is 7.01 m/s. If a simulated wind speed signal, based on the same basic mean wind speed and structure height, is considered, then the numerically standard deviation of the simulated signal is equal to roughly 0.66 m/s. This is almost a factor 10 smaller than the value used by the Eurocode.

It is therefore important to consider the implications of using a smaller standard deviation, and identify why this difference occurs in the first place. The reason the standard deviation is different has to do with how the simulated wind speed is calculated. The turbulent part of the wind is modeled by a summation of sinusoidal waves, whose amplitude is determined by the variance spectrum according to the frequency of the wave. When simulating the wind load a set of frequencies are sampled from the variance spectrum, whose range lies between the lower and upper cut-off frequency values discussed in chapter 3 section 3.2.3. If a larger range, i.e. a smaller lower cut-off frequency or a larger upper cut-off frequency, is chosen then the standard deviation of the simulated signal would be greater.

Changing the cut-off frequencies does however have consequences. If the range of frequencies from which is sampled is expanded by decreasing lower cut-off frequency or increasing the upper cut-off frequency, then the number of sampled waves should also increase to maintain accuracy. At each integration step the load vector is determined, which takes longer if more waves are sampled in the simulation.

When increasing the upper cut-off frequency, the frequencies of the loads increases. When performing the modal-analysis the number of modes that are taken into account for the solution directly

depends on the load frequency. The response to a load with a high frequency requires the modal response corresponding to a mode with a large eigen-frequency. As a result more modal responses need to be solved at each integration step.

When decreasing the lower cut-off frequency, the simulation length should be increased in order to accurately capture the total response. A wave with a very low frequency will have a long period which may exceed the 600 second simulation time, therefore to include the total behavior of said wave the simulation time should be sufficiently long. If this value is decreased too much the simulated wind speed is no longer valid for the variance spectrum in question. When considering the van der Hoven spectrum in figure 3.2 one can see that lower frequencies correspond to other variance spectra. The turbulence effects should be limited to wind speed changes in the order of magnitude of minutes. Wind speed changes in the order of magnitude of hours is taken into account through choosing a sub-set of data corresponding to a specific hour of the day. Wind speed changes in the order of magnitude of days is taken into account through the $c_{seasonal}$ factor.

Based on these considerations it is undesirable to change the chosen cut-off frequencies, which makes it important to consider whether or not choosing a smaller ranges of frequencies for the simulation will have a significant effect on the total response of the system. Decreasing the cut-off frequency has serious implications with regard to the validity of the wind speed simulation, therefore only increases in the upper cut-off frequency are considered. Changing the wind signal to include more waves with higher frequencies, will ultimately influence the stress signal within the welds of the structure. The weld stress signals are used to determine the estimated fatigue damage by using the Rainflow Cycle Counting algorithm to count the number of stress cycles and magnitude of these stress cycles. In order to gain a rudimentary understanding of the effect of increasing the load frequencies on the cycle counting output of the weld stress signals, one can perform a Rainflow Cycle Counting algorithm on the load signals directly.

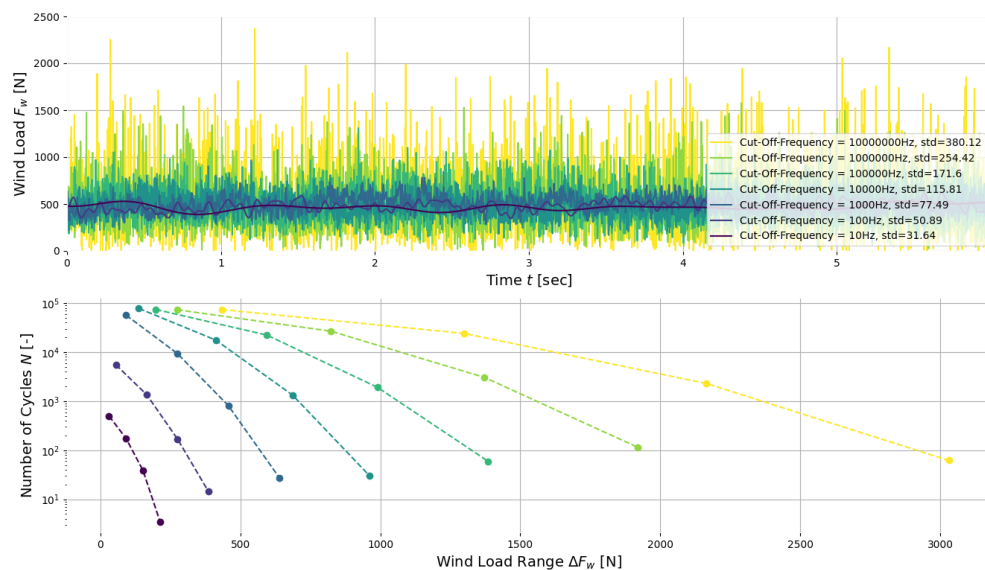


Figure 9.4: Rainflow cycle counting algorithm applied to wind load signals which have been simulated with different cut-off frequencies

Such a calculation is performed in figure 9.4, from which it can be seen that increasing the cut-off frequency of a signal based on the Solari turbulence spectrum will result in an increase in the magnitude and number of stress cycles. The larger number of cycles is due to waves with high frequencies, which therefore occur more often. The larger stress range is due to the fact that signal is composed of a summation of waves, using more waves results in a larger total amplitude. It is however important to consider that the fatigue damage is not directly based on the load signal $F(t)$, but based on the response signal $x(t)$ due to said load signal as shown in equations 9.5 and 9.6.

$$F(t) = \sum F_{0,n} \sin(\Omega_n t + \varphi_n) \quad (9.5)$$

$$x(t) = \sum |H(\Omega)| F_{0,n} \sin(\Omega_n t + \varphi_n) \quad (9.6)$$

$$H_{s dof}(\Omega) = \frac{x}{F} = \frac{1}{\sqrt{(k - \Omega^2 m)^2 + (\Omega c)^2}} \quad (9.7)$$

Where:

- H = Transfer function describing the relationship between a load and response signal
- F = Load signal
- x = Response signal
- Ω = Frequency of load signal F
- m = Mass
- c = Damping
- k = Stiffness F

In equation 9.6 the transfer function H represents the relationship between a the load signal F and response signal x . In the case of the structure in question the transfer function is rather complex as it consists of a multi degree of freedom dynamic system, and a set of curve-fitted functions based on the joint geometry. However the dynamic aspect of the transfer function for the complex structure in question is analogous to a simple single degree of freedom damped mass-spring system described by equation 9.7. From this equation it can be seen that the response x of a system due to a load signal F with a large frequency Ω will result in a small response amplitude, especially if the system is damped. It is therefore safe to assume that the response due to the waves with larger frequencies will be filtered out by the dynamic system. As a result the response to the waves with high frequencies can be disregarded as the amplitude of this response is negligibly small.

9.3.2. Cycle Counting

The magnitude and number of stress cycles of the weld stress signal gives a direct indication of the fatigue life of the structure. It is therefore useful to compare these values for the design norm method and the proposed simulation method. For a selection of simulations for wind speeds ranging between 3 and 31 m/s, and a traffic load simulation, the Rainflow cycle counting algorithm has been applied to the resulting weld normal stress signal in the governing *Column-to-End-Plate* weld. The number of cycles for each stress range within the 600 second simulation is extrapolated to a 50 year period, corresponding to the structure's life time. The results of the cycle count are plotted in figure 9.5, alongside the cycle count according to the norms and a SN curve corresponding to a detail category 36, which is representative of the weld in question.

The cycle count results plotted in figure 9.5 should all be below the SN curve to ensure no fatigue damage occurs for a particular combination of stress range S and number of stress cycles N . For the total fatigue evaluation the summation according to the Palmgren miner rule should be performed, but this type of plot gives an indication if the detail in question is expected to fail. In this case all of the data points from both the simulation and the calculations performed according to the norms are below the SN curve, indicating a safe design.

From figure 9.5 it can be seen that all of the wind speed simulation number of cycles falls between 10^6 and 10^9 cycles, which is to be expected based on the load frequencies. The weld stress signal will have a similar time signature as the wind speed simulation, whose frequencies lie between 10^{-4} and 10^1 Hz. If a wave of those frequencies is extrapolated to a 50 year period, it is expected to occur within the same 10^6 and 10^9 number of cycles. The magnitude of stress cycles increases with an increasing mean wind speed, which is to be expected as the wind load amplitudes don't scale by Δv , but by $2v_m \Delta v$ as can be seen by equations 9.8 and 9.9.

$$v(t) = v_m + \Delta v(t) \quad (9.8)$$

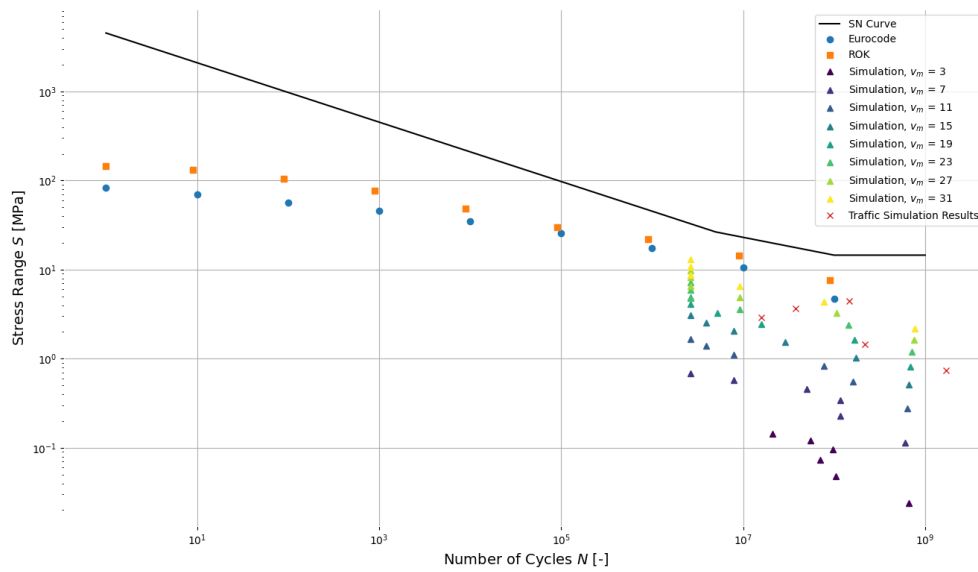


Figure 9.5: Weld normal stress signal cycle count results for various individual simulations of the reference structure plotted along side the methods used by the Eurocode and ROK. The maximum instantaneous stress used by the norms is 84 MPa, the SN curve corresponds to a detail category 36

$$F(t) \propto v^2(t) = v_m^2 + 2v_m\Delta v(t) + \Delta v^2(t) \quad (9.9)$$

The results in figure 9.5 cannot be used directly for a fatigue damage estimation as each wind speed simulation has been extrapolated to a 50 year period. Instead the number of cycles for each wind speed simulation have been multiplied by the probability of occurrence or said wind speed according to figure 7.6. The results are then binned together and the discrete stress ranges and number of cycles are plotted in figure 9.6 in a similar fashion as figure 9.5.

After the combination of the various simulations it can be seen that the higher stress ranges corresponding to high wind speeds in storm conditions such as 31 m/s have a much lower number of cycles N_g for the 50 year life time period. The reason for this is that such a wind speed of 31 m/s has a probability of occurrence of 1.64×10^{-6} . The resulting scatter plot of the simulation results adjusted by probabilities of occurrence, depicted by green triangles in figure 9.6, follows a similar distribution as the one found in the Eurocode and the ROK. For this reason it has been curve fitted by a function in the form of equation 9.10, which is the same form as the one used by the Eurocode.

$$\frac{\Delta S}{S_k} = c_1 (\log_{10}(N_g))^2 + c_2 \log_{10}(N_g) + c_3 \quad (9.10)$$

Where:

ΔS = Stress range

S_k = Maximum instantaneous stress expected to occur in a 50 year period

N_g = Number of cycles that stress range ΔS is expected to occur

c_i = Curve fit constants, $i = 1, 2, 3$

This calculation is repeated for the optimized structure, and the results are shown in figure 9.7. The curve fit constants for the Eurocode and the simulations is given in table 9.4. The curve fit constants for both the reference structure and optimized structure for the simulation results lie close together, this is to be expected as equation 9.10 relates the number of expected cycles to the stress range relative to the maximum stress, which in turn scales for more slender geometry. It can be seen that for the

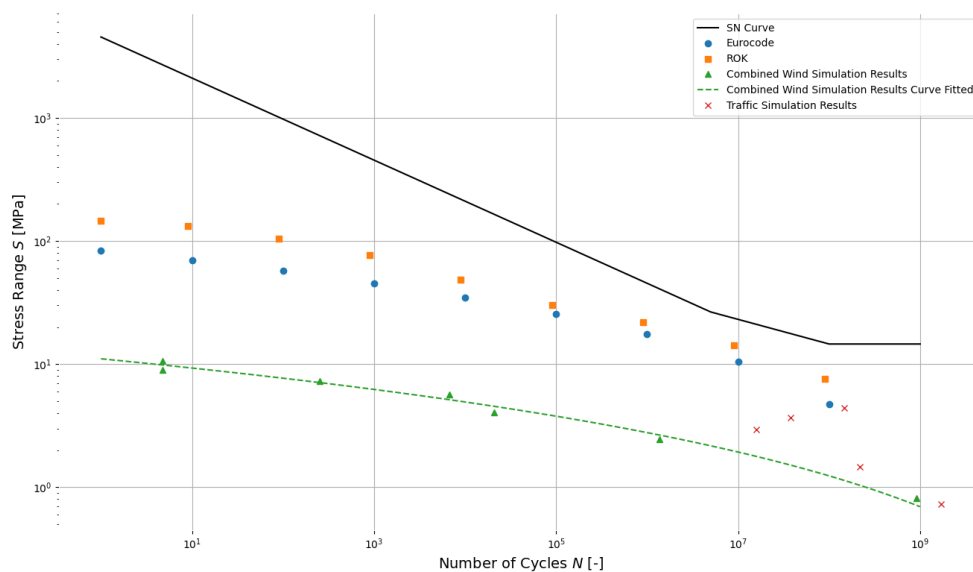


Figure 9.6: Weld normal stress signal cycle count results for combined simulated wind speeds according to the probability of occurrence of each wind speed for the reference structure. The resulting scatter plot is curve fitted with a similar function as the one found in the norms. The maximum instantaneous stress used by the norms is 84 MPa, the SN curve corresponds to a detail category 36

Table 9.4: Curve fit constants for equation 9.10

Description	Curve Fit Constants		
	C_1	C_2	C_3
Eurocode	0.700	-17.400	100.000
Simulation Reference Structure	0.090	-2.184	13.155
Simulation Optimized Structure	0.098	-1.972	10.515

optimized design the cycle count for both the Eurocode and the ROK is very close to the SN curve, leading to fatigue damage to be expected. The curve fitted data on the other hand remains well below this SN curve, resulting in no expected fatigue damage.

The cycle count for the traffic induced pulse loads is considered separately. The stress ranges induced by these type of loads are roughly the size of the pulses found in figure 9.2, which compared to the wind speeds are of large magnitude occurring with a large cycle count. The validity of the size of the stress range remains uncertain as the magnitude of the traffic induced aerodynamic pulse loads is very conservative. Most notably a load factor of 8.0 is used in order to match the peak pressure the sign experiences in other literary models. Previous research [10] suggests a load factor of 4.0, which would roughly half the stress ranges in figure 9.7, rendering them of similar order of magnitude as the stresses induced by wind loads. More research ought to be done with respect to the magnitude of these type of loads in order to determine their significance with respect to cycle counting and fatigue.

9.4. Fatigue

The fatigue damage is determined according to the Palmgren Miner rule [27], and is based on a set of stress ranges S and number of times this stress range occurs N_g . The damage is then evaluated based on the ratio of the number of cycles to failure N to the number of cycles to occurrence N_g for a given stress range S . The combinations of N_g and S follows from the cycle counting shown in figures 9.6 and 9.7 for the reference structure and optimized structure respectively, while the value of N may be calculated using the value of S in combination with the relevant SN curve.

Three different ways of performing the cycle count are presented in this thesis: the Eurocode, the

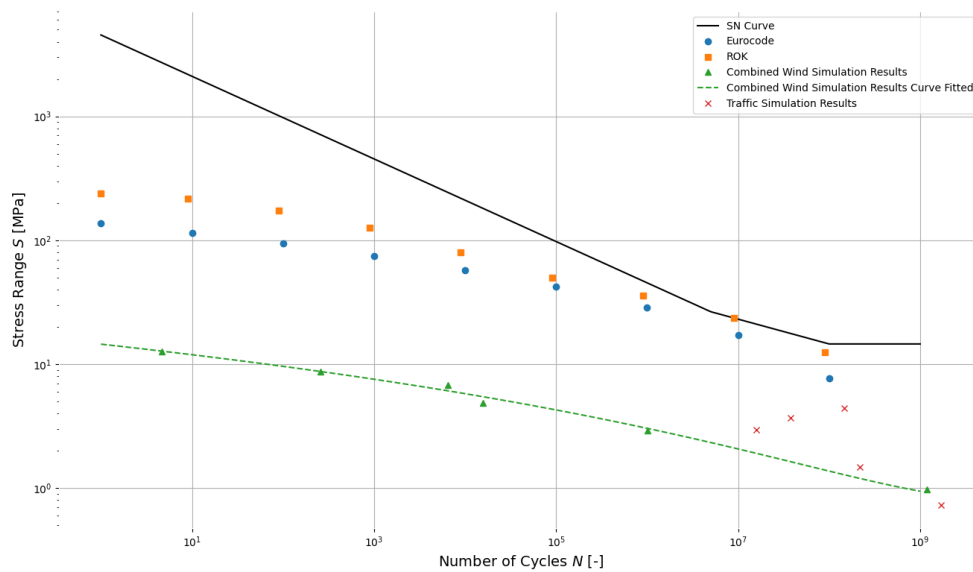


Figure 9.7: Weld normal stress signal cycle count results for combined simulated wind speeds according to the probability of occurrence of each wind speed for the optimized structure. The resulting scatter plot is curve fitted with a similar function as the one found in the norms. The maximum instantaneous stress used by the norms is 84 MPa, the SN curve corresponds to a detail category 36

Dutch ROK norm, and the proposed simulation approach. The Eurocode provides a way to determine a relationship between a stress range ΔS and the number of cycles this occurs N_g in the form of an equation, this same type of equation is used in order to curve-fit the simulation results, see equation 9.10 and table 9.4. The ROK on the other hand only provides a table of values between which one is allowed to interpolate linearly. In order to compare the fatigue damage of the three different methods the fixed values provided by the ROK norm will be used for all methods; the fixed N_g values from the ROK tables are used in equation 9.10 in order to obtain the equivalent stress ranges for the Eurocode and Simulation approach. The reason the ROK values are chosen is that linear interpolation between the given data points is less accurate than interpolation through curve fitting equation 9.10.

The results of the fatigue damage due to wind loads are given in table 9.5 and 9.6 for the reference structure and the optimized structure respectively. The over-dimensioned reference structure endures very little fatigue damage for the conservative Eurocode and ROK approach. The simulation approach has even smaller stress ranges and therefore endures zero fatigue damage. When considering the the optimized design on the other hand fatigue damage is expected for the Eurocode and ROK methods, especially since the cycle count data points in figure 9.7 lie so close to the SN curve. The Eurocode method does not result in fatigue failure, but the ROK one does due to slightly higher stress range values. The simulation approach has slightly increased values, but the stress ranges remain well below the fatigue cut-off limit, resulting in no damage.

9.4.1. Applicability of Simulated Results

Based on the simulation results in tables 9.5 and 9.6 it may seem as though no fatigue damage will occur within the welds of the structure. By running the simulation for at least 600 seconds, the wind loads in the simulation approach is representative of the full turbulence spectrum. The distribution of mean wind speeds results in the overall distribution of stress ranges and number of stress range cycles. What this approach does not take into account however are extreme instantaneous gust loads. The summation of sinusoidal loads of different frequencies will simulate some local gust peaks in the wind speeds due to the stochastic nature of the wind speed signal generation. However the true wind speed will not perfectly vary according to the Solari [19] spectrum, and random outlying values will show up.

Table 9.5: Fatigue damage in the Column-to-End-Plate weld in the reference structure due to aerodynamic turbulent wind loads according to the different methods. Ng: expected number of cycles, S: stress range, N: cycles to failure of stress range, D: fatigue damage

Ng	Eurocode			ROK			Simulation			Effective
	S	N	D	S	N	D	S	N	D	D
90,000,000	5	[-]	[-]	8	[-]	[-]	1	[-]	[-]	[-]
9,000,000	11	[-]	[-]	14	[-]	[-]	2	[-]	[-]	[-]
900,000	18	36591826	0.025	22	13229907	0.068	3	[-]	[-]	[-]
90,000	26	5510648	0.016	30	3374366	0.027	4	[-]	[-]	[-]
9,000	35	2103646	0.004	49	806892	0.011	5	[-]	[-]	0.011
900	46	961629	0.001	76	208918	0.004	6	[-]	[-]	0.004
90	58	486192	0.000	105	80606	0.001	8	[-]	[-]	0.001
9	71	265302	0.000	133	39914	0.000	9	[-]	[-]	0.000
1	84	157434	0.000	146	29885	0.000	11	[-]	[-]	0.000
Total			0.046			0.112			[-]	0.017

Table 9.6: Fatigue damage in the Column-to-End-Plate weld in the optimized structure due to aerodynamic turbulent wind loads according to the different methods. Ng: expected number of cycles, S: stress range, N: cycles to failure of stress range, D: fatigue damage

Ng	Eurocode			ROK			Simulation			Effective
	S	N	D	S	N	D	S	N	D	D
90,000,000	8	[-]	[-]	12	[-]	[-]	1	[-]	[-]	[-]
9,000,000	18	37500776	0.240	23	9250813	0.973	2	[-]	[-]	[-]
900,000	29	3719432	0.242	36	2020134	0.446	3	[-]	[-]	[-]
90,000	43	1194449	0.075	50	761014	0.118	4	[-]	[-]	[-]
9,000	58	474431	0.019	80	181977	0.049	6	[-]	[-]	0.049
900	75	216874	0.004	126	47117	0.019	8	[-]	[-]	0.019
90	95	109650	0.001	173	18179	0.005	10	[-]	[-]	0.005
9	116	59833	0.000	218	9002	0.001	12	[-]	[-]	0.001
1	138	35506	0.000	240	6740	0.000	15	[-]	[-]	0.000
Total			0.581			1.611			[-]	0.075

These extreme values are taken into account by the Davenport model [7] in the Eurocode in terms of an average extreme value. These type of extreme gusts will not show up often, and are thus confined to lower number of cycle values N . Furthermore the ROK has done supplementary research into the dynamic behavior of structures under aerodynamic wind loading which showed that for values of N_g below 10^4 the relative load $\Delta S/S_k$ may be underestimated by the Eurocode method. As these effects are not taken into account in the simulation model it is best to use the ROK values for stress ranges associated with numbers of cycles N below 10^4 . However for smaller loads occurring more often the simulation model gives an adequate representation of the loading and response. This concept has been illustrated in tables 9.5 and 9.6 through the last column indicating the effective damage, using the ROK fatigue damage values for $N_g < 10^5$ and using the simulation fatigue damage values for the remaining values of N_g . Even though the ROK specifies a value of 10^4 , a boundary value of 10^5 is taken conservatively in the effective fatigue damage calculation in order to avoid any overlap between the ROK model and the simulation model range of applicability.

The difference between the ROK method and the simulation method can be broken down into three steps: the load definition, the dynamic response, and the load-to-stress translation. In terms of the load definition, the difference has been extensively discussed in section 9.3. The main reason this difference in loads is acceptable is through the dynamic response of the structure, which yields insignificant responses to wind loads of higher frequencies. It is unclear what type of dynamic transfer function is used in the Eurocode and ROK approach, but it is safe to say it is less accurate and less representative of the structure considered in this thesis. Finally transforming the cross-sectional loads in the beam near the joint to weld stresses is discussed in section 9.1, where it is found that the governing normal weld stresses in the *Column-to-End-Plate* weld are on average overestimated by roughly 30%. This

makes the approach as a whole conservatively on the safe side for the structure in question.

9.4.2. Traffic Induced Fatigue Damage

The traffic loads are not directly combined with the wind loads in the simulations. The reason for this is that they are not explicitly present in the Eurocode or ROK, which means if they are included in the simulation, the results cannot be directly compared to the existing approaches in the norms. Furthermore it is unclear what the load magnitude of these types of traffic induced loads ought to be due to a lack of research in this field. For this reason a very conservative set of loads are calculated on their own. Their cycle count can be seen in figure 9.5 through 9.7 in the form of red crosses. The fatigue damage due to these loads on their own, completely disregarding the effects of wind loads, is given in table 9.7.

Table 9.7: Fatigue damage in the Column-to-End-Plate weld in the optimized structure due to traffic induced aerodynamic pulse loads. Ng: expected number of cycles, S: stress range, N: cycles to failure of stress range, D: fatigue damage

Reference Structure				Optimized Structure			
Ng	S	N	D	Ng	S	N	D
1,688,490,000	0.73	[-]	[-]	1,716,084,000	0.78	[-]	[-]
218,124,000	1.47	[-]	[-]	307,476,000	1.56	[-]	[-]
145,854,000	4.41	[-]	[-]	155,052,000	4.69	[-]	[-]
38,106,000	3.67	[-]	[-]	44,676,000	3.91	[-]	[-]
15,768,000	2.94	[-]	[-]	10,512,000	2.35	[-]	[-]

On their own these loads occur often, but are not of great magnitude, ranging between 0 and 5 MPa. The fatigue damage due to two loads cannot simply be considered on their own, but the stress ranges due to the combined load should be used in the analysis. In the most severe case for the optimized structure, the stress ranges depicted by red crosses in figure 9.7 can be added to the dashed green line, and the resulting stress range would still stay below the cut-off limit of the SN-curve. This suggests that the structure will not fail due to these types of traffic induced pulse loads, especially since such a conservative load has been taken into account. More research is required in this area before the truck loads can be taken into account directly in a meaningful way.

10

Conclusion

10.1. Calculation Model

In this thesis a calculation model is setup in order to more accurately analyze the dynamic response of a highway traffic sign steel portal frame support structure to aerodynamic loads, allowing for a less conservative fatigue verification. The first step in the model is determining the aerodynamic loads in the form of traffic induced pulse loads and turbulent atmospheric wind loads. For the traffic induced pulse loads there exists no guidelines in most common building codes, and even in literature there is limited information available. The three most relevant models from literature have been considered. The most detailed and comprehensive load model, the Lichtneger model, is chosen. However this model has not been verified to the same extent as the other models, therefore the pulse load is scaled in order to match the maximum pressure experienced by the traffic sign in the other load models.

For the atmospheric wind load there do exist models in the building codes, in the case of the Eurocode the model consists of a simple formula which relates the magnitude and number of stress range cycles to the maximum instantaneous wind gust load expected to occur in the structure's lifetime. This thesis proposes to simulate the wind load based on a turbulence spectrum such as the Solari spectrum provided by the Eurocode, instead of attempting to describe a spectrum of the dynamic responses based of a single static value. The cut-off frequencies of this spectrum are chosen based on relative values with respect to the maximum value of the spectrum, and are further limited by the simulation length for the lower bound value and the accuracy of the dynamic modal analysis for the upper bound value of the range of frequencies.

The dynamic model consists of a discretized system of one dimensional Euler-Bernoulli beams with six degrees of freedom at each node representing all possible translations and rotations of those nodes in 3D space. The system is then solved using a modal analysis in order to optimize the solver with respect to time, from which the the displacement signals of each node are determined. These can be transformed into internal load signals using the internal load conversion matrix. The element size of the system is governed by the accuracy of the largest eigen-mode of the system relevant in the modal analysis. One of the largest drawbacks of the dynamic FEM model is the computation time for a dynamic analysis, which may be improved by solving the system in the frequency domain instead of the time domain, but is beyond the scope of this thesis. If a more accurate response is required the element size can be decreased to the point where shear deformations start to play a significant role, at this point Timoshenko beam elements should be implemented.

The internal load signals are applied to a CBFEM model of the joint in *IDEA StatiCa*. Ideally the load distribution within the joint is modeled by an analytical model, and verified with the CBFEM model, but this too is beyond the scope of this thesis. Instead, for each specific joint design a separate analysis is performed, the results of which are curve fitted in order to determine the relationship between a cross-sectional load and the relevant weld stress. The problem with this approach is that an entirely new calculation needs to be performed for each joint design. Furthermore the load interactions are not taken into account as each load is considered in an isolated analysis.

From the joint weld stress signals a set of magnitudes and number of stress range cycles are determined using the Rainflow Cycle Counting algorithm. The output is combined with the wind speed

probability distribution and used in the Palmgren-Miner rule in combination with relevant SN curves provided by the Eurocode, in order to estimate the fatigue damage of the structure's lifetime.

10.2. Research Questions

For this thesis a set of sub-research questions have been developed in order to aid in investigating the main research topic of determining the dynamic behavior of the structure and its affect on its fatigue assessment. The sub-research questions are:

How well can the load distribution within a structural detail be approximated by analytical models?

How do simulated dynamic wind loads compare to static instantaneous wind gust loads, such as the ones employed by the design norms?

Do traffic induce aerodynamic loads play a significant role in the dynamic response of a traffic sign steel portal frame support structure, and to what extent does this influence the fatigue life of the structure?

The overall calculation model employed in this thesis is quite accurate and elaborate. However the relationship between the cross-sectional loads applied to the joint and the weld stresses within the joint remains one of the weaker aspects of the model with regards to accuracy. To answer the first sub-research question, when approximating the stresses using curve-fit data based on isolated loads, one overestimates the load by roughly 30% on average. Fortunately this is a conservative load conversion, and the structure is sufficiently safe that this overestimation does not negatively impact the verification in a significant way.

When comparing the dynamic wind loads in the simulation model with the calculation found in the design norms, the difference lies mainly in the underlying approach. To answer the second sub-research question: the simulation approach takes considers a variance spectrum and samples several points in order to create a signal, from which the number and magnitudes of stress range cycles is determined. The design norms use this same variance distribution, and add a secondary probabilistic model on top in order to determine the maximum instantaneous wind load. From this single value a distribution of magnitudes and number of stress cycles is determined. As a result the values found in the Eurocode are significantly less accurate, not only are they based on a single parameter, but the output is based on multiple conversions of probabilistic distributions and models where accuracy is lost along each step. In addition, the norms assume a much larger standard deviation, corresponding to wind loads of much higher frequencies. The simulation model does not take these high frequency loads into account as they do not yield significant dynamic responses.

Gust loads due to traffic passing are currently not taken into account in the design norms. To answer the third sub-research question: when using models from literature in an extremely conservative manner the results do not yield significant damage results. However this may still have to be evaluated on a case-to-case basis if extremely slender and optimized structures are of interest.

The overall research question is as follows:

What is the most appropriate way of modelling the dynamic behavior of traffic sign portal frame support structures, and what influence does this have on the fatigue assessment of the structure in question?

The overall aim of the thesis, which is encapsulated by the main research question, is answered through the results of the analysis of the reference structure and the optimized structure. Through these analyses it has been shown that using a finite element method model developed in Python, the

dynamic behavior can be described much less conservatively. From the dynamic results it can be seen that loads with high frequencies do not yield large responses. Furthermore the wind loads describing the most often occurring general turbulence in the simulation model result in much lower stress ranges when compared to those calculated using the design norms. However the model does not include seldom occurring extreme wind gust loads, which are taken into account in the Eurocode. As a result the simulation model is only valid for stress ranges that occur very often due to general turbulence.

10.3. Results and Design Recommendations

The simulation method proposed in this thesis can be used to more accurately depict the structure's response due to dynamic wind loads representative of general turbulence. Unfortunately it does not take extreme instantaneous wind gusts into account such as the ones in the Davenport model [7], which are relevant for dynamic loads which occur less than 10^4 times in a 50 year period. For this reason it is recommended that this model is only used for dynamic loads which occur more than 10^5 times in a 50 year period. Fortunately these type of loads induce the most fatigue damage in these type of structures, which means using the simulation model still allows structures to be further optimized with respect to fatigue.

The relationship between the joint weld stresses and the cross-sectional beam loads should be investigated in more depth. Ideally a generalized analytical model is developed, allowing for analytical expressions to be used directly in Python or Excel. Alternatively a Python script could be written for the commercial version of IDEA Statica which automatically determines the load cases, runs the CBFEM analyses, and reads out the stress values, which are then curve fitted.

In terms of traffic induced pulse loads the exact magnitude should be determined. Even for the extremely conservative case outlined in this thesis no fatigue damage is found, and can probably be omitted; though it is recommended to perform a cycle count with the proposed method and plot the results such as in figure 9.7, and include the cycle counts of the traffic loads to make sure the values lie well below the SN curve.

Ultimately no generalized conclusions may be drawn from this research as the calculation model described in this thesis is only applied to two structures of similar design. However the results to suggest that there is a significant potential in optimization with respect to fatigue limit state for stress ranges that occur often in the structure's lifetime. This thesis research has formed a solid foundation, and it is recommended that the calculation model is applied to more structures, or is expanded upon in order to form a more generalized analytical model.

10.4. Further Work

In this thesis only two structures with the same global parameters such as height, span, number of signs, etc. are analysed. It would be of interest to use the elaborate calculation model developed for this thesis to analyse more structures of larger spans, more signs, or even different geometry like poles or columns with cantilever beams. The current methodology is quite time consuming, each 600 second simulation takes an hour or more to run. If more structures of similar types are analyzed a set of general analytical expressions may be formed that estimate the dynamic response quicker.

Aside from the Python code being optimized, or switching to a quicker programming language such as C, the simulation run-time may also be reduced by changing the solver method. Currently the system is being solved in modal space, which reduces the number of equations that need to be solved, but still requires direct numerical integration, which requires many small time steps. If one solves the system in the frequency domain, one does not determine the dynamic behavior from the integration of the displacement vector according to the equations of motion, but by analysing the frequency response matrix. For this one would use the same general setup of the dynamic FEM model, but instead of using the matrices to set up an equation that is numerically integrated, one uses the matrices to determine the response of a single degree of freedom. The advantage of this is that no time is lost in the form of numerical integration, and time is saved because not the entire system has to be solved, one can determine the response of a specific set of degrees of freedom by taking into account the correct matrix elements. Another advantage of the frequency domain solver is in the form of accuracy. As depicted in figure 10.1, using a modal solver to run a 600 second simulation which is then extrapolated to a 50 year life time results in a loss of accuracy. In this case one uses this relatively small time frame of 600 seconds to characterize the entire life time of the structure. Using the frequency domain analysis one

is not required to go from a generalized form, i.e. turbulence spectrum, to specific situation, i.e. run a simulation, and extrapolate back to a generalized form, i.e. life time fatigue resistance.

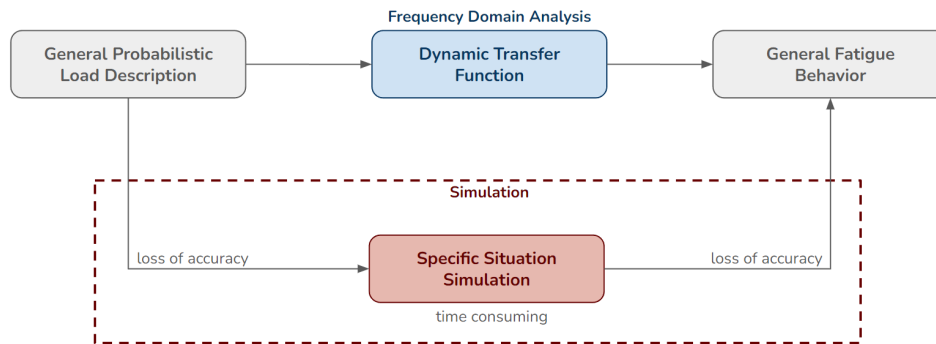


Figure 10.1: Comparison overview of a modal solver and a frequency domain solver

With respect to the loading, the traffic induce pulse loads should be researched further and the Lichtneger model should be verified with empirical data, including ways of scaling up the sign geometry from the maximum 1.5mx1.5m dimensions in the original research. In terms of the joint analysis a more generalized analytical model should be developed in order to save time and allow a broader range of connection designs to be analyzed without the need for a curve-fit calculation of finite element results of the joint. Furthermore the load interaction between the various cross-sectional loads should be investigated in order to achieve roughly 30% lower weld stresses.

In regards to the dynamic model several large assumptions are made. Firstly the dynamic load on the square hollow section profiles itself has been disregarded. Although the surface area is not as large as the signs themselves, the wind loads the system experiences on those elements is not negligible. Furthermore the joints in the frame, and the supports are assumed to be fully rigid. More sophisticated models could incorporate joint stiffness, which would allow more economical designs of the joint. The stiffeners for example could be removed entirely if there is no longer a stiffness requirement. This would result in more deformations within the joint, which would result in some additional damping, which could also be added into the damping matrix. Less stiff joints would also result in smaller cross-sectional loads near the joints as stiff parts of the structure attract most of the loads. Exposing the joints to lower loads would allow for further optimization of the connection detail, though the member profiles may need to be increased in size. One may also increase the accuracy of the dynamic model using Timoshenko beam elements, however the calibration of the element size suggests this is not necessary for the structures in question.

With less stiff supports and joints the global and local stability of the structure may come into question. In order to take this into account a second-order analysis could be performed. Especially if this is done dynamically this would result in much more complex models. A second-order analysis takes the deformed structure into account, which means that interaction between each degree of freedom in the system needs to be modelled. This is a serious consideration to take into account as this increases the complexity of the calculation and increases the computation time significantly. Most likely for traffic sign support structures this type of analysis is too elaborate, and it is more efficient to increase the stiffness and reduce the slenderness of the structure.

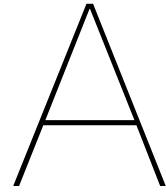
Finally this thesis has assumed that the welds are the governing detail with respect for fatigue. The bolts are assumed to be sufficiently pre-tensioned such that no significant stress ranges occur during loading. Using a more elaborate model for the joint may allow more accurate descriptions of the bolt stresses and their fatigue assessment. Furthermore there are other details within the structure to be considered, some of which are: holes in the hollow sections, end-plate splices in the beam, column-base foundations. These details may also be susceptible to fatigue damage, and should be evaluated in a similar manner.

Bibliography

- [1] Idea statica connection theoretical background. URL <https://www.ideastatica.com/support-center/general-theoretical-background>.
- [2] Nationaal dataportaal wegverkeer. URL <https://dexter.ndwcloud.nu/opendata>.
- [3] Numerical solutions of differential equations. URL <http://chms.csuohio.edu/tutorials/Matlab/General/DifferentialEquationSolve/>.
- [4] Brian H. Sako Alvar M. Kabe. *Structural Dynamics Fundamentals and Advanced Applications*. Elsevier Inc., 2020. ISBN 978-0-12-821615-6.
- [5] Ali Arafat. Cfd analysis of semi-trailer truck aerodynamics, 2015. URL https://www.simscale.com/projects/Ali_Arafat/aerodynamic_analysis_of_a_semi-truck_trailer_vehicle/.
- [6] R. E. Klingner B. M. Creamer, K. H. Frank. "fatigue loading of cantilever sign structures from truck wind gusts.". 1979.
- [7] A.G. Davenport. Note on the distribution of the largest value of a random function with application to gust loading. *Proceedings of the Institution of Civil Engineers*, 1964.
- [8] Van der Hoven. Power spectrum of horizontal wind speed in the frequency range from 0.0007 to 900 cycles per hour. *Journal of Meteorology*, 1957.
- [9] I. Hosch F. Foudad. Design of overhead vms structures for fatigue loads, 2011.
- [10] C.D. Fikkers. Overhead sign structures - gantry. Master's thesis, Delft University of Technology, 2018.
- [11] European Committee for Standardization. Nen-en 1991-1-4, eurocode 1: Actions on structures - part 1-4: General actions - wind actions, .
- [12] European Committee for Standardization. Nen-en 1991-2, eurocode 1: Actions on structures - part 2: Traffic loads on bridges, .
- [13] European Committee for Standardization. Nen-en 1993-1-1, eurocode 3: Design of steel structures - part 1-1: General rules and rules for buildings, .
- [14] European Committee for Standardization. Nen-en 1993-1-8, eurocode 3: Design of steel structures - part 1-8: Design of joints, .
- [15] European Committee for Standardization. Nen-en 1993-1-9, eurocode 3: Design of steel structures - part 1-9: Fatigue, .
- [16] S. Ginal. Fatigue performance of full-span sign support structures considering truck-induced gust and natural wind pressures. Master's thesis, Marquette University, 2003.
- [17] Google, January 2022. URL <https://www.google.com/maps/@52.3418651,4.8921659,3a,54.5y,181.63h,94.34t/data=!3m6!1e1!3m4!1sjSjJY13ojZUhfKU82tJZ0Q!2e0!7i16384!8i8192>.
- [18] Rijkswaterstaat GPO. Richtlijnen ontwerp kunstwerken rok 1.4.
- [19] G.Solari. Equivalent wind spectrum technique: Theory and application. *Journal of Structural Engineering*, 114(6), 1988.

- [20] Charles R. Harris, K. Jarrod Millman, Stéfan J van der Walt, Ralf Gommers, Pauli Virtanen, David Cournapeau, Eric Wieser, Julian Taylor, Sebastian Berg, Nathaniel J. Smith, Robert Kern, Matti Piccus, Stephan Hoyer, Marten H. van Kerkwijk, Matthew Brett, Allan Haldane, Jaime Fernández del Río, Mark Wiebe, Pearu Peterson, Pierre Gérard-Marchant, Kevin Sheppard, Tyler Reddy, Warren Weckesser, Hameer Abbasi, Christoph Gohlke, and Travis E. Oliphant. Array programming with NumPy. *Nature*, 585:357–362, 2020. doi: 10.1038/s41586-020-2649-2.
- [21] Edgar Matas Hidalgo. Study of optimization for vibration absorbing devices applied on airplane structural elements, 2014.
- [22] J. D. Hunter. Matplotlib: A 2d graphics environment. *Computing in Science & Engineering*, 9(3): 90–95, 2007. doi: 10.1109/MCSE.2007.55.
- [23] John T. Katsikadelis. Chapter 11 - the finite element method. In John T. Katsikadelis, editor, *Dynamic Analysis of Structures*, pages 359–522. Academic Press, 2020. ISBN 978-0-12-818643-5. doi: <https://doi.org/10.1016/B978-0-12-818643-5.00011-X>. URL <https://www.sciencedirect.com/science/article/pii/B978012818643500011X>.
- [24] J. Macdonald S. Hogan L. Arany, S Bhattacharya. Simplified critical mudline bending moment spectra of offshore wind turbine support structures. *Wind Energy*, 2014.
- [25] G. Deodatis M. Shinozuka. Simulation of stochastic processes by spectral representation. *American Society of Mechanical Engineers*, 44(4), 1991.
- [26] Anthony F. Molland. *The Maritime Engineering Reference Book: A Guide to Ship Design, Construction and Operation*. 2008.
- [27] Teresa L.M. Morgado. Chapter 20 - failure of steel couplings used in railway transport. In Abdel Salam Hamdy Makhlouf and Mahmood Aliofkhaezai, editors, *Handbook of Materials Failure Analysis with Case Studies from the Aerospace and Automotive Industries*, pages 449–470. Butterworth-Heinemann, Boston, 2016. ISBN 978-0-12-800950-5. doi: <https://doi.org/10.1016/B978-0-12-800950-5.00020-X>. URL <https://www.sciencedirect.com/science/article/pii/B978012800950500020X>.
- [28] AMITA GULATI SETHU RAMANT SUMAN RAOt M. P. SINGH S. NIGAM P. AGARWAL, ANIL KUMAR YADAV and NEERAJA REDDY. Surface layer turbulence processes in low wind speeds over land. *Atmospheric Environment*, 26(16):2089–2098, 1995.
- [29] B. Ruck P. Lichtneger. Full scale experiments on vehicle induced transient loads on roadside plates. *Journal of Wind Engineering and Industrial Aerodynamics*, 136:73–81, 2015.
- [30] A. Mohsen Shehata P.R. Wirsching. Fatigue under wide band random stresses using the rain-flow method. *Journal of Engineering Materials and Technology*, pages 205–211, July 1997.
- [31] A. Agosta R. Cook, D. Bloomquist. Truck-induced dynamic wind loads on variable-message signs. *Transportation Research Record*, 1997.
- [32] M. Wagenaar R. van den Brink, L. Brederode. Onderzoek naar de wegtypeverdeling en samenstelling van het wegverkeer, 2010.
- [33] A. Shahbazian C. Rebelo Y. Harada L. da Silva S. Oliveira, R. Costa. Component-based method for quasi-static cyclic behaviour of steel joints. *Journal of Constructional Steel Research*, 2021.
- [34] Y. Sun. Thermoelastic damping in micro-beam resonators. *International Journal of Solids and Structures*, 2006.
- [35] Abraham Askenazi Vince Adams. *Building better products with finite element analysis*. 1999.
- [36] K. Viridi. Numerical simulation of semi-rigid connections by the finite element method, 1999.

- [37] Pauli Virtanen, Ralf Gommers, Travis E. Oliphant, Matt Haberland, Tyler Reddy, David Cournapeau, Evgeni Burovski, Pearu Peterson, Warren Weckesser, Jonathan Bright, Stéfan J. van der Walt, Matthew Brett, Joshua Wilson, K. Jarrod Millman, Nikolay Mayorov, Andrew R. J. Nelson, Eric Jones, Robert Kern, Eric Larson, C J Carey, İlhan Polat, Yu Feng, Eric W. Moore, Jake VanderPlas, Denis Laxalde, Josef Perktold, Robert Cimrman, Ian Henriksen, E. A. Quintero, Charles R. Harris, Anne M. Archibald, Antônio H. Ribeiro, Fabian Pedregosa, Paul van Mulbregt, and SciPy 1.0 Contributors. SciPy 1.0: Fundamental Algorithms for Scientific Computing in Python. *Nature Methods*, 17:261–272, 2020. doi: 10.1038/s41592-019-0686-2.
- [38] Takashi Yokoyama. Vibrations of a hanging timoshenko beam under gravity. *Journal of Sound and Vibration*, 141:245–258, 09 1990. doi: 10.1016/0022-460X(90)90838-Q.



Setup of Dynamic Model

In this appendix a short report outlining the derivation of the dynamic model is presented.

Setup of Dynamic Numeric Model

Contents

A.1	Notation	2
A.2	Degrees of Freedom and Loads.....	2
A.3	Bending Element (bending around y -axis).....	4
A.3.1.	Curvature.....	5
A.3.2.	Velocity.....	5
A.3.3.	Mass and Stiffness Matrix.....	6
A.4	Axial Element.....	7
A.4.1.	Velocity.....	8
A.4.2.	Strain	8
A.4.3.	Mass and Stiffness Matrix.....	8
A.5	Torsional Element	10
A.5.1.	Velocity.....	10
A.5.2.	Firs Order Derivative.....	10
A.5.3.	Mass and Stiffness Matrix.....	10
A.6	Summary Individual Matrices and Vectors.....	12
A.7	Total System Element Matrices and Vectors.....	13
A.8	Local & Global Coordinates	14
A.9	Building the System Matrices.....	19
A.10	Boundary Conditions.....	20
A.11	Eigenfrequency and Eigenmatrix.....	22

A.1 Notation

Time derivative

$$\dot{u} = \frac{du}{dt}, \quad \ddot{u} = \frac{d^2u}{dt^2}$$

Coordinate derivative

$$u_x = \frac{du}{dx}, \quad u_{xx} = \frac{d^2u}{dx^2}$$

Vector (symbol = \bar{u})

$$\bar{u} = \begin{Bmatrix} a_1 \\ \vdots \\ a_n \end{Bmatrix}$$

Matrix (symbol = **U**)

$$\mathbf{U} = \begin{bmatrix} a_{11} & \dots & a_{1j} \\ \vdots & \ddots & \vdots \\ a_{i1} & \dots & a_{ij} \end{bmatrix}$$

A.2 Degrees of Freedom and Loads

The numerical model will be described by a series of nodes connected by elements. Each node will have 6 degrees of freedom, representative of all possible translations and rotations in 3D space.

Degrees of Freedom

u	displacement	in global x -direction	x -vector
v	displacement	in global y -direction	y -vector
w	displacement	in global z -direction	z -vector
ψ	rotation	in global yz -plane (y to z)	x -vector
φ	rotation	in global zx -plane (z to x)	y -vector
θ	rotation	in global xy -plane (x to y)	z -vector

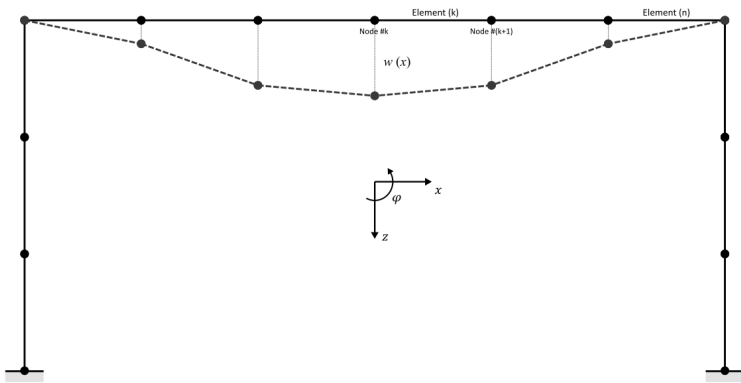
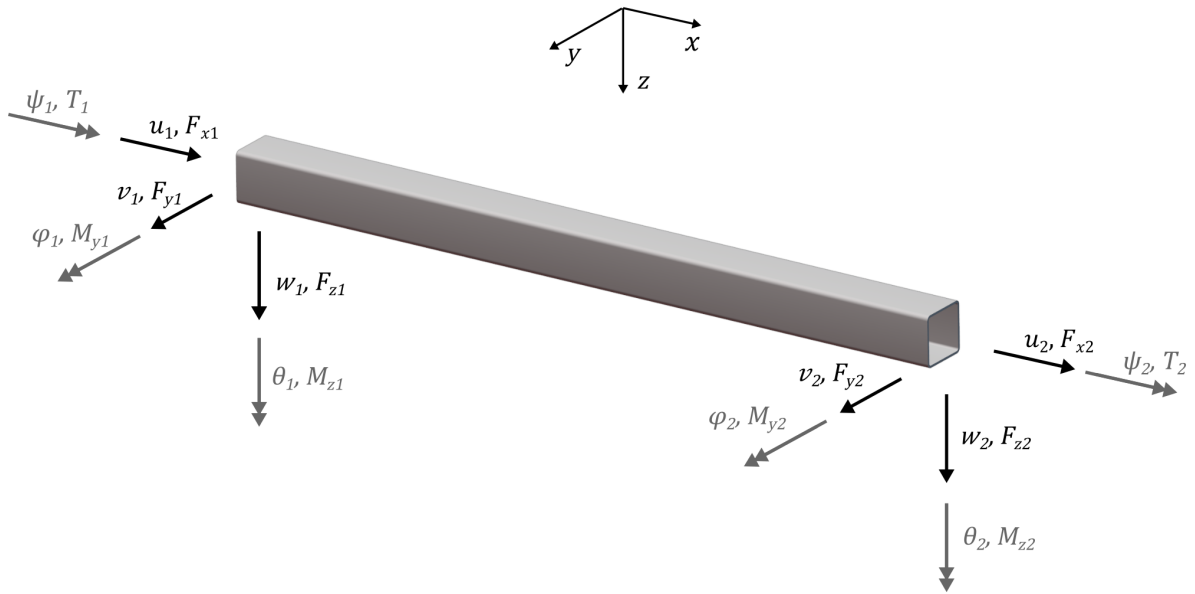
$$\bar{u} = \begin{Bmatrix} u \\ v \\ w \\ \psi \\ \varphi \\ \theta \end{Bmatrix}$$

$$\varphi = -\frac{dw}{dx}, \quad \theta = \frac{dv}{dx}$$

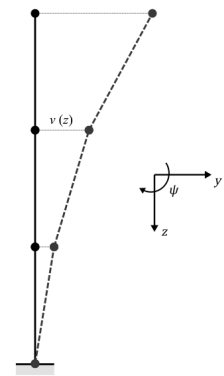
Loads

F_x	force	in global x -direction	x -vector
F_y	force	in global y -direction	y -vector
F_z	force	in global z -direction	z -vector
T	torsion moment	around x -axis	x -vector
M_y	bending moment	around y -axis	y -vector
M_z	bending moment	around z -axis	z -vector

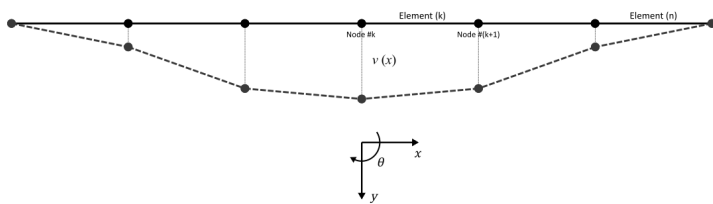
$$\bar{f} = \begin{Bmatrix} F_x \\ F_y \\ F_z \\ T \\ M_y \\ M_z \end{Bmatrix}$$



(a) Front View



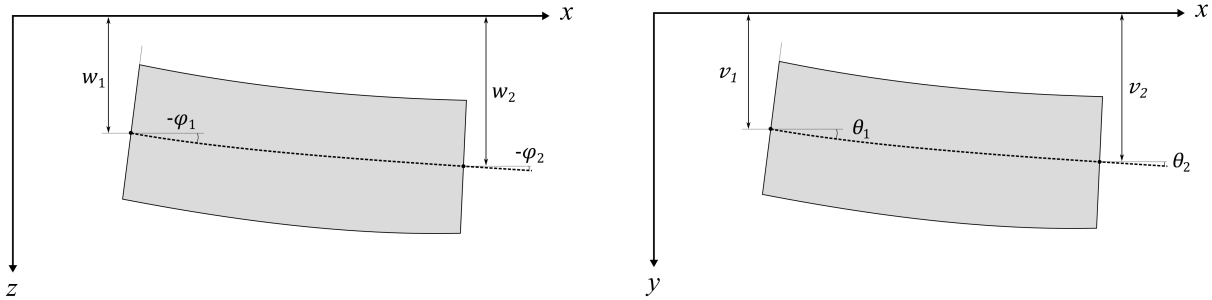
(b) Side View



(c) Top View

A.3 Bending Element (bending around y-axis)

A bending beam may be modeled by a series of nodes with 2 degrees of freedom (a displacement w and rotation φ on each end) connected by beam elements of length l resulting in a total of 4 degrees of freedom per element. These degrees of freedom are given in the element displacement vector \bar{w} .



$$\bar{w} = \begin{Bmatrix} w_1 \\ \varphi_1 \\ w_2 \\ \varphi_2 \end{Bmatrix}, \quad \bar{v} = \begin{Bmatrix} v_1 \\ \theta_1 \\ v_2 \\ \theta_2 \end{Bmatrix}$$

The displacement field along the length of the bending element are obtained using interpolated shape functions using third order polynomials (cubic shape functions), which are in the form of $N_i = a_3x^3 + a_2x^2 + a_1x + a_0$. The coefficients a_n for $n = 0,1,2,3$ can be determined by using the boundary conditions for each shape function.

$$N_{v1}(x) = N_{w1}(x) = 2\xi^3 - 3\xi^2 + 1$$

$$N_{v1}(x) = N_{w2}(x) = -2\xi^3 + 3\xi^2$$

$$N_{\theta1}(x) = -N_{\varphi1}(x) = l\xi^3 - 2l\xi^2 + l\xi$$

$$N_{\theta1}(x) = -N_{\varphi2}(x) = l\xi^3 - l\xi^2$$

With $\xi = \frac{x}{l}$

The displacement field of the beam element along its length is then given by:

$$w_e(x) = [N_{w1}, N_{\varphi1}, N_{w2}, N_{\varphi2}] \begin{Bmatrix} w_1 \\ \varphi_1 \\ w_2 \\ \varphi_2 \end{Bmatrix} = \mathbf{N}_w \bar{w}$$

$$v_e(x) = [N_{v1}, N_{\theta1}, N_{v2}, N_{\theta2}] \begin{Bmatrix} v_1 \\ \theta_1 \\ v_2 \\ \theta_2 \end{Bmatrix} = \mathbf{N}_v \bar{v}$$

A.3.1. Curvature

The curvature field of the beam element along its length is defined as the second co-ordinate derivative of the displacement field

$$\kappa_{e,w}(x) = \frac{\partial^2 w_e}{\partial x^2} = \frac{\partial^2}{\partial x^2} (\mathbf{N}_w) \bar{w} = \mathbf{B}_w \bar{w}$$

$$\kappa_{e,v}(x) = \frac{\partial^2 v_e}{\partial x^2} = \frac{\partial^2}{\partial x^2} (\mathbf{N})_v \bar{v} = \mathbf{B}_v \bar{v}$$

$$\kappa_{e,w}(x) = \frac{\partial^2}{\partial x^2} ([N_{w1}, N_{\varphi1}, N_{w2}, N_{\varphi2}]) \begin{Bmatrix} w_1 \\ w_2 \\ \varphi_1 \\ \varphi_2 \end{Bmatrix} = \frac{\partial^2}{\partial \xi^2} \frac{1}{l^2} ([N_{w1}, N_{\varphi1}, N_{w2}, N_{\varphi2}]) \begin{Bmatrix} w_1 \\ w_2 \\ \varphi_1 \\ \varphi_2 \end{Bmatrix}$$

$$\kappa_{e,v}(x) = \frac{\partial^2}{\partial x^2} ([N_{v1}, N_{\theta1}, N_{v2}, N_{\theta2}]) \begin{Bmatrix} v_1 \\ v_2 \\ \theta_1 \\ \theta_2 \end{Bmatrix} = \frac{\partial^2}{\partial \xi^2} \frac{1}{l^2} ([N_{v1}, N_{\theta1}, N_{v2}, N_{\theta2}]) \begin{Bmatrix} v_1 \\ v_2 \\ \theta_1 \\ \theta_2 \end{Bmatrix}$$

The curvature field $\kappa_{e,v,w}(x)$ is the product of the single row matrix $\mathbf{B}_v, \mathbf{B}_w$ and the vector \bar{w}, \bar{v} , the curvature squared can then be given by

$$\kappa_{e,w}^2(x) = (\mathbf{B}_w \bar{w})^2 = \bar{w}^T \mathbf{B}_w^T \cdot \mathbf{B}_w \bar{w}$$

$$\kappa_{e,v}^2(x) = (\mathbf{B}_v \bar{v})^2 = \bar{v}^T \mathbf{B}_v^T \cdot \mathbf{B}_v \bar{v}$$

A.3.2. Velocity

The velocity \dot{w}_e is given by the first time-derivative of the displacement field $w_e(x)$

$$\dot{w}_e(x, t) = \frac{\partial w_e}{\partial t} = \mathbf{N}_w \frac{\partial}{\partial t} (\bar{w}) = \mathbf{N}_w \dot{\bar{w}}$$

$$\dot{v}_e(x, t) = \frac{\partial v_e}{\partial t} = \mathbf{N}_v \frac{\partial}{\partial t} (\bar{v}) = \mathbf{N}_v \dot{\bar{v}}$$

$$\dot{w}_e(x, t) = [N_{w1}, N_{\varphi1}, N_{w2}, N_{\varphi2}] \begin{Bmatrix} \dot{w}_1 \\ \dot{w}_2 \\ \dot{\varphi}_1 \\ \dot{\varphi}_2 \end{Bmatrix}$$

$$v_e(x, t) = [N_{v1}, N_{\theta1}, N_{v2}, N_{\theta2}] \begin{Bmatrix} \dot{v}_1 \\ \dot{v}_2 \\ \dot{\theta}_1 \\ \dot{\theta}_2 \end{Bmatrix}$$

Similar to the squared curvature field the squared velocity is given by

$$\begin{aligned}\bar{w}_e^2(x) &= (\mathbf{N}_w \dot{\mathbf{w}})^2 = \dot{\mathbf{w}}^T \mathbf{N}_w^T \cdot \mathbf{N}_w \dot{\mathbf{w}} \\ \bar{v}_e^2(x) &= (\mathbf{N}_v \dot{\mathbf{v}})^2 = \dot{\mathbf{v}}^T \mathbf{N}_v^T \cdot \mathbf{N}_v \dot{\mathbf{v}}\end{aligned}$$

A.3.3. Mass and Stiffness Matrix

The Lagrangian is defined as the difference between the kinetic and potential energy of the system (or in this case the beam element)

$$\mathcal{L} = E_k - E_p$$

The Euler-Lagrange equation used to derive the equation of motion is given by

$$\frac{\partial}{\partial t} \left(\frac{\partial \mathcal{L}}{\partial \dot{q}} \right) - \frac{\partial \mathcal{L}}{\partial q} = Q$$

Here q denotes the degree of freedom under consideration, and Q the external load associated with said degree of freedom. In the current application to Euler-Bernoulli beams, the kinetic energy is only dependent on the velocity, and the potential energy only dependent on the curvature of the beam element (and no terms are dependent on the position). The Equation of Motion (EoM) is then given by the left hand side of the re-written Lagrangian:

$$\frac{\partial}{\partial t} \left(\frac{\partial E_k}{\partial \dot{w}_e} \right) - \frac{\partial^2}{\partial x^2} \left(\frac{\partial E_p}{\partial \kappa_e} \right) = EoM$$

The kinetic energy is given by the mass and velocity of the beam element

$$E_k = \int_0^l \frac{1}{2} \rho A \dot{w}_e^2 dx = \int_0^l \frac{1}{2} \rho A \dot{\mathbf{w}}^T \mathbf{N}^T \cdot \mathbf{N} \dot{\mathbf{w}} dx$$

$$E_k = \frac{1}{2} \dot{\mathbf{w}}^T \int_0^l \mathbf{N}^T \rho A \mathbf{N} dx \dot{\mathbf{w}}$$

$E_k = \frac{1}{2} \dot{\mathbf{w}}^T \mathbf{M} \dot{\mathbf{w}}$
$\mathbf{M} = \int_0^l \mathbf{N}^T \rho A \mathbf{N}$
$\mathbf{M} = \frac{\rho A l}{420} \begin{bmatrix} 156 & 22l & 54 & -13l \\ & 4l^2 & 13l & -3l^2 \\ & & 156 & -22l \\ \text{sym.} & & & 4l^2 \end{bmatrix}$

The potential energy is derived from the strain energy of a bending beam

$$E_{strain} = \int M d\kappa = \int EI\kappa d\kappa = \frac{1}{2}EI\kappa^2$$

$$E_p = \int_0^l \frac{1}{2}EI\kappa_e^2 dx = \int_0^l \frac{1}{2}EI\bar{w}^T \mathbf{B}^T \cdot \mathbf{B}\bar{w} dx$$

$$E_p = \frac{1}{2}\bar{w}^T \int_0^l \mathbf{B}^T EI \mathbf{B} dx \bar{w}$$

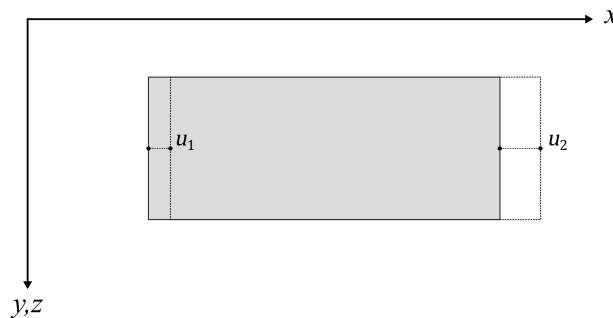
$$E_p = \frac{1}{2}\bar{w}^T \mathbf{K}\bar{w}$$

$$\mathbf{K} = \int_0^l \mathbf{B}^T EI \mathbf{B}$$

$$\mathbf{K} = \frac{EI}{l^3} \begin{bmatrix} 12 & 6l & -12 & 6l \\ & 4l^2 & -6l & 2l^2 \\ \text{sym.} & & 12 & -6l \\ & & & 4l^2 \end{bmatrix}$$

A.4 Axial Element

When considering an axial element, only the extension/compression is considered, resulting in two degrees of freedom u_1 and u_2 at each end of the axial element



The displacement field along the length of the element is again described using interpolation based on shape functions. For an axial element these are simple linear functions

$$N_{u1}(x) = 1 - \xi$$

$$N_{u2}(x) = \xi$$

With $\xi = \frac{x}{l}$

The displacement field can then be described as

$$u_e(x) = [N_{u1}, N_{u2}] \begin{Bmatrix} u_1 \\ u_2 \end{Bmatrix}$$

A.4.1. Velocity

The velocity \dot{u}_e is given by the first time-derivative of the displacement field $u_e(x)$

$$\dot{u}_e(x, t) = \frac{\partial u_e}{\partial t} = \mathbf{N} \frac{\partial}{\partial t} (\bar{u}) = \mathbf{N} \dot{\bar{u}}$$

$$\dot{u}_e(x, t) = [N_{u1}, N_{u2}] \begin{Bmatrix} \dot{u}_1 \\ \dot{u}_2 \end{Bmatrix}$$

A.4.2. Strain

The strain field of the beam element along its length is defined as the first co-ordinate derivative of the displacement field

$$\varepsilon_e(x) = \frac{\partial u_e}{\partial x} = \frac{\partial}{\partial x} (\mathbf{N}) \bar{u} = \mathbf{B} \bar{u}$$

$$\varepsilon_e(x) = \frac{\partial}{\partial x} ([N_{u1}, N_{u2}]) \begin{Bmatrix} u_1 \\ u_2 \end{Bmatrix}$$

$$\varepsilon_e(x) = \frac{\partial}{\partial \xi} \frac{1}{l} ([N_{u1}, N_{u2}]) \begin{Bmatrix} u_1 \\ u_2 \end{Bmatrix}$$

The strain field $\varepsilon_e(x)$ is the product of the single row matrix \mathbf{B} and the vector \bar{u} , the strain squared can then be given by

$$\varepsilon_e^2(x) = (\mathbf{B} \bar{u})^2 = \bar{u}^T \mathbf{B}^T \cdot \mathbf{B} \bar{u}$$

A.4.3. Mass and Stiffness Matrix

Similar to the bending element, the Lagrangian energy formulation can be used to obtain the mass and stiffness matrices. The kinetic energy is given by the mass and velocity of the beam element

$$E_k = \int_0^l \frac{1}{2} \rho A \dot{u}_e^2 dx = \int_0^l \frac{1}{2} \rho A \dot{\bar{u}}^T \mathbf{N}^T \cdot \mathbf{N} \dot{\bar{u}} dx$$

$$E_k = \frac{1}{2} \dot{\bar{u}}^T \int_0^l \mathbf{N}^T \rho A \mathbf{N} dx \dot{\bar{u}}$$

$$E_k = \frac{1}{2} \dot{\mathbf{u}}^T \mathbf{M} \dot{\mathbf{u}}$$

$$\mathbf{M} = \int_0^l \mathbf{N}^T \rho A \mathbf{N}$$

$$\mathbf{M} = \frac{\rho A l}{6} \begin{bmatrix} 2 & 1 \\ 1 & 2 \end{bmatrix}$$

The potential energy is derived from the strain energy of an axially loaded member

$$E_{strain} = \int F_N d\varepsilon = \int EA\varepsilon d\kappa = \frac{1}{2} EI \varepsilon^2$$

$$E_p = \int_0^l \frac{1}{2} EA \varepsilon_e^2 dx = \int_0^l \frac{1}{2} EA \bar{\mathbf{w}}^T \mathbf{B}^T \cdot \mathbf{B} \bar{\mathbf{w}} dx$$

$$E_p = \frac{1}{2} \bar{\mathbf{w}}^T \int_0^l \mathbf{B}^T EA \mathbf{B} dx \bar{\mathbf{w}}$$

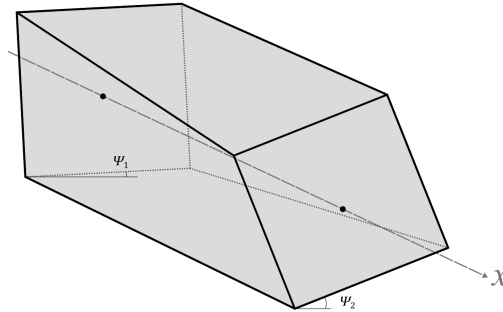
$$E_p = \frac{1}{2} \bar{\mathbf{w}}^T \mathbf{K} \bar{\mathbf{w}}$$

$$\mathbf{K} = \int_0^l \mathbf{B}^T EA \mathbf{B}$$

$$\mathbf{K} = \frac{EA}{l} \begin{bmatrix} 1 & -1 \\ -1 & 1 \end{bmatrix}$$

A.5 Torsional Element

When considering a torsional element, only the rotation around its own axis is considered, resulting in two degrees of freedom ψ_1 and ψ_2 at each end of the axial element.



The displacement field along the length of the element is described using interpolation based on shape functions. For a torsional element these are simple linear functions

$$N_{\psi_1}(x) = 1 - \xi$$

$$N_{\psi_2}(x) = \xi$$

With $\xi = \frac{x}{l}$

The displacement field can then be described as

$$\psi_e(x) = [N_{\psi_1}, N_{\psi_2}] \begin{Bmatrix} \psi_1 \\ \psi_2 \end{Bmatrix}$$

A.5.1. Velocity

The angular velocity of the element is given by the first time-derivative of the rotation field $\psi_e(x)$

$$\dot{\psi}_e(x, t) = \frac{\partial \psi_e}{\partial t} = \mathbf{N} \frac{\partial}{\partial t} (\bar{\psi}) = \mathbf{N} \dot{\bar{\psi}}$$

$$\dot{\psi}_e(x, t) = [N_{\psi_1}, N_{\psi_2}] \begin{Bmatrix} \dot{\psi}_1 \\ \dot{\psi}_2 \end{Bmatrix}$$

A.5.2. First Order Derivative

$$(\mathbf{B}\bar{\psi})^2 = \bar{\psi}^T \mathbf{B}^T \cdot \mathbf{B}\bar{\psi}$$

A.5.3. Mass and Stiffness Matrix

The kinetic energy is given by the rotational inertia (polar moment of inertia) I_0 and angular velocity $\dot{\psi}_e$ of the beam element

$$E_k = \int_0^l \frac{1}{2} \rho I_0 \dot{\psi}_e^2 dx = \int_0^l \frac{1}{2} \rho I_0 \dot{\bar{\psi}}^T \mathbf{N}^T \cdot \mathbf{N} \dot{\bar{\psi}} dx$$

$$E_k = \frac{1}{2} \dot{\psi}^T \int_0^l \mathbf{N}^T \rho I_0 \mathbf{N} dx \dot{\psi}$$

$$E_k = \frac{1}{2} \dot{\psi}^T \mathbf{M} \dot{\psi}$$

$$\mathbf{M} = \int_0^l \mathbf{N}^T \rho I_0 \mathbf{N} dx$$

$$\mathbf{M} = \frac{\rho I_0 l}{6} \begin{bmatrix} 2 & 1 \\ 1 & 2 \end{bmatrix} = \frac{\rho A l}{6} r_g^2 \begin{bmatrix} 2 & 1 \\ 1 & 2 \end{bmatrix}$$

Where

r_g = radius of gyration ($\sqrt{I_0/A}$)

The potential energy is derived from the strain energy of a bending beam

$$E_{strain} = \int T d\psi = \int G I_t \psi dx = \frac{1}{2} G I_t \psi_e^2$$

$$E_p = \int_0^l \frac{1}{2} G I_t \psi_e^2 dx = \int_0^l \frac{1}{2} G I_t \bar{\psi}^T \mathbf{B}^T \cdot \mathbf{B} \bar{\psi} dx$$

$$E_p = \frac{1}{2} \bar{\phi}^T \int_0^l \mathbf{B}^T G I_t \mathbf{B} dx \bar{\phi}$$

$$E_p = \frac{1}{2} \bar{\phi}^T \mathbf{K} \bar{\phi}$$

$$\mathbf{K} = \int_0^l \mathbf{B}^T G I_t \mathbf{B} dx$$

$$\mathbf{K} = \frac{G I_t}{l} \begin{bmatrix} 1 & -1 \\ -1 & 1 \end{bmatrix}$$

A.6 Summary Individual Matrices and Vectors

Bending Elements (around y and z axis)

$$\mathbf{M}_y = \frac{\rho A l}{420} \begin{bmatrix} 156 & -22l & 54 & 13l \\ & 4l^2 & -13l & -3l^2 \\ \text{sym.} & & 156 & 22l \\ & & & 4l^2 \end{bmatrix}$$

$$\mathbf{K}_y = \frac{EI}{l^3} \begin{bmatrix} 12 & -6l & -12 & -6l \\ & 4l^2 & 6l & 2l^2 \\ \text{sym.} & & 12 & 6l \\ & & & 4l^2 \end{bmatrix} \begin{Bmatrix} w_1 \\ \varphi_1 \\ w_2 \\ \varphi_2 \end{Bmatrix}$$

$$\mathbf{M}_z = \frac{\rho A l}{420} \begin{bmatrix} 156 & 22l & 54 & -13l \\ & 4l^2 & 13l & -3l^2 \\ \text{sym.} & & 156 & -22l \\ & & & 4l^2 \end{bmatrix}$$

$$\mathbf{K}_z = \frac{EI}{l^3} \begin{bmatrix} 12 & 6l & -12 & 6l \\ & 4l^2 & -6l & 2l^2 \\ \text{sym.} & & 12 & -6l \\ & & & 4l^2 \end{bmatrix} \begin{Bmatrix} v_1 \\ \theta_1 \\ v_2 \\ \theta_2 \end{Bmatrix}$$

Axial Elements

$$\mathbf{M}_a = \frac{\rho A l}{6} \begin{bmatrix} 2 & 1 \\ 1 & 2 \end{bmatrix}$$

$$\mathbf{K}_a = \frac{EA}{l} \begin{bmatrix} 1 & -1 \\ -1 & 1 \end{bmatrix} \begin{Bmatrix} u_1 \\ u_2 \end{Bmatrix}$$

Torsion Elements

$$\mathbf{M}_T = \frac{\rho A l}{6} r_g^2 \begin{bmatrix} 2 & 1 \\ 1 & 2 \end{bmatrix}$$

$$\mathbf{K}_T = \frac{GI_t}{l} \begin{bmatrix} 1 & -1 \\ -1 & 1 \end{bmatrix} \begin{Bmatrix} \psi_1 \\ \psi_2 \end{Bmatrix}$$

A.7 Total System Element Matrices and Vectors

Assembling the various elements allows the total element mass and stiffness matrices to be created

$$K_{el} = \begin{bmatrix} \frac{EA}{l} & 0 & 0 & 0 & 0 & 0 & -\frac{EA}{l} & 0 & 0 & 0 & 0 & 0 \\ 0 & \frac{12EI}{l^3} & 0 & 0 & 0 & \frac{6EI}{l^2} & 0 & -\frac{12EI}{l^3} & 0 & 0 & 0 & \frac{6EI}{l^2} \\ 0 & 0 & \frac{12EI}{l^3} & 0 & -\frac{6EI}{l^2} & 0 & 0 & 0 & -\frac{12EI}{l^3} & 0 & -\frac{6EI}{l^2} & 0 \\ 0 & 0 & 0 & \frac{GI_t}{l} & 0 & 0 & 0 & 0 & 0 & -\frac{GI_t}{l} & 0 & 0 \\ 0 & 0 & 0 & 0 & \frac{4EI}{l} & 0 & 0 & \frac{6EI}{l^2} & 0 & \frac{2EI}{l} & 0 & 0 \\ 0 & 0 & 0 & 0 & 0 & \frac{4EI}{l} & 0 & -\frac{6EI}{l^2} & 0 & 0 & 0 & \frac{2EI}{l} \\ 0 & 0 & 0 & 0 & 0 & 0 & \frac{EA}{l} & 0 & 0 & 0 & 0 & 0 \\ 0 & 0 & 0 & 0 & 0 & 0 & 0 & \frac{12EI}{l^3} & 0 & 0 & 0 & -\frac{6EI}{l^2} \\ 0 & 0 & 0 & 0 & 0 & 0 & 0 & 0 & \frac{12EI}{l^3} & 0 & \frac{6EI}{l^2} & 0 \\ 0 & 0 & 0 & 0 & 0 & 0 & 0 & 0 & 0 & \frac{GI_t}{l} & 0 & 0 \\ 0 & 0 & 0 & 0 & 0 & 0 & 0 & 0 & 0 & 0 & \frac{4EI}{l} & 0 \\ 0 & 0 & 0 & 0 & 0 & 0 & 0 & 0 & 0 & 0 & 0 & \frac{4EI}{l} \end{bmatrix} \quad \bar{u}_{el} = \begin{Bmatrix} u_1 \\ v_1 \\ w_1 \\ \psi_1 \\ \varphi_1 \\ \theta_1 \\ u_2 \\ v_2 \\ w_2 \\ \psi_2 \\ \varphi_2 \\ \theta_2 \end{Bmatrix}$$

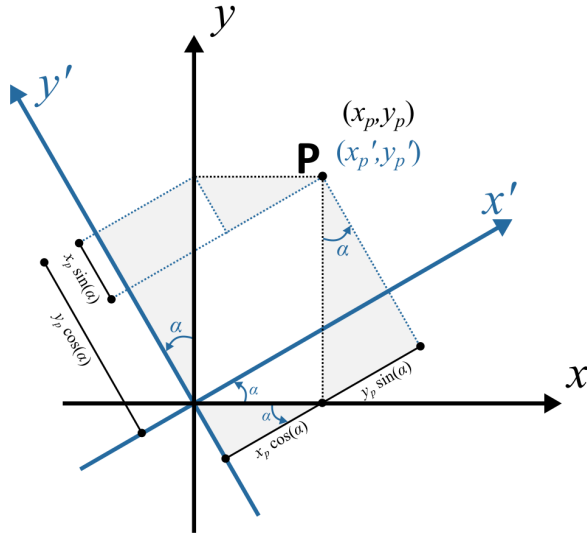
sym.

$$M_{el} = \rho Al \begin{bmatrix} \frac{1}{3} & 0 & 0 & 0 & 0 & 0 & \frac{1}{6} & 0 & 0 & 0 & 0 & 0 \\ 0 & \frac{156}{420} & 0 & 0 & 0 & \frac{22l}{420} & 0 & \frac{54}{420} & 0 & 0 & 0 & -\frac{13l}{420} \\ 0 & 0 & \frac{156}{420} & 0 & -\frac{22l}{420} & 0 & 0 & 0 & \frac{54}{420} & 0 & \frac{13l}{420} & 0 \\ 0 & 0 & 0 & \frac{r_g^2}{3} & 0 & 0 & 0 & 0 & 0 & \frac{r_g^2}{6} & 0 & 0 \\ 0 & 0 & 0 & 0 & \frac{4l^2}{420} & 0 & 0 & 0 & -\frac{13l}{420} & 0 & -\frac{3l^2}{420} & 0 \\ 0 & 0 & 0 & 0 & 0 & \frac{4l^2}{420} & 0 & \frac{13l}{420} & 0 & 0 & 0 & -\frac{3l^2}{420} \\ 0 & 0 & 0 & 0 & 0 & 0 & \frac{1}{3} & 0 & 0 & 0 & 0 & 0 \\ 0 & 0 & 0 & 0 & 0 & 0 & 0 & \frac{156}{420} & 0 & 0 & 0 & -\frac{22l}{420} \\ 0 & 0 & 0 & 0 & 0 & 0 & 0 & 0 & \frac{156}{420} & 0 & \frac{22l}{420} & 0 \\ 0 & 0 & 0 & 0 & 0 & 0 & 0 & 0 & 0 & \frac{r_g^2}{3} & 0 & 0 \\ 0 & 0 & 0 & 0 & 0 & 0 & 0 & 0 & 0 & 0 & \frac{4l^2}{420} & 0 \\ 0 & 0 & 0 & 0 & 0 & 0 & 0 & 0 & 0 & 0 & 0 & \frac{4l^2}{420} \end{bmatrix} \quad \bar{f}_{el} = \begin{Bmatrix} F_{x1} \\ F_{y1} \\ F_{z1} \\ T_1 \\ M_{y1} \\ M_{z1} \\ F_{x2} \\ F_{y2} \\ F_{z2} \\ T_2 \\ M_{y2} \\ M_{z2} \end{Bmatrix}$$

sym.

A.8 Local & Global Coordinates

Given a local set of axes x' and y' which is rotated by an angle α relative to the global set of axes x and y , an arbitrary point P can be described in both global coordinate systems by (x_p, y_p) and in the local system by (x'_p, y'_p) . The relationship between these two coordinate systems can be found according to figure below.



According to this figure, the mathematical relationship between the two coordinate systems is given by

$$\begin{aligned} x'_p &= x_p \cos \alpha + y_p \sin \alpha \\ y'_p &= -x_p \sin \alpha + y_p \cos \alpha \end{aligned}$$

$$\begin{bmatrix} x'_p \\ y'_p \end{bmatrix} = \begin{bmatrix} \cos \alpha & \sin \alpha \\ -\sin \alpha & \cos \alpha \end{bmatrix} \begin{bmatrix} x_p \\ y_p \end{bmatrix}$$

$$\bar{x}' = R \bar{x}$$

For the nodal degrees of freedom the applied transformation is as follows.

$$\bar{u}' = R \bar{u} \quad \leftrightarrow \quad \bar{u} = R^T \bar{u}'$$

For the force terms used to describe the equation of motion of the element the transformation is given by

$$\bar{F}' = R \bar{F} \quad \leftrightarrow \quad \bar{F} = R^T \bar{F}'$$

$$\bar{F}' = K \bar{u}' = K R \bar{u}$$

$$\bar{F} = R^T \bar{F}' = R^T K R \bar{u}$$

The equation of motion is then given by

$$R^T M R \ddot{\bar{u}} + R^T K R \bar{u} = F$$

According to the right-hand-rule a rotation vector is given in the direction perpendicular to the plane of rotation. This entails that a rotation around a given axis can be described by a vector in the same direction as said axis.

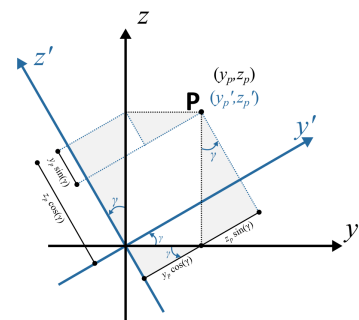
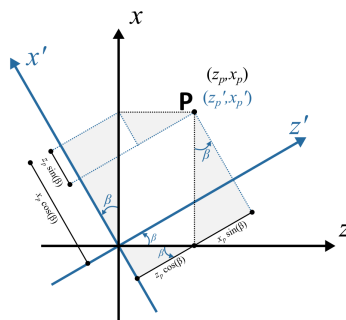
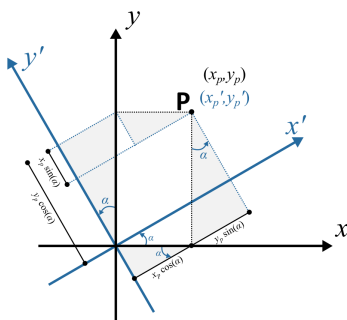
θ_{yz}	rotation in yz -plane, around x -axis	described by vector in x -direction
θ_{zx}	rotation in zx -plane, around y -axis	described by vector in y -direction
θ_{xy}	rotation in xy -plane around z -axis	described by vector in z -direction

A rotation φ in the xy -plane can therefore be described as a vector in the z -direction. This vector's direction will remain unchanged when applying a rotation α in the xy -plane, meaning the rotational degree of freedom φ is unaffected by a coordinate system rotation α .

$$R = \begin{bmatrix} \cos \alpha & \sin \alpha & 0 & 0 & 0 & 0 \\ -\sin \alpha & \cos \alpha & 0 & 0 & 0 & 0 \\ 0 & 0 & 1 & 0 & 0 & 0 \\ 0 & 0 & 0 & \cos \alpha & \sin \alpha & 0 \\ 0 & 0 & 0 & -\sin \alpha & \cos \alpha & 0 \\ 0 & 0 & 0 & 0 & 0 & 1 \end{bmatrix}, \quad \vec{u} = \begin{Bmatrix} u_1 \\ w_1 \\ \varphi_1 \\ u_2 \\ w_2 \\ \varphi_2 \end{Bmatrix}$$

This transformation can be extended from 2D deformations to 3D deformations including all 6 degrees of freedom described in section A.2. Three possible rotational transformations of the coordinate system can be identified.

α	rotation around the global z -axis	from x to y axis
β	rotation around the global y -axis	from z to x axis
γ	rotation around the global x -axis	from y to z axis



$$R_\alpha = \begin{bmatrix} \cos \alpha & \sin \alpha & 0 & 0 & 0 & 0 \\ -\sin \alpha & \cos \alpha & 0 & 0 & 0 & 0 \\ 0 & 0 & 1 & 0 & 0 & 0 \\ 0 & 0 & 0 & \cos \alpha & \sin \alpha & 0 \\ 0 & 0 & 0 & -\sin \alpha & \cos \alpha & 0 \\ 0 & 0 & 0 & 0 & 0 & 1 \end{bmatrix}, \quad \vec{u} = \begin{Bmatrix} x \\ y \\ z \\ \theta_{yz} \\ \theta_{zx} \\ \theta_{xy} \end{Bmatrix}$$

$$\mathbf{R}_\beta = \begin{bmatrix} \cos \beta & 0 & -\sin \beta & 0 & 0 & 0 \\ 0 & 1 & 0 & 0 & 0 & 0 \\ \sin \beta & 0 & \cos \beta & 0 & 0 & 0 \\ 0 & 0 & 0 & \cos \beta & 0 & -\sin \beta \\ 0 & 0 & 0 & 0 & 1 & 0 \\ 0 & 0 & 0 & \sin \beta & 0 & \cos \beta \end{bmatrix}, \quad \bar{\mathbf{u}} = \begin{Bmatrix} x \\ y \\ z \\ \theta_{yz} \\ \theta_{zx} \\ \theta_{xy} \end{Bmatrix}$$

$$\mathbf{R}_\gamma = \begin{bmatrix} 1 & 0 & 0 & 0 & 0 & 0 \\ 0 & \cos \gamma & \sin \gamma & 0 & 0 & 0 \\ 0 & -\sin \gamma & \cos \gamma & 0 & 0 & 0 \\ 0 & 0 & 0 & 1 & 0 & 0 \\ 0 & 0 & 0 & 0 & \cos \gamma & \sin \gamma \\ 0 & 0 & 0 & 0 & -\sin \gamma & \cos \gamma \end{bmatrix}, \quad \bar{\mathbf{u}} = \begin{Bmatrix} x \\ y \\ z \\ \theta_{yz} \\ \theta_{zx} \\ \theta_{xy} \end{Bmatrix}$$

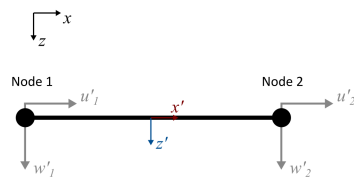
For a single node the translational matrix is given by

$$\mathbf{R} = \mathbf{R}_\alpha \cdot \mathbf{R}_\beta \cdot \mathbf{R}_\gamma$$

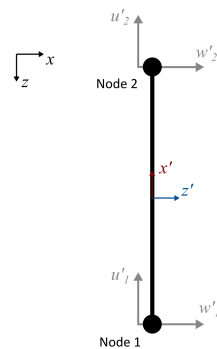
$$\mathbf{R} := \begin{bmatrix} \cos(\alpha) \cos(\beta) & \sin(\alpha) \cos(\gamma) + \cos(\alpha) \sin(\beta) \sin(\gamma) & \sin(\alpha) \sin(\gamma) - \cos(\alpha) \sin(\beta) \cos(\gamma) & 0 & 0 & 0 \\ -\sin(\alpha) \cos(\beta) & \cos(\alpha) \cos(\gamma) - \sin(\alpha) \sin(\beta) \sin(\gamma) & \cos(\alpha) \sin(\gamma) + \sin(\alpha) \sin(\beta) \cos(\gamma) & 0 & 0 & 0 \\ \sin(\beta) & -\cos(\beta) \sin(\gamma) & \cos(\beta) \cos(\gamma) & 0 & 0 & 0 \\ 0 & 0 & 0 & \cos(\alpha) \cos(\beta) & \sin(\alpha) \cos(\gamma) + \cos(\alpha) \sin(\beta) \sin(\gamma) & \sin(\alpha) \sin(\gamma) - \cos(\alpha) \sin(\beta) \cos(\gamma) \\ 0 & 0 & 0 & -\sin(\alpha) \cos(\beta) & \cos(\alpha) \cos(\gamma) - \sin(\alpha) \sin(\beta) \sin(\gamma) & \cos(\alpha) \sin(\gamma) + \sin(\alpha) \sin(\beta) \cos(\gamma) \\ 0 & 0 & 0 & \sin(\beta) & -\cos(\beta) \sin(\gamma) & \cos(\beta) \cos(\gamma) \end{bmatrix}$$

The portal frame in question can be split up into two portions: the beam at the top, and the two columns supporting said beam. Both sections are composed of beam elements, which can be defined in their local coordinate systems.

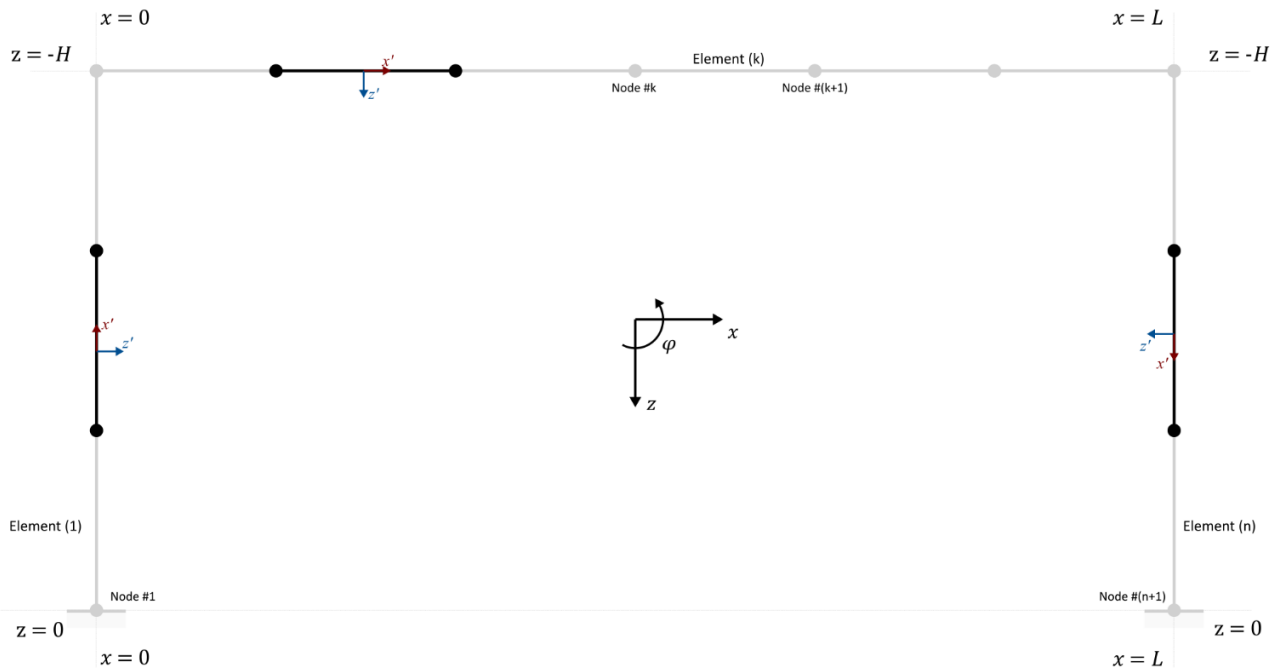
Beam Coordinate System



Column Coordinate System



The local coordinates of the beam section coincide with the global coordinate system of the portal. The local coordinate system of the columns however is perpendicular to the global coordinate system. The columns located at $x = 0$ have a local coordinate system which is rotated by $\beta = 90^\circ$ or $\beta = \frac{\pi}{2}$ rad with respect to the global coordinate system. Similarly the columns located at $x = L$ have a local coordinate system which is rotated by $\beta = -90^\circ$ or $\beta = -\frac{\pi}{2}$ rad

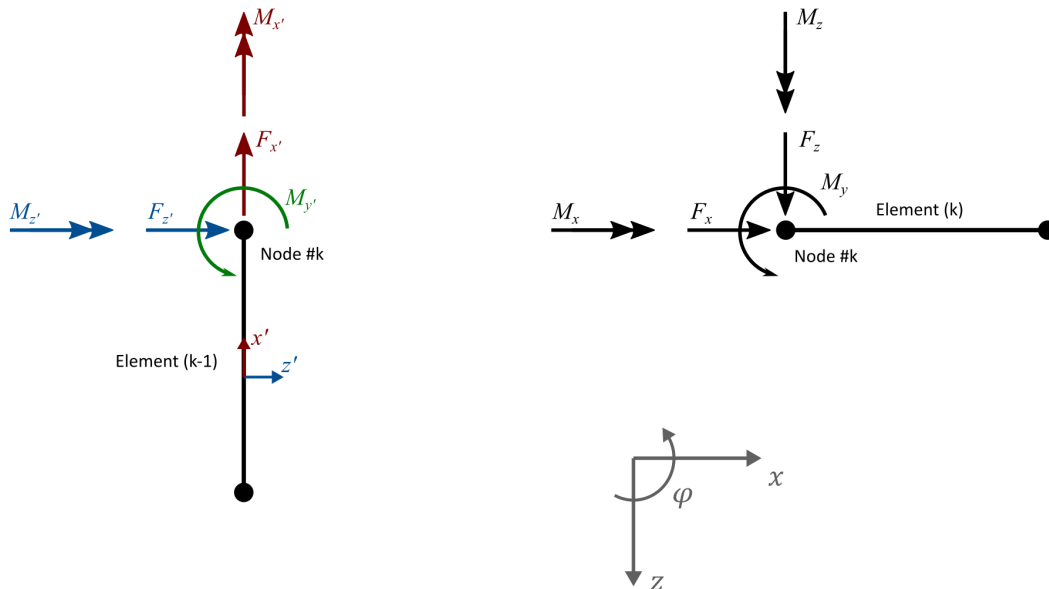


As a result the transformation matrix for nodes in the left ($x = 0$) and right ($x = L$) column are given by

$$R_{\text{left}} = R_{\alpha=0} \cdot R_{\beta=\frac{\pi}{2}} \cdot R_{\gamma=0} = \begin{bmatrix} 0 & 0 & -1 & 0 & 0 & 0 \\ 0 & 1 & 0 & 0 & 0 & 0 \\ 1 & 0 & 0 & 0 & 0 & 0 \\ 0 & 0 & 0 & 0 & 0 & -1 \\ 0 & 0 & 0 & 0 & 1 & 0 \\ 0 & 0 & 0 & 1 & 0 & 0 \end{bmatrix}, \quad \bar{u} = \begin{Bmatrix} u \\ v \\ w \\ \phi \\ \theta \end{Bmatrix}$$

$$R_{\text{right}} = R_{\alpha=0} \cdot R_{\beta=-\frac{\pi}{2}} \cdot R_{\gamma=0} = \begin{bmatrix} 0 & 0 & 1 & 0 & 0 & 0 \\ 0 & 1 & 0 & 0 & 0 & 0 \\ -1 & 0 & 0 & 0 & 0 & 0 \\ 0 & 0 & 0 & 0 & 0 & 1 \\ 0 & 0 & 0 & 0 & 1 & 0 \\ 0 & 0 & 0 & -1 & 0 & 0 \end{bmatrix}, \quad \bar{u} = \begin{Bmatrix} u \\ v \\ w \\ \phi \\ \theta \end{Bmatrix}$$

To verify the rotational transformation matrices the top left corner node ($x = 0, z = -H$) is analyzed. The figure below shows all the possible loads on the node (safe for the concentrated load in the y -direction). The loads can either be described in the local coordinate system of the column element (k-1) or in the global coordinate system (which coincides with the local coordinate system of the beam element (k)).



$$\bar{F}' = \mathbf{R}\bar{F}$$

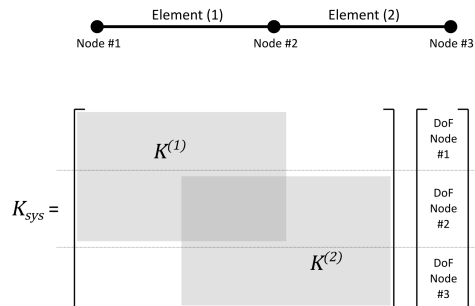
$$\begin{Bmatrix} F_{x'} \\ F_{y'} \\ F_{z'} \\ M_{x'} \\ M_{y'} \\ M_{z'} \end{Bmatrix} = \begin{bmatrix} 0 & 0 & -1 & 0 & 0 & 0 \\ 0 & 1 & 0 & 0 & 0 & 0 \\ 1 & 0 & 0 & 0 & 0 & 0 \\ 0 & 0 & 0 & 0 & 0 & -1 \\ 0 & 0 & 0 & 0 & 1 & 0 \\ 0 & 0 & 0 & 1 & 0 & 0 \end{bmatrix} \begin{Bmatrix} F_x \\ F_y \\ F_z \\ M_x \\ M_y \\ M_z \end{Bmatrix}$$

The transformation matrix implies (as expected) that:

Column axial extension	$F_{x'}$	=	Beam shear force	$-F_z$
Column shear force	$F_{y'}$	=	Beam shear force	F_y
Column shear force	$F_{z'}$	=	Beam axial force	F_x
Column torsion moment	$M_{x'}$	=	Beam bending moment	$-M_z$
Column bending moment	$M_{y'}$	=	Beam bending moment	M_y
Column bending moment	$M_{z'}$	=	Beam torsion moment	M_x

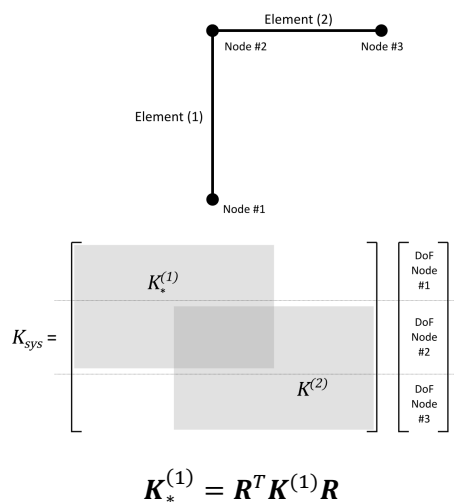
A.9 Building the System Matrices

For a system consisting of multiple elements the total stiffness matrix is composed by superimposing the individual stiffness matrices at the relevant location. For a system comprised of nodes with only one degree of freedom, the super position of two arbitrary elements (1) and (2) is given by:



$$K^{(1)+(2)} \bar{u}^{(1)+(2)} = \begin{bmatrix} k_{11}^{(1)} & k_{12}^{(1)} & 0 \\ k_{21}^{(1)} & k_{22}^{(1)} + k_{11}^{(2)} & k_{12}^{(2)} \\ 0 & k_{21}^{(2)} & k_{22}^{(2)} \end{bmatrix} \begin{Bmatrix} u_1 \\ u_2 \\ u_3 \end{Bmatrix}$$

Beam element (1) and (2) both share node 2, which is why the superimposing occurs at the matrix elements corresponding to the degrees of freedom associated with node 2. In case of a column element connected to a beam element the stiffness matrix of the column element needs to have the rotational transformation matrix applied to it.



$$\mathbf{K}^{(1)+(2)}\bar{\mathbf{u}}^{(1)+(2)} = \begin{bmatrix} k_{*11}^{(1)} & k_{*12}^{(1)} & 0 \\ k_{*21}^{(1)} & k_{*22}^{(1)} + k_{11}^{(2)} & k_{12}^{(2)} \\ 0 & k_{21}^{(2)} & k_{22}^{(2)} \end{bmatrix} \begin{Bmatrix} u_1 \\ u_2 \\ u_3 \end{Bmatrix}$$

In this case the rotational transformation matrix R is the matrix corresponding to the entire element (not just a single node) and is given by

$$R = \begin{bmatrix} R_{11} & R_{12} \\ R_{21} & R_{22} \end{bmatrix}$$

Where

$$\begin{aligned} R_{11}, R_{22} &= \text{node rotational transformation matrix } R_{\text{left}} \text{ or } R_{\text{right}} \\ R_{21}, R_{12} &= \text{empty (zero) matrix} \end{aligned}$$

The system can then be described by the following (matrix) equation of motion

$$\mathbf{M}_{\text{sys}}\ddot{\bar{\mathbf{u}}} + \mathbf{K}_{\text{sys}}\bar{\mathbf{u}} = \bar{\mathbf{F}}$$

A.10 Boundary Conditions

The mass and stiffness matrix determined thus-far are for elements where the displacement and rotation are unknown (those at the center of the beam). At the boundary conditions certain degrees of freedom are constrained, the rows and columns associated with the restricted degrees of freedom can be eliminated from the matrix.

Pinned

For a pinned support the displacement w_L or w_R is constrained

Left-hand-side of element is supported

$$Kw = \frac{EI}{l^3} \begin{bmatrix} 12 & 6l & -12 & 6l \\ & 4l^2 & -6l & 2l^2 \\ \text{sym.} & & 12 & -6l \\ & & & 4l^2 \end{bmatrix} \begin{Bmatrix} w_L \\ \varphi_L \\ w_R \\ \varphi_R \end{Bmatrix}$$

$$Kw = \frac{EI}{l^3} \begin{bmatrix} 4l^2 & -6l & 2l^2 \\ \text{sym.} & 12 & -6l \\ & & 4l^2 \end{bmatrix} \begin{Bmatrix} \varphi_L \\ w_R \\ \varphi_R \end{Bmatrix}$$

$$M\ddot{w} = \frac{\rho Al}{420} \begin{bmatrix} 156 & 22l & 54 & -13l \\ & 4l^2 & 13l & -3l^2 \\ \text{sym.} & & 156 & -22l \\ & & & 4l^2 \end{bmatrix} \begin{Bmatrix} \ddot{w}_L \\ \ddot{\varphi}_L \\ \ddot{w}_R \\ \ddot{\varphi}_R \end{Bmatrix}$$

Right-hand-side of element is supported

$$Kw = \frac{EI}{l^3} \begin{bmatrix} 12 & 6l & -12 & 6l \\ & 4l^2 & -6l & 2l^2 \\ \text{sym.} & & 12 & -6l \\ & & & 4l^2 \end{bmatrix} \begin{Bmatrix} w_L \\ \varphi_L \\ w_R \\ \varphi_R \end{Bmatrix}$$

$$Kw = \frac{EI}{l^3} \begin{bmatrix} 12 & 6l & 6l \\ \text{sym.} & 4l^2 & 2l^2 \\ & & 4l^2 \end{bmatrix} \begin{Bmatrix} w_L \\ \varphi_L \\ \varphi_R \end{Bmatrix}$$

$$M\ddot{w} = \frac{\rho Al}{420} \begin{bmatrix} 156 & 22l & 54 & -13l \\ & 4l^2 & 13l & -3l^2 \\ \text{sym.} & & 156 & -22l \\ & & & 4l^2 \end{bmatrix} \begin{Bmatrix} \ddot{w}_L \\ \ddot{\varphi}_L \\ \ddot{w}_R \\ \ddot{\varphi}_R \end{Bmatrix}$$

$$M\ddot{w} = \frac{\rho Al}{420} \begin{bmatrix} 4l^2 & 13l & -3l^2 \\ \text{sym.} & 156 & -22l \\ & & 4l^2 \end{bmatrix} \begin{Bmatrix} \ddot{\varphi}_L \\ \ddot{w}_R \\ \ddot{\varphi}_R \end{Bmatrix}$$

$$M\ddot{w} = \frac{\rho Al}{420} \begin{bmatrix} 156 & 22l & -13l \\ \text{sym.} & 4l^2 & -3l^2 \\ & & 4l^2 \end{bmatrix} \begin{Bmatrix} \ddot{w}_L \\ \ddot{\varphi}_L \\ \ddot{\varphi}_R \end{Bmatrix}$$

Fixed

For a fixed (clamped) support the displacement w_L or w_R and rotation φ_L or φ_R are constrained

Left-hand-side of element is supported

Right-hand-side of element is supported

$$Kw = \frac{EI}{l^3} \begin{bmatrix} 12 & -6l \\ -6l & 4l^2 \end{bmatrix} \begin{Bmatrix} w_R \\ \varphi_R \end{Bmatrix}$$

$$M\ddot{w} = \frac{\rho Al}{420} \begin{bmatrix} 156 & -22l \\ -22l & 4l^2 \end{bmatrix} \begin{Bmatrix} w_R \\ \varphi_R \end{Bmatrix}$$

$$Kw = \frac{EI}{l^3} \begin{bmatrix} 12 & 6l \\ 6l & 4l^2 \end{bmatrix} \begin{Bmatrix} w_L \\ \varphi_L \end{Bmatrix}$$

$$M\ddot{w} = \frac{\rho Al}{420} \begin{bmatrix} 156 & 22l \\ 22l & 4l^2 \end{bmatrix} \begin{Bmatrix} w_L \\ \varphi_L \end{Bmatrix}$$

A.11 Eigenfrequency and Eigenmatrix

The solution to this n degree of freedom system is assumed to be a time dependent sinusoidal function multiplied by an amplitude vector (eigenvector).

$$\bar{w} = \sum_k^n \hat{w}_k \cdot A_k e^{i\omega_k t} = \sum_k^n \bar{W}_k e^{i\omega_k t} = \sum_k^n \hat{w}_k \cdot u_k(t)$$
$$\bar{w} = [\hat{w}_1 \quad \hat{w}_2 \quad \dots \quad \hat{w}_n] \begin{Bmatrix} h_1 \\ h_2 \\ \vdots \\ h_n \end{Bmatrix} = E \bar{u}$$

Each degree of freedom will have its own Eigenmode represented by an eigenfrequency ω_k and an eigenvector \hat{w}_k .

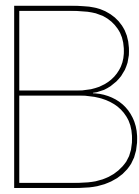
$$\Omega^2 = \begin{bmatrix} \omega_1 & & 0 \\ & \ddots & \\ 0 & & \omega_n \end{bmatrix}, \quad E = [\hat{w}_1 \quad \dots \quad \hat{w}_n]$$

The Eigenfrequencies can be determined by inserting the assumed solution into the equation of motion

$$(-\omega_k^2 \mathbf{M} + \mathbf{K}) \bar{w} = 0$$

$$\mathbf{K} \bar{w} = \omega_k^2 \mathbf{M} \bar{w}$$

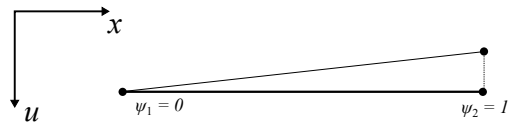
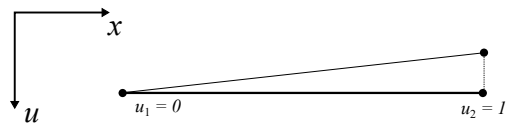
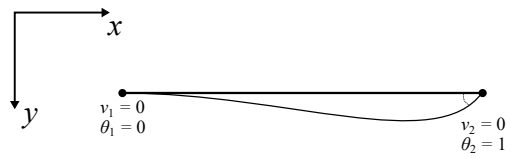
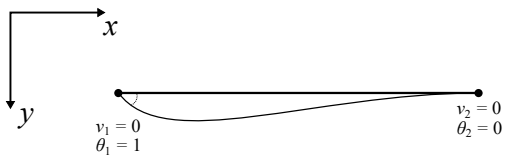
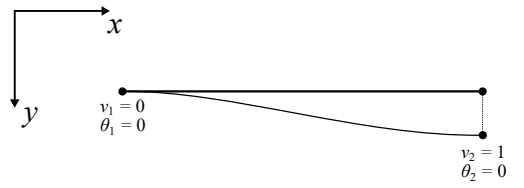
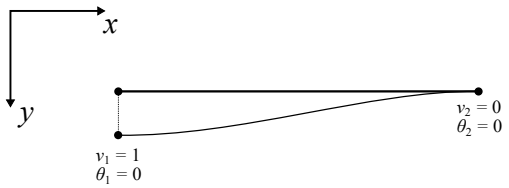
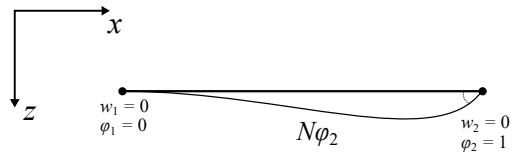
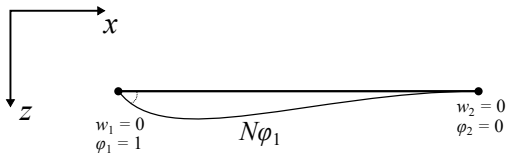
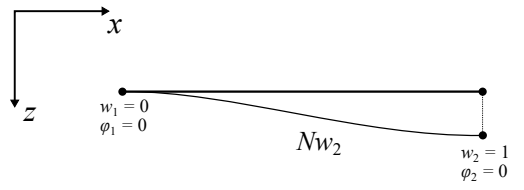
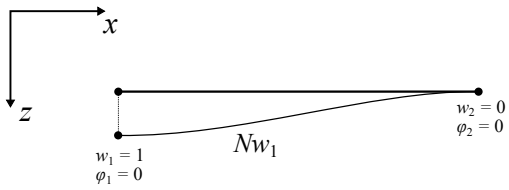
This is known as the generalized eigenvalue problem. The third party python package SciPy is able to solve this using the function `eig()` which returns the eigenfunction and the (right) eigenvectors.

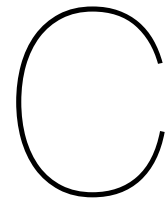


Shape Functions

In this appendix an overview of the relevant shape functions is given.

Shape Functions





Analytical Eigenfrequencies

In this appendix a short report outlining the derivation of analytical eigenfrequencies of a clamped-clamped beam.

Analytical Eigenfrequencies

Notation

Time derivative

$$\dot{u} = \frac{du}{dt}, \quad \ddot{u} = \frac{d^2u}{dt^2}$$

Coordinate derivative

$$u_x = \frac{du}{dx}, \quad u_{xx} = \frac{d^2u}{dx^2}$$

or

$$u' = \frac{du}{dx}, \quad u'' = \frac{d^2u}{dx^2}$$

Homogeneous Solution

The equation of motion for a standard Euler-Bernoulli beam can be derived based on equilibrium of a small section of the beam. The final equation for free vibrations ends up being

$$\rho A \ddot{w} + EI w_{xxxx} = 0$$

The general solution to the displacement field (varying over time) is assumed to be in the form of

$$w(x, t) = W(x) \cdot e^{i\omega t}$$

Substituting this into the equation of motion yields

$$-\omega^2 \rho A W + EI W'''' = 0$$

$$W''''(x) - \omega^2 \frac{\rho A}{EI} W(x) = 0$$

Based on this linear differential equation the amplitude function $W(x)$ has the assumed general solution in the form of

$$W(x) = \sum_k C_k e^{i\lambda_k x}$$

Substituting this back into the differential equation describing $W(x)$ results in

$$\lambda_k^4 - \omega^2 \frac{\rho A}{EI} = 0$$

$$\lambda_k^4 - \beta^4 = 0, \quad \text{where } \beta^4 = \omega^2 \frac{\rho A}{EI}$$

The solution for the spatial frequency λ is then

$$\lambda_{1,2} = \pm\beta, \quad \lambda_{3,4} = \pm i\beta$$

The complex form of the amplitude function can then be written as

$$W(x) = C_1 e^{\beta x} + C_2 e^{-\beta x} + C_3 e^{i\beta x} + C_4 e^{-i\beta x}$$

The real form can be expressed as

$$C_1 e^{\beta x} + C_2 e^{-\beta x} = A \cosh \beta x + B \sinh \beta x$$

$$C_3 e^{i\beta x} + C_4 e^{-i\beta x} = C \cos \beta x + D \sin \beta x$$

$$W(x) = A \cosh \beta x + B \sinh \beta x + C \cos \beta x + D \sin \beta x$$

$$W'(x) = A\beta \sinh \beta x + B\beta \cosh \beta x - C\beta \sin \beta x + D \cos \beta x$$

Eigenfrequency

The eigenfrequency of the system as a whole ω_n can be found by determining the eigenfrequency β of the amplitude function $W(x)$. This follows from the non-trivial solution of $W(x)$, which depends on its boundary conditions.

For a clamped-clamped beam the boundary conditions are:

$$w(0) = 0 \quad \rightarrow \quad W(0) = 0$$

$$w(L) = 0 \quad \rightarrow \quad W(L) = 0$$

$$\varphi(0) = 0 \quad \rightarrow \quad W'(0) = 0$$

$$\varphi(L) = 0 \quad \rightarrow \quad W'(L) = 0$$

These boundary conditions result in the following equations

$$W(0) = A + C = 0$$

$$W(L) = A \cosh \beta L + B \sinh \beta L + C \cos \beta L + D \sin \beta L = 0$$

$$W'(0) = \beta B + \beta D = 0$$

$$W'(L) = A\beta \sinh \beta L + B\beta \cosh \beta L - C\beta \sin \beta L + D \cos \beta L = 0$$

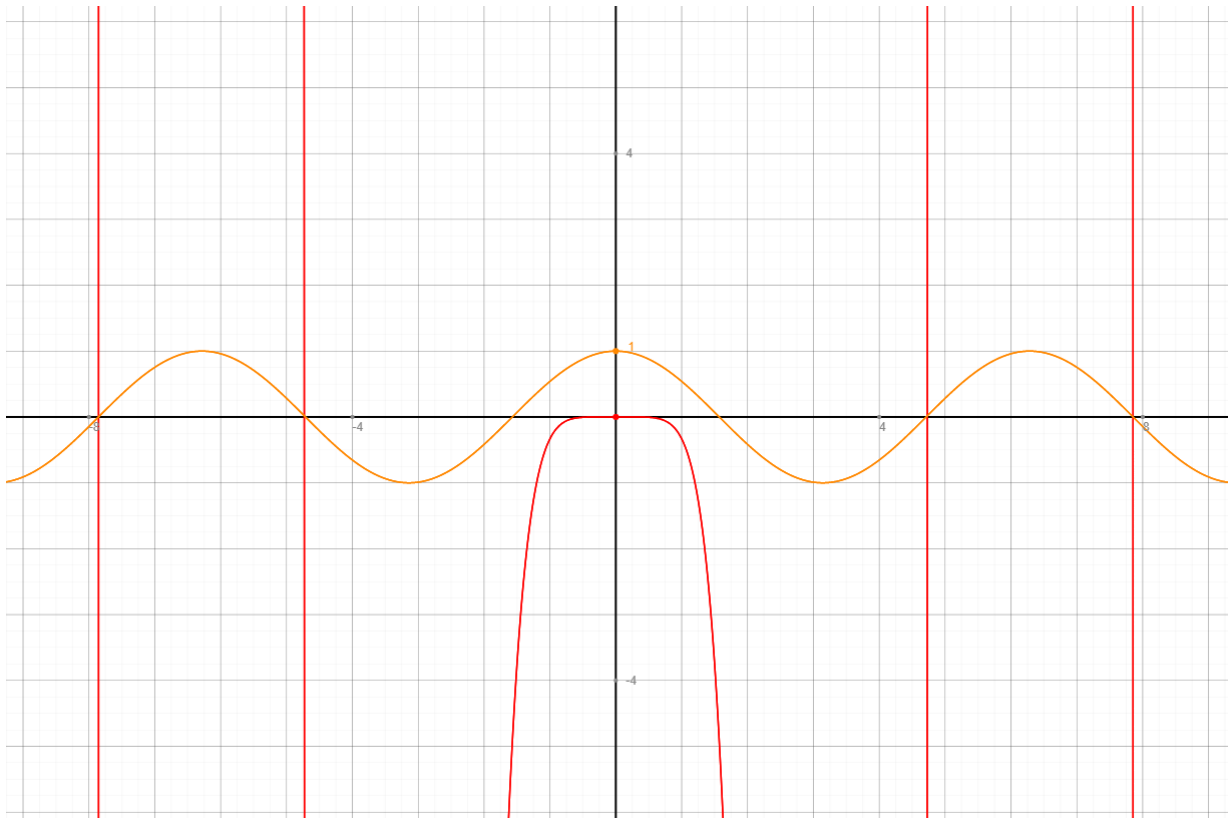
In matrix notation this becomes

$$\begin{bmatrix} 1 & 0 & 1 & 0 \\ \cosh \beta L & \sinh \beta L & \cos \beta L & \sin \beta L \\ 0 & \beta & 0 & \beta \\ \beta \sinh \beta L & \beta \cosh \beta L & -\beta \sin \beta L & \beta \cos \beta L \end{bmatrix} \begin{bmatrix} A \\ B \\ C \\ D \end{bmatrix} = \begin{bmatrix} 0 \\ 0 \\ 0 \\ 0 \end{bmatrix}$$

The non-trivial solution can only exist if the above coefficient matrix has a determinant equal to zero.

$$\begin{vmatrix} 1 & 0 & 1 & 0 \\ \cosh \beta L & \sinh \beta L & \cos \beta L & \sin \beta L \\ 0 & \beta & 0 & \beta \\ \beta \sinh \beta L & \beta \cosh \beta L & -\beta \sin \beta L & \beta \cos \beta L \end{vmatrix} = 0$$

$$2\beta^2(\cosh \beta L \cos \beta L - 1) = 0$$



The terms β^2 and $\cosh(\beta L)$ do not contribute to the circular behavior, and only have roots for $\beta = 0$ (trivial solution). The roots (eigenvalues of $W(x)$) can therefore be described as:

$$\beta L = \frac{3}{2}\pi + n\pi$$

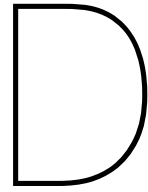
$$\beta = \frac{3 + 2n\pi}{2} \frac{1}{L}$$

The Eigenfrequencies of the system as a whole can then be determined

$$\beta^4 = \omega^2 \frac{\rho A}{EI}$$

$$\omega^2 = \frac{EI}{\rho A} \left(\frac{3 + 2n\pi}{2L} \right)^4$$

$$\omega = \pm \sqrt{\frac{EI}{\rho A} \left(\frac{3 + 2n\pi}{2L} \right)^2}$$



Case Study

In this appendix a case study report is presented, in which various portal frame structures are evaluated with respect to the ultimate, serviceability, and fatigue limit state according to the Eurocode and ROK norms.

Case Study

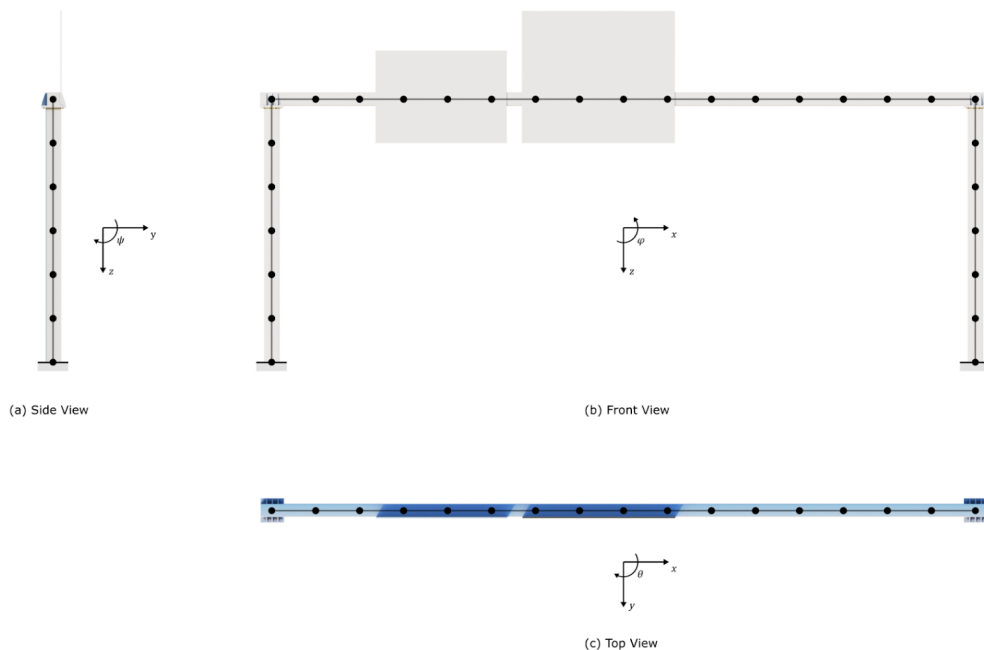
Verification of Hollow Section Steel Portal Frame Traffic Sign Support Structures

1 Introduction

The engineering firm *Antea Group* designs various highway sign support structures. As part of a master thesis structure the dynamic response and subsequent fatigue behavior due to aerodynamic loads is analyzed. The thesis focuses mainly on loading and resistance in the fatigue limit state of steel portal signs with square hollow sections (SHS). This document serves as supplementary information about the structures in question by analyzing and verifying several designs of characteristic structures in the Ultimate Limit State.

1.1 Calculation Tool

As part of the master thesis a Finite Element Method (FEM) program has been developed in the coding language Python with the capabilities of performing static and dynamic analyses. The discretization of a given geometry consists of 1D Euler-Bernoulli beam elements connecting nodes containing six degrees of freedom, namely displacements and rotations in the x, y, and z directions. This allows shear forces, bending moments, and torsion moments in all directions to be described. More properties of this FEM program can be found in the main body of the master thesis report.



1.2 Case Study Overview

This case study will analyze 3 different frames. Each frame will have the same basic design: two columns consisting of steel square hollow sections (SHS), which support a SHS beam. To this beam a number of traffic signs are attached at different locations.

This report first goes over how the external actions, mainly the self-weight and wind loads, are defined. Then an overview of the ULS and SLS checks is given, and finally the results of these checks for a variety of frames is documented.

2 Load Definitions

According to the Eurocode, in the ultimate limit state (ULS) the loading is separated into different components. Due to the nature of the structure this case study will focus primarily on two types of loads: permanent loads (self-weight) and variable loads (wind).

2.1 Permanent Loads

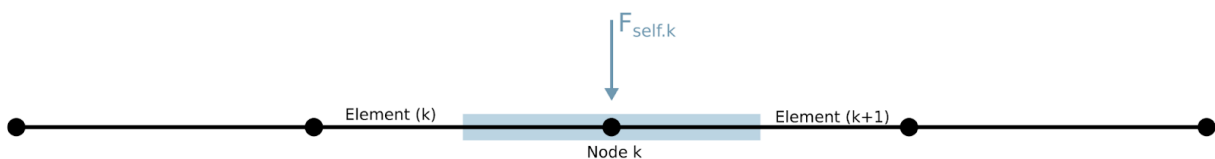
The permanent load on the structure is purely its self-weight. The self weight of the members (beams and columns) of the frame are calculated according to

$$q_{self} = \rho A g$$

Where

- q = distributed self-weight of the structure in N/mm
- ρ = density of steel in kg/mm³
- A = cross-sectional area of profile in mm²
- g = gravitational acceleration in m/s

The limitations of the FEM program being used is that the loads can only be applied as concentrated loads at the location of the nodes. As a result each node will carry half the weight from each adjacent element.



$$F_{self,k} = \frac{1}{2} (q_{self} \cdot l_{(k)} + q_{self} \cdot l_{(k+1)})$$

Where

- F_{self} = concentrated self-weight of the structure in N
- q_{self} = distributed self-weight of the structure in N/mm
- $l_{(k)}$ = length of element (k)

$l_{(k+1)}$ = length of element (k+1)

The self-weight of the joints will be disregarded and assumed to be negligibly small compared to the other loads. The signs are attached to the beam at multiple locations, but for the ease of calculation it will be assumed that the loads from the signs are applied at a single location (i.e. applied to a single node).

$$F_{sign} = g A_{sign} m_{sign}$$

Where

F_{sign} = concentrated self-weight of the sign in N

m_{sign} = distributed mass of the sign in kg/mm²

A_{sign} = surface area of sign in mm²

g = gravitational acceleration in m/s²

Some of the variables in the aforementioned equations follow from the chosen dimensions and profiles of the structure, others remain constant and are given below

Name	Symbol	Value	Units
Steel density	ρ	$7800 \cdot 10^{-9}$	kg/mm ³
Gravitational Acceleration	g	9.81	m/s ²
Distributed mass of sign	m_{sign}	$30 \cdot 10^{-6}$	kg/mm ²

2.2 Variable Loads

The variable load is determined according to *Eurocode 1: Actions on structures - Part 1-4: General actions - Wind actions* (EN 1991-1-4). The first step is to determine the fundamental value of the basic wind velocity $v_{b,0}$, which can be done according to EN 1991-1-4 NB, table NB.1

Tabel NB.1 — $v_{b,0}$ voor toepassing in Nederland

Windgebied	I	II	III
$v_{b,0}$ [m/s]	29,5	27,0	24,5

From the fundamental value the basic wind velocity may be determined according to a directional and seasonal factor. These two factors are both equal to 1.0 according to EN 1991-1-4 NB section 4.2(2)P

$$v_b = c_{dir} \cdot c_{season} \cdot v_{b0}$$

Where

- v_b = basic wind velocity in m/s
- c_{dir} = directional factor (= 1.0)
- $c_{seasonal}$ = seasonal factor (= 1.0)
- v_{b0} = fundamental basic wind velocity in m/s

The mean wind velocity follows from the basic wind velocity multiplied by a roughness and orography factor. It will be assumed that the structures under consideration are located on flat land (which is often the case in the Netherlands), resulting in an orography factor of 1.0.

$$v_m = c_r(z) \cdot c_o(z) \cdot v_b$$

Where

- v_m = mean wind velocity in m/s
- c_r = roughness factor
- c_o = orography factor (=1.0)
- v_b = basic wind velocity in m/s

The roughness factor depends on the terrain factor and the height of the structure above the ground. EN 1991-1-4 section 4.3.2(1) and 1991-1-4 NB section 4.3.2(1) define the roughness factor as

$$c_r(z) = k_r \cdot \ln\left(\frac{z}{z_0}\right) \quad \text{for} \quad z_{min} \leq z < z_{max}$$

$$c_r(z) = c_r(z_{min}) \quad \text{for} \quad z_{min} < z$$

$$k_r = 0.19 \left(\frac{z_0}{0.05}\right)^{0.07}$$

Where

- c_r = roughness factor
- k_r = terrain factor
- z = structure height
- z_0 = reference height in m (see EN 1991-1-4 NB, table NB.3-4.1)
- z_{min} = minimum height in m (see EN 1991-1-4 NB, table NB.3-4.1)
- z_{max} = maximum height (= 200m)

Tabel NB.3 – 4.1 — Terreincategorieën en terreinparameters

Terreincategorie		z_0 m	z_{min} m
0	Zee of kustgebied aan zee	0,005	1
II	Onbebouwd gebied	0,2	4
III	Bebouwd gebied	0,5	7

The effects of turbulence are taken into account according to the turbulence intensity, which indirectly takes the standard deviation of the wind speed distribution into account, and is given by EN 1991-1-4 section 4.4(1).

$$I_v(z) = \frac{k_t}{c_0 \cdot \ln\left(\frac{z}{z_0}\right)} \quad \text{for} \quad z_{min} \leq z < z_{max}$$

$$I_v(z) = I_v(z_{min}) \quad \text{for} \quad z_{min} < z$$

Where

- I_v = turbulence intensity
 k_t = turbulence factor (= 1.0)

The mean wind velocity and the turbulence intensity may be combined in order to determine the peak velocity pressure exerted by the wind on a structure, and is given by EN 1991-1-4 section 4.5(1)

$$q_p(z) = [1 + 7I_v(z)] \cdot \frac{1}{2} \rho_{air} v_m^2(z)$$

$$q_p(z) = c_e(z) \cdot q_b$$

$$c_e(z) = [1 + 7I_v(z)] c_r^2(z) \cdot c_o^2(z)$$

$$q_b = \frac{1}{2} \rho_{air} v_b^2$$

Where

- q_p = peak velocity pressure in N/m²
 q_b = basic velocity pressure in N/m²
 c_e = exposure factor
 ρ_{air} = air density in kg/m³ (= 1.25, see EN 1991-1-4 NB, section 4.5(1))

The total load generated by the wind acting on a sign, which is transferred to the supporting frame structure, is calculated according to sign surface area, a structural factor and a force coefficient factor. The structural factor may be taken as 1.0 as the sign is close to the ground

($z_e < 15m$). The force coefficient for signboards is 1.80 according to EN 1991-1-4 section 7.4.3(1). The equation for the wind force is given by EN 1991-1-4 section 5.3(2).

$$F_w = c_s c_d \cdot c_f \cdot q_p(z_e) \cdot A_{ref}$$

Where

F_w	=	wind force in N
$c_s c_d$	=	structural factor (= 1.0, see EN 1991-1-4, section 6.2(1))
c_f	=	force coefficient (= 1.0, see EN 1991-1-4, section 7.4.3(1))
z_e	=	structure height above ground (see EN 1991-1-4 section 7.5(2))
A_{ref}	=	reference surface area (total sign surface area, see EN 1991-1-4 section 7.4.3 Note 2)

2.3 Load Combination

2.3.1 ULS

When verifying the structural integrity in the ultimate limit state, the permanent load and variable load may be combined according EN 1990 equation 6.10a or 6.10b. The partial safety factors follow from EN 1990 NB table NB.4-A1.2(B)

$$1.35G + \sum_{i \geq 1} 1.5\psi_{0,i} Q_{k,i}$$

$$1.20G + 1.5Q_{k,1} + \sum_{i > 1} 1.5\psi_{0,i} Q_{k,i}$$

As the wind load is the governing load for these type of structures the latter combination (the one that follows from 6.10b) will be governing, leading to the following combination

$$1.2G + 1.5Q$$

2.3.2 SLS

In the serviceability limit state two combinations are considered:

- *characteristic combination* in order to ensure no inelastic response occurs under regular loading

$$G + \psi_0 Q = G + 0.6Q$$

- *frequent combination* in order to ensure no excessive deflections occur

$$G + \psi_1 Q = G + 0.2Q$$

3 ULS Verification: Cross-Sectional Resistance

When verifying the members for the ultimate limit state the structural integrity of the beam and columns of the traffic sign support structure need to be verified, taking the effects of member-buckling into account.

The structure in question is loaded by concentrated loads in the global y and z direction with small eccentricities. As a result shear loads, bending, torsion, and normal forces all need to be taken into account. These loads should be considered both individually and the interaction between them.

The structure in question consists of square hollow sections (SHS). This case study will only consider class 1 cross-sections, a classification valid for most SHS profiles.

3.1 Individual Loads

3.1.1 Axial

Under the assumption that the cross-section has a class 1 classification and that no fasteners are present, the axial resistance is provided by EN 1993-1-1 sections 5.2.3 and 6.2.4

$$\frac{N_{Ed}}{Af_y/\gamma_{M0}} \leq 1.0$$

Where

- N_{Ed} = axial load action in N
- A = gross cross-sectional area mm²
- f_y = steel yield strength in N/mm²
- γ_{M0} = partial safety factor for cross-sectional resistance (= 1.0)

3.1.2 Bending

For bending moments of a class 1 or 2 cross-section the following criterion should be satisfied based on EN 1993-1-1 sections 6.2.5(1)P and 6.2.5(2).

$$\frac{M_{Ed}}{W_{pl}f_y/\gamma_{M0}} \leq 1.0$$

Where

- M_{Ed} = bending moment action in Nmm
- W_{pl} = plastic section modulus in mm³

3.1.3 Torsion

Similar to the bending moments, the torsion moment is verified according to EN 1993-1-1 section 6.2.7(1)

$$\frac{T_{Ed}}{W_T f_y / \sqrt{3} / \gamma_{M0}} \leq 1.0$$

Where

T_{Ed} = torsion moment action in Nmm

W_T = torsion section modulus in mm³

3.1.4 Shear

If torsion is present the plastic shear resistance of a structural hollow section is reduced by the effects of torsion. According to EN 1993-1-1 sections 6.2.6(2) and 6.2.7(9) the (reduced) plastic shear resistance is provided

$$\frac{V_{Ed}}{V_{pl,T,Rd}} \leq 1.0$$

$$V_{pl,T,Rd} = \left[1 - \frac{\tau_{t,Ed}}{(f_y / \sqrt{3}) / \gamma_{M0}} \right] \cdot V_{pl,Rd}$$

$$V_{pl,Rd} = \frac{A_v (f_y / \sqrt{3})}{\gamma_{M0}}$$

$$\tau_{t,Ed} = \frac{T_{Ed}}{W_T}$$

Where

V_{Ed} = shear load action in N

$V_{pl,T,Rd}$ = plastic shear resistance reduced by torsion effects in N

$V_{pl,Rd}$ = plastic shear resistance in the absence of shear in N

$\tau_{t,Ed}$ = torsional shear stress in N/mm²

T_{Ed} = torsion moment action in Nmm

3.2 Interaction of Loads

The Dutch national annex to eurocode 3 (EN 1993-1-1 NB) provides a method to combine the effects of shear, bending, torsion, and axial loads. The torsion effects are taken into account by reducing the plastic shear resistance in the same way it is done for the individual checks. The bending moment and normal force are then reduced based on the ratio of the shear load action to the shear load resistance. The final verification is performed by combining the

reduced bending moment resistance and reduced axial resistance into an effective bending moment resistance.

3.2.1 Shear Load Reduction Factors

As there is bending around two axes, two different shear reduction factors need to be considered. For square hollow sections these are given by EN 1993-1-1 NB sections 6.2.8(8) and 6.2.8(9)

$$q_y = 1.03 \sqrt{1 - \left(\frac{V_{y,Ed}}{V_{pl,y,T,Rd}} \right)^2}$$

$$q_z = 1.03 \sqrt{1 - \left(\frac{V_{z,Ed}}{V_{pl,z,T,Rd}} \right)^2}$$

Where

- q_y = shear load reduction factor for the y-direction
- q_z = shear load reduction factor for the z-direction
- $V_{y,Ed}$ = shear load action for the y-direction in N
- $V_{z,Ed}$ = shear load action for the z-direction in N
- $V_{pl,y,T,Rd}$ = plastic shear resistance reduced by torsion effects for the y-direction in N
- $V_{pl,z,T,Rd}$ = plastic shear resistance reduced by torsion effects for the z-direction in N

3.2.2 Reduced Axial Resistance

For square and rectangular hollow sections the axial resistance is reduced by the shear load reduction factors according to EN 1993-1-1 NB section 6.2.10(4) and 6.2.10(5) for the y and z directions.

$$N_{Vy,Rd} = \frac{N_{pl,Rd} - 2(1-q_y) \cdot t \cdot b \cdot f_y}{\gamma_{M0}}$$

$$N_{Vz,Rd} = \frac{N_{pl,Rd} - 2(1-q_z) \cdot t \cdot h \cdot f_y}{\gamma_{M0}}$$

Where

- $N_{Vy,Rd}$ = axial design resistance reduced by shear load effects in N
- $N_{Vz,Rd}$ = axial design resistance reduced by shear load effects in N
- $N_{pl,Rd}$ = axial plastic design resistance in N
- t = SHS wall thickness in mm
- b = SHS width in mm
- h = SHS height in mm

3.2.3 Reduced Bending Moment Resistance

For square and rectangular hollow sections the bending moment resistance is reduced by the shear load reduction factors according to EN 1993-1-1 NB section 6.2.8(8) and 6.2.8(9) for the y and z directions.

$$M_{y,V,Rd} = \frac{M_{pl,y,Rd} - ((1-q_z) \cdot \frac{1}{2} t h^2 \cdot f_y)}{\gamma_{M0}}$$

$$M_{z,V,Rd} = \frac{M_{pl,z,Rd} - ((1-q_y) \cdot \frac{1}{2} t b^2 \cdot f_y)}{\gamma_{M0}}$$

Where

- $M_{y,V,Rd}$ = bending moment (around the y-axis) design resistance reduced by shear load effects in Nmm
- $M_{z,V,Rd}$ = bending moment (around the z-axis) design resistance reduced by shear load effects in Nmm
- $M_{pl,y,Rd}$ = bending moment (around y-axis) design resistance in Nmm
- $M_{pl,z,Rd}$ = bending moment (around z-axis) design resistance in Nmm

3.2.4 Effective Bending Moment Resistance

The reduced bending moment resistance and reduced axial resistance are combined into an effective bending moment resistance according to EN 1993-1-1 NB section 6.2.10(7)

$$M_{y,N,V,Rd} = M_{y,V,Rd} \cdot \frac{1 - N_{Ed}/N_{Vy,Rd}}{1 - a_{4z}/2}$$

$$M_{z,N,V,Rd} = M_{z,V,Rd} \cdot \frac{1 - N_{Ed}/N_{Vz,Rd}}{1 - a_{4y}/2}$$

$$a_{4y} = q_y a_3$$

$$a_{4z} = q_z a_3$$

$$a_3 = \min \left(\frac{A - 2bt}{A}; 0.5 \right)$$

Where

- $M_{y,N,V,Rd}$ = effective bending moment design resistance (around y-axis) in Nmm
- $M_{z,N,V,Rd}$ = effective bending moment design resistance (around z-axis) in Nmm
- a_{4y} = conversion factor
- a_{4z} = conversion factor
- a_3 = conversion factor

3.2.5 Verification

The final verification uses the effective bending moment in combination with several factors according to EN 1993-1-1 NB section 6.2.10(7)

$$\beta_0 \left(\frac{M_{y,Ed}}{M_{y,N,V,Rd}} \right)^{\alpha_1} + \beta_1 \left(\frac{M_{z,Ed}}{M_{z,N,V,Rd}} \right)^{\alpha_2} \leq 1.0$$

Case	α_1	α_2	β_0	β_1
$M_{Ed}/N_{N,V,Rd} \leq 2/3$	1.0	2.0	1.0	0.75
$M_{Ed}/N_{N,V,Rd} > 2/3$	2.0	1.0	0.75	1.0

4 ULS Verification: Stability

4.1 Flexural Buckling

The effects of (in)stability in members due to flexural buckling are taken into account by performing a resistance check for compression while reducing the resistance with a flexural buckling factor.

First the relative slenderness is determined based on the elastic critical buckling load of the cross-section according to EN 1993-1-1 section 6.3.1.2(1), which for cross-sections up to class 3 is defined as follows

$$\bar{\lambda} = \sqrt{\frac{Af_y}{N_{cr}}}$$

$$N_{cr} = \frac{\pi^2 EI}{l_k^2}$$

Where

$\bar{\lambda}$	=	member relative slenderness
A	=	gross cross-sectional area in mm ²
f_y	=	steel strength in N/mm ²
N_{cr}	=	elastic critical buckling load in N
E	=	steel modulus of elasticity in N/mm ²
I	=	moment of inertia mm ⁴
l_k	=	critical buckling length in mm

The resistance reduction factor is then computed based on the relative slenderness and the imperfection factor (which follows from the buckling curves) according to EN 1993-1-1 sections 6.3.1.2(1) and 6.3.1.2(2)

$$\Phi = 0.5[1 + \alpha(\bar{\lambda} - 0.2) + \bar{\lambda}^2]$$

$$\chi = \frac{1}{\Phi + \sqrt{\Phi^2 - \bar{\lambda}^2}} \leq 1.0$$

Where

χ = resistance reduction factor
 α = imperfection factor

Table 6.1: Imperfection factors for buckling curves

Buckling curve	a ₀	a	b	c	d
Imperfection factor α	0,13	0,21	0,34	0,49	0,76

The buckling resistance is then checked according to EN 1993-1-1 section 6.3.1.1

$$\frac{N_{Ed}}{N_{b,Rd}} \leq 1.0$$

$$N_{b,Rd} = \frac{\chi A f_y}{\gamma_{M1}}$$

Where

$N_{b,Rd}$ = buckling resistance

4.2 Lateral Torsional Buckling

The procedure for checking lateral torsional buckling (LTB) is similar to that of flexural buckling. Once again the relative slenderness (in this case with respect to LTB) is calculate according to EN 1993-1-1 section 6.3.2.2

$$\bar{\lambda}_{LT} = \sqrt{\frac{W f_y}{M_{cr}}}$$

Where

$\bar{\lambda}_{LT}$ = member relative slenderness with respect to LTB
 W = member section modulus for bending around the relevant axis in mm³
 f_y = steel strength in N/mm²
 M_{cr} = elastic critical moment

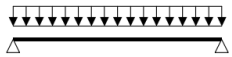
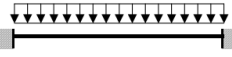
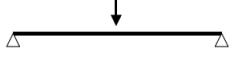
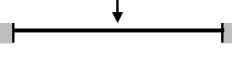
The elastic critical bending moment M_{cr} may be calculated using the non-contradictory complementary information document published by the EUrocode: SN003a-EN-EU: "NCCI: Elastic critical moment for lateral torsional buckling". In the common case of normal support conditions, assuming that the load is applied at the shear center, and assuming that the warping constant for closed sections is negligibly small, the elastic critical bending moment M_{cr} is calculated according to:

$$M_{cr} = C_1 \frac{\pi^2 EI}{L^2} \sqrt{\frac{L^2 GI_t}{\pi^2 EI}}$$

Where

- M_{cr} = elastic critical bending moment
- C_1 = coefficient depending on the loading and end restraints
- E = steel modulus of elasticity
- I = cross-section moment of inertia around relevant bending axis
- L = member length
- G = steel shear modulus
- I_t = cross-section torsion constant

The value of C_1 can be determined based on table 3.2 in SN003a-EN-EU. In the case of the portal frame the bending moment of the beam is governed by the concentrated wind load acting on the traffic signs: $C_1 = 1.348$

Loading and support conditions	Bending moment diagram	C_1	C_2
		1,127	0,454
		2,578	1,554
		1,348	0,630
		1,683	1,645

Note : the critical moment M_{cr} is calculated for the section with the maximal moment along the member

The resistance reduction factor is then computed based on the relative slenderness and the imperfection factor (which follows from the buckling curves) according to EN 1993-1-1 sections 6.3.2.2

$$\Phi_{LT} = 0.5[1 + \alpha_{LT}(\bar{\lambda}_{LT} - 0.2) + \bar{\lambda}_{LT}^2]$$

$$\chi_{LT} = \frac{1}{\Phi_{LT} + \sqrt{\Phi_{LT}^2 - \bar{\lambda}_{LT}^2}} \leq 1.0$$

Where

χ_{LT} = resistance reduction factor for LTB

α_{LT} = imperfection factor for LTB

Table 6.3: Recommended values for imperfection factors for lateral torsional buckling curves

Buckling curve	a	b	c	d
Imperfection factor α_{LT}	0,21	0,34	0,49	0,76

The buckling resistance is then checked according to EN 1993-1-1 section 6.3.2.1

$$\frac{M_{Ed}}{M_{b,Rd}} \leq 1.0$$

$$M_{b,Rd} = \frac{\chi_{LT} W_f}{\gamma_{M1}}$$

Where

$M_{b,Rd}$ = buckling resistance

5 ULS Verification: Joint Design

The structural integrity of the joint is verified using a finite element method software which performs analyses specifically for joints: *IDEA StatiCa*. A summary report for each frame is given in a separate report.

6 SLS Verification: Maximum Deflections

The serviceability limit state for the support structures of traffic signs is not very significant as the only function the structure has is supporting and displaying traffic signs. Deformations will not significantly impede this functionality. The main aspect to consider is to ensure the deformations are not too large such that automobilists feel uneasy or unsafe driving underneath a deformed structure.

The main members' deflections are checked according to the national annex. The deflections maximum deflections for the beam and column are determined according to EN 1990 NB section A1.4.3 (4) and A1.4.3 (7) respectively.

$$v_{beam.max} = \frac{L_{span}}{250}$$

$$v_{column.max} = \frac{H}{150}$$

Where:

$v_{beam.max}$	=	Maximum allowed deflection of beam at midspan
$v_{column.max}$	=	Maximum allowed deflection of column at top
L_{span}	=	Beam span
H	=	Column height

7 FLS Verification: Weld Fatigue Damage

As discussed in the main thesis report, the fatigue damage will be governing in the welds of the structure. The maximum stress in the fatigue limit state is determined according to the FEM model used in the *ULS Verification: Joint Design*. According to EN 1991-1-4 Section B.3(1) dynamic loads in a 50 year structure life-time can be described by a stress range ΔS relative to the maximum stress S_k as a function of the number of times this stress range occurs N_g

$$\frac{\Delta S}{S_k} = 0.7(\log N_g)^2 - 17.4 \log N_g + 100$$

Where

ΔS	=	Stress range
S_k	=	Maximum stress in a 50 year period
N_g	=	Number of times ΔS occurs in a 50 year period

8 Cost Calculations

IDEA Statica provides default values for the costs of materials and installation of the joint. These values will be used to estimate the total cost of the structure. An overview of these values is given in the following table:

Description	Price
Steel parts	2 €/kg
Fillet welds	40 €/kg
Butt welds	50 €/kg
Bolts	5 €/kg
Hole drilling	30 % of bolts

9 Results

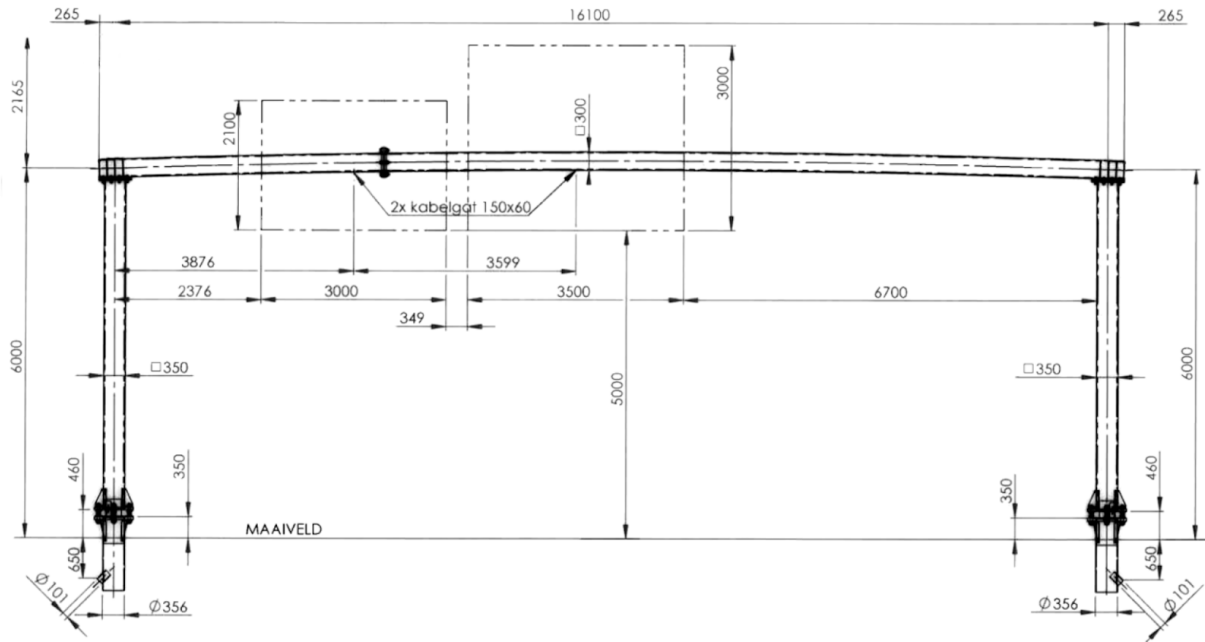
In this section a summary of the results in table format is given. In these tables **blue values** are considered input values for the calculation at hand, and **red values** are considered output values for the calculation at hand.

9.1 General Properties

The general properties that will remain unchanged for all frame designs are the partial safety factors for resistance and the steel properties.

Property	Symbol	Value	Unit
<i>Load Factors</i>			
SLS permanent	ψ_{SLSp}	1.0	[-]
SLS variable	ψ_{SLSv}	0.2	[-]
ULS permanent	ψ_{ULSp}	1.2	[-]
ULS variable	ψ_{ULSv}	1.5	[-]
<i>Resistance Factors</i>			
Partial factor resistance cross-sections	ψ_{Mo}	1.00	[-]
Partial factor resistance member (in)stability	ψ_{M1}	1.00	[-]
<i>Loads</i>			
Wind Area	[-]	I	[-]
Terrain Category	[-]	II	[-]
Air density	ρ	1.25	kg/m ³
Sign mass	ms	30	kg/m ²
Gravitational acceleration	g	9.81	m/s ²
<i>Steel</i>			
Modulus of Elasticity	E	210	GPa
Shear Modulus	G	80	GPa
Density	ρ	7800	kg/m ³
Yield Strength	f_y	355	MPa

9.2 Frame #1

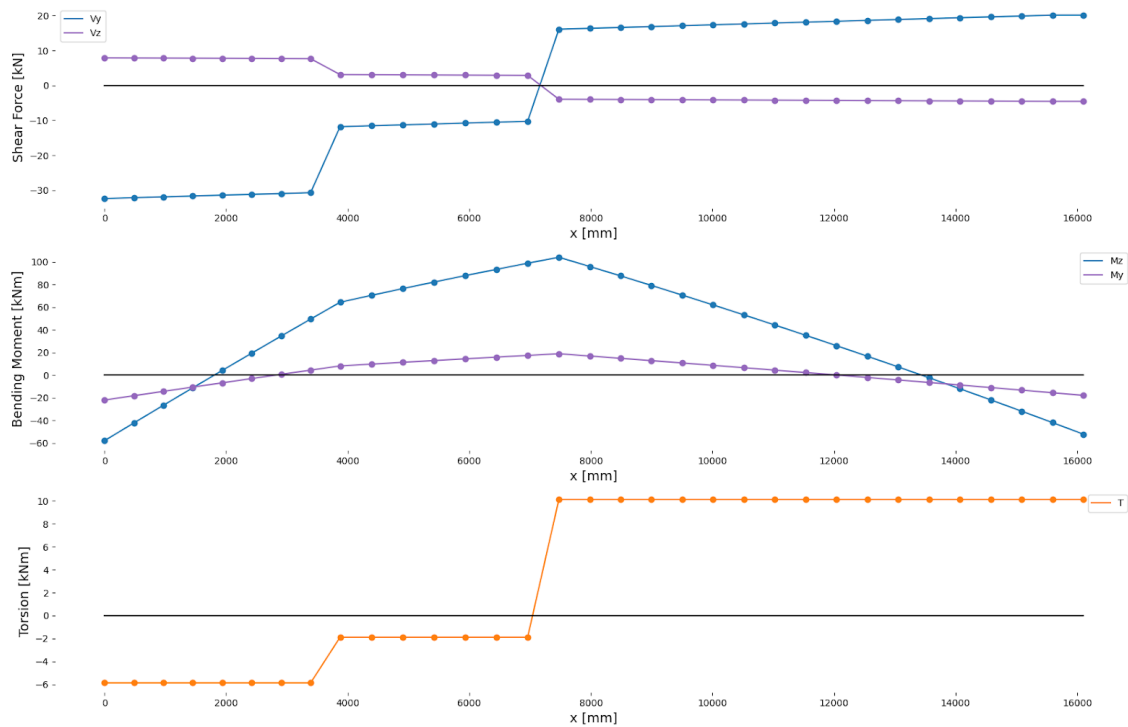


Geometry	Symbol	Value	Unit
<i>Frame</i>			
Span	L	16.1	m
Height	H	6.0	m
Beam profile	[-]	SHS 200 / 10	[-]
Column Profile	[-]	SHS 200 / 12.5	[-]
<i>Sign1</i>			
Structure height	z	6.00	m
Sign width	b	3.00	m
Sign height	h	2.50	m
Bottom of sign height	z_b	5.00	m
Beam width	w_b	0.30	m
<i>Sign2</i>			
Structure height	z	6.00	m
Sign width	b	3.50	m
Sign height	h	3.00	m
Bottom of sign height	z_b	5.00	m
Beam width	w_b	0.30	m

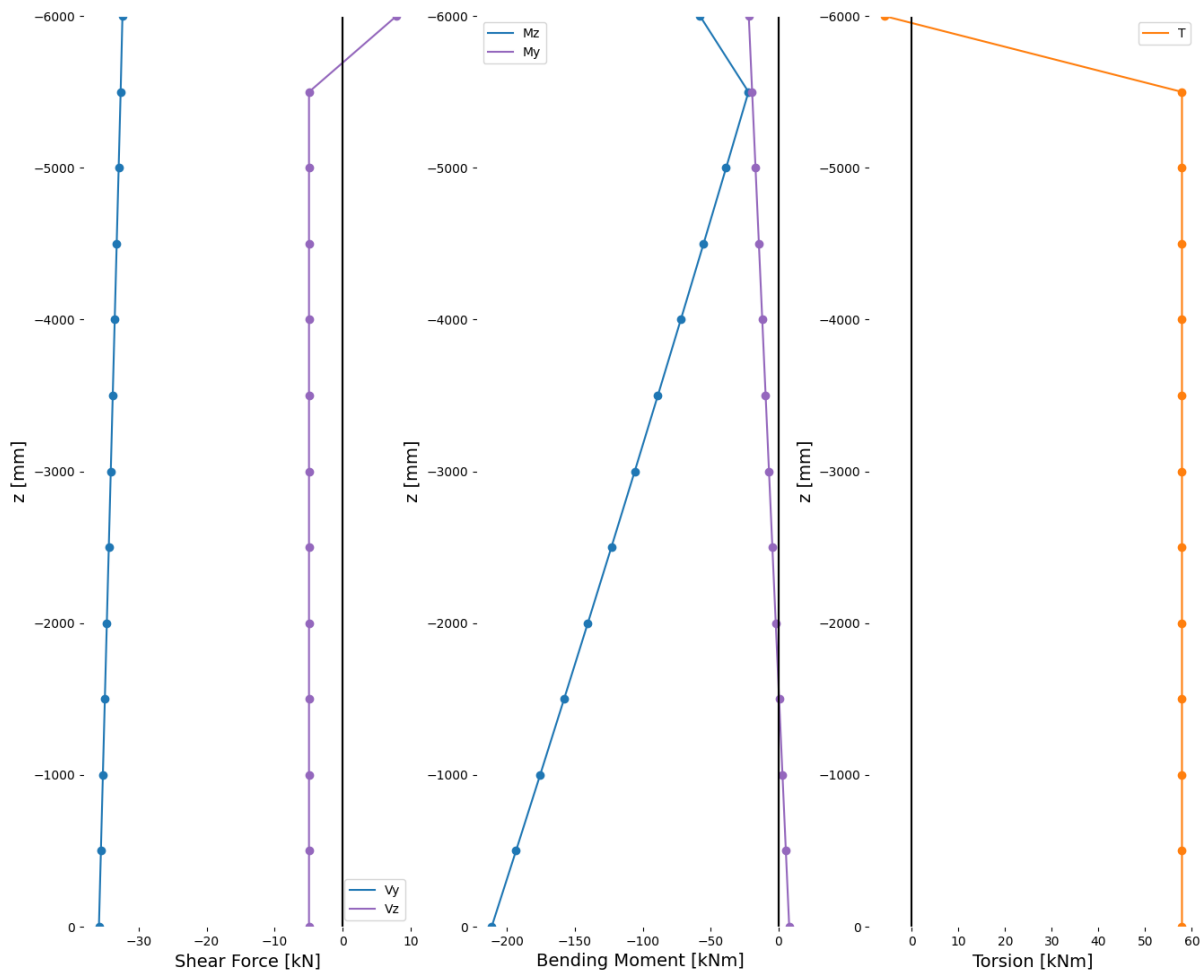
Loads	Symbol	Sign 1		Sign 2	
		Value	Unit	Value	Unit
<i>Computed Loads on Signs</i>					
Wind force	F_w	12.42	kN	17.39	kN
Self-weight	F_{self}	2.21	kN	3.09	kN
<i>ULS Combination</i>					
Force (x-direction)	F_x	0.00	kN	0.00	kN
Force (y-direction)	F_y	-18.63	kN	-26.09	kN
Force (z-direction)	F_z	2.65	kN	3.71	kN
Moment (x-axis)	M_x	-4.26	kNm	-12.49	kNm
Moment (y-axis)	M_y	0.00	kNm	0.00	kNm
Moment (z-axis)	M_z	0.00	kNm	0.00	kNm
<i>SLS Combination</i>					
Force (x-direction)	F_x	0.00	kN	0.00	kN
Force (y-direction)	F_y	-2.48	kN	-3.48	kN
Force (z-direction)	F_z	2.21	kN	3.09	kN
Moment (x-axis)	M_x	-0.29	kNm	-1.28	kNm
Moment (y-axis)	M_y	0.00	kNm	0.00	kNm
Moment (z-axis)	M_z	0.00	kNm	0.00	kNm
<i>FLS Combinations</i>					
Force (x-direction)	F_x	0.00	kN	0.00	kN
Force (y-direction)	F_y	-12.42	kN	-17.39	kN
Force (z-direction)	F_z	2.21	kN	3.09	kN
Moment (x-axis)	M_x	-2.77	kNm	-8.23	kNm
Moment (y-axis)	M_y	0.00	kNm	0.00	kNm
Moment (z-axis)	M_z	0.00	kNm	0.00	kNm

9.2.1 ULS Member Verification: Member Internal Load Distributions

Beam:

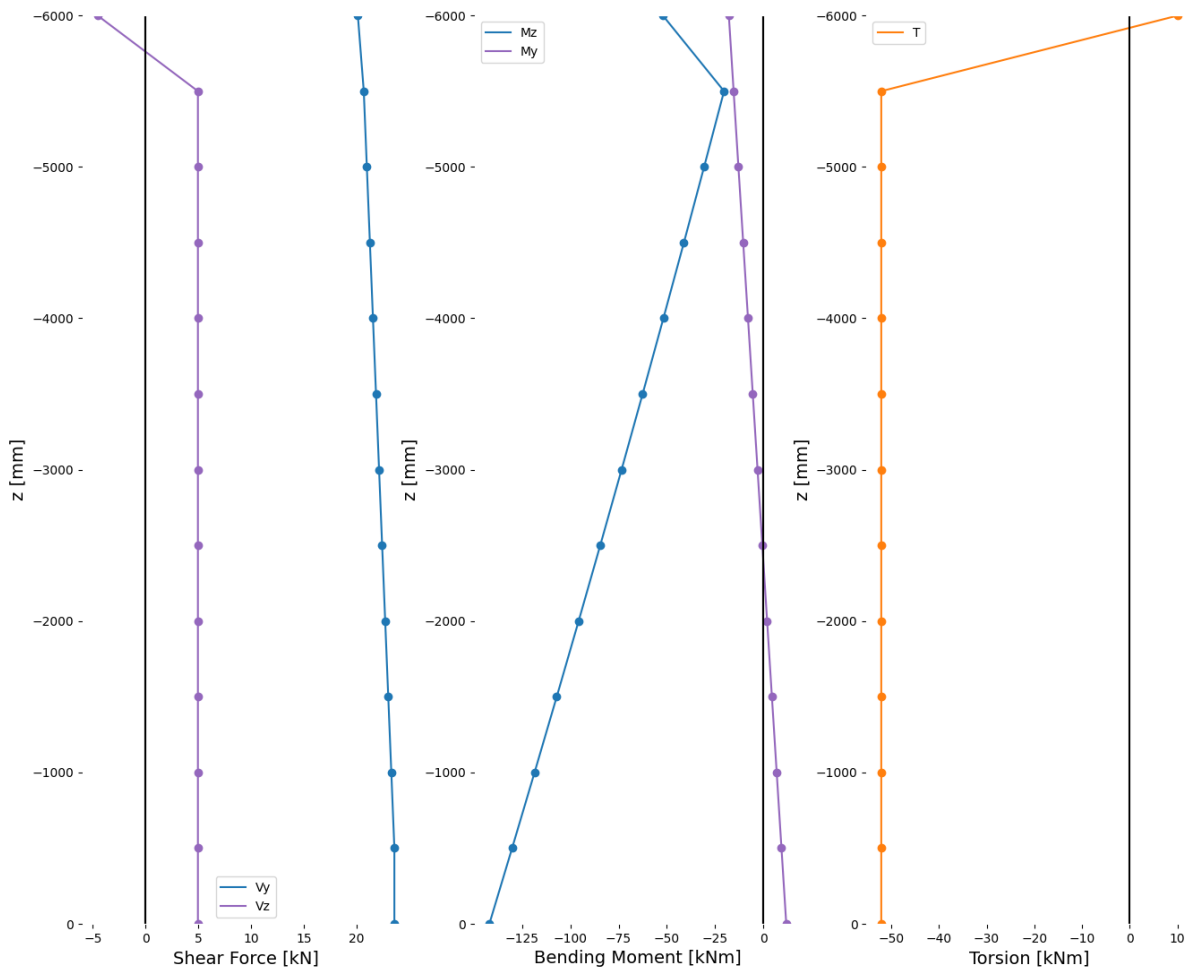


Left Column:



The reason there is a kink in the internal load diagram at the top of the column (uppermost node) has to do with the way the Python script converts the nodal values from the global to the local axes. Unfortunately there is no time to change the python script, therefore the values of the top node should be disregarded, fortunately the governing cross-section is always located at the bottom of the column.

Right Column:



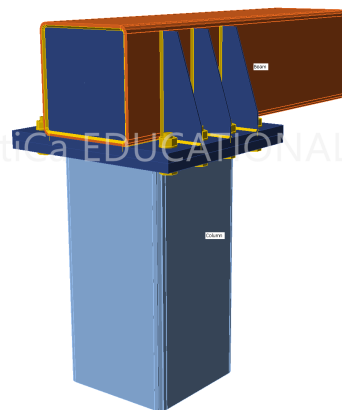
The reason there is a kink in the internal load diagram at the top of the column (uppermost node) has to do with the way the Python script converts the nodal values from the global to the local axes. Unfortunately there is no time to change the python script, therefore the values of the top node should be disregarded, fortunately the governing cross-section is always located at the bottom of the column.

9.2.2 ULS Member Verification: Summary

Beam Verification		Symbol	Value	Unit
<i>Governing Loads</i>				
	Axial action	N_{Ed}	5	kN
	Shear action y-direction	V_{yEd}	16	kN
	Shear action z-direction	V_{zEd}	4	kN
	Torsion action	T_{Ed}	10	kNm
	Bending moment action y-axis	M_{yEd}	19	kNm
	Bending moment action z-axis	M_{zEd}	104	kNm
<i>Individual Resistance</i>				
	Axial	N_{pRd}	3293	kN
	Shear	V_{pRd}	951	kN
	Torsion	T_{Rd}	265	kNm
	Bending	M_{Rd}	311	kNm
<hr/>				
<i>Individual Unity Checks</i>				
	Axial	[-]	0.00	[-]
	Shear	[-]	0.40	[-]
	Torsion	[-]	0.04	[-]
	Bending	[-]	0.02	[-]
<i>Interaction Unity Check</i>				
	Axial+Shear+Torsion+Bending	[-]	0.09	[-]
<i>Stability Unity Check</i>				
	Lateral torsional buckling	[-]	0.33	[-]
<hr/>				
Column Verification		Symbol	Value	Unit
<i>Governing Loads</i>				
	Axial action	N_{Ed}	9	kN
	Shear action y-direction	V_{yEd}	36	kN
	Shear action z-direction	V_{zEd}	5	kN
	Torsion action	T_{Ed}	58	kNm
	Bending moment action y-axis	M_{yEd}	8	kNm
	Bending moment action z-axis	M_{zEd}	211	kNm
<i>Individual Resistance</i>				
	Axial	N_{pRd}	4790	kN
	Shear	V_{pRd}	1383	kN
	Torsion	T_{Rd}	448	kNm
	Bending	M_{Rd}	525	kNm
<hr/>				
<i>Individual Unity Checks</i>				
	Axial	[-]	0.00	[-]
	Shear	[-]	0.42	[-]
	Torsion	[-]	0.13	[-]
	Bending	[-]	0.03	[-]
<i>Interaction Unity Check</i>				
	Axial+Shear+Torsion+Bending	[-]	0.08	[-]
<i>Stability Unity Check</i>				
	Flexural buckling	[-]	0.01	[-]

9.2.3 ULS Joint Design

Joint Loads ULS	Symbol	Value	Unit
<i>Cross-Sectional Loads</i>			
Axial action	N_{Ed}	-4.96	kN
Shear action y-direction	V_{yEd}	-31.88	kN
Shear action z-direction	V_{zEd}	7.82	kN
Torsion action	T_{Ed}	-5.87	kNm
Bending moment action y-axis	M_{yEd}	-14.35	kNm
Bending moment action z-axis	M_{zEd}	-26.63	kNm



Plates	✓	0.0 < 5.0%
Preloaded bolts	✓	22.7 < 100%
Welds	✓	26.3 < 100%

9.2.4 FLS Joint Design

Joint Loads FLS	Symbol	Value	Unit
<i>Cross-Sectional Loads</i>			
Axial action	N_{Ed}	-4.53	kN
Shear action y-direction	V_{yEd}	-18.99	kN
Shear action z-direction	V_{zEd}	7.12	kN
Torsion action	T_{Ed}	-3.67	kNm
Bending moment action y-axis	M_{yEd}	-13.10	kNm
Bending moment action z-axis	M_{zEd}	-15.84	kNm

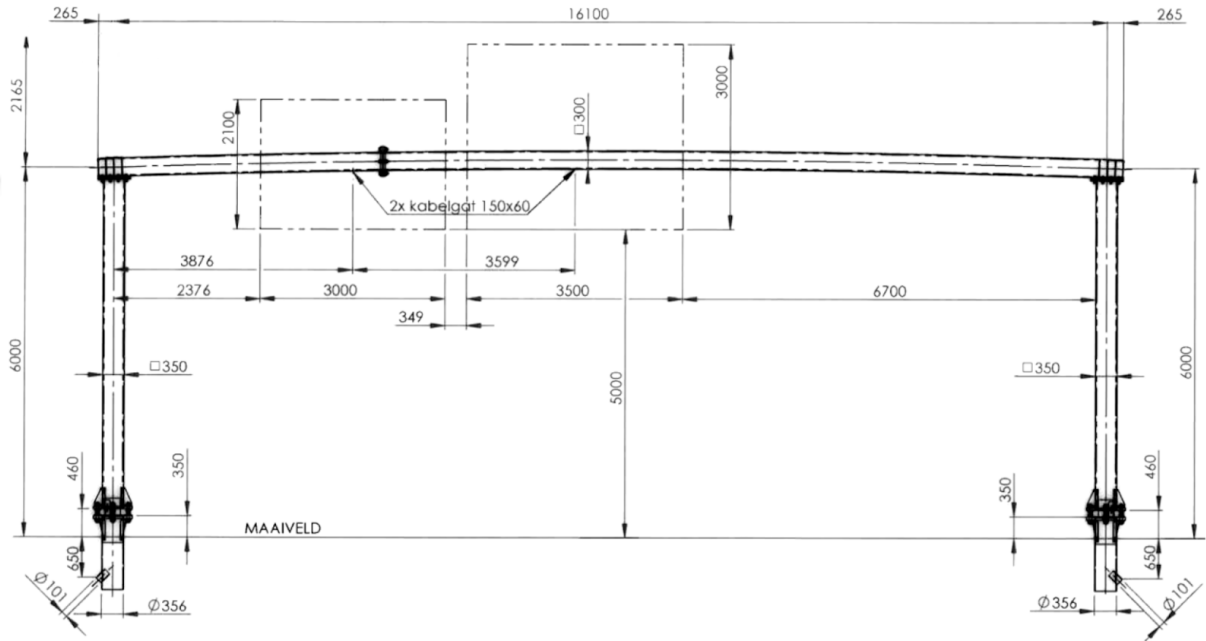
Property	Column-to-End-Plate	Beam-to-End-Plate	Horizontal Stiffener	Vertical Stiffener
<i>Action</i>				
Perpendicular normal stress	71.9 MPa	23.8 MPa	22.5 MPa	25.8 MPa
Perpendicular shear stress	42.6 MPa	10.8 MPa	19.9 MPa	24.5 MPa
Parallel shear stress	4.8 Mpa	74.1 Mpa	22.3 Mpa	22.4 Mpa
<i>Verification</i>				
Eurocode normal stress fatigue damage	0.05 [-]	0.00 [-]	0.00 [-]	0.00 [-]
Eurocode shear stress fatigue damage	0.00 [-]	0.00 [-]	0.00 [-]	0.00 [-]
ROK normal stress fatigue damage	0.11 [-]	0.00 [-]	0.00 [-]	0.00 [-]
ROK shear stress fatigue damage	0.00 [-]	0.01 [-]	0.00 [-]	0.00 [-]

9.2.5 SLS Deflections

Property	Symbol	Value	Unit
<i>Deflections</i>			
Beam maximum deflection [mm]	U_{beam}	18	[-]
Column maximum deflection [mm]	U_{column}	10	[-]
<i>Deflection Limits</i>			
Beam deflection limit [mm]	$U_{beam,max}$	64	[-]
Column deflection limit [mm]	$U_{column,max}$	40	[-]

9.3 Frame #2

The overall dimensions in the picture below are representative of the frame in question, but the dimensions of the member profiles are smaller.

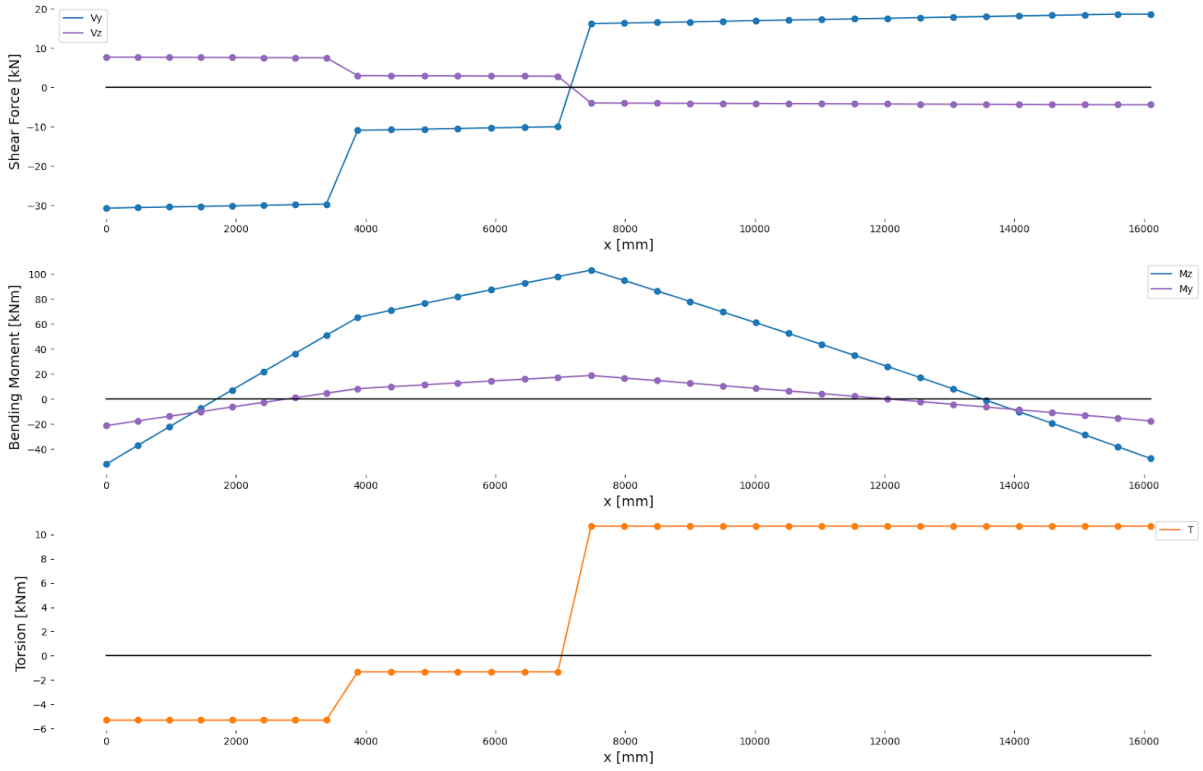


Geometry	Symbol	Value	Unit
<i>Frame</i>			
Span	L	16.1	m
Height	H	6.0	m
Beam profile	[-]	SHS 200 / 10	[-]
Column Profile	[-]	SHS 200 / 12.5	[-]
<i>Sign1</i>			
Structure height	z	6.00	m
Sign width	b	3.00	m
Sign height	h	2.50	m
Bottom of sign height	z_b	5.00	m
Beam width	w_b	0.30	m
<i>Sign2</i>			
Structure height	z	6.00	m
Sign width	b	3.50	m
Sign height	h	3.00	m
Bottom of sign height	z_b	5.00	m
Beam width	w_b	0.30	m

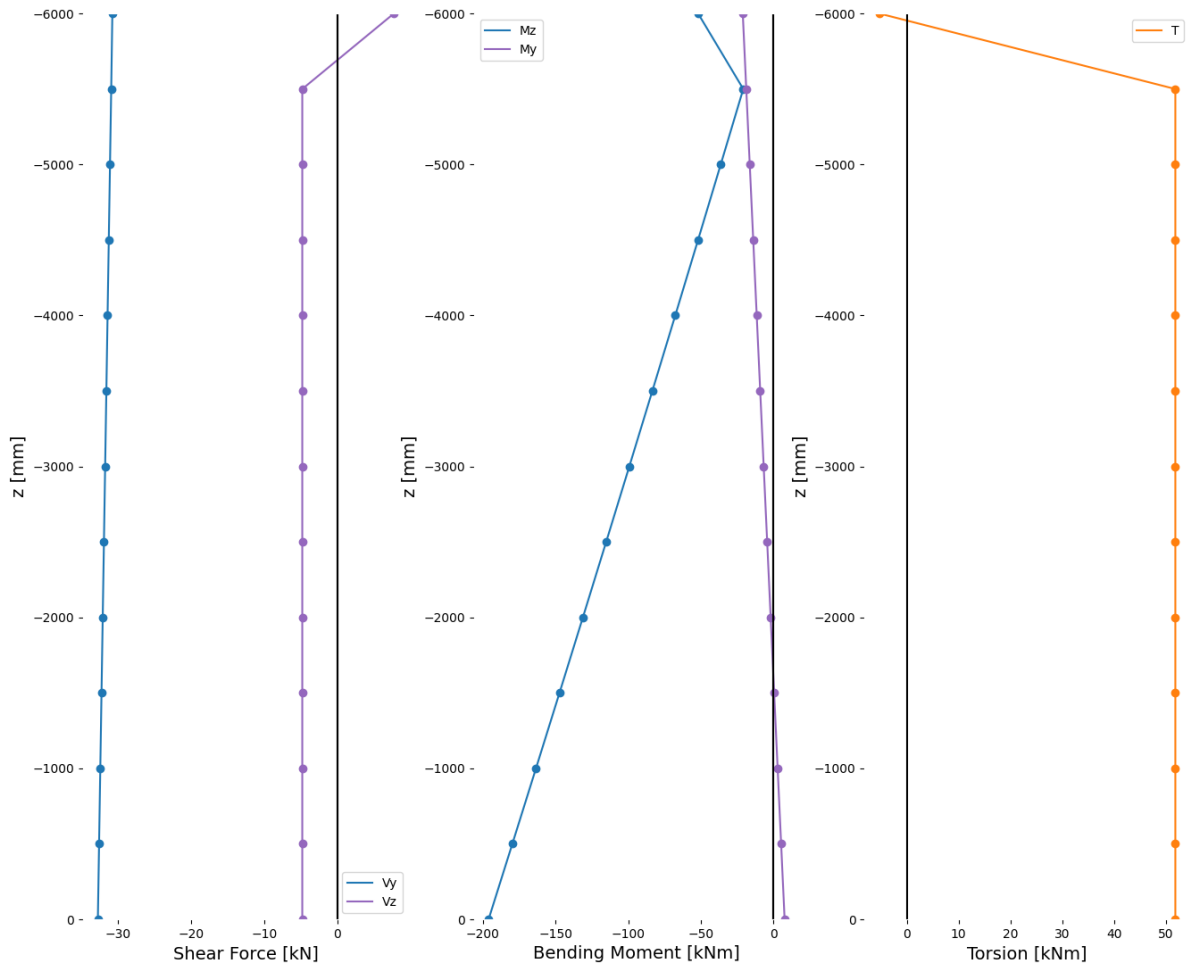
Loads	Symbol	Sign 1		Sign 2		
		Value	Unit	Value	Unit	
<i>Computed Loads on Signs</i>						
	Wind force	\vec{F}_w	12.42	kN	17.39	kN
	Self-weight	\vec{F}_{self}	2.21	kN	3.09	kN
<i>ULS Combination</i>						
	Force (x-direction)	F_x	0.00	kN	0.00	kN
	Force (y-direction)	F_y	-18.63	kN	-26.09	kN
	Force (z-direction)	F_z	2.65	kN	3.71	kN
	Moment (x-axis)	M_x	-4.26	kNm	-12.49	kNm
	Moment (y-axis)	M_y	0.00	kNm	0.00	kNm
	Moment (z-axis)	M_z	0.00	kNm	0.00	kNm
<i>SLS Combination</i>						
	Force (x-direction)	F_x	0.00	kN	0.00	kN
	Force (y-direction)	F_y	-2.48	kN	-3.48	kN
	Force (z-direction)	F_z	2.21	kN	3.09	kN
	Moment (x-axis)	M_x	-0.29	kNm	-1.28	kNm
	Moment (y-axis)	M_y	0.00	kNm	0.00	kNm
	Moment (z-axis)	M_z	0.00	kNm	0.00	kNm
<i>FLS Combinations</i>						
	Force (x-direction)	F_x	0.00	kN	0.00	kN
	Force (y-direction)	F_y	-12.42	kN	-17.39	kN
	Force (z-direction)	F_z	2.21	kN	3.09	kN
	Moment (x-axis)	M_x	-2.77	kNm	-8.23	kNm
	Moment (y-axis)	M_y	0.00	kNm	0.00	kNm
	Moment (z-axis)	M_z	0.00	kNm	0.00	kNm

9.3.1 ULS Member Verification: Member Internal Load Distributions

Beam:

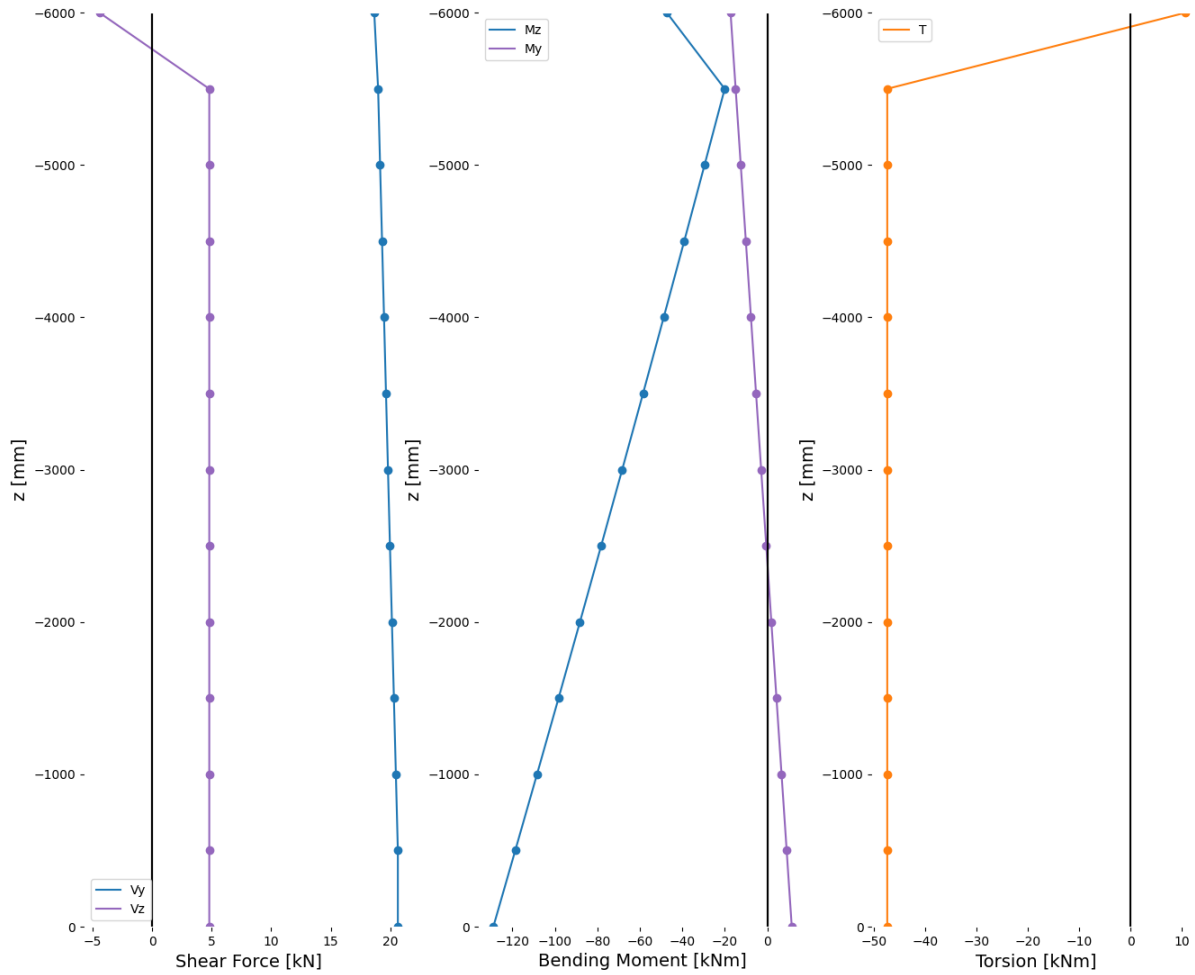


Left Column:



The reason there is a kink in the internal load diagram at the top of the column (uppermost node) has to do with the way the Python script converts the nodal values from the global to the local axes. Unfortunately there is no time to change the python script, therefore the values of the top node should be disregarded, fortunately the governing cross-section is always located at the bottom of the column.

Right Column:



The reason there is a kink in the internal load diagram at the top of the column (uppermost node) has to do with the way the Python script converts the nodal values from the global to the local axes. Unfortunately there is no time to change the python script, therefore the values of the top node should be disregarded, fortunately the governing cross-section is always located at the bottom of the column.

9.3.2 ULS Member Verification: Summary

Beam Verification		Symbol	Value	Unit
<i>Governing Loads</i>				
	Axial action	N_{Ed}	5	kN
	Shear action y-direction	V_{yEd}	16	kN
	Shear action z-direction	V_{zEd}	4	kN
	Torsion action	T_{Ed}	11	kNm
	Bending moment action y-axis	M_{yEd}	19	kNm
	Bending moment action z-axis	M_{zEd}	103	kNm
<i>Individual Resistance</i>				
	Axial	N_{pRd}	2660	kN
	Shear	V_{pRd}	768	kN
	Torsion	T_{Rd}	134	kNm
	Bending	M_{Rd}	188	kNm
<hr/>				
<i>Individual Unity Checks</i>				
	Axial	[-]	0.00	[-]
	Shear	[-]	0.65	[-]
	Torsion	[-]	0.08	[-]
	Bending	[-]	0.02	[-]
<i>Interaction Unity Check</i>				
	Axial+Shear+Torsion+Bending	[-]	0.21	[-]
<i>Stability Unity Check</i>				
	Lateral torsional buckling	[-]	0.66	[-]
<hr/>				
Column Verification		Symbol	Value	Unit
<i>Governing Loads</i>				
	Axial action	N_{Ed}	8	kN
	Shear action y-direction	V_{yEd}	33	kN
	Shear action z-direction	V_{zEd}	5	kN
	Torsion action	T_{Ed}	52	kNm
	Bending moment action y-axis	M_{yEd}	8	kNm
	Bending moment action z-axis	M_{zEd}	196	kNm
<i>Individual Resistance</i>				
	Axial	N_{pRd}	3268	kN
	Shear	V_{pRd}	944	kN
	Torsion	T_{Rd}	159	kNm
	Bending	M_{Rd}	228	kNm
<hr/>				
<i>Individual Unity Checks</i>				
	Axial	[-]	0.00	[-]
	Shear	[-]	0.89	[-]
	Torsion	[-]	0.33	[-]
	Bending	[-]	0.05	[-]
<i>Interaction Unity Check</i>				
	Axial+Shear+Torsion+Bending	[-]	0.36	[-]
<i>Stability Unity Check</i>				
	Flexural buckling	[-]	0.02	[-]

9.3.3 ULS Joint Design

Joint Loads ULS	Symbol	Value	Unit
<i>Cross-Sectional Loads</i>			
Axial action	N_{Ed}	-4.80	kN
Shear action y-direction	V_{yEd}	-30.44	kN
Shear action z-direction	V_{zEd}	7.65	kN
Torsion action	T_{Ed}	-5.32	kNm
Bending moment action y-axis	M_{yEd}	-13.65	kNm
Bending moment action z-axis	M_{zEd}	-22.14	kNm



Plates	✓	0.0 < 5.0%
Preloaded bolts	✓	22.7 < 100%
Welds	✓	26.3 < 100%

9.3.4 FLS Joint Design

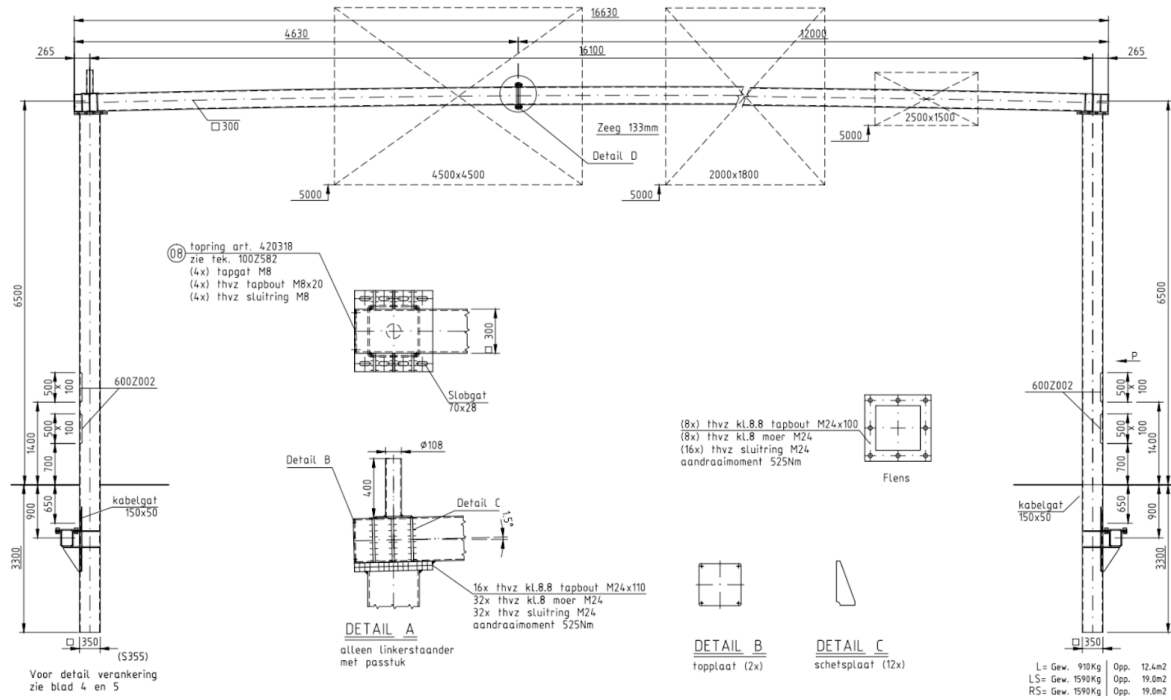
Joint Loads FLS	Symbol	Value	Unit
<i>Cross-Sectional Loads</i>			
Axial action	N_{Ed}	-4.38	kN
Shear action y-direction	V_{yEd}	-18.94	kN
Shear action z-direction	V_{zEd}	6.97	kN
Torsion action	T_{Ed}	-3.30	kNm
Bending moment action y-axis	M_{yEd}	-12.44	kNm
Bending moment action z-axis	M_{zEd}	-13.75	kNm

Property	Column-to-End-Plate	Beam-to-End-Plate	Horizontal Stiffener	Vertical Stiffener
<i>Action</i>				
Perpendicular normal stress	121.5 MPa	88.9 MPa	42.6 MPa	66.3 MPa
Perpendicular shear stress	66.1 MPa	46.8 MPa	38.0 MPa	62.8 MPa
Parallel shear stress	117.4 Mpa	208.7 Mpa	36.8 Mpa	80.1 Mpa
<i>Verification</i>				
Eurocode normal stress fatigue damage	0.60 [-]	0.00 [-]	0.00 [-]	0.00 [-]
Eurocode shear stress fatigue damage	0.16 [-]	0.45 [-]	0.00 [-]	0.00 [-]
ROK normal stress fatigue damage	1.63 [-]	0.00 [-]	0.00 [-]	0.00 [-]
ROK shear stress fatigue damage	0.82 [-]	3.12 [-]	0.00 [-]	0.04 [-]

9.3.5 SLS Deflections

Property	Symbol	Value	Unit
<i>Deflections</i>			
Beam maximum deflection [mm]	U_{beam}	62	[-]
Column maximum deflection [mm]	U_{column}	36	[-]
<i>Deflection Limits</i>			
Beam deflection limit [mm]	$U_{beam,max}$	64	[-]
Column deflection limit [mm]	$U_{column,max}$	40	[-]

9.4 Frame #3

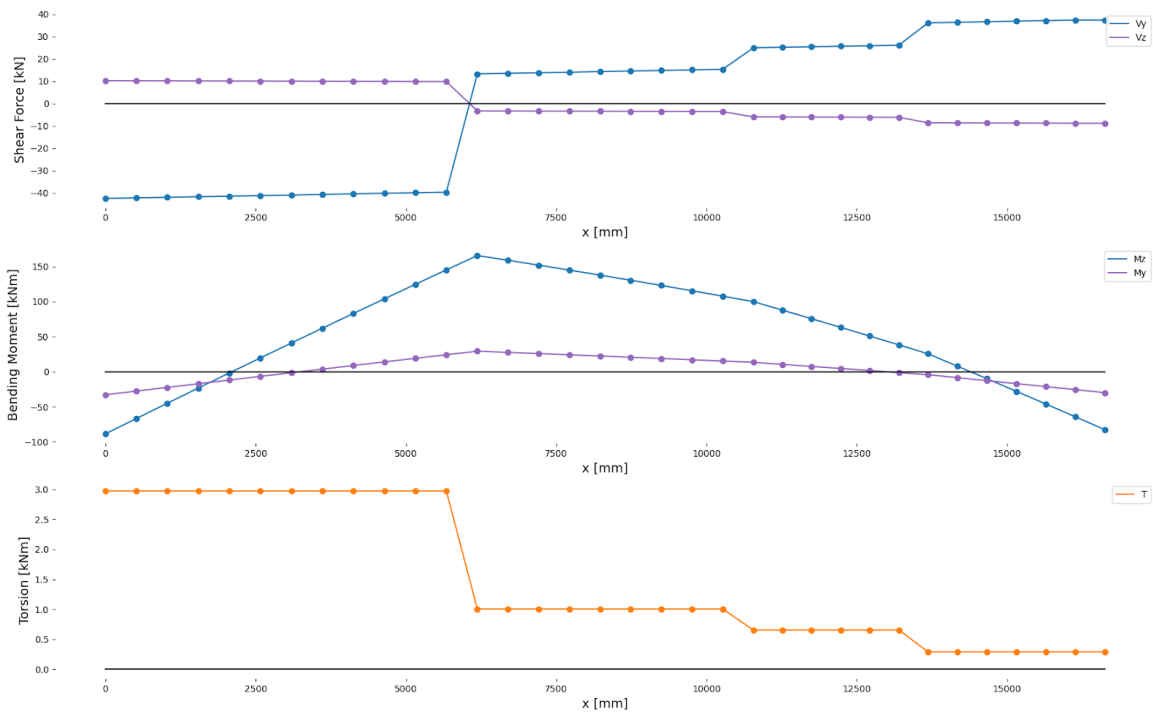


Geometry	Symbol	Value	Unit
<i>Frame</i>			
Span	L	16.6	m
Height	H	6.5	m
Beam profile	[-]	SHS 300/8	[-]
Column Profile	[-]	SHS 350/10	[-]
<i>Sign1</i>			
Structure height	z	6.50	m
Sign width	b	4.50	m
Sign height	h	4.50	m
Bottom of sign height	z_b	4.30	m
Beam width	w_b	0.30	m
<i>Sign2</i>			
Structure height	z	6.50	m
Sign width	b	2.00	m
Sign height	h	1.80	m
Bottom of sign height	z_b	5.60	m
Beam width	w_b	0.30	m
<i>Sign3</i>			
Structure height	z	6.50	m
Sign width	b	2.50	m
Sign height	h	1.50	m
Bottom of sign height	z_b	5.80	m
Beam width	w_b	0.30	m

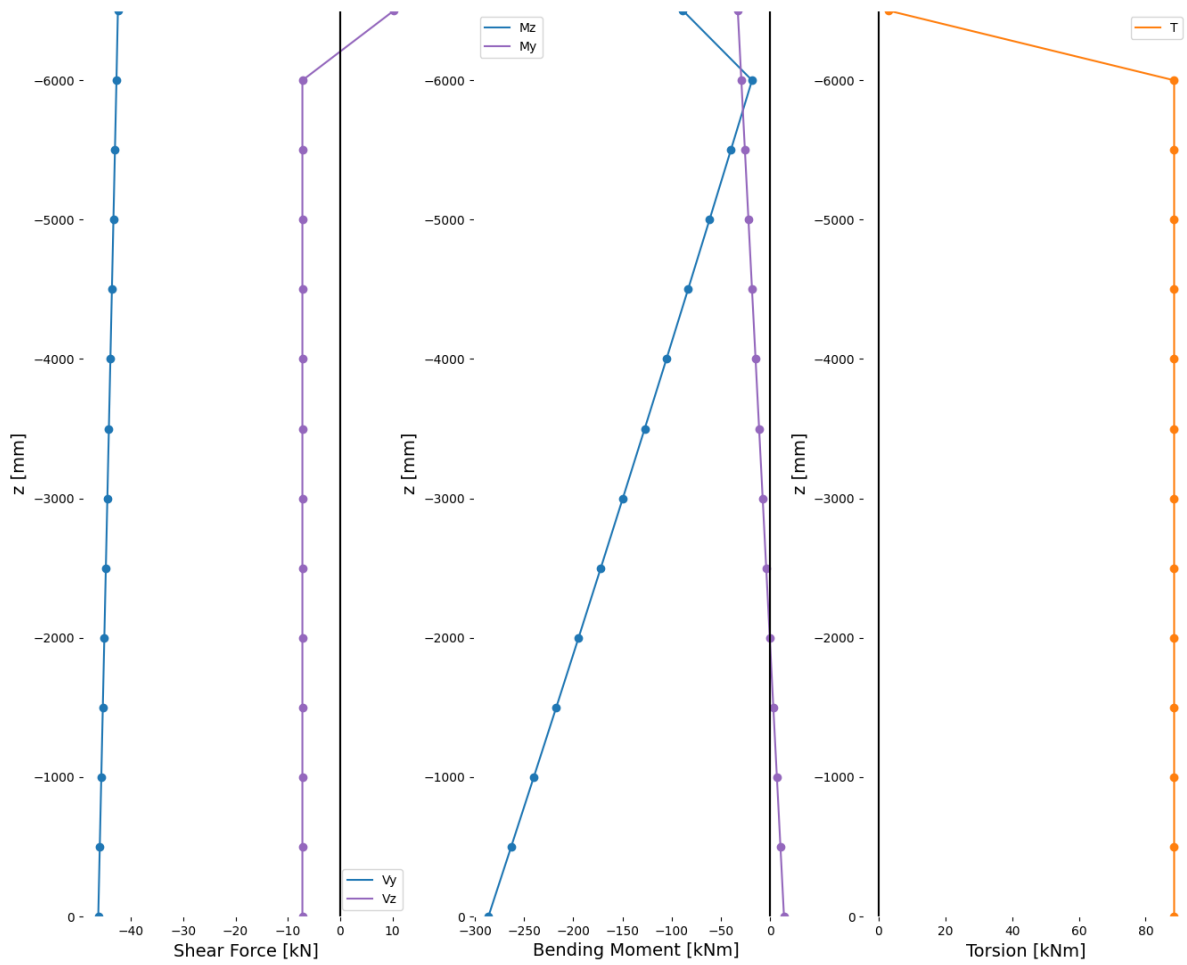
Loads	Symbol	Sign 1		Sign 2		Sign 3		
		Value	Unit	Value	Unit	Value	Unit	
<i>Computed Loads on Signs</i>								
	Wind force	F_w	35.14	kN	6.25	kN	6.51	kN
	Self-weight	F_{self}	5.96	kN	1.06	kN	1.10	kN
<i>ULS Combination</i>								
	Force (x-direction)	F_x	0.00	kN	0.00	kN	0.00	kN
	Force (y-direction)	F_y	-52.71	kN	-9.37	kN	-9.76	kN
	Force (z-direction)	F_z	7.15	kN	1.27	kN	1.32	kN
	Moment (x-axis)	M_x	1.07	kNm	0.19	kNm	0.20	kNm
	Moment (y-axis)	M_y	0.00	kNm	0.00	kNm	0.00	kNm
	Moment (z-axis)	M_z	0.00	kNm	0.00	kNm	0.00	kNm
<i>SLS Combination</i>								
	Force (x-direction)	F_x	0.00	kN	0.00	kN	0.00	kN
	Force (y-direction)	F_y	-7.03	kN	-1.25	kN	-1.30	kN
	Force (z-direction)	F_z	5.96	kN	1.06	kN	1.10	kN
	Moment (x-axis)	M_x	0.89	kNm	0.16	kNm	0.17	kNm
	Moment (y-axis)	M_y	0.00	kNm	0.00	kNm	0.00	kNm
	Moment (z-axis)	M_z	0.00	kNm	0.00	kNm	0.00	kNm
<i>FLS Combinations</i>								
	Force (x-direction)	F_x	0.00	kN	0.00	kN	0.00	kN
	Force (y-direction)	F_y	-35.14	kN	-6.25	kN	-6.51	kN
	Force (z-direction)	F_z	5.96	kN	1.06	kN	1.10	kN
	Moment (x-axis)	M_x	0.89	kNm	0.16	kNm	0.17	kNm
	Moment (y-axis)	M_y	0.00	kNm	0.00	kNm	0.00	kNm
	Moment (z-axis)	M_z	0.00	kNm	0.00	kNm	0.00	kNm

9.4.1 ULS Member Verification: Member Internal Load Distributions

Beam:

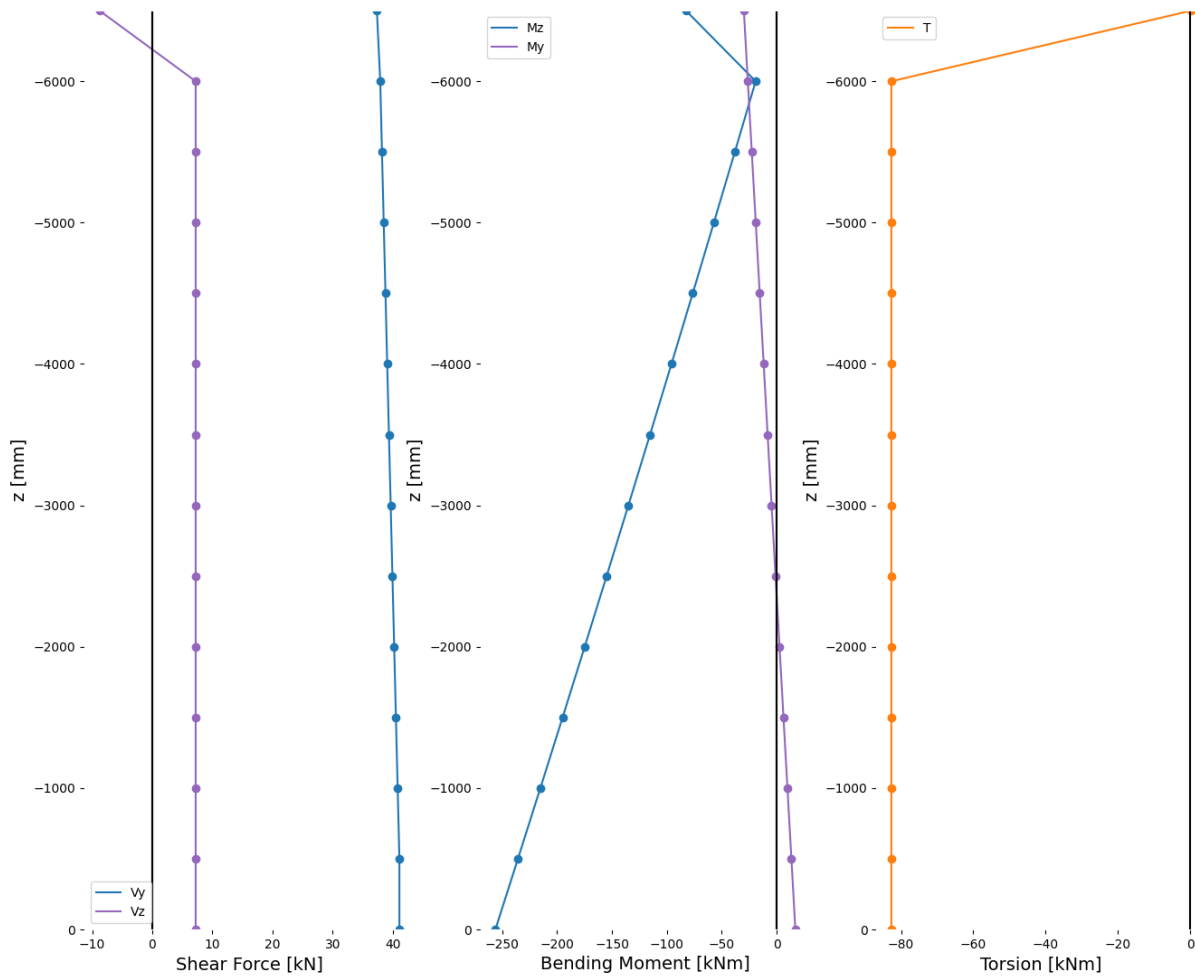


Left Column:



The reason there is a kink in the internal load diagram at the top of the column (uppermost node) has to do with the way the Python script converts the nodal values from the global to the local axes. Unfortunately there is no time to change the python script, therefore the values of the top node should be disregarded, fortunately the governing cross-section is always located at the bottom of the column.

Right Column:



The reason there is a kink in the internal load diagram at the top of the column (uppermost node) has to do with the way the Python script converts the nodal values from the global to the local axes. Unfortunately there is no time to change the python script, therefore the values of the top node should be disregarded, fortunately the governing cross-section is always located at the bottom of the column.

9.4.2 ULS Member Verification: Summary

Beam Verification		Symbol	Value	Unit
<i>Governing Loads</i>				
	Axial action	N_{Ed}	7	kN
	Shear action y-direction	V_{yEd}	13	kN
	Shear action z-direction	V_{zEd}	3	kN
	Torsion action	T_{Ed}	1	kNm
	Bending moment action y-axis	M_{yEd}	29	kNm
	Bending moment action z-axis	M_{zEd}	166	kNm
<i>Individual Resistance</i>				
	Axial	N_{plRd}	3293	kN
	Shear	V_{plRd}	951	kN
	Torsion	T_{Rd}	265	kNm
	Bending	M_{Rd}	311	kNm
<hr/>				
<i>Individual Unity Checks</i>				
	Axial	[-]	0.00	[-]
	Shear	[-]	0.63	[-]
	Torsion	[-]	0.00	[-]
	Bending	[-]	0.01	[-]
<i>Interaction Unity Check</i>				
	Axial+Shear+Torsion+Bending	[-]	0.19	[-]
<i>Stability Unity Check</i>				
	Lateral torsional buckling	[-]	0.52	[-]
<hr/>				
Column Verification		Symbol	Value	Unit
<i>Governing Loads</i>				
	Axial action	N_{Ed}	11	kN
	Shear action y-direction	V_{yEd}	46	kN
	Shear action z-direction	V_{zEd}	7	kN
	Torsion action	T_{Ed}	89	kNm
	Bending moment action y-axis	M_{yEd}	14	kNm
	Bending moment action z-axis	M_{zEd}	286	kNm
<i>Individual Resistance</i>				
	Axial	N_{plRd}	4790	kN
	Shear	V_{plRd}	1383	kN
	Torsion	T_{Rd}	448	kNm
	Bending	M_{Rd}	525	kNm
<hr/>				
<i>Individual Unity Checks</i>				
	Axial	[-]	0.00	[-]
	Shear	[-]	0.57	[-]
	Torsion	[-]	0.20	[-]
	Bending	[-]	0.04	[-]
<i>Interaction Unity Check</i>				
	Axial+Shear+Torsion+Bending	[-]	0.15	[-]
<i>Stability Unity Check</i>				
	Flexural buckling	[-]	0.01	[-]

9.4.3 ULS Joint Design

Joint Loads ULS	Symbol	Value	Unit
<i>Cross-Sectional Loads</i>			
Axial action	N_{Ed}	-7.22	kN
Shear action y-direction	V_{yEd}	-41.97	kN
Shear action z-direction	V_{zEd}	10.17	kN
Torsion action	T_{Ed}	2.97	kNm
Bending moment action y-axis	M_{yEd}	-22.33	kNm
Bending moment action z-axis	M_{zEd}	-44.87	kNm



Plates ✓ 0.0 < 5.0%
 Preloaded bolts ✓ 53.6 < 100%
 Welds ✓ 48.2 < 100%

9.4.4 FLS Joint Design

Joint Loads FLS	Symbol	Value	Unit
<i>Cross-Sectional Loads</i>			
Axial action	N_{Ed}	-6.60	kN
Shear action y-direction	V_{yEd}	-25.65	kN
Shear action z-direction	V_{zEd}	9.30	kN
Torsion action	T_{Ed}	2.32	kNm
Bending moment action y-axis	M_{yEd}	-20.39	kNm
Bending moment action z-axis	M_{zEd}	-28.03	kNm

Property	Column-to-End-Plate	Beam-to-End-Plate	Horizontal Stiffener	Vertical Stiffener
<i>Action</i>				
Perpendicular normal stress	89.6 MPa	44.2 MPa	38.2 MPa	19.9 MPa
Perpendicular shear stress	53 MPa	5.9 MPa	39.6 MPa	19 MPa
Parallel shear stress	12.7 Mpa	118.3 Mpa	19.0 Mpa	17.2 Mpa
<i>Verification</i>				
Eurocode normal stress fatigue damage	0.12 [-]	0.00 [-]	0.00 [-]	0.00 [-]
Eurocode shear stress fatigue damage	0.00 [-]	0.01 [-]	0.00 [-]	0.00 [-]
ROK normal stress fatigue damage	0.51 [-]	0.00 [-]	0.00 [-]	0.00 [-]
ROK shear stress fatigue damage	0.00 [-]	0.09 [-]	0.00 [-]	0.00 [-]

9.4.5 SLS Deflections

Property	Symbol	Value	Unit
<i>Deflections</i>			
Beam maximum deflection [mm]	u_{beam}	25	[-]
Column maximum deflection [mm]	u_{column}	16	[-]
<i>Deflection Limits</i>			
Beam deflection limit [mm]	$u_{beam,max}$	64	[-]
Column deflection limit [mm]	$u_{column,max}$	40	[-]

9.5 Cost Comparison

Property	Frame #1	Frame #2	Frame #3
Joint	357 €	164 €	357 €
Members	4145 €	2908 €	4432 €
Total	4502 €	3072 €	4789 €

Project: Case Study
Project no:
Author: Bela Stamenkovits

Project data

Project name	Case Study
Project number	
Author	Bela Stamenkovits
Description	Steel Hollow Section Portal Frame Case Study
Date	12-5-2022
Design code	EN

Material

Steel	S 355
Concrete	C25/30

Project: Case Study
 Project no:
 Author: Bela Stamenkovits

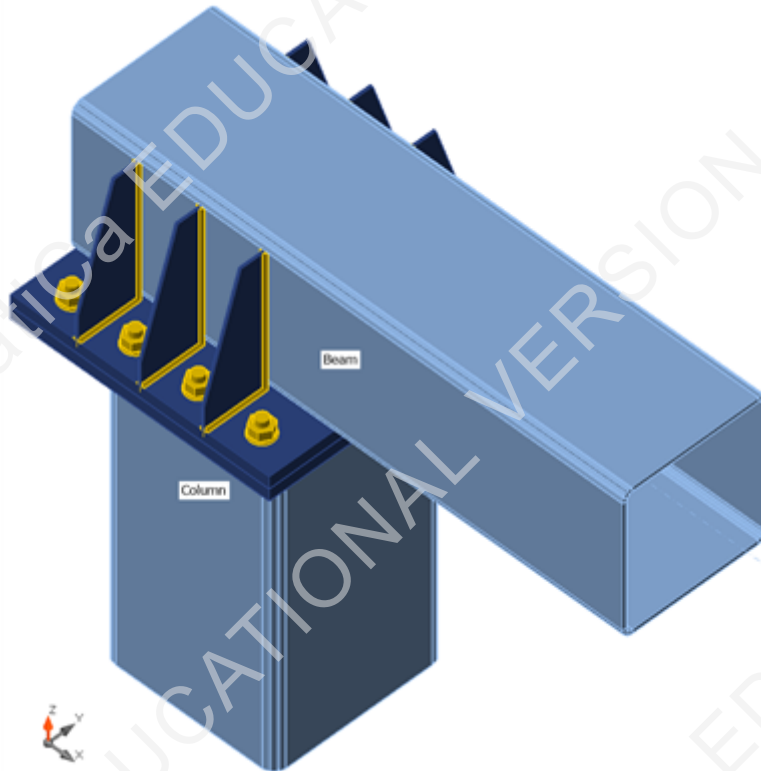
Project item Frame #1 ULS

Design

Name: Frame #1 ULS
 Description:
 Analysis: Stress, strain/ loads in equilibrium

Beams and columns

Name	Cross-section	β - Direction [°]	γ - Pitch [°]	α - Rotation [°]	Offset ex [mm]	Offset ey [mm]	Offset ez [mm]	Forces in
Beam	1 - SHS300/300/8.0	0.0	0.0	180.0	-265	0	0	Node
Column	5 - SHS350/350/10.0	0.0	90.0	0.0	0	0	0	Node



Cross-sections

Name	Material
1 - SHS300/300/8.0	S 355
5 - SHS350/350/10.0	S 355

Bolts

Name	Bolt assembly	Diameter [mm]	f_u [MPa]	Gross area [mm ²]
M24 10.9	M24 10.9	24	1000.0	452

Project: Case Study
 Project no:
 Author: Bela Stamenkovits

Load effects (forces in equilibrium)

Name	Member	N [kN]	Vy [kN]	Vz [kN]	Mx [kNm]	My [kNm]	Mz [kNm]
ULS load	Beam	-5.0	-31.9	7.8	-5.9	-14.4	-26.6
	Column	0.0	0.0	0.0	0.0	0.0	0.0

Check

Summary

Name	Value	Status
Analysis	100.0%	OK
Plates	0.0 < 5.0%	OK
Preloaded bolts	41.6 < 100%	OK
Welds	41.8 < 100%	OK
Buckling	Not calculated	
GMNA	Calculated	

Plates

Name	Thickness [mm]	Loads	σ_{Ed} [MPa]	ϵ_{pl} [%]	σ_{cEd} [MPa]	Status
Beam	8.0	ULS load	117.3	0.0	0.0	OK
Column	10.0	ULS load	58.4	0.0	0.0	OK
End Plate Beam	25.0	ULS load	46.3	0.0	3.7	OK
End Plate Column	25.0	ULS load	39.2	0.0	4.6	OK
Stiffeners +Ya	5.0	ULS load	48.9	0.0	0.0	OK
Stiffeners +Yb	5.0	ULS load	42.8	0.0	0.0	OK
Stiffeners +Yc	5.0	ULS load	66.2	0.0	0.0	OK
Stiffeners -Ya	5.0	ULS load	15.7	0.0	0.0	OK
Stiffeners -Yb	5.0	ULS load	27.0	0.0	0.0	OK
Stiffeners -Yc	5.0	ULS load	51.7	0.0	0.0	OK
Cap Plate	12.0	ULS load	25.9	0.0	0.0	OK

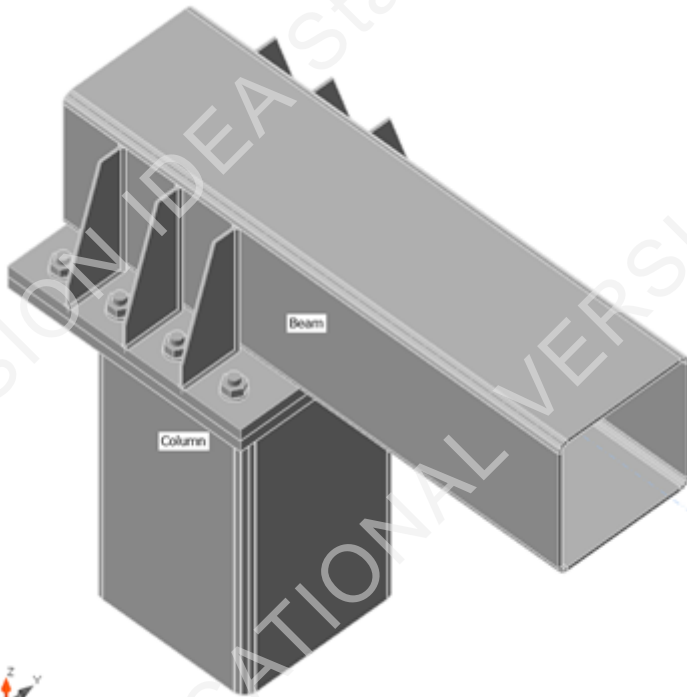
Design data

Material	f_y [MPa]	ϵ_{lim} [%]
S 355	355.0	5.0

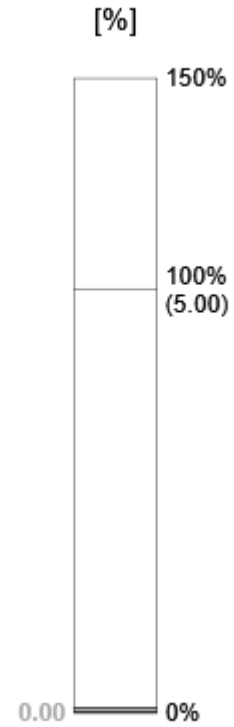
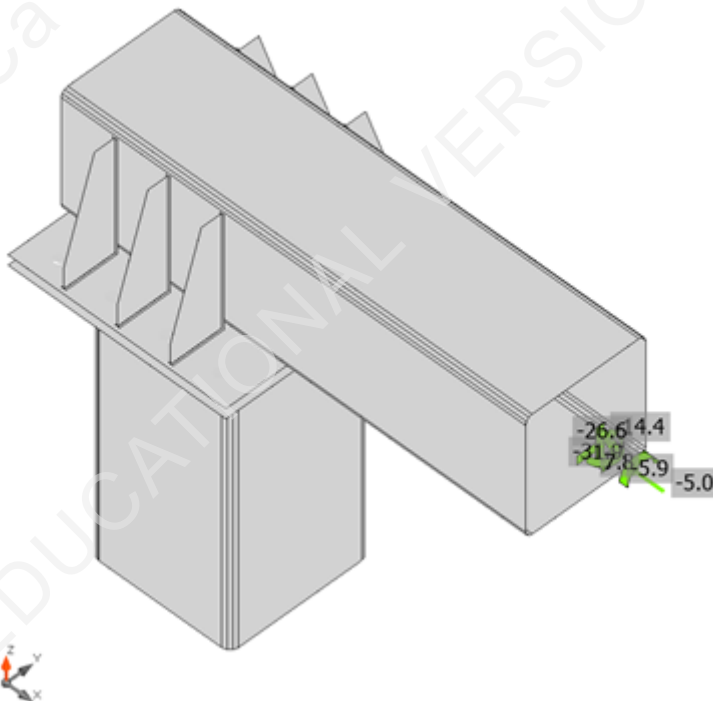
Symbol explanation

ϵ_{pl} Strain
 σ_{Ed} Eq. stress
 σ_{cEd} Contact stress
 f_y Yield strength
 ϵ_{lim} Limit of plastic strain

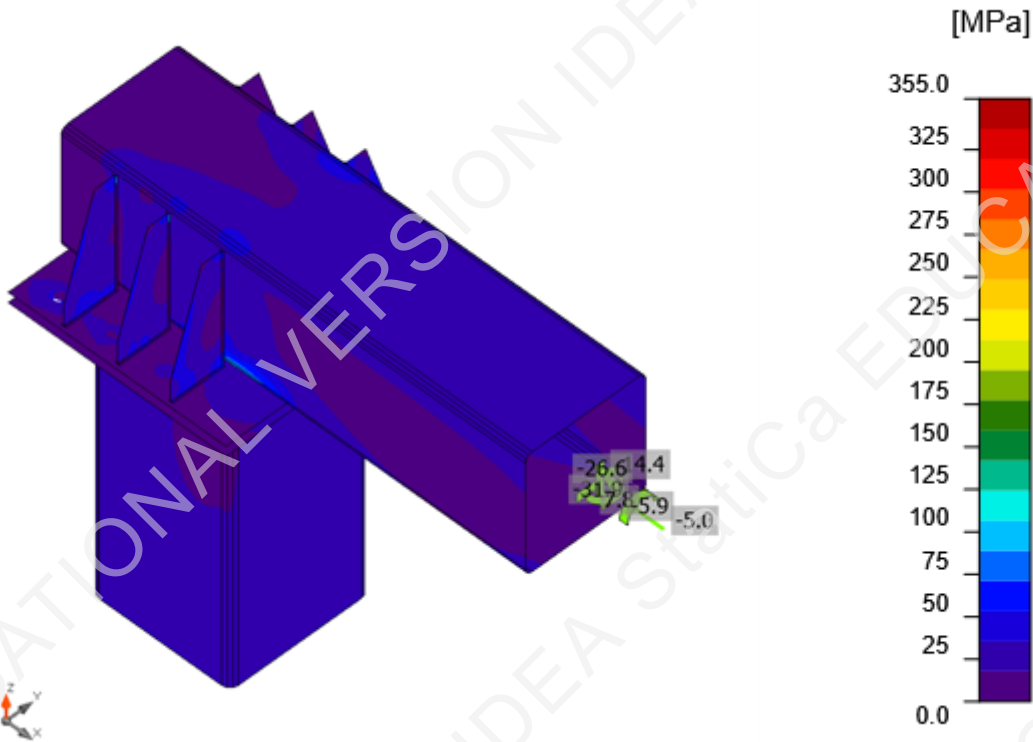
Project: Case Study
Project no:
Author: Bela Stamenkovits



Overall check, ULS load



Strain check, ULS load



Equivalent stress, ULS load

Preloaded bolts

	Name	Bolt assembly	Loads	$F_{t,Ed}$ [kN]	V [kN]	$B_{p,Rd}$ [kN]	$F_{t,Rd}$ [kN]	$F_{s,Rd}$ [kN]	U_{t_t} [%]	U_{t_s} [%]	Status
	B5	M24 10.9 - 1	ULS load	0.0	12.7	796.2	254.2	37.4	0.0	34.1	OK
	B6	M24 10.9 - 1	ULS load	0.0	13.1	796.2	254.2	37.4	0.0	35.0	OK
	B7	M24 10.9 - 1	ULS load	1.0	8.5	796.2	254.2	37.2	0.4	22.9	OK
	B8	M24 10.9 - 1	ULS load	4.5	3.9	796.2	254.2	36.8	1.8	10.7	OK
	B9	M24 10.9 - 1	ULS load	20.4	2.4	796.2	254.2	34.9	8.0	6.7	OK
	B10	M24 10.9 - 1	ULS load	18.9	10.2	796.2	254.2	35.1	7.4	29.1	OK
	B11	M24 10.9 - 1	ULS load	8.2	13.2	796.2	254.2	36.4	3.2	36.2	OK
	B12	M24 10.9 - 1	ULS load	2.5	15.4	796.2	254.2	37.1	1.0	41.6	OK

Symbol explanation

- $F_{t,Rd}$ Bolt tension resistance EN 1993-1-8 tab. 3.4
- $F_{t,Ed}$ Tension force
- $B_{p,Rd}$ Punching shear resistance
- V Resultant of shear forces V_y and V_z in shear planes transferred by friction
- $F_{v,Rd}$ Bolt shear resistance EN_1993-1-8 table 3.4
- $F_{b,Rd}$ Plate bearing resistance EN 1993-1-8 tab. 3.4
- $F_{s,Rd}$ Design slip resistance EN_1993-1-8 chapter 3.9
- F_{pc} Pretension force
- U_{t_t} Utilization in tension
- U_{t_s} Utilization in shear

Welds (Plastic redistribution)

Item	Edge	Throat th. [mm]	Length [mm]	Loads	$\sigma_{w,Ed}$ [MPa]	ϵ_{pl} [%]	σ_{\perp} [MPa]	τ_{\parallel} [MPa]	τ_{\perp} [MPa]	Ut [%]	Ut _c [%]	Status
End Plate Column	Column	▲6.0	1324	ULS load	138.3	0.0	96.2	8.8	-56.7	31.8	8.6	OK
Beam-w 2	Beam	▲4.0▲	840	ULS load	83.1	0.0	32.5	27.7	34.4	19.1	3.7	OK
Beam-w 4	Beam	▲4.0▲	840	ULS load	86.4	0.0	-34.3	-30.2	-34.4	19.8	2.9	OK
Beam-arc 6	Beam	▲4.0▲	1114	ULS load	41.6	0.0	13.0	-18.1	13.9	9.5	1.1	OK
		▲4.0▲	840	ULS load	84.9	0.0	34.8	-30.2	-32.9	19.5	4.4	OK
		▲4.0▲	840	ULS load	86.6	0.0	-34.5	30.4	34.4	19.9	2.4	OK
		▲4.0▲	1114	ULS load	48.4	0.0	17.5	20.0	-16.7	11.1	0.9	OK
End Plate Beam	Stiffeners +Ya	▲4.0▲	125	ULS load	47.2	0.0	22.6	-13.3	19.8	10.8	7.2	OK
		▲4.0▲	125	ULS load	44.9	0.0	19.3	7.6	-22.1	10.3	6.1	OK
End Plate Beam	Stiffeners +Yb	▲4.0▲	125	ULS load	42.3	0.0	14.2	-18.3	13.9	9.7	6.5	OK
		▲4.0▲	125	ULS load	43.5	0.0	11.8	-21.2	-11.6	10.0	6.1	OK
End Plate Beam	Stiffeners +Yc	▲4.0▲	125	ULS load	41.2	0.0	-3.6	23.4	-3.9	9.5	6.3	OK
		▲4.0▲	125	ULS load	48.9	0.0	-22.8	-9.6	23.1	11.2	6.4	OK
End Plate Beam	Stiffeners - Ya	▲4.0▲	125	ULS load	11.6	0.0	3.7	-5.0	3.9	2.7	1.4	OK
		▲4.0▲	125	ULS load	12.9	0.0	4.3	5.7	-4.1	3.0	1.6	OK
End Plate Beam	Stiffeners - Yb	▲4.0▲	125	ULS load	23.3	0.0	-7.4	-10.9	-6.5	5.3	3.4	OK
		▲4.0▲	125	ULS load	20.0	0.0	-6.7	7.8	7.5	4.6	3.3	OK
End Plate Beam	Stiffeners - Yc	▲4.0▲	125	ULS load	41.9	0.0	-21.3	3.8	-20.5	9.6	6.8	OK
		▲4.0▲	125	ULS load	43.9	0.0	-21.2	-3.0	22.0	10.1	7.3	OK
End Plate Beam	Beam-w 3	▲6.0	530	ULS load	115.1	0.0	12.4	27.2	60.2	26.4	8.7	OK
End Plate Beam	Beam-w 3	▲6.0	530	ULS load	181.9	0.0	-35.0	103.0	3.3	41.8	7.2	OK

Design data

	β_w [-]	$\sigma_{w,Rd}$ [MPa]	0.9 σ [MPa]
S 355	0.90	435.6	352.8

Project: Case Study
 Project no:
 Author: Bela Stamenkovits

Symbol explanation

ϵ_{Pl}	Strain
$\sigma_{w,Ed}$	Equivalent stress
$\sigma_{w,Rd}$	Equivalent stress resistance
σ_{\perp}	Perpendicular stress
τ_{\parallel}	Shear stress parallel to weld axis
τ_{\perp}	Shear stress perpendicular to weld axis
0.9σ	Perpendicular stress resistance - $0.9 \cdot f_u / \gamma_{M2}$
β_w	Corelation factor EN 1993-1-8 tab. 4.1
U_t	Utilization
U_{tc}	Weld capacity utilization

Buckling

Buckling analysis was not calculated.

Code settings

Item	Value	Unit	Reference
Y_{M0}	1.00	-	EN 1993-1-1: 6.1
Y_{M1}	1.00	-	EN 1993-1-1: 6.1
Y_{M2}	1.25	-	EN 1993-1-1: 6.1
Y_{M3}	1.25	-	EN 1993-1-8: 2.2
Y_C	1.50	-	EN 1992-1-1: 2.4.2.4
Y_{Inst}	1.20	-	EN 1992-4: Table 4.1
Joint coefficient β_j	0.67	-	EN 1993-1-8: 6.2.5
Effective area - influence of mesh size	0.10	-	
Friction coefficient - concrete	0.25	-	EN 1993-1-8
Friction coefficient in slip-resistance	0.30	-	EN 1993-1-8 tab 3.7
Limit plastic strain	0.05	-	EN 1993-1-5
Weld stress evaluation	Plastic redistribution		
Detailing	No		
Distance between bolts [d]	2.20	-	EN 1993-1-8: tab 3.3
Distance between bolts and edge [d]	1.20	-	EN 1993-1-8: tab 3.3
Concrete breakout resistance check	Both		EN 1992-4: 7.2.1.4 and 7.2.2.5
Use calculated a_b in bearing check.	Yes		EN 1993-1-8: tab 3.4
Cracked concrete	Yes		EN 1992-4
Local deformation check	No		CIDECT DG 1, 3 - 1.1
Local deformation limit	0.03	-	CIDECT DG 1, 3 - 1.1
Geometrical nonlinearity (GMNA)	Yes		Analysis with large deformations for hollow section joints
Braced system	No		EN 1993-1-8: 5.2.2.5

Software info

Application: IDEA StatiCa Connection
 Version: 21.1.1.1638

Project: Case Study
Project no:
Author: Bela Stamenkovits

Developed by IDEA StatiCa



Project: Case Study
Project no:
Author: Bela Stamenkovits

Project data

Project name Case Study
Project number
Author Bela Stamenkovits
Description Steel Hollow Section Portal Frame Case Study
Date 12-5-2022
Design code EN

Material

Steel S 355
Concrete C25/30

Project: Case Study
 Project no:
 Author: Bela Stamenkovits

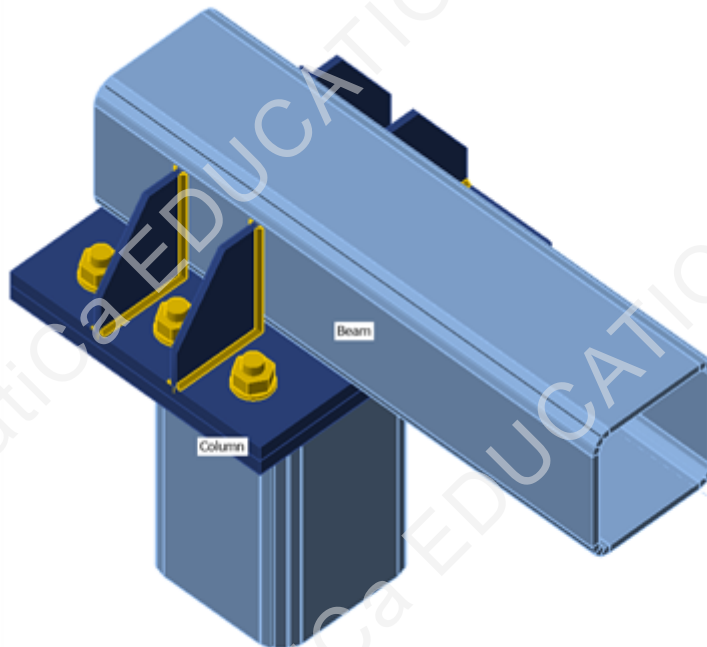
Project item Frame #2 ULS

Design

Name: Frame #2 ULS
 Description:
 Analysis: Stress, strain/ loads in equilibrium

Beams and columns

Name	Cross-section	β - Direction [°]	γ - Pitch [°]	α - Rotation [°]	Offset ex [mm]	Offset ey [mm]	Offset ez [mm]	Forces in
Beam	7 - SHS180/180/10.0	0.0	0.0	180.0	-180	0	0	Node
Column	9 - SHS200/200/12.5	0.0	90.0	0.0	0	0	0	Node



Cross-sections

Name	Material
7 - SHS180/180/10.0	S 355
9 - SHS200/200/12.5	S 355

Bolts

Name	Bolt assembly	Diameter [mm]	f_u [MPa]	Gross area [mm ²]
M24 10.9	M24 10.9	24	1000.0	452

Project: Case Study
 Project no:
 Author: Bela Stamenkovits

Load effects (forces in equilibrium)

Name	Member	N [kN]	Vy [kN]	Vz [kN]	Mx [kNm]	My [kNm]	Mz [kNm]
ULS Load	Beam	-4.8	-30.4	7.7	-5.3	-13.7	-22.2
	Column	0.0	0.0	0.0	0.0	0.0	0.0

Check

Summary

Name	Value	Status
Analysis	100.0%	OK
Plates	0.0 < 5.0%	OK
Preloaded bolts	72.6 < 100%	OK
Welds	98.0 < 100%	OK
Buckling	Not calculated	
GMNA	Calculated	

Plates

Name	Thickness [mm]	Loads	σ_{Ed} [MPa]	ϵ_{pl} [%]	σ_{CEd} [MPa]	Status
Beam	10.0	ULS Load	211.5	0.0	0.0	OK
Column	12.5	ULS Load	104.5	0.0	0.0	OK
End Plate Beam	20.0	ULS Load	100.1	0.0	7.4	OK
End Plate Column	20.0	ULS Load	116.7	0.0	9.1	OK
Stiffeners +Ya	8.0	ULS Load	117.6	0.0	0.0	OK
Stiffeners +Yb	8.0	ULS Load	100.5	0.0	0.0	OK
Stiffeners -Ya	8.0	ULS Load	49.4	0.0	0.0	OK
Stiffeners -Yb	8.0	ULS Load	97.6	0.0	0.0	OK
Cap Plate	12.0	ULS Load	17.4	0.0	0.0	OK

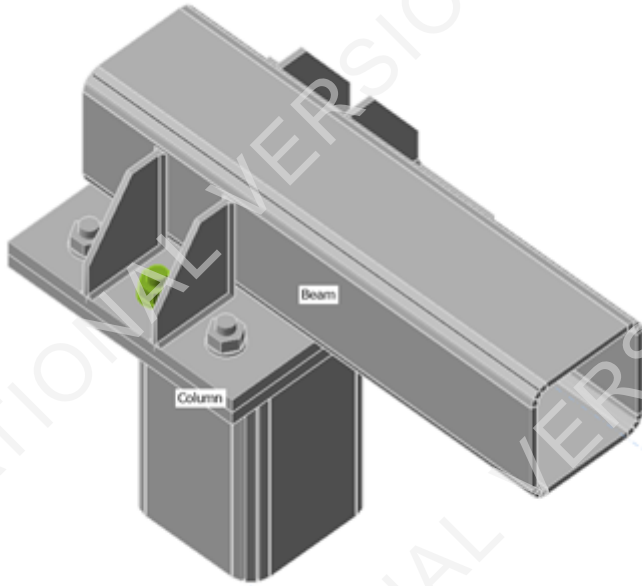
Design data

Material	f_y [MPa]	ϵ_{lim} [%]
S 355	355.0	5.0

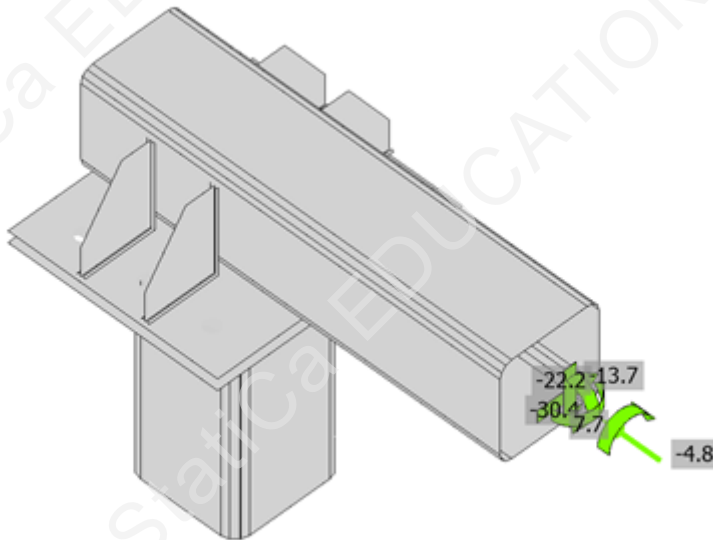
Symbol explanation

ϵ_{pl}	Strain
σ_{Ed}	Eq. stress
σ_{CEd}	Contact stress
f_y	Yield strength
ϵ_{lim}	Limit of plastic strain

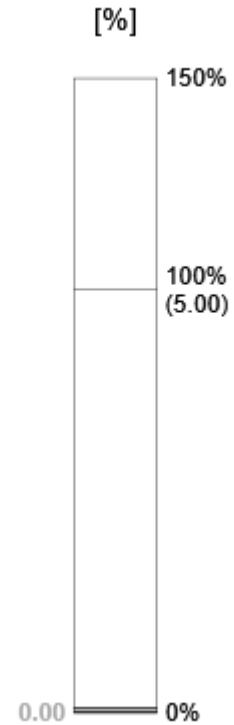
Project: Case Study
Project no:
Author: Bela Stamenkovits

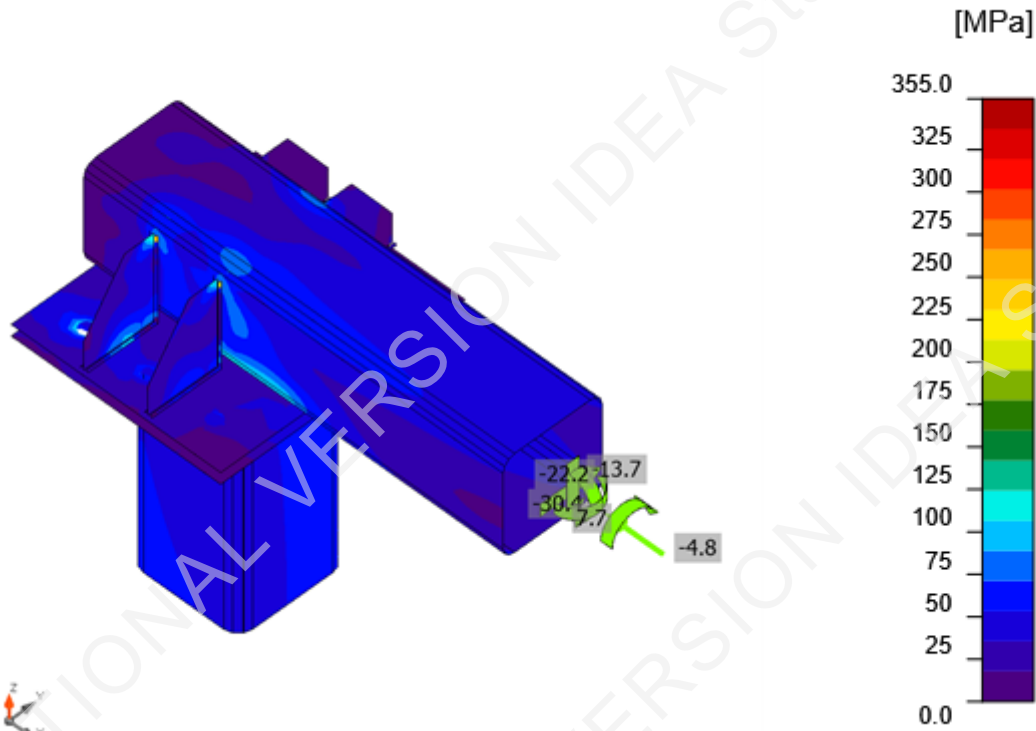


Overall check, ULS Load



Strain check, ULS Load





Equivalent stress, ULS Load

Preloaded bolts

	Name	Bolt assembly	Loads	$F_{t,Ed}$ [kN]	V [kN]	$B_{p,Rd}$ [kN]	$F_{t,Rd}$ [kN]	$F_{s,Rd}$ [kN]	U_{t_t} [%]	U_{t_s} [%]	Status
	B5	M24 10.9 - 1	ULS Load	0.8	21.4	636.9	254.2	37.3	0.3	57.5	OK
	B6	M24 10.9 - 1	ULS Load	4.8	21.2	636.9	254.2	36.8	1.9	57.5	OK
	B7	M24 10.9 - 1	ULS Load	20.3	10.2	636.9	254.2	34.9	8.0	29.1	OK
	B8	M24 10.9 - 1	ULS Load	38.7	13.3	636.9	254.2	32.7	15.2	40.6	OK
	B9	M24 10.9 - 1	ULS Load	5.5	18.7	636.9	254.2	36.7	2.1	50.9	OK
	B10	M24 10.9 - 1	ULS Load	29.5	24.5	636.9	254.2	33.8	11.6	72.6	OK

Symbol explanation

- $F_{t,Rd}$ Bolt tension resistance EN 1993-1-8 tab. 3.4
- $F_{t,Ed}$ Tension force
- $B_{p,Rd}$ Punching shear resistance
- V Resultant of shear forces V_y and V_z in shear planes transferred by friction
- $F_{v,Rd}$ Bolt shear resistance EN_1993-1-8 table 3.4
- $F_{b,Rd}$ Plate bearing resistance EN 1993-1-8 tab. 3.4
- $F_{s,Rd}$ Design slip resistance EN_1993-1-8 chapter 3.9
- F_{pc} Pretension force
- U_{t_t} Utilization in tension
- U_{t_s} Utilization in shear

Welds (Plastic redistribution)

Item	Edge	Throat th. [mm]	Length [mm]	Loads	$\sigma_{w,Ed}$ [MPa]	ϵ_{pl} [%]	σ_{\perp} [MPa]	τ_{\parallel} [MPa]	τ_{\perp} [MPa]	Ut [%]	Ut _c [%]	Status
End Plate Column	Column	▲4.5	705	ULS Load	336.8	0.0	148.8	154.5	-81.0	77.3	31.0	OK
Beam-w 2	Beam	▲4.0	300	ULS Load	222.1	0.0	74.3	91.1	79.4	51.0	10.1	OK
Beam-w 4	Beam	▲4.0	300	ULS Load	153.1	0.0	-55.2	-61.2	-55.2	35.1	8.4	OK
Beam-w 3	Beam	▲4.0	612	ULS Load	38.3	0.0	13.0	16.7	12.4	8.8	2.0	OK
		▲4.0	300	ULS Load	237.8	0.0	84.6	-100.9	-79.3	54.6	12.6	OK
		▲4.0	300	ULS Load	150.2	0.0	-54.7	59.4	54.6	34.5	7.9	OK
		▲4.0	612	ULS Load	51.3	0.0	6.5	27.7	-9.7	11.8	3.2	OK
End Plate Beam	Stiffeners +Ya	▲4.0	120	ULS Load	123.7	0.0	53.1	-43.1	48.0	28.4	16.8	OK
		▲4.0	120	ULS Load	92.0	0.0	35.6	-27.2	-40.7	21.1	12.7	OK
End Plate Beam	Stiffeners +Yb	▲4.0	120	ULS Load	68.4	0.0	33.3	1.2	34.5	15.7	9.5	OK
		▲4.0	120	ULS Load	60.8	0.0	19.7	-27.1	-19.2	14.0	8.9	OK
End Plate Beam	Stiffeners - Ya	▲4.0	120	ULS Load	47.4	0.0	10.5	-25.2	8.9	10.9	5.7	OK
		▲4.0	120	ULS Load	64.6	0.0	14.7	32.4	-16.3	14.8	8.0	OK
End Plate Beam	Stiffeners - Yb	▲4.0	120	ULS Load	78.1	0.0	-31.2	9.4	-40.3	17.9	10.3	OK
		▲4.0	120	ULS Load	69.8	0.0	-41.4	-3.8	32.2	16.0	10.1	OK
End Plate Beam	Beam-w 3	▲6.0	360	ULS Load	262.0	0.0	35.6	44.9	143.0	60.1	17.3	OK
End Plate Beam	Beam-w 3	▲6.0	360	ULS Load	427.0	0.1	-113.8	235.1	34.0	98.0	16.3	OK

Design data

	β_w [-]	$\sigma_{w,Rd}$ [MPa]	0.9σ [MPa]
S 355	0.90	435.6	352.8

Project: Case Study
 Project no:
 Author: Bela Stamenkovits

Symbol explanation

ϵ_{Pl}	Strain
$\sigma_{w,Ed}$	Equivalent stress
$\sigma_{w,Rd}$	Equivalent stress resistance
σ_{\perp}	Perpendicular stress
τ_{\parallel}	Shear stress parallel to weld axis
τ_{\perp}	Shear stress perpendicular to weld axis
0.9σ	Perpendicular stress resistance - $0.9 \cdot f_u / \gamma_{M2}$
β_w	Corelation factor EN 1993-1-8 tab. 4.1
U_t	Utilization
U_{tc}	Weld capacity utilization

Buckling

Buckling analysis was not calculated.

Code settings

Item	Value	Unit	Reference
γ_{M0}	1.00	-	EN 1993-1-1: 6.1
γ_{M1}	1.00	-	EN 1993-1-1: 6.1
γ_{M2}	1.25	-	EN 1993-1-1: 6.1
γ_{M3}	1.25	-	EN 1993-1-8: 2.2
γ_C	1.50	-	EN 1992-1-1: 2.4.2.4
γ_{Inst}	1.20	-	EN 1992-4: Table 4.1
Joint coefficient β_j	0.67	-	EN 1993-1-8: 6.2.5
Effective area - influence of mesh size	0.10	-	
Friction coefficient - concrete	0.25	-	EN 1993-1-8
Friction coefficient in slip-resistance	0.30	-	EN 1993-1-8 tab 3.7
Limit plastic strain	0.05	-	EN 1993-1-5
Weld stress evaluation	Plastic redistribution		
Detailing	No		
Distance between bolts [d]	2.20	-	EN 1993-1-8: tab 3.3
Distance between bolts and edge [d]	1.20	-	EN 1993-1-8: tab 3.3
Concrete breakout resistance check	Both		EN 1992-4: 7.2.1.4 and 7.2.2.5
Use calculated a_b in bearing check.	Yes		EN 1993-1-8: tab 3.4
Cracked concrete	Yes		EN 1992-4
Local deformation check	No		CIDECT DG 1, 3 - 1.1
Local deformation limit	0.03	-	CIDECT DG 1, 3 - 1.1
Geometrical nonlinearity (GMNA)	Yes		Analysis with large deformations for hollow section joints
Braced system	No		EN 1993-1-8: 5.2.2.5

Software info

Application: IDEA StatiCa Connection
 Version: 21.1.1.1638

Project: Case Study
Project no:
Author: Bela Stamenkovits
Developed by IDEA StatiCa



Project: Case Study
Project no:
Author: Bela Stamenkovits

Project data

Project name Case Study
Project number
Author Bela Stamenkovits
Description Steel Hollow Section Portal Frame Case Study
Date 12-5-2022
Design code EN

Material

Steel S 355
Concrete C25/30

Project: Case Study
 Project no:
 Author: Bela Stamenkovits

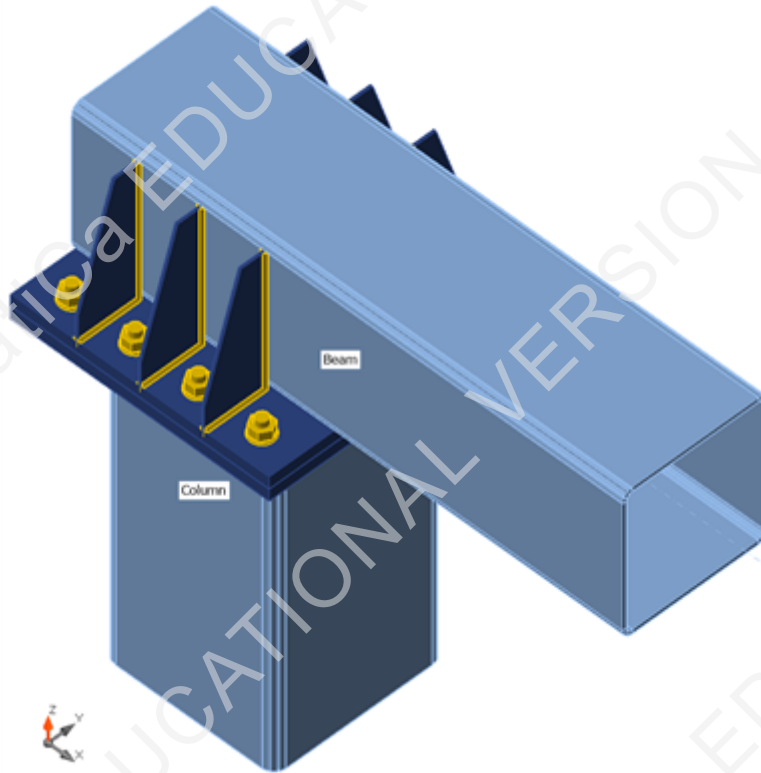
Project item Frame #3 ULS

Design

Name: Frame #3 ULS
 Description:
 Analysis: Stress, strain/ loads in equilibrium

Beams and columns

Name	Cross-section	β - Direction [°]	γ - Pitch [°]	α - Rotation [°]	Offset ex [mm]	Offset ey [mm]	Offset ez [mm]	Forces in
Beam	1 - SHS300/300/8.0	0.0	0.0	180.0	-265	0	0	Node
Column	5 - SHS350/350/10.0	0.0	90.0	0.0	0	0	0	Node



Cross-sections

Name	Material
1 - SHS300/300/8.0	S 355
5 - SHS350/350/10.0	S 355

Bolts

Name	Bolt assembly	Diameter [mm]	f_u [MPa]	Gross area [mm ²]
M24 10.9	M24 10.9	24	1000.0	452

Load effects (forces in equilibrium)

Name	Member	N [kN]	Vy [kN]	Vz [kN]	Mx [kNm]	My [kNm]	Mz [kNm]
ULS Load	Beam	-7.2	-42.0	10.2	3.0	-22.3	-44.9
	Column	0.0	0.0	0.0	0.0	0.0	0.0

Check

Summary

Name	Value	Status
Analysis	100.0%	OK
Plates	0.0 < 5.0%	OK
Preloaded bolts	66.1 < 100%	OK
Welds	65.6 < 100%	OK
Buckling	Not calculated	
GMNA	Calculated	

Plates

Name	Thickness [mm]	Loads	σ_{Ed} [MPa]	ϵ_{pl} [%]	σ_{cEd} [MPa]	Status
Beam	8.0	ULS Load	181.2	0.0	0.0	OK
Column	10.0	ULS Load	77.5	0.0	0.0	OK
End Plate Beam	25.0	ULS Load	59.5	0.0	6.2	OK
End Plate Column	25.0	ULS Load	44.3	0.0	7.0	OK
Stiffeners +Ya	5.0	ULS Load	56.3	0.0	0.0	OK
Stiffeners +Yb	5.0	ULS Load	42.6	0.0	0.0	OK
Stiffeners +Yc	5.0	ULS Load	120.4	0.0	0.0	OK
Stiffeners -Ya	5.0	ULS Load	34.6	0.0	0.0	OK
Stiffeners -Yb	5.0	ULS Load	28.0	0.0	0.0	OK
Stiffeners -Yc	5.0	ULS Load	50.1	0.0	0.0	OK
Cap Plate	12.0	ULS Load	25.1	0.0	0.0	OK

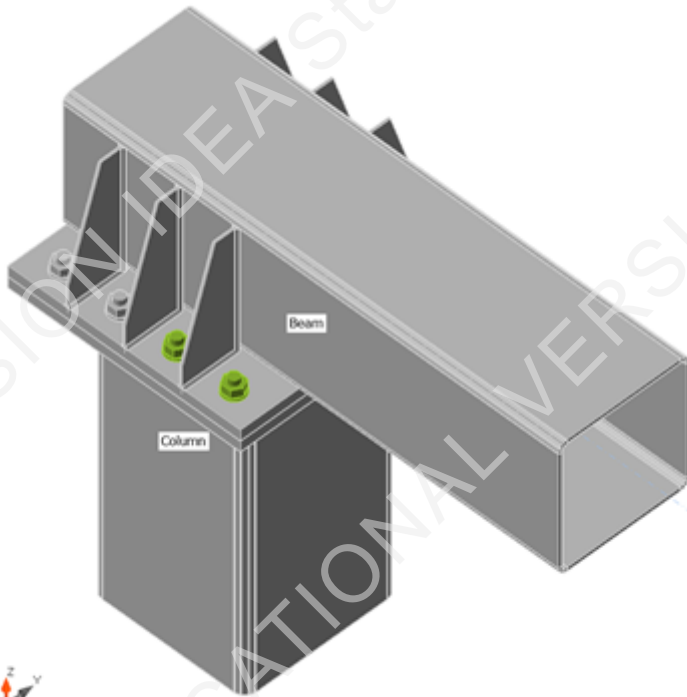
Design data

Material	f_y [MPa]	ϵ_{lim} [%]
S 355	355.0	5.0

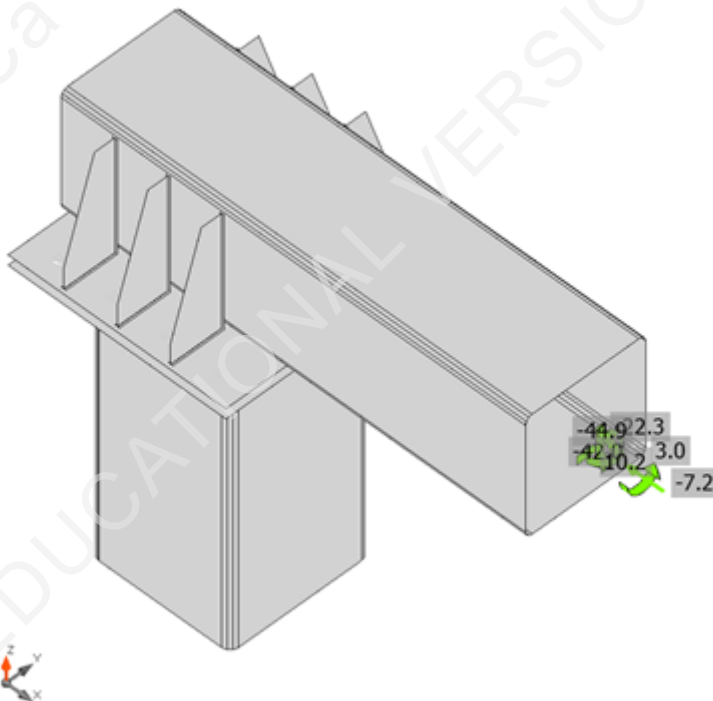
Symbol explanation

ϵ_{pl}	Strain
σ_{Ed}	Eq. stress
σ_{cEd}	Contact stress
f_y	Yield strength
ϵ_{lim}	Limit of plastic strain

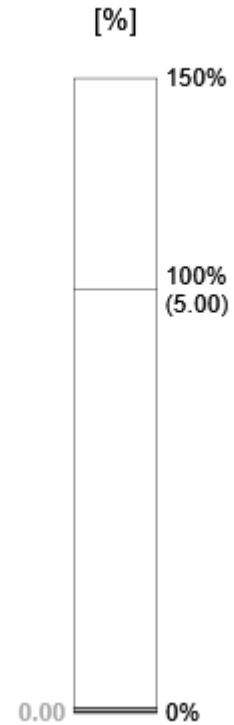
Project: Case Study
Project no:
Author: Bela Stamenkovits

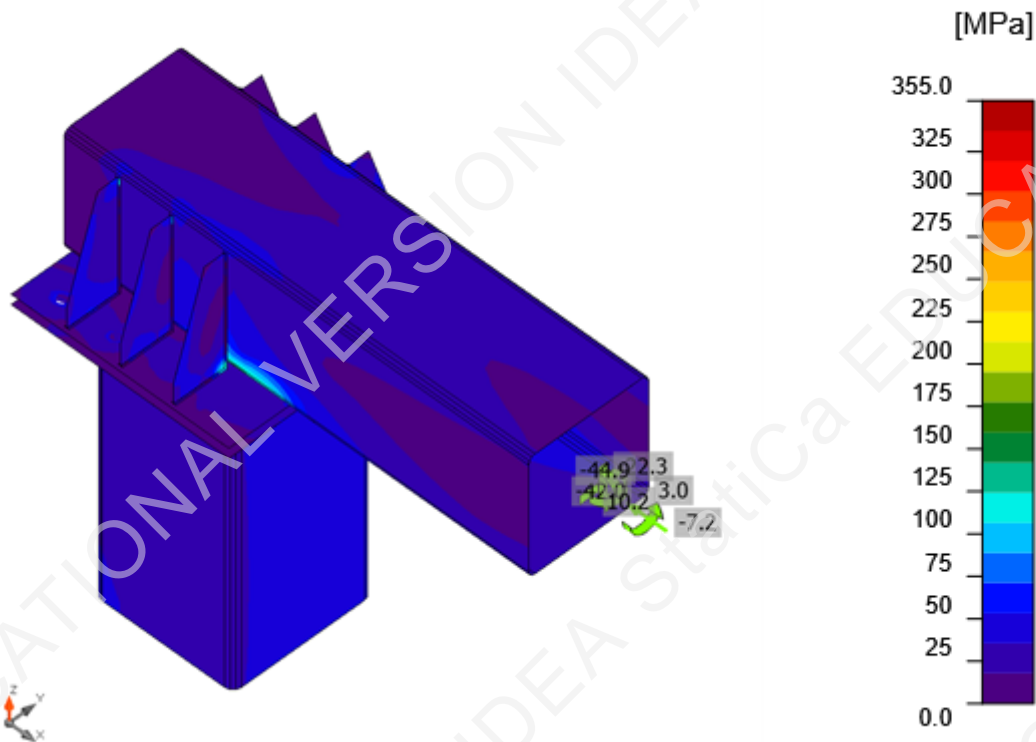


Overall check, ULS Load



Strain check, ULS Load





Equivalent stress, ULS Load

Preloaded bolts

	Name	Bolt assembly	Loads	$F_{t,Ed}$ [kN]	V [kN]	$B_{p,Rd}$ [kN]	$F_{t,Rd}$ [kN]	$F_{s,Rd}$ [kN]	U_{t_t} [%]	U_{t_s} [%]	Status
	B5	M24 10.9 - 1	ULS Load	0.0	20.5	796.2	254.2	37.4	0.0	54.8	OK
	B6	M24 10.9 - 1	ULS Load	0.2	21.5	796.2	254.2	37.3	0.1	57.7	OK
	B7	M24 10.9 - 1	ULS Load	8.5	15.0	796.2	254.2	36.3	3.4	41.3	OK
	B8	M24 10.9 - 1	ULS Load	14.9	10.0	796.2	254.2	35.6	5.9	28.1	OK
	B9	M24 10.9 - 1	ULS Load	25.3	9.0	796.2	254.2	34.3	10.0	26.2	OK
	B10	M24 10.9 - 1	ULS Load	21.5	18.2	796.2	254.2	34.8	8.4	52.4	OK
	B11	M24 10.9 - 1	ULS Load	6.2	22.0	796.2	254.2	36.6	2.4	60.1	OK
	B12	M24 10.9 - 1	ULS Load	1.3	24.6	796.2	254.2	37.2	0.5	66.1	OK

Symbol explanation

- $F_{t,Rd}$ Bolt tension resistance EN 1993-1-8 tab. 3.4
- $F_{t,Ed}$ Tension force
- $B_{p,Rd}$ Punching shear resistance
- V Resultant of shear forces V_y and V_z in shear planes transferred by friction
- $F_{v,Rd}$ Bolt shear resistance EN_1993-1-8 table 3.4
- $F_{b,Rd}$ Plate bearing resistance EN 1993-1-8 tab. 3.4
- $F_{s,Rd}$ Design slip resistance EN_1993-1-8 chapter 3.9
- F_{pc} Pretension force
- U_{t_t} Utilization in tension
- U_{t_s} Utilization in shear

Welds (Plastic redistribution)

Item	Edge	Throat th. [mm]	Length [mm]	Loads	$\sigma_{w,Ed}$ [MPa]	ϵ_{pl} [%]	σ_{\perp} [MPa]	τ_{\parallel} [MPa]	τ_{\perp} [MPa]	Ut [%]	Ut _c [%]	Status
End Plate Column	Column	▲6.0	1324	ULS Load	164.2	0.0	112.1	20.7	-66.1	37.7	12.7	OK
Beam-w 2	Beam	▲4.0▲	840	ULS Load	98.0	0.0	-39.2	-36.0	-37.3	22.5	4.3	OK
Beam-w 4	Beam	▲4.0▲	840	ULS Load	74.0	0.0	-29.6	-25.4	-29.8	17.0	2.7	OK
Beam-arc 6	Beam	▲4.0▲	1114	ULS Load	42.5	0.0	10.7	-21.0	11.1	9.8	1.2	OK
		▲4.0▲	840	ULS Load	107.1	0.0	-35.2	45.1	37.1	24.6	4.9	OK
		▲4.0▲	840	ULS Load	74.3	0.0	-29.9	25.5	29.8	17.1	2.6	OK
		▲4.0▲	1114	ULS Load	48.0	0.0	15.9	21.0	-15.5	11.0	2.2	OK
End Plate Beam	Stiffeners +Ya	▲4.0▲	125	ULS Load	56.0	0.0	26.7	-16.6	23.1	12.9	8.7	OK
		▲4.0▲	125	ULS Load	52.6	0.0	22.3	9.1	-25.9	12.1	7.1	OK
End Plate Beam	Stiffeners +Yb	▲4.0▲	125	ULS Load	45.6	0.0	15.3	-19.8	15.0	10.5	6.7	OK
		▲4.0▲	125	ULS Load	47.9	0.0	12.0	-24.1	-11.8	11.0	6.5	OK
End Plate Beam	Stiffeners +Yc	▲4.0▲	125	ULS Load	85.3	0.0	-37.5	25.0	-36.5	19.6	8.5	OK
		▲4.0▲	125	ULS Load	103.1	0.0	-47.2	-22.0	48.1	23.7	9.1	OK
End Plate Beam	Stiffeners - Ya	▲4.0▲	125	ULS Load	30.1	0.0	11.4	-12.5	10.1	6.9	3.7	OK
		▲4.0▲	125	ULS Load	33.9	0.0	10.1	14.8	-11.5	7.8	4.1	OK
End Plate Beam	Stiffeners - Yb	▲4.0▲	125	ULS Load	20.6	0.0	7.5	-8.8	6.7	4.7	2.7	OK
		▲4.0▲	125	ULS Load	21.2	0.0	5.9	9.7	-6.7	4.9	2.7	OK
End Plate Beam	Stiffeners - Yc	▲4.0▲	125	ULS Load	39.8	0.0	-20.3	5.1	-19.1	9.1	6.2	OK
		▲4.0▲	125	ULS Load	42.8	0.0	-20.1	-4.6	21.3	9.8	6.7	OK
End Plate Beam	Beam-w 3	▲6.0	530	ULS Load	208.7	0.0	26.8	36.8	113.7	47.9	14.2	OK
End Plate Beam	Beam-w 3	▲6.0	530	ULS Load	285.6	0.0	-63.2	160.5	-9.6	65.6	11.1	OK

Design data

	β_w [-]	$\sigma_{w,Rd}$ [MPa]	0.9 σ [MPa]
S 355	0.90	435.6	352.8

Project: Case Study
 Project no:
 Author: Bela Stamenkovits

Symbol explanation

ϵ_{Pl}	Strain
$\sigma_{w,Ed}$	Equivalent stress
$\sigma_{w,Rd}$	Equivalent stress resistance
σ_{\perp}	Perpendicular stress
τ_{\parallel}	Shear stress parallel to weld axis
τ_{\perp}	Shear stress perpendicular to weld axis
0.9σ	Perpendicular stress resistance - $0.9 \cdot f_u / \gamma_{M2}$
β_w	Corelation factor EN 1993-1-8 tab. 4.1
U_t	Utilization
U_{tc}	Weld capacity utilization

Buckling

Buckling analysis was not calculated.

Code settings

Item	Value	Unit	Reference
Y_{M0}	1.00	-	EN 1993-1-1: 6.1
Y_{M1}	1.00	-	EN 1993-1-1: 6.1
Y_{M2}	1.25	-	EN 1993-1-1: 6.1
Y_{M3}	1.25	-	EN 1993-1-8: 2.2
Y_C	1.50	-	EN 1992-1-1: 2.4.2.4
Y_{Inst}	1.20	-	EN 1992-4: Table 4.1
Joint coefficient β_j	0.67	-	EN 1993-1-8: 6.2.5
Effective area - influence of mesh size	0.10	-	
Friction coefficient - concrete	0.25	-	EN 1993-1-8
Friction coefficient in slip-resistance	0.30	-	EN 1993-1-8 tab 3.7
Limit plastic strain	0.05	-	EN 1993-1-5
Weld stress evaluation	Plastic redistribution		
Detailing	No		
Distance between bolts [d]	2.20	-	EN 1993-1-8: tab 3.3
Distance between bolts and edge [d]	1.20	-	EN 1993-1-8: tab 3.3
Concrete breakout resistance check	Both		EN 1992-4: 7.2.1.4 and 7.2.2.5
Use calculated a_b in bearing check.	Yes		EN 1993-1-8: tab 3.4
Cracked concrete	Yes		EN 1992-4
Local deformation check	No		CIDECT DG 1, 3 - 1.1
Local deformation limit	0.03	-	CIDECT DG 1, 3 - 1.1
Geometrical nonlinearity (GMNA)	Yes		Analysis with large deformations for hollow section joints
Braced system	No		EN 1993-1-8: 5.2.2.5

Software info

Application: IDEA StatiCa Connection
 Version: 21.1.1.1638

Project: Case Study
Project no:
Author: Bela Stamenkovits

Developed by IDEA StatiCa

